Cobaltocenium Amides

Photoinduced Electron Transfer Processes in

Donor-Acceptor Amides

Dissertation

Zur Erlangung des Grades

„Doktor der Naturwissenschaften"

Im Promotionsfach Chemie

am Fachbereich Chemie, Pharmazie, Geographie und Geowissenschaften

der Johannes Gutenberg-Universität Mainz

Maximilian Thomas Johannes Lauck

Geboren in Mainz am 22. April 1990

Mainz 2019

Die vorliegende Arbeit wurde unter der Betreuung von Prof. _____ in der Zeit vom Juni 2014 bis November 2019 am Institut für Anorganische Chemie und Analytische Chemie der Johannes Gutenberg-Universität Mainz angefertigt.

Mainz, den 27. November 2019

Dekan: _____

1. Berichterstatter: _____

2. Berichterstatter: _____

Tag der mündlichen Prüfung: 17. Januar 2020

Ich, Maximilian Thomas Johannes Lauck, Matrikelnummer _____, versichere, dass ich meine Promotionsarbeit selbstständig verfasst und keine anderen als die angegebenen schriftlichen und elektronischen Quellen benutzt habe. Alle Ausführungen, die anderen Schriften wörtlich oder Sinngemäß entnommen wurden, habe ich kenntlich gemacht.

Datum   Unterschrift

Abstract

Natural processes like photosynthesis, energy storage, energy transformation and energy transport are very efficient. Scientists are still working on the understanding of the basic principles of these processes, whereby the technology transfer on biomimetic model complexes and efficient applications is forced. Thus, the dependency on fossil fuels should be reduced and efficient energy storage and transport should be facilitated.

Organometallic „Sandwich" complexes, like ferrocene and cobaltocenium, are competent to reversibly accept and donate electrons. Linked by peptide bridges, oligometallocenes can be used as nanowires for information transfer. By oxidation or reduction, respectively, the oligomers can change their conformation and operate as molecular switches. The development of a synthesis for N-cobaltocenium peptides [Cc-NH-CO-R]$^+$ makes the manufacturing of oligopeptides, consisting of a cationic cobaltocenium backbone, possible. The new substitution pattern will expand the bandwidth of possible redox properties for substituted cobaltocenium complexes, which opens new fields for research. The here presented N-cobaltocenium amides (R = Ph, Fc, Cc$^+$) were prepared and analyzed by multiple techniques, like NMR, IR and UV/vis spectroscopy, cyclic voltammetry, spectroelectrochemistry and single crystal X-ray diffraction. Here, electron transfer bands could be observed, which were assigned by Density Functional Theory calculations. By Hush analysis of these charge transfer bands, the properties of the investigated bimetallocenes could be compared with similar bimetallocenes and understood.

Porphyrins are chromophores, which are similar to the natural pigments of the photosynthesis cascade and possess distinctive properties for light absorption. By irradiation, the porphyrin is excited and energy is emitted via fluorescence or phosphorescence. With potential electron acceptors close by, photoinduced electron transfer to this acceptor is possible. Cobaltocenium is a suitable electron acceptor, which is a powerful reductant after reduction to cobaltocene. The reduction force is strong enough to reduce protons to molecular hydrogen. The here presented amide linked cobaltocenium porphyrin conjugate was investigated in terms of the catalytic hydrogen evolution. NMR, IR und UV/vis spectroscopy, cyclic voltammetry, spectroelectrochemistry, transient-absorption spectroscopy and single crystal X-ray diffraction were used to understand the principle electron transfer processes of this donor acceptor peptide. The redox potentials of the dyad show, that the charge-shifted state is able to reduce protons. Photoinduced electron transfers from porphyrin to cobaltocenium, starting from the excited singlet S_1 and triplet T_1 states of the porphyrin, were demonstrated.

Kurzzusammenfassung

Die natürlichen Prozesse der Photosynthese, Energiespeicherung, Energietransformation und des Energietransportes stellen eine Meisterleistung der Effizienz dar. Immer noch wird mit Hochdruck an der Entschlüsselung der grundlegenden Prinzipien gearbeitet, wobei der Transfer auf biomimetische Modelkomplexe und effiziente Anwendungen forciert wird. Hierdurch soll die Abhängigkeit von fossilen Energieträgern verringert und eine effizientere Energiespeicherung und -übertragung ermöglicht werden.

Organometallische „Sandwich"-Komplexe wie z.B. Ferrocen und Cobaltocenium sind befähigt, reversibel Elektronen aufzunehmen und wieder abzugeben. Als verknüpfte Oligopeptide könnten diese als Nanodrähte Informationen übermitteln, oder als molekulare Schalter durch Oxidation oder Reduktion ihre Konformation ändern. Die neu entwickelte Synthese von *N*-Cobaltoceniumamiden [Cc-NH-CO-R]$^+$ ermöglicht hierbei die Herstellung von Oligopeptiden mit Cobaltocenium Rückgrat. Durch das neue Substitutionsmuster wird zudem die Bandbreite möglicher Redoxeigenschaften von substituierten Cobaltocenium Komplexen erhöht, was wiederum neue Forschungsfelder eröffnet. Die hier dargestellten *N*-Cobaltoceniumamide (R = Ph, Fc, Cc$^+$) wurden mittels einer Vielzahl analytischer Methoden untersucht, u.a. NMR, IR und UV/Vis Spektroskopie, Cyclovoltammetrie, Spektroelektrochemie und Einkristallstrukturanalyse. Hierbei konnten Elektronentransferbanden beobachtet werden, welche durch dichtefunktionaltheoretische Berechnungen erklärt werden konnten. Mittels Hush-Analyse der Elektronentransferbanden konnten die Eigenschaften der hier untersuchten Bimetallocene mit ähnlichen Bimetallocenen verglichen und verstanden werden.

Porphyrine sind Chromophore, welche den natürlichen Pigmenten der Photosynthesekaskade gleichen und sehr ausgeprägte Lichtabsorptionseigenschaften besitzten. Das Porphyrin wird durch elektromagnetische Strahlung im sichtbaren Bereich angeregt, welches Energie in Form von Fluoreszenz oder Phosphoreszenz abstrahlen kann. Ist ein potentieller Elektronenakzeptor zugegen, so ist ein photoinduzierter Elektrontransfer zu diesem Akzeptor möglich. Hierfür ist Cobaltocenium ein geeigneter Elektronenakzeptor, welcher im reduzierten Zustand ein potentes Reduktionsmittel darstellt und Protonen zu molekularem Wasserstoff reduzieren kann. Die hier dargestellte Amid-verbrückte Cobaltocenium-Porphyrin Verbindung wurde unter dem Aspekt der katalytischen Wasserstoff Herstellung untersucht. Hierbei wurden u.a. NMR, IR und UV/Vis Spektroskopie, Cyclovoltammetrie, Spektroelektrochemie, Transienten-Absorptionsspektroskopie und Einkristallstrukturanalyse angewendet, um die grundlegenden Elektronentransferprozesse innerhalb dieses Donor-Akzeptor Peptids zu verstehen. Die ermittelten Redoxpotentiale beweisen, dass der Modellkomplex im ladungsverschobenen Zustand ausreichend Energie besitzt um Protonen zu molekularem Wasserstoff zu reduzieren. Der erwartete Elektrontransfer vom angeregten Porphyrin

zum Cobaltocenium-Substituenten konnte ausgehend vom angeregten Porphyrin Singulett- als auch vom Triplett-Zustand (S_1/T_1) nachgewiesen werden.

Contents

Abbreviations

Ac	acetyl (CH_3-CO-)
ATP	adenosine triphosphate
Bn	benzyl group (C_6H_6-CH_2-)
Boc	*tert*-butyloxycarbonyl group (($H_3C)_3$-O-CO-)
calcd.	calculated
Cc	cobaltocenyl group (Co(C_5H_5)(C_5H_4-))
CcH	cobaltocene (Co($C_5H_5)_2$)
COSY	correlated spectroscopy (NMR spectroscopy)
Cp	cyclopentadienyl anion ($[C_5H_5]^-$)
CR	charge recombination
CRes	charge resonance
CSh	charge shift
Cyt	cytochrome
δ	chemical shift (NMR spectroscopy)
ΔT	temperature difference
DFT	Density Functional Theory
ε_{max}	extinction coefficient of the absorption maximum
EH	electron hole
EnT	energy transfer
ES	excited state
ESI	electrospray ionization
ET	electron transfer
Fc	ferrocenyl group (Fe(C_5H_5) (C_5H_4-))
Fca	ferrocenyl amino acid group ((C_5H_4CO-)Fe(C_5H_4NH-))
FcH	ferrocene (Fe($C_5H_5)_2$)
FD	field desorption
Fmoc	fluorenylmethyloxycarbonyl group ($C_{13}H_8$-CH_2O-CO-)
FNR	ferredoxin-NADP$^+$ reductase
FRET	Förster resonance energy transfer
G	Gibbs energy
GS	ground state
H_{AB}	electronic coupling matrix element
HER	hydrogen evolution reaction
HMBC	heteronuclear multiple bond correlation (NMR spectroscopy)

HOMO	highest occupied molecular orbital
HR	high resolution
HSQC	heteronuclear single quantum coherence (NMR spectroscopy)
IC	internal conversion
Int	intensity
IR	infrared
ISC	intersystem crossing
IVCT	intervalence charge transfer
λ	reorganization energy
LHC	light-harvesting complex
LMCT	ligand-to-metal charge transfer
LUMO	lowest unoccupied molecular orbital
m	mass
Me	methyl group (H_3C-)
MLCT	metal-to-ligand charge transfer
$\Delta\tilde{\nu}_{0.5}$	bandwidth at half-height of the IVCT band
$\tilde{\nu}_{max}$	maximum of the IVCT band
$NADP^+$	nicotinamide adenine dinucleotide phosphate
NADPH	protonated and reduced nicotinamide adenine dinucleotide phosphate
NIR	near-infrared
NMR	nuclear magnetic resonance
NOE	nuclear Overhauser effect
obs.	observed
OEC	oxygen-evolving complex
OER	oxygen evolution reaction
P	see P(Zn)
P(2H)	free base tetraphenyl porphyrin
P(Zn)	also Zn(P); zinc tetraphenylporphyrin
PET	photoinduced electron transfer
phthyl	phthyl group ((2E,7R,11R)-3,7,11,15-tetramethyl-2-hexadecenyl)
r.c.	reaction coordinate
r.t.	room temperature
r_{AB}	distance between two reaction centers
R_f	retention factor
SP	special pair

T	triplet recombination
^{t}Bu	*tert*-butyl ((H$_3$C)C-)
TD-DFT	time-dependent Density Functional Theory
THF	tetrahydrofuran
TLC	thin layer chromatography
TON	turn over number in mole substrate per mole catalyst per time
TPP^{2-}	*meso*-tetraphenylporphyrinato
tpphz	tetrapyridophenazine
UV	ultraviolet
VE	valence electron
vis	visible
z	charge

1   Introduction

Natural bioinorganic processes, such as light harvesting, energy transfer and energy storage in the photosynthesis system, show high efficiencies under the given conditions i.e. light intensity and spectral distribution.[1–4] Most of the underlying mechanisms rely on the vast mutability of the properties of transition metals.[1] The oxidation or reduction of transition metals affect the favored coordination number and the metal to ligand bonding. Furthermore, new electron transfer (ET) reactions are made possible due to new formed electron acceptor or donor properties.

Ferrocene (FcH) as an 18 valence electron (VE) complex shows a high redox stability and possesses a large substitution pattern, wherefore FcH is used as redox reference in electrochemistry. These properties make ferrocene a popular electron donor for donor-acceptor systems to investigate ET reactions. Especially Fc complexes with amide linkage attract wide interest, since transition metals in biological systems are commonly surrounded by well-defined peptides. This makes an amide linkage a favored bridging tool for biomimetic model complexes.[5,6]
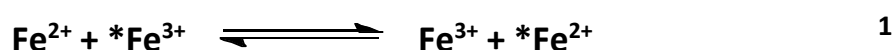
Cobaltocene (CcH) owns 19 valence electrons and is isostructural to ferrocene (18 VE). Cobaltocene is a strong reductant, due to the additional electron, which can reduce protons.[7] In opposite, the oxidized cobaltocene (CcH$^+$) (18 VE) is an easy to handle compound. The CcH/CcH$^+$ couple shows a similar redox stability compared to FcH/FcH$^+$, so that the use as electron acceptor in biomimetic model complexes is obvious. Due to the charge, the reactivity of CcH$^+$ in substitution reactions is drastically changed compared to FcH. The positive charge facilitates nucleophilic reactions at the cobalt center and inhibits electrophilic substitution reactions at the ligand, which are typical for ferrocene. Thereby, the known range of substituted cobaltocenium derivatives is quite small.[8,9] The use as electron acceptor in artificial photosynthesis models was neglected up to date.

Porphyrins are chromophores, which artificial synthesis was inspired by natural chlorophylls, cobalamines and heme.[1] Porphyrins show high extinction coefficients,[10] which makes them suitable pigments for artificial photosynthesis models.[11,12] Over the last decades, the research on substituted derivatives was forced by metalation of the porphyrin or substitution at the ligand backbone to achieve improved absorption properties or to enable catalytic activity. The development of porphyrinic "amino acid" was an important step to synthesize peptide linked model systems,[10] whereby the linkage plays a crucial role in the electron transfer dynamics. The used catalytically active electron acceptors often based on noble metals, which lead to high activities and knowledge to understand the fundamental mechanisms of the electron transfer reactions. However, the utilization of noble metals also prevents the extensive use at a large scale, which enforces to carry on research on transition metal catalysts.[12–14]

1.1 Electron Transfer Reactions

The redox reaction is a fundamental type of chemical reactions. Typical redox reactions are known since the beginning of modern chemistry, but the knowledge of the basic principles of the mechanisms started to be collected in the 1940th.[13–18] The upcoming of nuclear chemistry made the investigation of self-exchange reactions possible due to the availability of radionuclides (Equations 1 and 2, * denotes the radionuclide).[17,18] In here, the metal center of the complex as well as the ligands can be labeled. The development of new analytical instruments on the other hand made the observation of these reactions feasible. The research of such mechanisms is important for the understanding of biological systems like photosynthesis or in vivo energy storage.[2,4]

$$Fe^{2+} + *Fe^{3+} \rightleftharpoons Fe^{3+} + *Fe^{2+} \tag{1}$$

$$Fe(CN)_6^{4-} + *Fe(CN)_6^{3-} \rightleftharpoons Fe(CN)_6^{3-} + *Fe(CN)_6^{4-} \tag{2}$$

In future, with the change to efficient green energy concepts, the knowledge and use of these principles can help to develop new ways to transform and store natural resources such as more efficient solar energy harvesting or *Power-to-Gas* techniques.[19]

1.1.1 Marcus Theory

In the 1950s, Marcus investigated self-exchange reactions between metal ions of different valences.[13,14,20] For diabatic systems with a low electronic communication between the redox sites, Marcus summarized, that electron transfer processes occur via thermal and optical charge transfer, as well as tunneling.[21] In Figure 1, all the involved atoms of reactants, solvent and products are summed up, moving on a potential energy hypersurface.
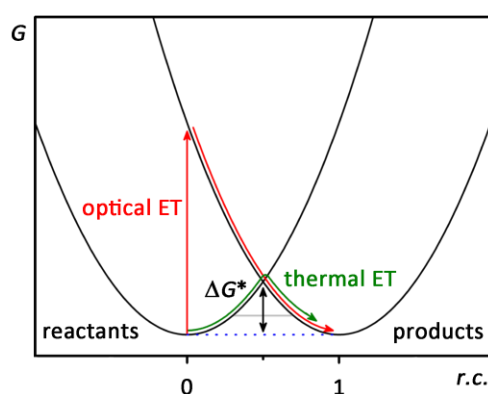
Figure 1. Plot of the free energy *G* versus the reaction coordinate *r.c.* showing the reactants (left curve) and the products (right curve). Additionally, the pathways of the optical ET (red line), the thermal ET (green line) and tunneling (grey line), as well as the activation energy Δ*G** are depicted.

Marcus ascertained, that two rules are applicable for the electron transfer: the Frank-Condon principle[22–24] and energy conservation.[20]

This means, the optical electron transfer and the diabatic thermal charge transfer are significantly faster than the motion of the atoms. Therefore, the distance of the redox sites during the electron transfer can be considered as fixed. On the other hand, the electron transfer occurs on the saddle point of the potential hypersurface, whereby activation energy is necessary to climb the energy barrier ΔG^*. The overall system has to absorb the activation energy prior the electron transfer. This is possible via optical excitation or thermally via vibrational fluctuations to higher vibrational modes.[20,25]

The rate constant for the thermal electron transfer is given by Equation 3, involving the energy barrier ΔG^* and the temperature.[20,25]

$$k_{ET} = A \exp\left(\frac{-\Delta G^*}{k_B T}\right) \qquad \textbf{3}$$

Marcus was also able to identify a relation between the energy barrier ΔG^*, the change of the free energy ΔG^0 and the reorganization energy λ (Equation 4):[21,25]

$$\Delta G^* = \frac{\lambda}{4}\left(1 + \frac{\Delta G^0}{\lambda}\right)^2 \qquad \textbf{4}$$

The reorganization energy λ includes the inner and outer sphere of the reactants, like the reorientation of solvent molecules and the adjustment of intramolecular bond lengths and angles.

For self-exchange reactions, there is no change of the free energy ΔG^0 ($\Delta G^0 = 0$) given, so Equation 4 simplifies to Equation 5:[25]

$$\Delta G^* = \frac{\lambda}{4} \qquad \textbf{5}$$

By inserting Equation 4 in Equation 3, a correlation between the rate constant of the electron transfer k_{ET} and the change of the free energy ΔG^0 is possible:

$$k_{ET} = A \exp\left(\frac{-\lambda\left(1 + \frac{\Delta G^0}{\lambda}\right)^2}{4 k_B T}\right) \qquad \textbf{6}$$

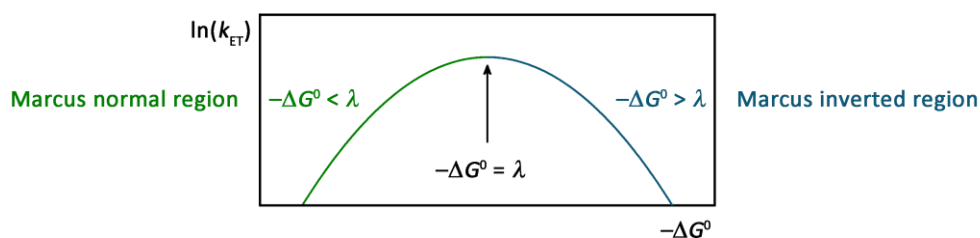Plotted as a logarithmical curve as in Figure 2, it is possible to predict the maximum rate for the electron transfer.[21]

Figure 2. Plot of the logarithmic ET reaction rate ln(k_{ET}) versus the negative standard free energy $-\Delta G^0$ showing the Marcus normal region (green line left side) and the Marcus inverted region (blue line right side).

Thereby, the rate constant k_{ET} ascends from $-\Delta G^0 = 0$ up to $0 < -\Delta G^0 < \lambda$ (Marcus normal region) until the maximum rate is reached with $-\Delta G^0 = \lambda$. For $-\Delta G^0 = \lambda$, no energy barrier exits, so the charge transfer occurs by the contact of both redox centers. Following the graph (Figure 2) with $-\Delta G^0 > \lambda$ (Marcus inverted region), k_{ET} decreases, while the reaction becomes more exergonic.[21] The effects of these three classes of $-\Delta G^0$ are depicted in Figure 3 in dependence of the reaction coordinate. By appropriate exchange of the ligands for example, a reaction can be shifted from one region to another.
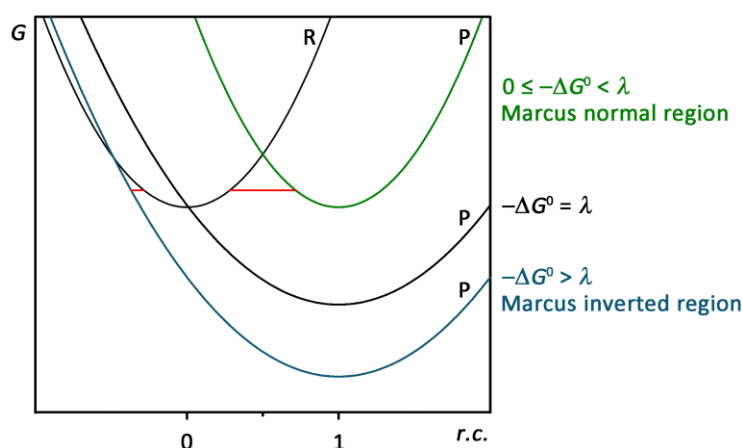

Figure 3. Plot of the free energy G versus the reaction coordinate *r.c.* showing the reactants (left curve) and the products (right curves). From the top to the bottom, the products switch from the Marcus normal region to the Marcus inverted region. The red lines show possible "tunneling paths".

By switching from the Marcus normal region to the Marcus inverted region, the chance for nuclear tunneling rises, which distorts the curve of ln(k_{ET}) in Figure 2 asymmetrically. This phenomenon can be explained by a "shorter path" for the tunneling process (Figure 3, red lines).[21]

1.1.2   Marcus-Hush Theory

Since Marcus theory uses a diabatic system with a moderate electronic communication, Hush expanded his theoretical approach (Marcus-Hush Theory) on adiabatic systems.[26,27] These systems show a high electronic communication between the active sites, which are linked by a rigid bridging ligand. This commitment is possible for the case that the thermal energy is smaller than the energy needed for the electronic communication between the two involved redox centers.
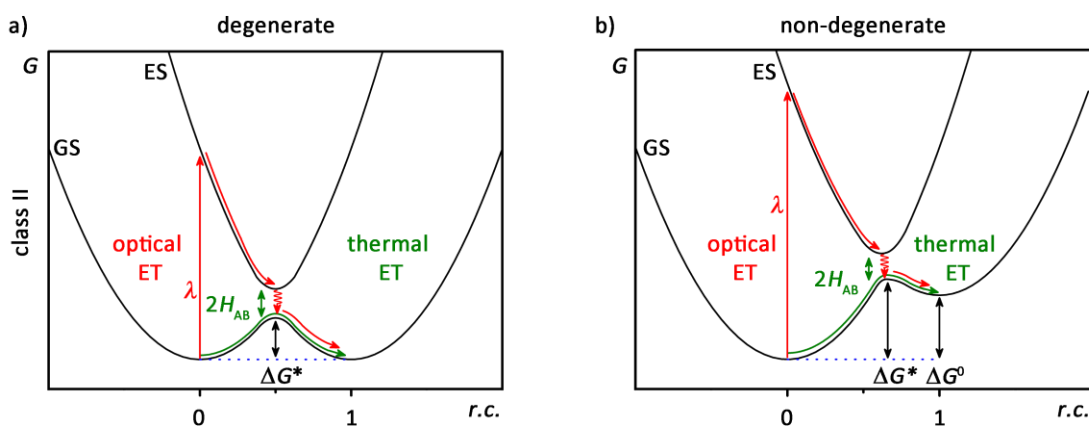
Figure 4. Marcus-Hush diagrams depicting the adiabatic approach. Plots of the free energy *G* versus the reaction coordinate *r.c.* showing the pathways of the optical ET (red line) and the thermal ET (green line), as well as the activation energy Δ*G** and the standard free energy of the reaction Δ*G*⁰.

In the adiabatic system, the excited state (ES) is separated from the ground state (GS) by a 2 H_{AB} energy gap.[28] Due to electronic interactions of the reactants, the energy barrier decreases and the two minima are more stabilized compared to the diabatic system (Chapter 1.1.1), resulting in a lowering of their energy by $(H_{AB})^2/\lambda$.[28] In opposite, the energy of the excited state increases with increasing H_{AB}. The energy of barrier between the two minima can be calculated in dependence of H_{AB} as

$$\Delta G^* = \frac{(\lambda - 2H_{AB})^2}{4\lambda} \qquad\qquad 7$$

for degenerate systems[28] (Figure 4a) and for non-degenerate systems (Figure 4b) as follows:[28]

$$\Delta G^* = \frac{\lambda}{4} + \frac{\Delta G^0}{3} + \frac{(\Delta G^0)^2}{4(\lambda - 2H_{AB})} - H_{AB} + \frac{(H_{AB})^2}{\lambda + \Delta G^0} \qquad\qquad 8$$

1.1.3 Robin-Day Classification

Mixed-valent systems own two or more redox active sites, which possess different oxidation states. Depending on the linkage between these centers, different levels of communication between these redox sites are possible.[29,30]

To classify the level of communication between two mixed-valent redox centers, Robin and Day developed a three-class system, with H_{AB} as the electronic coupling element.[31,32] Plotting the reaction coordinate against the potential energy of the system, H_{AB} is given as the energy between the ground state and the first electronically excited state at the diabatic crossing point.[33]
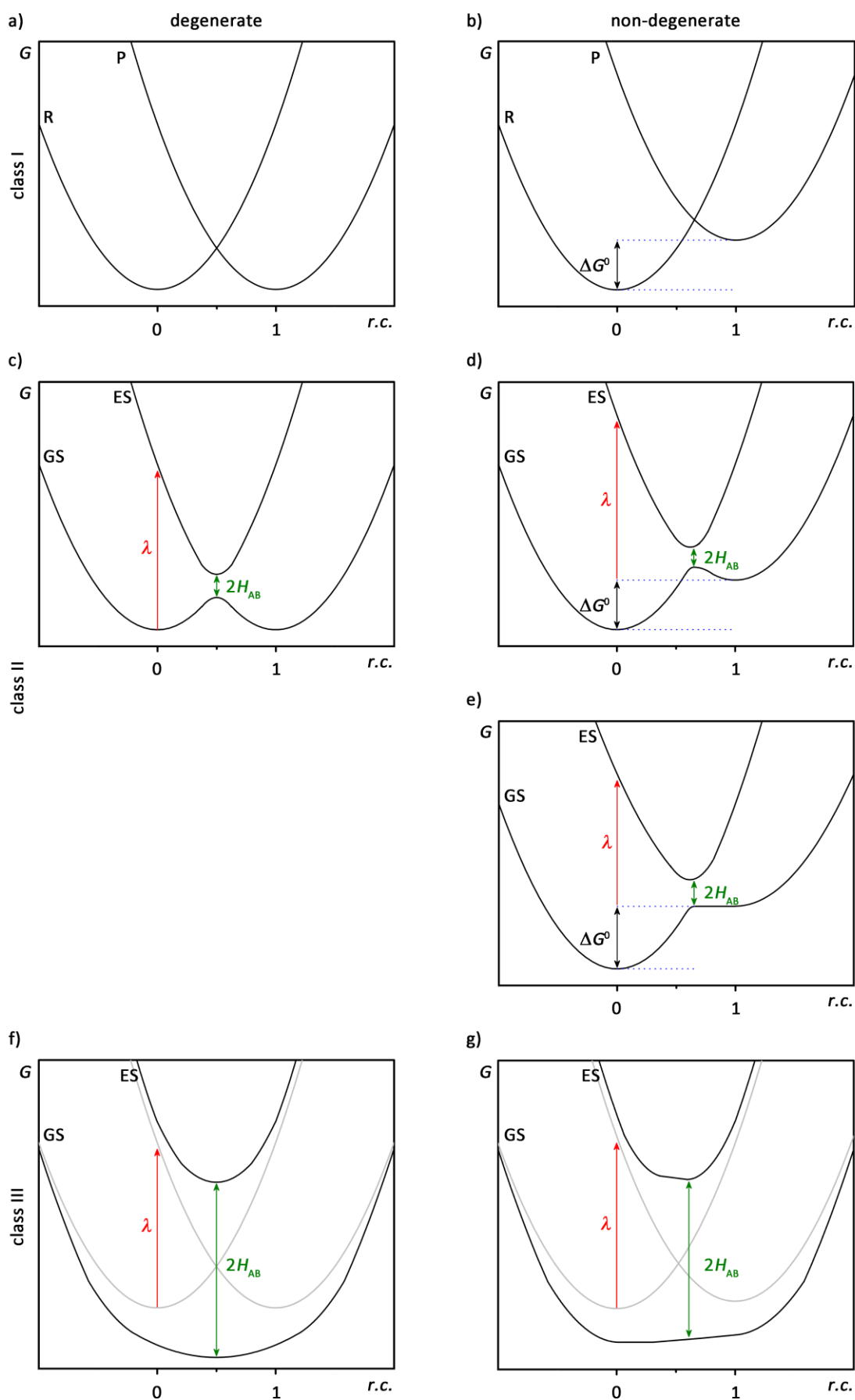
Figure 5. Plots of the free energy _G_ versus the reaction coordinate _r.c._ showing the reactants (left curves) and the products (right curves). From the top to the bottom, the products switch from Robin Day class I to class III and the symmetry changes from the left to the right.

A Robin-Day Class I system describes a system, which possesses no electronically communication ($H_{AB} = 0$), so no thermal or optical ET is possible, regardless of the symmetry of the system (Figure 5a and b). Both redox sites behave and react like two individual independent redox sites, which do not interact with each other (Figure 6a).[31]

Compounds with two mixed-valent redox centers, which do influence each other, are categorized as Robin-Day class II system and show a medium electronic communication, with $0 < 2H_{AB} < \lambda$. These interactions for example are observable due to the upcoming of an intervalence charge transfer (IVCT) band in the electronic spectrum (Figure 8a and b) or via shifted redox potentials, compared to these of the single independent redox centers (Figure 6b).[31,34]
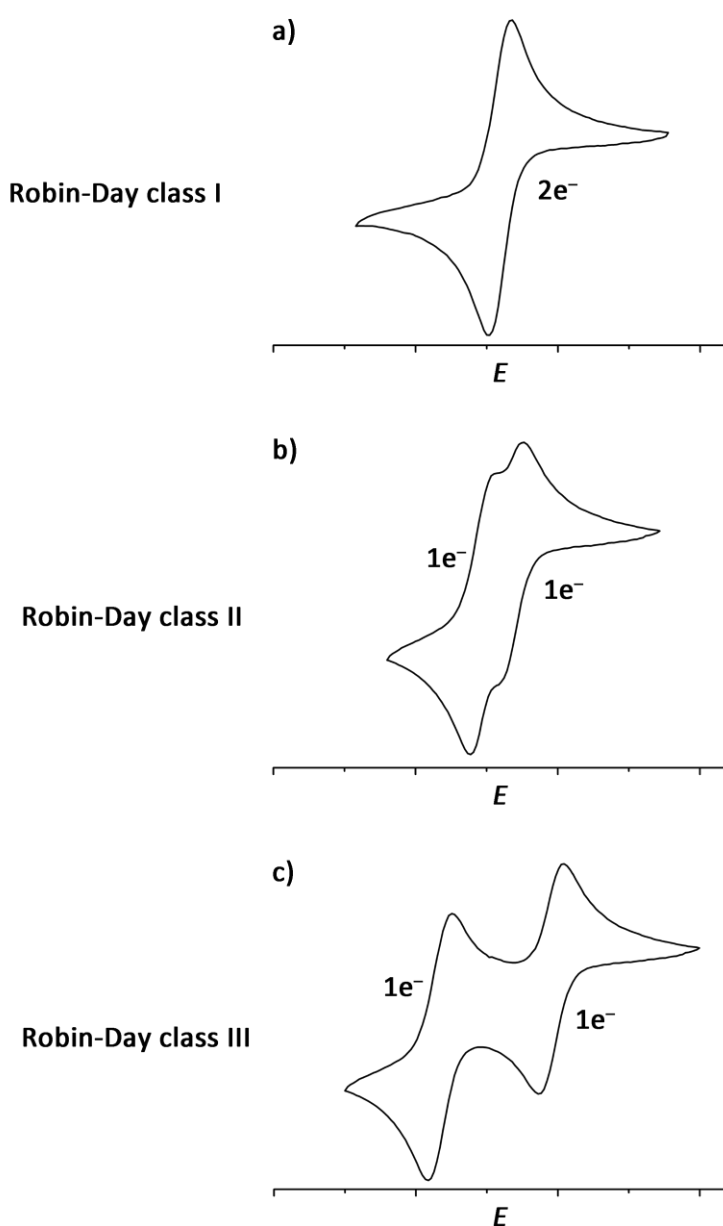

Figure 6. Cyclic voltammograms of Robin-Day class I-III systems (schematic), with identical environments for both redox sites.

In cases, that an IVCT band is observable (Figure 5c-e), H_{AB} is given as follows[35,36] (Equation 9), using the absorption maximum $\tilde{v}_{max}$, the extinction coefficient ε_{max} of the absorption maximum, the bandwidth at half-height of the band $\Delta\tilde{v}_{0.5}$ and the distance between the two redox sites r_{AB}:

$$H_{AB} = 2.06 \times 10^{-2} \frac{\sqrt{\varepsilon_{max}\, \Delta\tilde{v}_{0.5}\, \tilde{v}_{max}}}{r_{AB}} \qquad\qquad 9$$

The redox centers of Robin-Day class III compounds show no individual properties, they are always depending on each other (Figure 6c).[31] The electron is fully delocalized and $2H_{AB}$ is larger than λ (Figure 5f and g). Optical excitation does not lead to an electron transfer between both redox centers, but to an electronically excited state with a charge resonance (CRes) band (Figure 8c and d).[37] The most famous example for a mixed valent transition metal class III system is the Creutz-Taube ion (Figure 7).
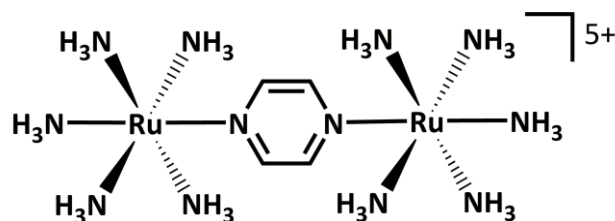

Figure 7. Creutz-Taube ion.

The Creutz-Taube ion with a charge of 5+ possesses two ruthenium metal centers in the formal oxidation states of 2+ and 3+. Due to the identical environment and the small conjugated bridging ligand (pyrazine), the electronic communication is too fast to localize the moving electron. Therefore, only an averaged oxidation state of 2.5+ for both metal centers can be assigned. These properties make the Creutz-Taube ion a well-studied compound for electron transfer reactions. Nowadays, the classification of the Creutz-Taube ion as class III system is still controversial discussed.[32,38] Over the years, several mixed-valent systems were synthesized, also for electron transfer studies. They show highly delocalized electrons, like biferrocenium,[39] Prussian blue[32] or organic radicals[40].

1.1.4 Photoinduced Electron Transfer – Intervalence Charge Transfer and Charge Resonance

For Robin-Day class II systems, optical transitions allow the electron transfer from one redox center to another. These transitions arise from the ground state and, due to thermal activation (Boltzmann distribution), also from several vibrational excited states. The resulting intervalence charge transfer band (IVCT) shows a bandwidth with a Gaussian distribution[35,36] (Figure 8a and b).

For symmetric Robin-Day class III systems (Figure 8c), the ground state and the excited state curves show both a single symmetric minimum. Here, only half of the energetically different transitions are possible compared to the class II systems. The result is a charge resonance band, which possesses the shape of a Gaussian curve, whereby the second half of the curve is cut off.[36] Borderline cases between

class II and III show a relatively strong coupling H_{AB} due to the increase of the gap between ground and excited state, resulting in asymmetric IVCT bands.[29,30,36,41,42] For non-degenerate class III systems, the curves are asymmetric, but still own one minimum each. Therefore, the observable charge resonance band shows an asymmetric shape (Figure 8d).[29,30]
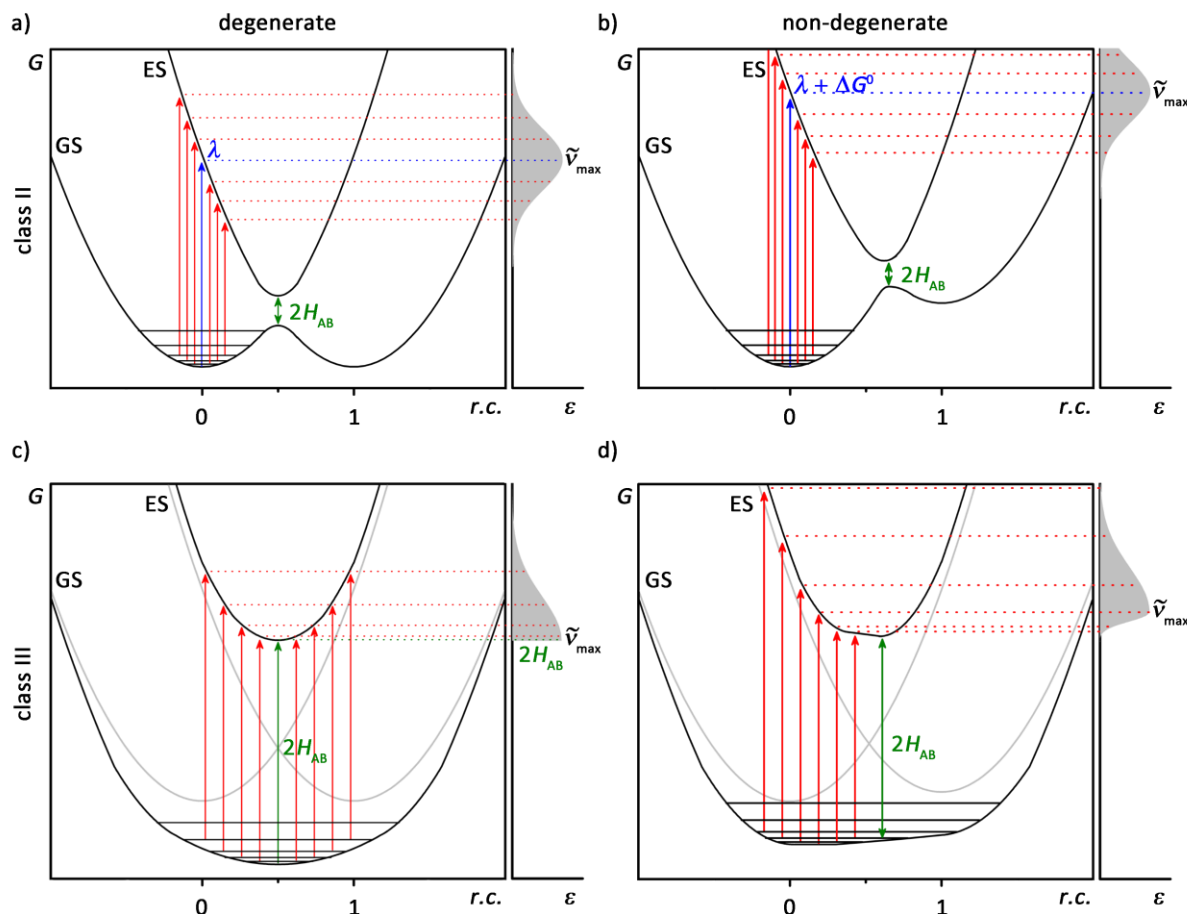

Figure 8. Plots of the free energy *G* versus the reaction coordinate *r.c.* showing the reactants (left curves) and the products (right curves). From the top to the bottom, the products switch from Robin-Day class II to class III and the symmetry changes from the left to the right. The curves on the right of each graph show the band shape of the IVCT/CRes band.

The main transition $\tilde{\nu}_{max}$ depicts the sum of the standard free energy ΔG^0 and the reorganization energy λ (Equation 10).[36]

$$\tilde{\nu}_{max} = \lambda + \Delta G^0 \qquad\qquad \textbf{10}$$

For degenerate class II and III systems ($\Delta G^0 = 0$), the reorganization energy λ and the maximum absorption of the IVCT band $\tilde{\nu}_{max}$ are equal (Equation 11):

$$\tilde{\nu}_{max} = \lambda \qquad\qquad \textbf{11}$$

Additionally, the calculation of the electronic coupling element H_{AB} is possible by the so-called Hush analysis, by analyzing the observed IVCT/CRes band. For degenerate class III systems, the absorption maximum $\tilde{\nu}_{max}$ equals $2H_{AB}$ (Figure 8c; Equation 12):[36]

$$\tilde{v}_{max} = \lambda = 2H_{AB} \qquad \qquad \textbf{12}$$

For symmetric class II systems, the calculation of H_{AB} is more complicated, using the absorption maximum $\tilde{v}_{max}$, the extinction coefficient ε_{max} of the absorption maximum, the bandwidth at half-height of the band $\Delta\tilde{v}_{0.5}$ and the distance between the two redox sites r_{AB} in Equation 9.[36]

Tuczek et al investigated ET processes in ferrocene-ferrocenium and ferrocene-cobaltocenium conjugates. The Fc-Fc⁺ dyad possesses a single unpaired electron (open-shell system) located on Fc⁺, before and after ET occurs. In contrary, the Fc-Cc⁺ dyad owns only paired electrons (closed-shell system). During the electron transfer, one electron pair of Fc is split and a single electron is transferred from Fc to Cc⁺. The dyad Fc⁺-Cc owns two single unpaired electrons (open-shell system), one located on each metallocene. For a closer view on the electron configuration of the single metallocenes (paired versus unpaired electrons), see Figure 9. To take the process of the electron pair splitting into account, which consumes additional energy, Equation 9 was modified for closed-shell class II systems (Equation 13):[43]

$$H_{AB} = 2.05 \times 10^{-2} \; \frac{\sqrt{0.5\,\tilde{v}_{max}\varepsilon_{max}\Delta\tilde{v}_{0.5}}}{r_{AB}} \qquad \qquad \textbf{13}$$

1.2 Metallocenes

During the last 65 years, the world of metallocenes changed the view on organometallic chemistry.[44] These "sandwich complexes" are used in homogeneous catalysis,[45–47] sensing applications,[48–51] electrochemistry as references,[52,53] redox mediation[54–56] and redox switchable catalysts.[57–59] The metal center controls the reactivity of the open amenable organic rings, depending on the electron configuration and the charge. By varying the tilt angle of the sandwich complex, the metal ion is better (or less) accessible, which allows to control the catalytical activity or to protect the nuclei against decomposition reactions.[60]

1.2.1 Electronic Configuration of d^6 Metallocenes

Cobaltocenium and ferrocene are 18 VE complexes, which are isolobal to each other. Both possess an $(e_{2g})^4(a_{1g})^2$ electron configuration with an $^1A_{1g}$ ground state (Figure 9). Whereby FcH is able to be oxidized to FcH$^+$, and CcH$^+$ can be reduced to CcH at a potential of -1.33 V$^{[53]}$ (vs. FcH/FcH$^+$), owning electronic configurations of $(e_{2g})^4(a_{1g})^1$ and $(e_{2g})^4(a_{1g})^2(e_{1g})^1$ (Figure 9), respectively.[61–63]
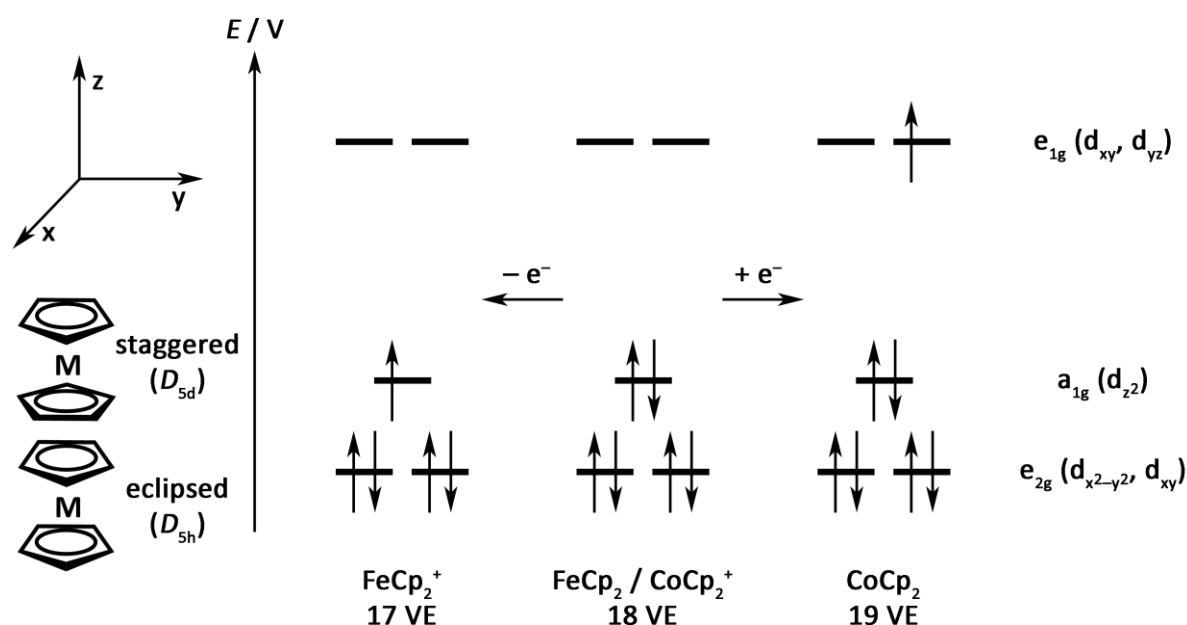

Figure 9. Electron configuration of the 3d orbitals of ferrocenium, ferrocene/cobaltocenium and cobaltocene, Cp = cyclopentadienyl.

The oxidation of FcH to FcH$^+$ involves the a_{1g} orbital, which is essentially metal-centered and slightly bonding (Figure 9), leading in the elongation of the Cp-Fe distance (Cp = cyclopentadienyl) due to the weakening of a bonding orbital (2.05 Å (FcH)$^{[64]}$/2.06-2.10 Å (FcH$^+$)$^{[65]}$). In contrary, the reduction of CcH$^+$ involves the e_{1g} orbital (Figure 9), which possesses Co-Cp antibonding character. The occupation of the e_{1g} orbital leads also to a significant elongation of the Cp-Co distance from CcH$^+$ to CcH (2.02Å (CcH$^+$)$^{[66]}$/2.10Å (CcH)$^{[67]}$). Additionally, the strong ligand-centered character of the e_{1g} orbital lowers the energy barrier for ET reactions involving Cc/Cc$^+$ units, observable in rising HAB values (compared to Fc/Fc$^+$). The reason can be found in the short distance of the ligand centered e_{1g} orbitals (compared

to the metal centered a_{1g} orbital) to the amide linkage (and therefore the other electron donor/acceptor).

1.2.2 Cobaltocenium Derivatives

Metallocenes can be functionalized in two ways: either the ligand is substituted prior to the complexation reaction,[68,69] or after complexation.[6,70,71] The substitution of the free ligand is challenging because cyclopentadiene dimerises in short times[72] and the cyclopentadienyl anion is water and oxygen sensitive.[73] Substitutions by this method are limited to electrophilic reactions with hydroxylamine derivatives, for example.[68,74,75] Hence, substitution after metal complexation is more popular.

Ferrocene as 18 VE homologous of cobaltocenium is an electron rich uncharged complex. The substitution possibilities are numerous, often initiated by electrophilic reactions such as lithiation.[76] As a result, the redox potential of ferrocene is easily adjustable by its substitution pattern.[6,54] In contrary, cobaltocenium is positively charged and nucleophiles like chloride and carbanions are attacking the highly charged Co^{III} metal center. The reduced form (cobaltocene) is not easy to handle due to its high reduction potential.[53] As a result electrophiles are reduced prior reaction.

As a result, the known substitution pattern of cobaltocenium was limited and the synthetic routes are difficult to reproduce.[9] For synthesis, modified cyclopentadienes such as methylcyclopentadiene are often used.[9] In the recent years, the group of Bildstein published reliable pathways for the preparation of $[Cc-X]^+$ with X = NH_2, COOH, Cl, Br, I, C≡C-H (Figure 10).[8,77,78] Hence, more cobaltocenium containing molecules like redox switchable catalysts[58,59] and other cobaltocenium building blocks[79] are accessible.[79,80]
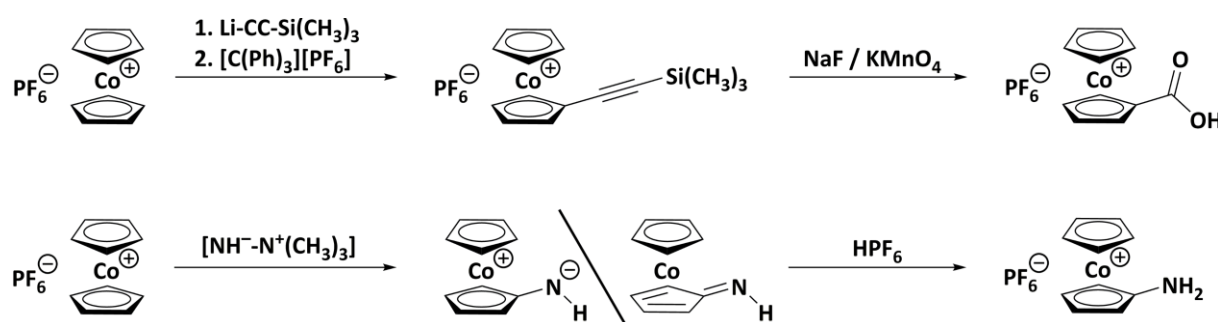

Figure 10. Improved syntheses of carboxycobaltocenium hexafluoridophosphate and aminocobaltocenium hexafluorido-phosphate by Bildstein.

1.2.3 Cobaltocenium Containing Peptides

Ferrocene containing peptides are well accessible from amino or acid compounds, or artificial amino acids.[81–86] Oligomers containing peptide-linked ferrocene building blocks (Figure 12), were intensively investigated by Heinze et al.[87–90] Application of an oxidative potential yields in the oxidation of ferrocene units, depending on the position of the ferrocene subunit in the oligomer (Figure 11).[88]
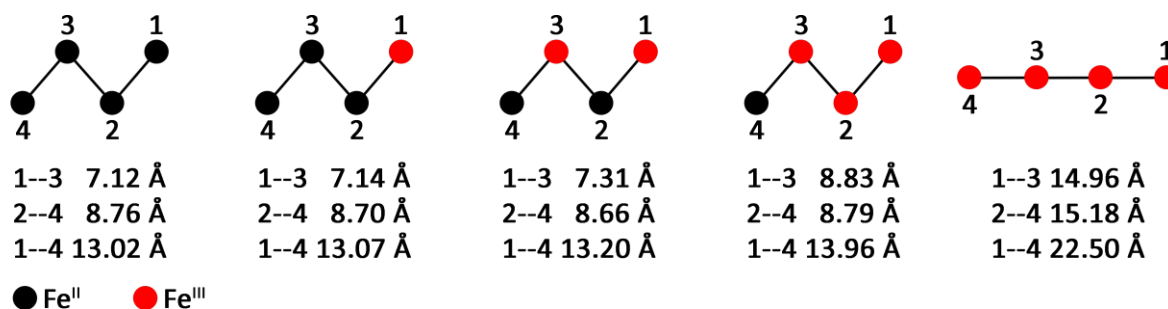
Figure 11. Scheme of the DFT optimized geometries of [Ac-Fca$_4$-OMe]$^{n+}$ and the relevant distances of the iron centers of the ferrocene subunits, starting from the neutral oligomer (left side) to the fourfold oxidized oligomer (right side). Fca = [(C$_5$H$_4$CO-)Fe(C$_5$H$_4$NH-)].[88]

The result is a conformational switch from a coil to a rod formation of the oligomer (Figure 12, from left to right). UV/vis spectroscopy measurements of these partially oxidized peptides show IVCT bands, changing with the oxidation state.[89] ^{1}H^{1}H NOE NMR spectroscopy allows the detection of amide-hydrogen bonds in the neutral, diamagnetic state.[89,91] The paramagnetism of the ferrocenium units hinder the possibility of ^{1}H^{1}H NOE NMR spectroscopy. For the future, ferrocene amide containing polymers are under investigation for the use as nanowires[92] and for sensing applications.[93,94]
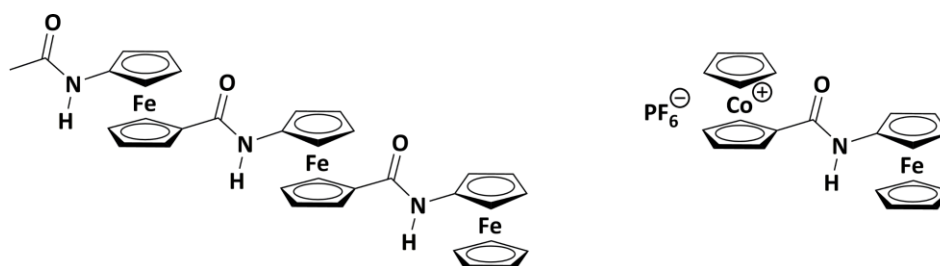

Figure 12. Ferrocene oligopeptide and cobaltocenium-ferrocene dyad by Heinze.

Carboxycobaltocenium peptides are a well-known part of the cobaltocenium chemistry (Figure 12).[81,95–99] The use of cobaltocenium carboxylic acid for peptide bonding is simplified due to the activation of the acid function by the negative inductive effect the charge of the Cc$^+$.

Beer et al. used cobaltocenium peptides to develop anion sensors, whereby coordination differences of the anions can be detected via optical and/or redox properties.[93,100–107] Two special sensors are based on *meso*-tetraphenylporphyrin, which was fourfold substituted by cobaltocenium (Figure 13) and ferrocene, respectively.[93] The metallocenes organize on one side of the porphyrin plane and are able to cage anions between each other. The strong optical absorption properties of the porphyrin were influenced by the environment, which allows the detection of varying anions.

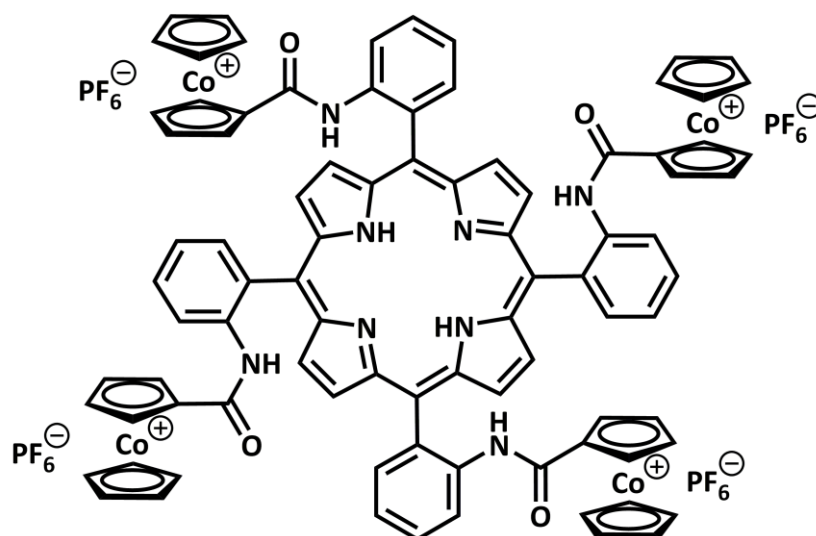**Figure 13. Fourfold cobaltocenium substituted *meso*-tetraphenylporphyrin for anion sensing..**

On contrary, the cobaltocenium amine was not yet successfully used for peptide synthesis. The reason is the positive charge of the complex, which switches the electron rich amine to an electron poor, even slightly acidic amine.[9] Therefore, the synthesis of cobaltocenium oligopeptides was not possible so far.

1.3 Porphyrins

Porphyrins are aromatic macrocycles with the same central pattern, the porphin. Porphin consists of four pyrrol units linked via methin bridges, which form a planar aromatic system. The planarity lead to a low solubility due to π-π stacking[108] and the aromatic system causes intense absorption/emission properties.[109] The porphin backbone possess three substitution positions, *α*, *β* and *meso* (Figure 14).[110]
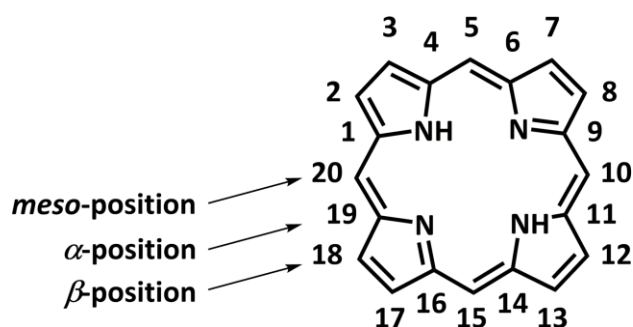

Figure 14. Porphin with IUPAC nomenclature for the porphyrin backbone.

The substitution of the backbone is popular (also by nature) to diminish the poor solubility and for the tuning of the excited state properties. Substitution in *β* and *meso* position keeps the conjugated system intact, whereby an *α* substitution requires a former reduction of the alpha carbon nucleus.

The nitrogen nuclei in the porphyrin center show acid-base activity, resulting in an amphoteric behavior.[111,112] The inner protons are versatile, their exchange is faster than the NMR time scale, resulting in a single ^{1}H resonance at room temperature.[113] The strong ring current of the porphyrin macrocycle lead additionally to a strong upfield shift compared to pyrrole,[114] whereby the ^{1}H resonance is characteristically shifted to –2 / –3 ppm.[115] Fourfold protonation of the porphyrin center is possible using weak acids and causes a distinctive color change from purple/red to green.[116] However, deprotonation to the anionic form requires strong bases.[111,112] Complexation of metals simplifies the deprotonation drastically.

1.3.1 Natural Porphyrins

In nature, the use of porphyrins is widely spread from bacteria and plants to animals and humans.[117,118] The human organism uses heme in its blood circle, whereby heme consists of a porphyrin (protoporphyrin IX) which is metallated by an iron cation. The iron nucleus reversibly binds oxygen and transports it by the bloodstream from the lung to the reaction centers. Figure 15 shows the crystal structure of a subunit of human deoxyhemoglobin with heme b in the center.[119–122]
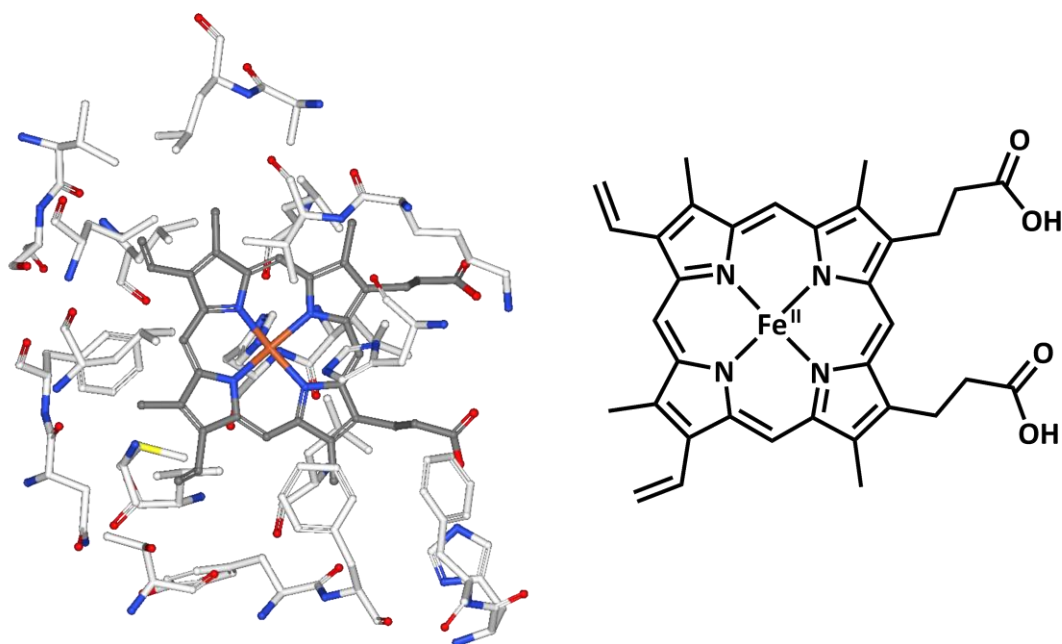
Figure 15. Crystal structure of human deoxyhemoglobin protein (heme b subunit) with close-by neighbor ligands[119–122] (left) and heme b as structural formula (right).

Many plants, algaes, cyanobacteria and purple bacteria use substituted porphyrins such as chlorophyll[118] or bacteriochlorphyll[118] as light-harvesting complexes (LHC) for photosynthesis. Via the photosystems (PS), the collected light is used for the photoinduced charge separation and finally energy storage in the form of adenosine triphosphate (ATP) and nicotinamide adenine dinucleotide phosphate (NADPH). Figure 16 shows the structure of chlorophyll a in the LHC of PS II in spinach.[121–124]

Figure 16. Structure of spinach PS II-LHC II supercomplex (chlorophyll a subunit) determined by electron microscopy[121–124] (left) and chlorophyll a as structural formula (right).

1.3.2 Photosynthesis
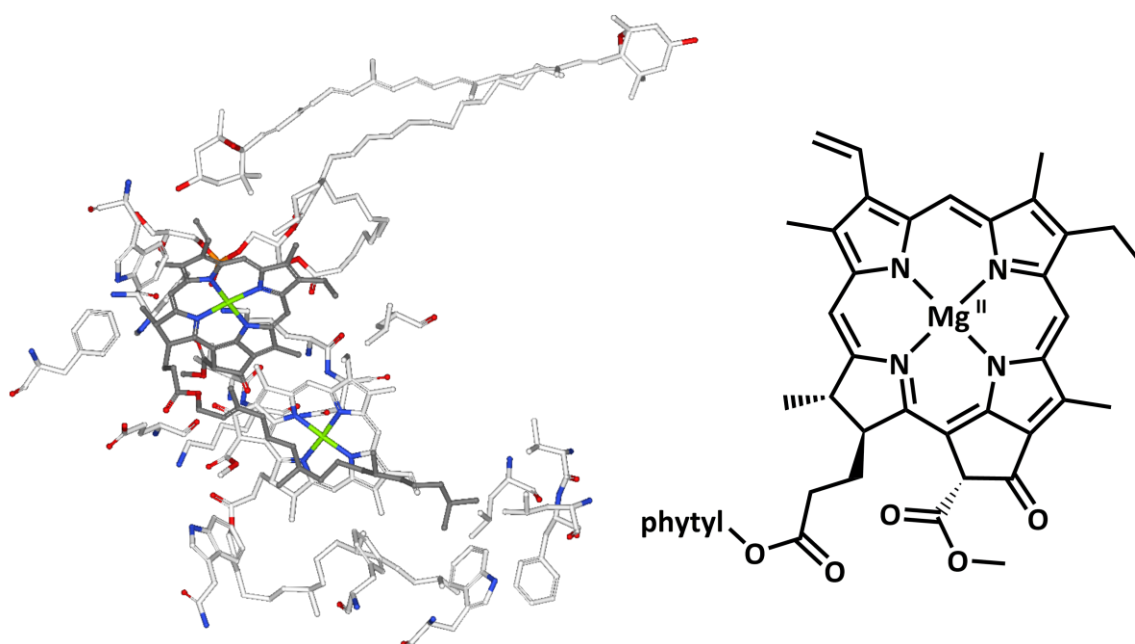
Photosynthesis is a major biological process due to its natural efficiency of absorbing light and converting the energy, and the possibility to transfer the knowledge on artificial technologies.[125–127] Therefore, the structure determination of the porphyrins, the influencing surrounding proteins and the following parts of the reaction cascades are still under investigation.

Plants use light energy to force a long-lived charge separation, to finally produce hydrocarbons and oxygen out of water and carbon dioxide (Equation 14).

$$\text{n } H_2O + \text{n } CO_2 \xrightarrow{\;h\nu\;} 1/n\ (CH_2O)_n + \text{n } O_2 \qquad\qquad \textbf{14}$$
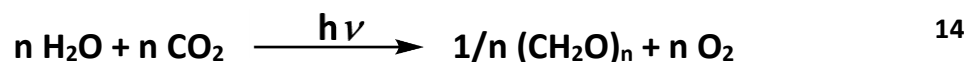
The energy is collected by light-harvesting molecules, which absorb light like antennas. These pigments consist of chlorophylls (Figure 16) and carotenoids to cover large parts of the light spectrum and therefore extend the absorbance efficiency. Further, the collected energy in terms of excitons, is transferred via Förster resonance energy transfer (FRET) to the reaction center, the special pair (SP).[128] The special pair was evolutionary placed in the center of the photosystem, to ensure a short distance of the surrounding antenna molecules, resulting in an efficient and fast energy transfer.

The SP consists of two chlorophyll molecules, which are arranged in a characteristic coordination to each other. This is reasoned in the interactions of the chelated Mg^{II} cation (Lewis acid), which coordinates water molecules and the CO group of the close-by chlorophyll.[1][129] The coordination causes an energetic lowering of the lowest unoccupied molecular orbital (LUMO) and a broadening of the absorption bands. This allows accepting of the energy from the surrounding antenna molecules due to the energetic driving force. The excited special pair acts as electron donor, followed by the piping of the electron to the following electron transfer chain.[1] Delocalization of the positive charge between both chlorophylls is one aspect, which hinders the electron from back-hopping.

Bacteria, that utilize anoxygenic photosynthesis, use one photosystem, PS I or PS II. For the oxidation of water and the release of molecular oxygen, the energy of a single photosystem is not sufficient. So organisms, which use the oxygenic photosynthesis, connect PS II and PS I in series to gain a higher potential. This process is illustrated by the so-called Z scheme in Figure 17.[130–132]

The reaction cascade of the oxygenic photosynthesis (Figure 17) starts from P700, the special pair of PS I. Excited via photoexcitation, the special pair (P700*) transfers one electron over the iron sulphur clusters F_X, F_A and F_B to ferredoxin.[1,132,133] In P700, an electron hole (EH) remains. Concurrently, P680, the SP of PS II, was excited via FRET or photoexcitation and transfers one electron over the cytochrome b_6f complex (Cyt b_6f) to the SP of PS I (P700), recombining the former formed EH. Over all, the two photosystems yield a charge separation with a potential difference of 2.26 V.[131]
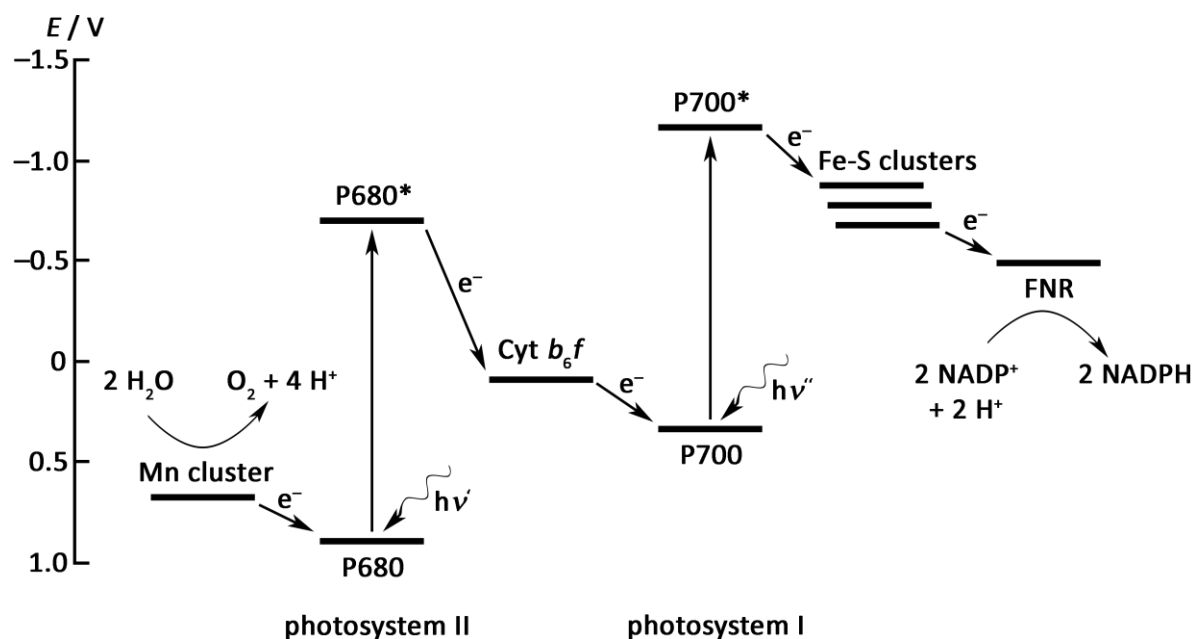
Figure 17. Z scheme of oxygenic photosynthesis.[131,132]

In the end of the photosynthesis cascade, ferredoxin-NADP$^+$ reductase (FNR) catalyses the reduction of NADP$^+$ and one proton by two reduced ferredoxin units, resulting in NADPH. The combined reactions are comparable to a hydride transfer (2 e$^-$/H$^+$ ≙ H$^-$). In the further ongoing process (Calvin cycle), NADPH, ATP and protons reduce and fix carbon dioxide in the form of carbohydrates. Figure 18 shows a more detailed view on the major involved molecules of the electron transfer cascade of PS I and the reaction timeline.[133]

Important are the fast initial steps of the cascade, the charge separation and the ET with lifetimes of 1 ps and 20 ps,[133] so the excited electron can depart from the special pair and prevent charge recombination. By larger distances from the associated electron hole, the time (and therefore the chance) for a further reaction increases. Thus, the transferred electron obtains more time for the ET cascade and NADP$^+$ reduction.

On the other side of the photosynthesis cascade, an electron hole was formed in P680. This EH is a strong oxidant, which is able to oxidize the oxygen-evolving complex (OEC), a manganese cluster. During the Kok cycle, the OEC is oxidized several times by P680$^+$, and splits water into oxygen and protons with release of the electrons (Equation 15).[134–136]

$$2\ H_2O \xrightarrow{\ h\nu\ } O_2 + 4\ H^+ + 4\ e^- \qquad\qquad \textbf{15}$$
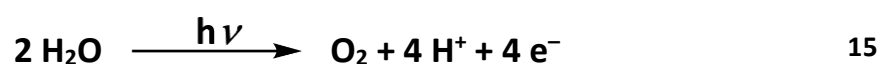
Nature proves the capability to use porphyrins in long-lived, high energetic charge separation processes. Hence, the synthesis of artificial porphyrins is a major topic of mimicking these reaction centers systems.
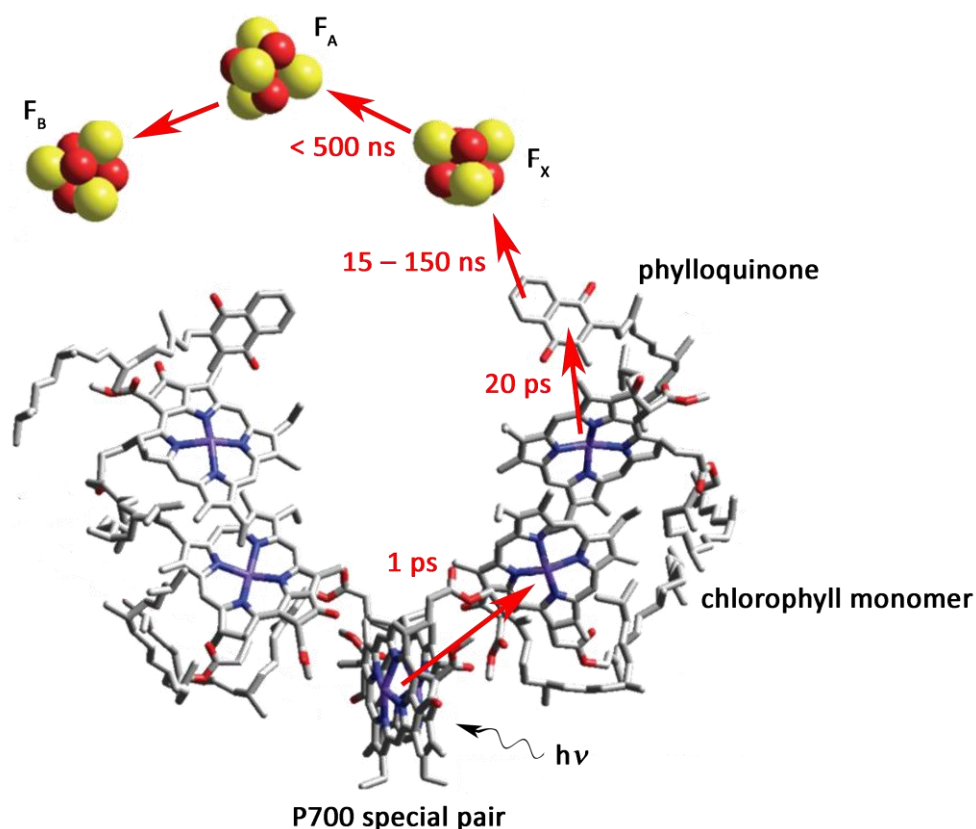
Figure 18. Electron transfer cascade of photosystem I showing the major steps from P700 to the iron sulphur clusters and invers rate constants. Figure adapted from Reichert et. al..[133]

1.3.3 Synthesis of Artificial Porphyrins

Natural porphyrins often show an asymmetric substitution pattern, which makes the artificial synthesis challenging and expensive. The substitution pattern is necessary to influence the photophysical properties of the porphyrin and to connect electron acceptors for electron transfer reactions (in photosynthesis). Therefore, the usage of simplified and "easy-to-synthesize" porphyrins is necessary and forced.

As shown in Figure 14, substitutions are possible at three positions: α, β and *meso* position. Substitution in α position is known from nature (like in cofactor F430), but partially destroys the porphyrin π-system, strongly influencing the absorption properties. The β substitution is clearly more common. The substitution of one proton in this position keeps the porphyrin system intact (Figure 15), solubility can be increased (due to the reduction of π-π stacking) and the porphyrin can be linked to the surrounding protein environment. For the insertion of β position substituents, the artificial and natural synthesis often starts from the substituted pyrrol subunit.[137]

For artificial biomimetic model complexes, the use of *meso* substitution is very popular due to its high versatility. The variation of the substitution pattern using different aldehydes allows a broad

application of substituted porphyrins. Via one-pot synthesis, symmetric substituted A_4 porphyrins are accessible using an aldehyde and pyrrol (Figure 19).[138–140] The use of various aldehydes in one synthesis leads to A_2B_2 and AB_2C porphyrins, which makes the synthesis of push-pull systems via dipyrromethanes possible.[10,141] Substituted benzaldehydes as starting material result in substituted *meso*-tetraphenylporphyrins, whereby the phenyl ring rotates out of plane of the porphyrin. Due to this arrangement, the phenyl substitution is popular to prohibit π-π stacking of the porphyrins.
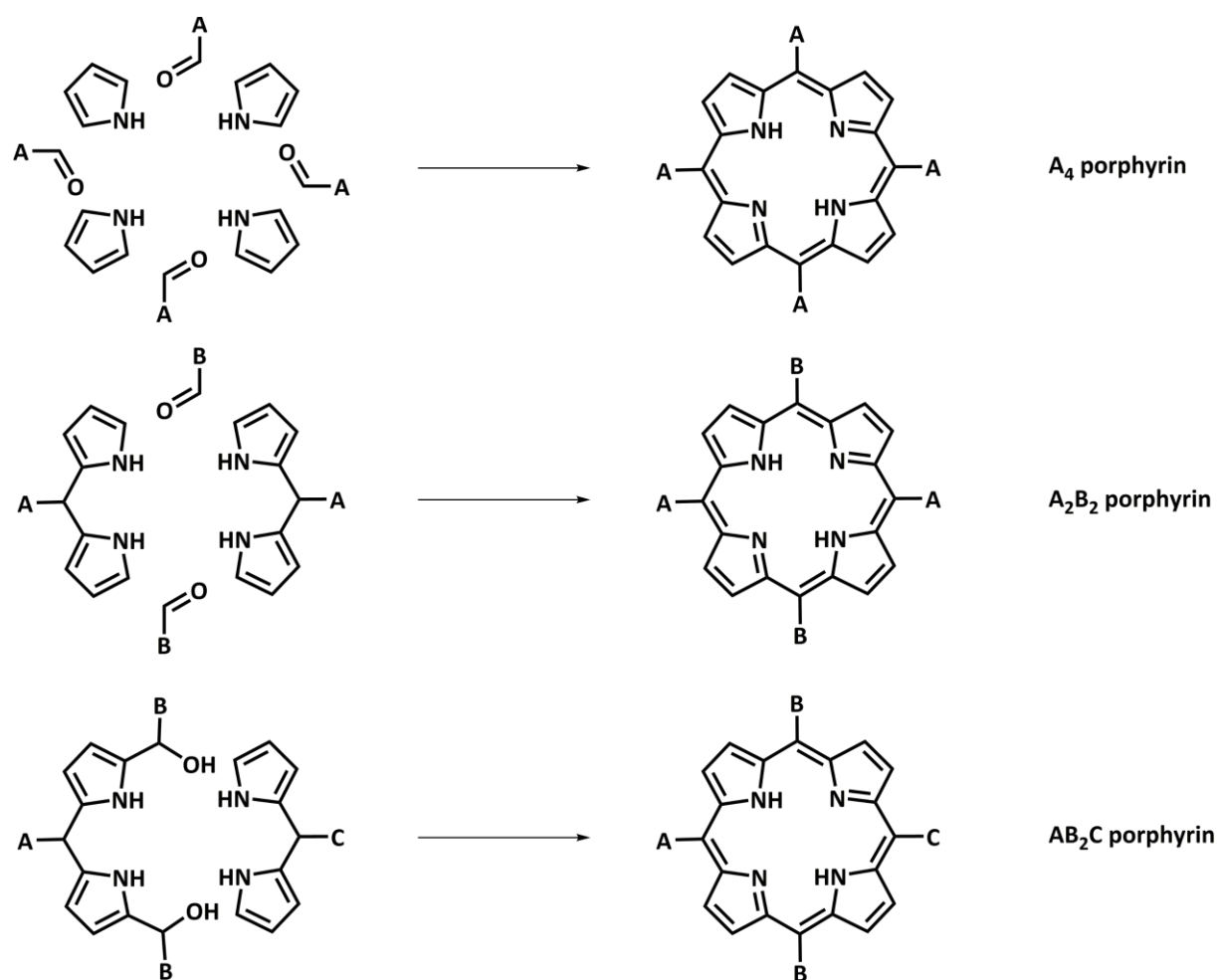
Figure 19. Synthesis of artificial *meso* substituted porphyrins.

1.3.4 Photophysical Properties of Porphyrins

(Metallo)Porphyrins are deeply colored, and show characteristic absorption and emission spectra. Figure 20 shows exemplary the normalized absorption spectra of zinc(II) *meso*-tetraphenylporphyrin (a, Zn(TPP)) and free base *meso*-tetraphenylporphyrin (b, H_2(TPP)). The absorption spectra show a very intense band, known as Soret or B-band, and several less intense redshifted bands (Q-bands).[109] Since the extinction coefficient of the Soret band can easily exceed a factor of $4 \cdot 10^5$ M^{-1} cm^{-1}, porphyrins are common as chromophores in nature and artificial light harvesting complexes.[10]

Figure 20. Normalized absorption spectra of zinc(II) *meso*-tetraphenylporpyrin (a) and free base *meso*-tetraphenylporpyrin (b) in tetrahydrofuran at room temperature.

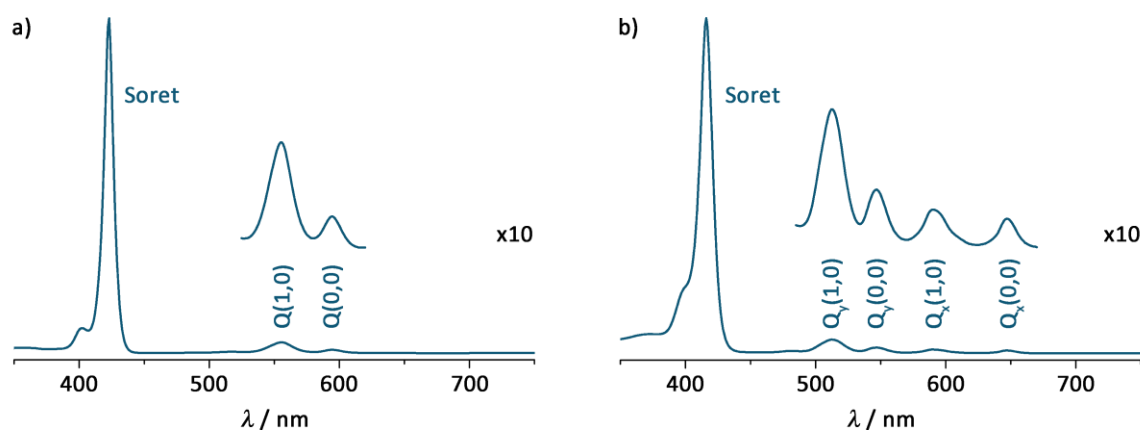The established explanation for the splitting of the absorption in Soret and Q-bands can be given by the Gouterman four-orbital model. The highest occupied molecular orbitals (HOMO and $HOMO_{-1}$) and the lowest unoccupied molecular orbitals (LUMO and $LUMO_{+1}$) give rise to several via π-π* transitions. In (metallo) porphyrins with D_{4h} point symmetry, the HOMOs are labeled as a_{2u} and a_{1u}, whereby the LUMOs are labeled as $e_{g,x}$ and $e_{g,y}$. The additional notification of x and y is necessary to distinguish the different orientations of the orbitals. The orbital notation b_1, b_2, c_1 and c_2 is also common and used by Gouterman. A consistent labeling of the orbitals is also possible for systems with a lower symmetry, such as $H_2(TPP)$ (D_{2h}). The profiles of the mentioned orbitals are depicted in Figure 21. [109,142,143]

In porphyrins with D_{4h} symmetry, the two HOMOs possess nearly similar energies, whereby the two LUMOs are exactly degenerate by symmetry. Hereby the two LUMOs and HOMOs are regarded as equal in energy, respectively. π-π* transitions between these orbitals allow four different one-electron excited singlet states: $(a_{1u})^1(e_{g,y})^1$, $(a_{2u})^1(e_{g,x})^1$, $(a_{1u})^1(e_{g,x})^1$ and $(a_{2u})^1(e_{g,y})^1$. The two former excited states are polarized in x direction, the latter excited states are polarized in y direction. The similar energy levels and symmetry allow the mixing of the x and y polarized excited states (Figure 22a), resulting in two degenerate high-energy transitions and two degenerate low-energy transitions. The two high-energy transitions own parallel transition dipoles, whereby these add up resulting in two high-intensity bands (B_x and B_y).[144] These are commonly not resolved and observable as single Soret band (Figure 22b). The two low-energy transitions own destructive anti-parallel transition dipoles, which results in two less intense low-energy bands (Q_x and Q_y) of similar energy. Vibronic progression of the bands allow a multiplication of the bands.[109,142,143]
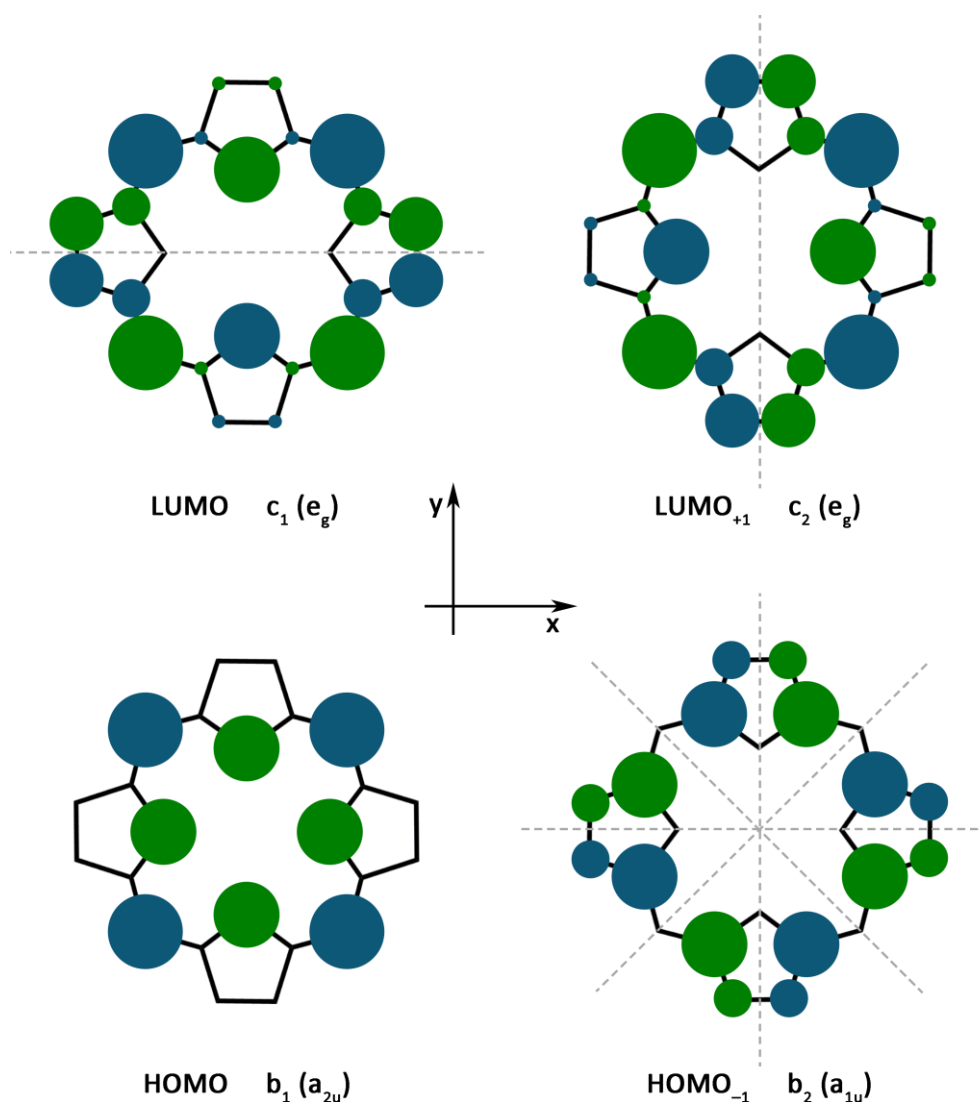
Figure 21. Schematic orbitals of porphin, with LUMO and LUMO$_{+1}$ on the top, as well as HOMO and HOMO$_{-1}$ on the bottom. Dashed lines show the orbital nodes.

The Gouterman four-orbital model behaves well for D_{4h} point symmetric systems. For systems with lower symmetry, such as $H_2(TPP)$ with D_{2h} symmetry, the decreased symmetry has to be taken into account. In opposite to Zn(TPP), $H_2(TPP)$ possesses two protons, which are fixed on their position (compared to the speed of the movement of the electrons). This lowers the symmetry and removes the degeneracy of c_1 and c_2 (Figure 22c). Mixing of the excited states results in excited state transitions with unequal energy. Thus, two different Q- and B-bands are formed (Figure 22d), whereby the two B-bands are similar in energy. Vibrational progression is applicable like in the D_{4h} system. Hence, one broadened Soret and four Q-bands can be observed (Figure 20b).[142]
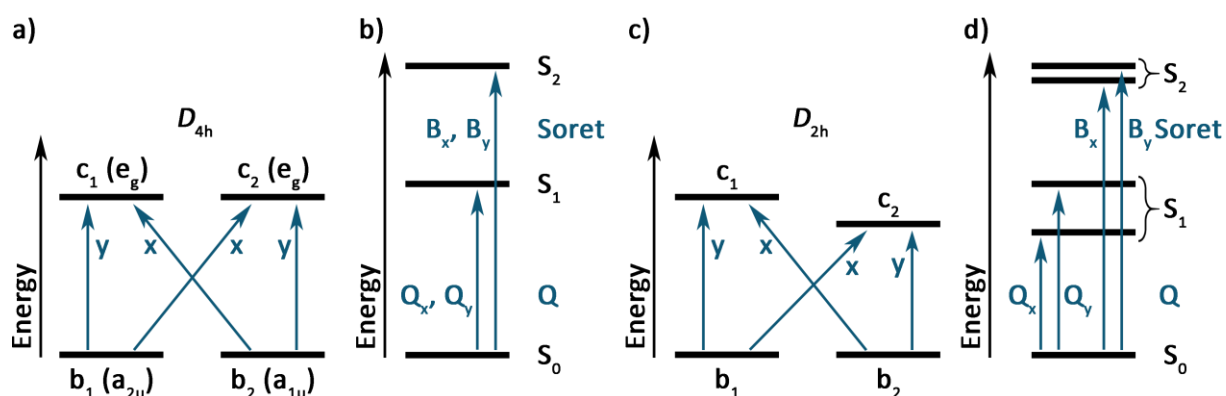
Figure 22. a) Simplified π-π* transitions in D_{4h} symmetric porphyrins, b) electronic transitions in D_{4h} porphyrins, c) simplified π-π* transitions in D_{2h} symmetric porphyrins, d) electronic transitions in D_{2h} porphyrins.

After excitation, relaxation of the electron to the vibrational ground state of the excited state S_1 (Q) occurs. From there, relaxation under emission is possible. At low temperatures, phosphorescence from T_1 is observable, at higher temperatures fluorescence with quantum yields of over 10 % is possible.[10,142] Fluorescence from the S_2 state is feasible, but relaxation to the S_1 state is faster.[145] Hence, fluorescence occurs from the first excited state (S_1, vibrational ground state) to the ground state, and the first vibrational excited state of the ground state (Figure 23), respectively.
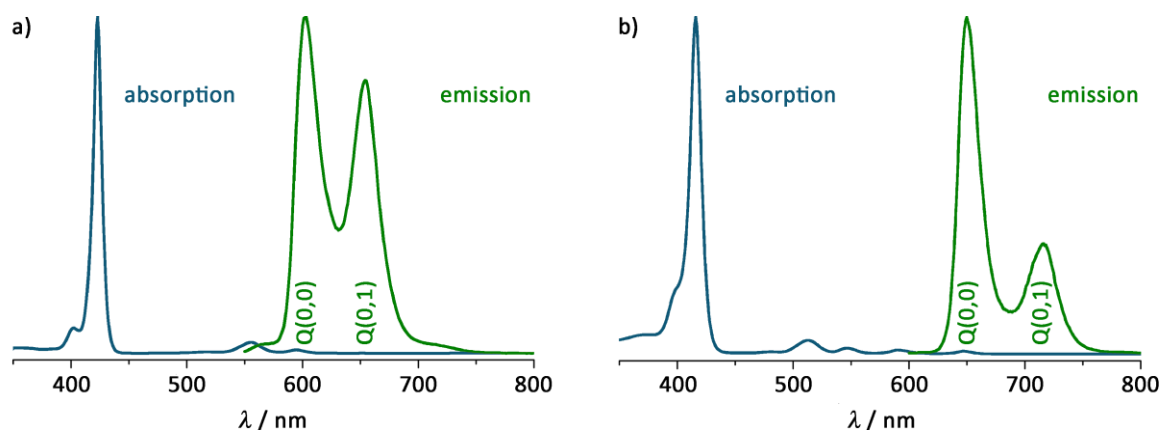
Figure 23. Normalized absorption and emission spectra of zinc(II) *meso*-tetraphenylporpyrin (a) and free base *meso*-tetraphenylporpyrin (b) in tetrahydrofuran at room temperature.

1.3.5 Electrochemistry of Porphyrins

In general, porphyrins possess five different oxidation states. Starting from the neutral complex, oxidation is doubly possible, forming the monoradical cation followed by the diradical dication (Equation 16). In opposite, also doubly reduction forming the monoradical anion and the diradical dianion is possible.

$$P^{2-} \xleftarrow{e^-} P^{\bullet-} \xleftarrow{e^-} P \xrightarrow{e^-} P^{\bullet+} \xrightarrow{e^-} P^{2+} \qquad \textbf{16}$$
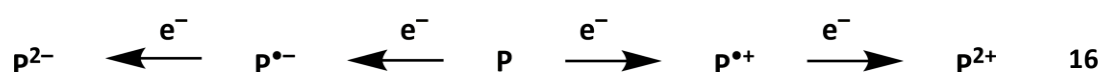
The redox potentials of protected artificial porphyrin amino acid (MeOOC-P-NHAc) can be placed at around −2.0 V (2. reduction), −1.7 V (1. reduction), +0.5 V (1. oxidation) and 0.8 V (2. reduction) (vs.

FcH/FcH$^+$).[10,115] The redox potentials of the porphyrin are influenced by two ways, substitution and metalation of the porphyrin, respectively. The substitution of the porphyrin by electron withdrawing substituents like pentafluorophenyl (-C$_6$F$_5$) shifts the redox potentials to the positive. Electron donating substitution groups like mesityl (-C$_6$H$_2$(CH$_3$)$_3$) shift the redox potentials to the negative.[10,115] The influence of the metalation of the porphyrin center strongly depends on the special properties of the metal ion. For the case of the exchange of the central amino protons by zinc(II) cations, the redox potentials are shifted to the negative.[10,115] Over all, the porphyrins oxidation/reduction processes are reversible. In dependence of the solvent environment and the range of the redox potential, the second oxidation of the porphyrin occurs irreversible.[10]

1.3.6 Porphyrins in Biomimetic Model Complexes

Since scientists are able to clarify substeps of photosynthesis processes[2,4] for example via X-ray crystallography[146,147] and femtosecond spectroscopy,[148] the synthesis of model complexes to imitate these biological systems has become popular.[125,149,150] To catch this goal, the basic biological mechanisms of electron and energy transfer, and energy storage have to be transferred into efficient working schemes.

PSII and PS I use chromophores for light harvesting and photoinduced charge separation. The long lifetime of $\tau \approx 1$ s allows water oxidation by the manganese clusters on the one hand and reduction of NADP$^+$ by ferrodoxins on the other hand.[151]

The increase of the charge-separated state lifetime is possible via several factors:

By increasing the distance between the electron and the electron hole, the chance for a recombination decreases. This can be realized by adding electron donor or acceptor building blocks to restore the chromophore[115,152] or to spatially separate the chromophore from the final acceptor subunit.[153] On the one hand the choice of the bridging ligand[154] can also increase the distances between acceptor and donor by using phenyl groups or aliphatic building blocks[155]. On the other hand, asymmetric functional groups like amides or esters inside the connecting bridges can allow electron hopping from donor to acceptor, but hinders back hopping and charge recombination.

The delocalization of the electron hole or the excited electron is another possibility to extend the lifetime of the charge-separated state. This can help to analyze excited states properties for fundamental research or allows the further reaction of the localized electron (or hole) for reduction (or oxidation) processes. A famous example are fullerenes, which can be used cage-like to store a single electron.[151,156,157]

To work efficiently, the natural photosynthesis was set up on the principles of the Marcus theory (see Chapter 1.1.1) to prolong the lifetime of the charge-separated state. The electron transfer processes

after excitation were designed to be in the Marcus normal region ($-\Delta G \leq \lambda$) to lose as few as possible of the harvested light energy. Therefore, the reorganization energies of the involved molecules have to be low, which was implemented by the large size of the involved molecules and the shielding surrounding nonpolar protein environment. On the other side, the process of charge recombination is highly exergonic ($-\Delta G \gg \lambda$), which shifted the ET cascade in the Marcus inverted region.[13,14]

Artificial photosynthesis models are based on three subunits,[158] the chromophore(s) (LHCs, special pairs), the electron acceptor (ferrodoxin) and the electron donor (OEC). Due to the complex substitution pattern of the involved compounds and the surrounding protein and membrane environment, the entire synthesis of the systems in laboratory is not reasonable. Therefore, artificial building blocks are necessary, whereby the substitution pattern is varied to obtain better solubility or electron donor/acceptor properties, respectively.[10,115,141,159]

By excitation, a charge-separation occurs inside the chromophore and the electron is transferred to the electron acceptor. To extend the lifetime of the charge-separated state, an additional electron donor can be used to regenerate the chromophore, whereby the distance of the electron hole and the electron is increased.[160] Porphyrins,[10,156,161–163] carotenoids[158,164] and ferrocenes[115,151,165–167] are favored electron donors, due to their comparability to nature and their redox stability, respectively. Alternatively, the electron acceptor can be chosen by the function that should be conducted, whereby chinones[115,164,166,167] are mimicking phylloquinone (PS I), fullerenes[151,156,157] own a low reorganization energy and act cage-like to extend the lifetime of the charge separation,[168] and catalytic active building blocks can be used for hydrogen evolution[11,169,170] or medical applications,[162,171] for instance.

Fukuzumi et al. were highly dedicated to clarify basic principles of ET and developed efficient biomimetic model systems around the photosynthesis systems. To mimic the photoinduced water splitting, two cobalt porphyrins were linked close to each other imitating a special pair.[172] With artificial electron donors/acceptors, the influence of peptide bonding was investigated[152,166,167] and electron cascade systems of 2 to 5 subunits were synthesized.[151,173]

In Figure 24 a pentad consisting of a ferrocene subunit as electron donor, a fullerene as electron acceptor and three porphyrins as chromophores is depicted. The large amount of porphyrin subunits raises the chance of excitation, thus the efficiency. After excitation of one porphyrin, the electron is transferred to the electron acceptor, whereby one electron of ferrocene fill the electron hole of the porphyrin radical. The two other non-irradiated porphyrins initially transfer the electrons from the donors to the acceptors. Later, they act as large spacers to separate the oxidized donor (ferrocene), from the reduced acceptor (fullerene). As a result, this pentad yields a very long lifetime for the charge-separated state of 0.53 seconds at 163 K in the frozen state. For comparison, the lifetime of an excited bacteriochlorophyll dimer/quinone pair scales at around 1 second.[151] The pentad with its multistep

mechanism and the long charge separation are mimicking the natural photosynthesis process in a realistic time-scale.

electron peptide   chromophores and spacer   peptide   electron
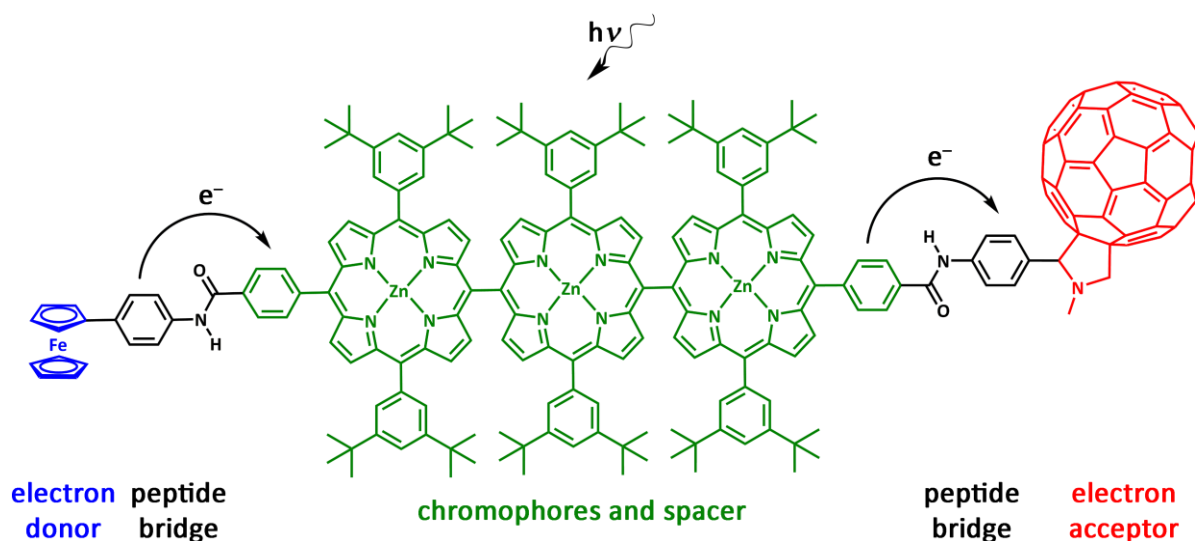donor   bridge   bridge   acceptor

Figure 24. Biomimetic pentad by Fukuzumi et al. with ferrocene as electron donor, three zinc(II) porphyrins as chromophores and spacers, a fullerene as electron acceptor and peptide bridging ligands.

Heinze et al. investigated basic electron transfer processes in bioinspired metallocene peptides and porphyrins, also considering influences by hydrogen bonds and ions.[10,81,90] The development of suitable porphyrin building blocks with varying electron donor/acceptor strength lead to the synthesis of artificial porphyrin amino acid and made the synthesis and survey of new photosynthesis models possible.[10,115,141,162,174]
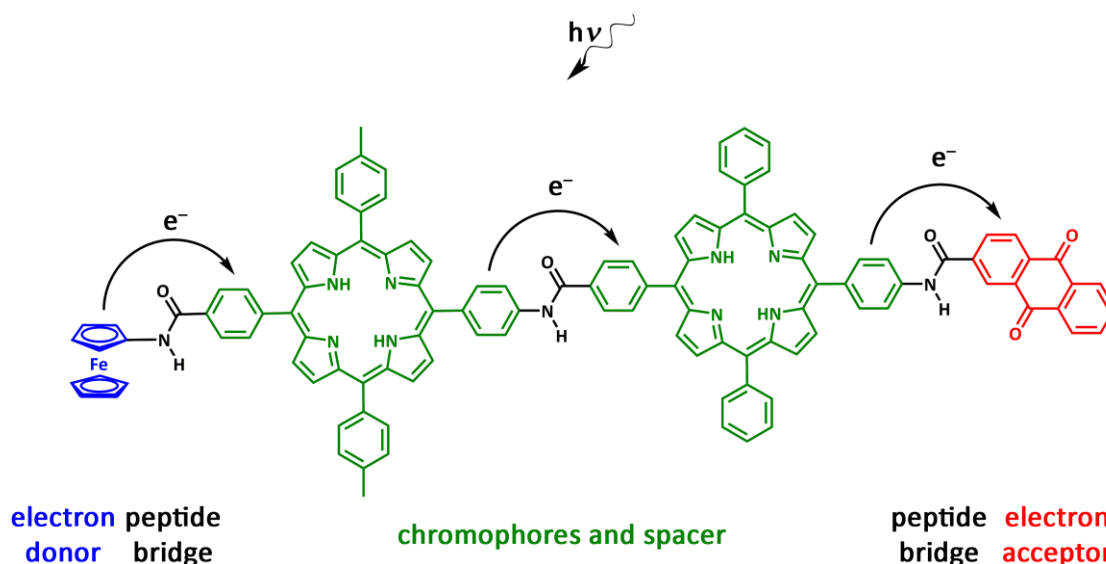

electron peptide   chromophores and spacer   peptide electron
donor   bridge   bridge   acceptor

Figure 25. Biomimetic tetrad by Heinze et al. with ferrocene as electron donor, two porphyrins as chromophores and spacers, antharaquinone as electron acceptor and peptide bridging ligands.

Figure 25 shows a photosynthesis model by Heinze et al., with porphyrin-amides as bridging ligands.[115] The tetrad consists of an electron donor (Fc), photosensitizer (porphyrins) and electron acceptor (antharaquinone). The time resolved fluorescence decays after photoexcitation show, that the initial

photoinduced electron transfer (PET) occurs reductively from ferrocene. Initial oxidation by the quinone is also possible, but the reductive PET owns a more suitable thermodynamic driving force.[115] The substitution patterns of the porphyrins form a potential gradient between the two chromophores. In combination with the orientation of the peptide bonds, PETs are directed to the electron acceptor, which mimics phylloquinone of PS II.[115]

1.4 Hydrogen evolution catalysis

The use of elemental hydrogen as secondary energy source is an important possibility to reduce fossil fuels in the world economy.[175] Nowadays, green hydrogen is used for heating as admixture to natural gas and for transportation (i.e. train or car) in hydrogen fuel cells. The development of an efficient synthesis of methanol from carbon dioxide/carbon monoxide and hydrogen is forced, using the modified Sabatier process for example (Equations 17 and 18).[176–178]

modified
Sabatier reaction

$$CO + 2\ H_2 \rightleftharpoons CH_3OH \qquad\qquad\qquad 17$$

$$CO_2 + 3\ H_2 \rightleftharpoons CH_3OH + H_2O \qquad\qquad 18$$
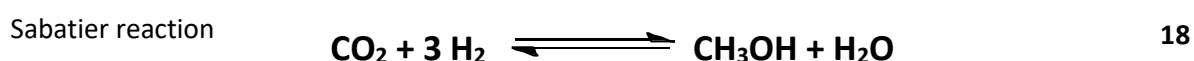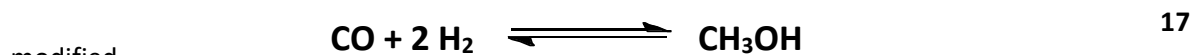
The main part of elemental hydrogen that is used in industry is produced by the combined process of steam reforming (Equation 19), partial oxidation (Equation 20) and water-gas shift reaction (Equation 21) from fossil hydrocarbons[60,179] or by electrolysis through electricity from fossil energy sources. Green hydrogen is produced by electrolysis from solar or wind electricity (*Power-to-Gas*) or by steam reforming from biomass hydrocarbons.

steam reforming

$$CH_4 + H_2O \rightleftharpoons CO + 3\ H_2 \qquad\qquad 19$$

partial oxidation

$$CH_4 + \tfrac{1}{2}\ O_2 \rightleftharpoons CO + H_2 \qquad\qquad 20$$

water-gas shift reaction

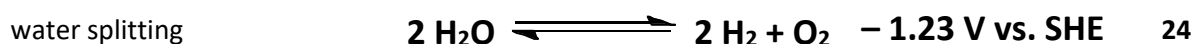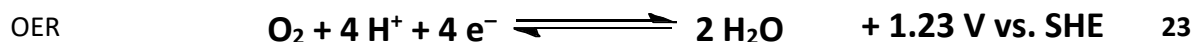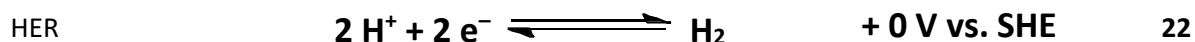$$H_2O + CO \rightleftharpoons H_2 + CO_2 \qquad\qquad 21$$
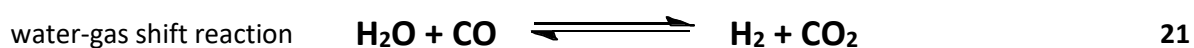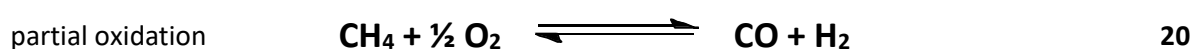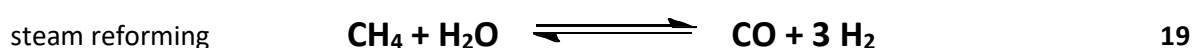
All these techniques lose a significant amount of energy by transforming hydrocarbons or electric power to hydrogen. Therefore, an increase of the efficiency of proton reduction by electrocatalysts[180] or a direct synthesis of hydrogen from water and solar energy[181] is desirable (*Solar-to-Hydrogen*). One way to achieve this goal are artificial photosystems with chromophores as light harvester and catalytically active sites as hydrogen producer. Examples for these systems are photoelectrochemical cells[182] based on semiconductors.[183–185] or molecular photocatalysts.[186–189]

Another target is the exchange of rare metals like platinum, palladium or ruthenium by earth abundant metals like iron, cobalt or nickel to make large-scale techniques available.

1.4.1 Electrolysis

The most famous hydrogen evolution method, developed by Volta and improved by Faraday, is water splitting by electricity.[190] The process can be separated in the oxygen evolution reaction (OER, Equation 22) at the anode and the hydrogen evolution reaction (HER, Equation 23) at the cathode, whereby elemental oxygen and hydrogen are formed.[191] Over all, the process of water splitting

depicts a four-electron mechanism with a thermodynamic potential of −1.23 V, strongly depending on the pH of the solution (see Kok cycle in Chapter 1.3.2).

HER	$2\,H^+ + 2\,e^- \rightleftharpoons H_2$	$+\,0\ V\ vs.\ SHE$	22
OER	$O_2 + 4\,H^+ + 4\,e^- \rightleftharpoons 2\,H_2O$	$+\,1.23\ V\ vs.\ SHE$	23
water splitting	$2\,H_2O \rightleftharpoons 2\,H_2 + O_2$	$-\,1.23\ V\ vs.\ SHE$	24

Due to the slow OER, high potential overloads are necessary for the water splitting, which lowers the efficiency of the reaction significantly.[192,193] The right choice of the electrode materials facilitates smaller potential overloads, for example by using platinum.[194–197]

The group of Sakai is working on homogenous hydrogen evolution catalysis with ruthenium chromophores[198–202] and linked platinum catalysts[198,201–204] on the one hand, and hydrogenase models of iron[205] (Figure 26) and nickel[206] (Figure 27), respectively, on the other hand.

$$2\,H^+ + 2\,e^- \rightleftharpoons H^+ + H^- \rightleftharpoons H_2 \qquad \textbf{25}$$
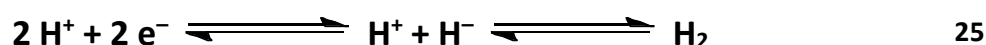
Hydrogenases reversibly catalyze the activation of molecular hydrogen, and vice versa the reduction of protons (Equation 25).[60,207–209] By adding pressure on the equilibrium, biomimetic hydrogenase model complexes are able to evolve molecular hydrogen. In 2009, Sakai started to carry on research on metal dithiolate complexes, inspired by iron hydrogenase clusters (Figure 26).[210]
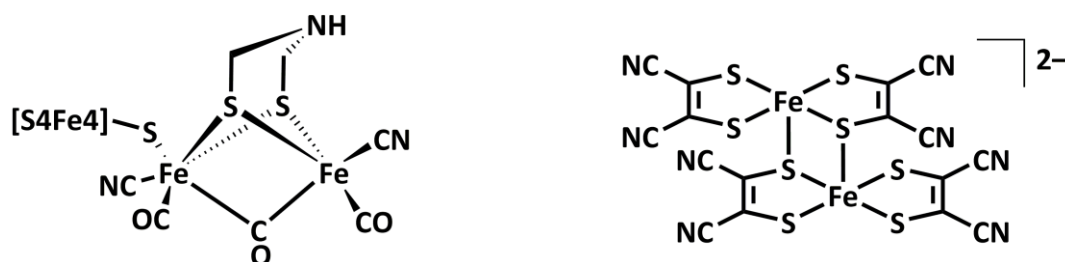

Figure 26. Active site of [FeFe] Hydrogenase (left) and iron(III) dimaleonitriledithiolate, forming iron-sulfur clusters (right).[210]

Electrocatalytic reduction of protons using the dissolved iron complex [Fe^{III}((SCCN)$_2$)$_2$]$_2$ $^{2-}$ reached a turn over number (TON) of 158 over 5 h with an efficiency of 98 %.[210] Moreover, the needed overpotential for known iron hydrogenase models was lowered on 560 mV. Controlled functionalization of an electrode by crystallization and repetition of the electrocatalysis experiment increased the efficiency to 99 % and the turn over number (TON) to 3900.[210] This depicts a growth by the factor of nearly 25, proving the high stability of the catalyst. The author assumes, that the iron(III) complex centers form [Fe$_2$(μ-S)$_2$] cluster, which is the active catalyst of the hydrogen evolution.[210] The

crystal structure shows an interaction of the iron(III) dithiolato-planes (Figure 26), resembling iron sulfur clusters similar to the natural pendant.[210]

Later on, Sakai exchanged iron by nickel (Nickel hydrogenase) and extended the former thiolato ligand by a pyrazine subunit (Figure 27).[211,212] The Ni[II] complex shows pH depending electrocatalytic hydrogen evolution, with low overpotentials of 0.31 to 0.41 V and TONs of 3300 to 20000 (in 24 h, at pH 5). Interestingly, the hydrogen evolution is not metal-centered; the nickel core fixes the ligands and facilitates the ligand-centered reaction. The nitrogen nuclei of the pyrazine subunit are protonated depending on the pH value. Single protonation at pH 5 forms an ammonium species, which is reduced electrocatalytically to a hydride. The reaction with protons releases molecular hydrogen.[211,212]
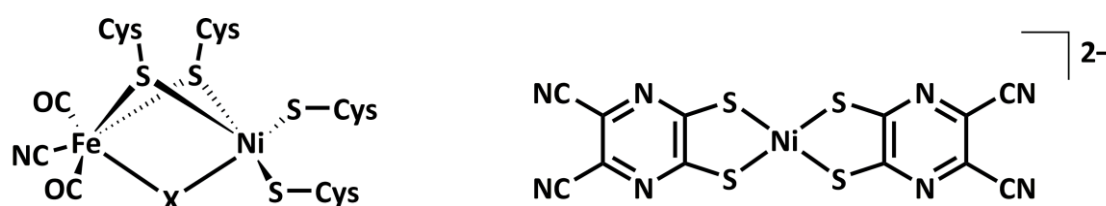

Figure 27. Active site of [FeNi] Hydrogenase (left) and a nickel(II) pyrazinedithiolate (right).

For the hydrogen evolution reaction, the ligand acts like an electron storage, so the further extension of the π system of the ligand was reasonable. The cyanide groups of the ligand (Figure 27) were removed and exchanged by one pyridine and one benzene subunit, respectively. Again, the extension of the ligand system lead to a decrease of the HER overpotentials on 173 and 227 mV. This allows the assumption, that the overpotentials are lowered with the increasing number of nitrogen atoms in the ligand, enhancing the "electron reservoir". Unfortunately, the improvement is accompanied by the poor solubility of the complexes at low pH, resulting from the protonation of the organometallic nickel complexes.[213] Experimentally, it was still not possible to detail the mechanism of the catalytic reaction. If the nickel core supplies electron density and fixes the ligands, or if the nickel nuclei also forms nickel hydride, which would play a crucial role in the unclear mechanism. Density functional theoretical (DFT) calculations suggest a mechanism, involving twofold protonation and reduction of the nickel(II) complex via proton coupled electron transfer.[214,215] A reaction pathway via the reaction of N-H and S-H, was calculated with an intermediate Gibbs energy of +36.8 kcal/mol. Whereas the formation of a nickel hydride intermediate complex, with two close-by bonded hydrogen atoms, owns an intermediate step with an activation energy of +16.6 kcal/mol, allowing the release of molecular hydrogen.[214] Finally, the synthesis of a heteroleptic nickel(II) dithiolene bipyridine complex lead to the knowledge, that highly electron donating ligands (like dithiolenes) are important for the hydrogen evolution reaction. The ligand induces electron density to the nickel core, which rises the basicity and makes the formation of metal hydrides possible.[215]

1.4.2 Photocatalysis

Nowadays, photocatalytic hydrogen production is possible via several pathways, using nano tubes,[216] quantum dots,[217] photochemical semiconductors[183–185] or homogenous photocatalysis[186]. Therefore, this chapter will focus on the progress in the photocatalyst development.

The Rau group focused on homogenous hydrogen catalysis using heterobinuclear polypyridyl complexes, with one chromophore for photosensitizing and a bridged hydrogen generating catalyst. The variation of the connecting bridge for the understanding of the principle electron transfer processes is important. The exchange of the catalytic active metal helps to clarify the mechanism of hydrogen catalysis. Substituted bipyridine was utilized as ligand for the ruthenium chromophore and palladium, saturated with chlorido ligands, was applied as catalytic active site. Irradiation leads to an oxidation of Ru^{II} (to Ru^{III}) and an intramolecular ET to palladium. Bipyrimidine as bridging ligand did not yield a catalytic activity, whereby the usage of tetrapyridophenazine (tpphz) was effective with a turnover number (TON) of 238 H$_2$ molecules per mole catalyst.[218–220] Tuning of the tpphz ligand did not improve the performance.[219] Triethylamine as sacrificial reductant re-reduces the chromophore. The catalyst needs an induction period of 20 h to reach the full hydrogen evolution activity and entirely collapses after 30 h. Further experiments proof that dissociation of the chloride ligands leads to an agglomeration of the palladium nuclei. Dissociation in the beginning of the reaction explains the long induction period of the catalyst, whereby the formation of colloids accounts for the collapse of the reactivity later on.[218,220]
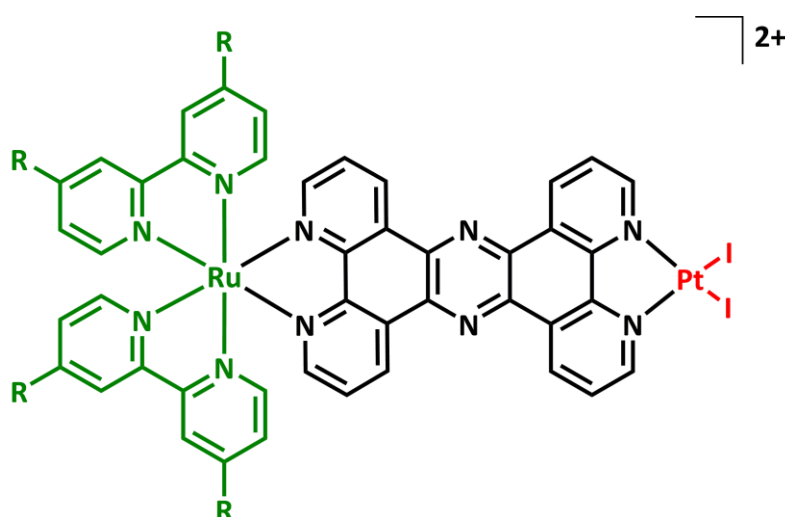
Figure 28. Ruthenium(II) polypyridyl chromophore with tpphz bridging ligand and platinum(II) iodide as catalytic center for hydrogen evolution.

Exchange of the palladium by platinum leads to a constant reactivity and a higher stability of the catalyst, whereby the amount of produced hydrogen is lowered (TON = 7 vs. 238).[187,189,219] Variation of the halide ligands at the platinum from chloride to iodide increases the reactivity significantly by a factor of 40 after 70 h. The bridging ligand and the chromophore did not change at all and the electron

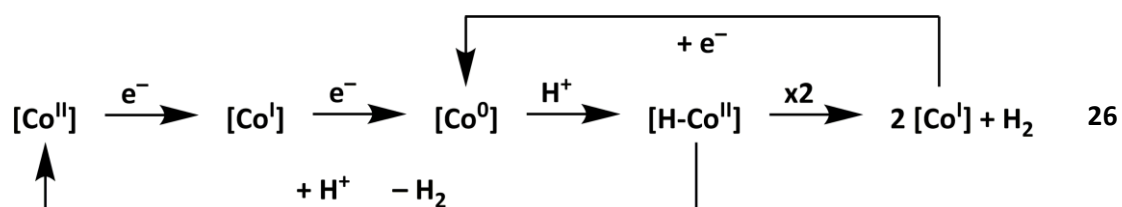transfer kinetics did not change significantly, but the reactivity of the platinum increased drastically.[221,222] This behavior was addressed to the improved stabilization of the platinum orbitals by the iodide ligand.[198,221,222] Improvement of the presented catalysts is still ongoing by exchanging single parts of the chromophore-bridge-catalyst cascade, step by step.[11,186,223–226] One important observation is the possibility of in situ tuning of platinum chloride catalysts by the addition of iodine salt.[186]

1.4.3   Cobalt Catalysts

Cobalt as a first row transition metal owns a $3d^7 4s^2$ electron configuration and shows ferromagnetic behavior. Elemental cobalt and many of its complexes possess catalytic activity,[227,228] driving high interest to their use in the hydrogen evolution reaction (also for oxygen evolving reaction[228,229]) and replace common noble and rare metals like platinum and palladium. Due to the broad applicability, only a few examples of cobalt complexes will be discusses here.[230–235]

One of the most stable class of organometallic cobalt complexes is the class of cobalt porphyrins.[228,236–240] These porphyrins can be used in solution or applied on electrodes for electrocatalytic hydrogen production. Addition of a photosensitizer makes photoinduced H_2 evolution possible. The mechanism for the catalytic proton reduction is still highly discussed in literature, whereby heterolytic and homolytic ligand elimination pathways are conceivable (Equation 26).

$$[Co^{II}] \xrightarrow{e^-} [Co^{I}] \xrightarrow{e^-} [Co^{0}] \xrightarrow{H^+} [H\text{-}Co^{II}] \xrightarrow{x2} 2\,[Co^{I}] + H_2 \qquad \textbf{26}$$
$$+ e^-$$
$$+ H^+ \quad - H_2$$

In Equation 26, a cobalt(II) porphyrin [Co^{II}] is reduced to the catalytically active cobalt (0) complex [Co^0], which binds one proton under oxidative addition [H-Co^{II}]. The formed hydridic complex reacts with another proton, forming molecular hydrogen and cobalt(II) porphyrin [Co^{II}]. Another option is the homolytic reaction of two hydridic complexes with each other, forming molecular hydrogen and two porphyrins with cobalt(I) in the center [Co^I]. After elimination of H_2, reduction of the organometallic complex restarts the catalytic cycle. In other cases, the cycle passes Co^{III} until Co^I, or the first protonation occurs between the two reductive steps of the cycle.[228,236,239,241,242] An example is cobalt(II) *meso*-tetra-(*p*-sulfonatophenyl)porphyrin, which exists at neutral pH in its anionic form and reaches turnover numbers of more than 10^4 moles molecular hydrogen per mole catalyst.[239]

Closer to natural vitamin B12 are artificial cobalt corrole complexes (Figure 29). Corroles own one more negative charge in the metallated state (compared to porphyrins) and are more competent to stabilize

highly charged metal ions.[243,244] They also show hydrogen evolution behavior[245–248] during electrocatalysis, which is similar to the cobalt porphyrins.
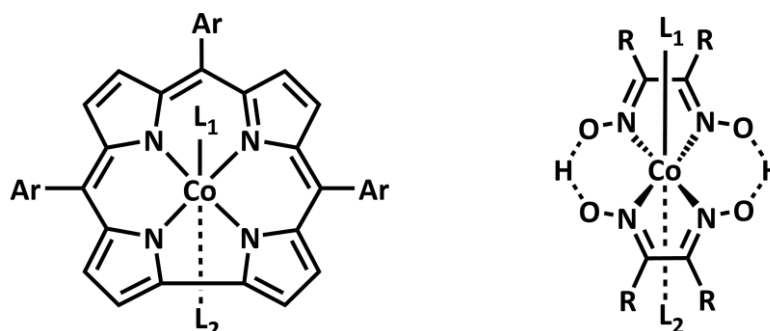

Figure 29. Cobalt triarylcorrole on the left and cobaloxime octahedral coordinated by two glyoximes and two further ligands.

Cobaloximes represent a non-aromatic macrocyclic class of hydrogen evolving cobalt catalysts. The key motive consists of a cobalt center, surrounded by two chelating glyoximes and two further ligands to generate an octahedral coordination sphere (Figure 29).[249] Improvements of the complex pattern are the single linkage of the two chelating ligands to close one reaction side of the metalorganic compound (Figure 30). Ligands (L_1/L_2) like pyridines, are suitable for the coordination at the axial positions out of the plane. Thus, there remains only one reactive site (hydroxyl bridge) for catalysis, which is easier to control by steric effects.[250]
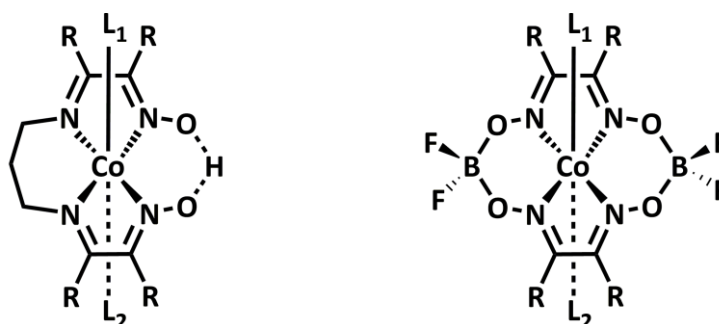

Figure 30. Improved cobaloxime complexes with a single propyl linkage (left side) and two difluoroboryl bridges (right side).

The possible reactions are similar to the one of the cobalt porphyrins. An electron (from electrode or chromophore) reduces the cobalt(II) complex [Co^{II}] once, protonation forms the hydride [$H\text{-}Co^{III}$]. Over a homolytic reaction of two hydrides [$H\text{-}Co^{III}$], molecular hydrogen and the starting complex [Co^{II}] are generated. Alternative pathways are also feasible.[250] In this complex, the oxime functional group represents an important proton donor/mediator, located close to the cobalt center. Exchange of the glyoximes by bis(iminopyridine) increases the stability of the complex due to the extended π-system.[251] Exchange of terminal oxime protons by difluoroboryl groups ($\text{-}BF_2$, Figure 30) yields in low overpotentials of 40 mV for instance, associated with low reaction rates.[252] Hydrolysis leads to the decomposition of the complex.[253]

1.4.4 Cobaltocene as Proton Reductant

Cobaltocene is known as a strong reductant with a reduction potential of -1.33 V vs. FcH/FcH^+ in dichloromethane.[53] Since the first attempts to synthesize CcH, the need of the absence of oxygen and protons was always challenging[254] due to the formation of peroxides[254,255] and hydroxides,[60] as well as the evolution of hydrogen.[256] Therefore, the use of CcH for hydrogen evolution techniques was feasible.

In 1988, Grätzel focused on the reaction of cobaltocene with protons.[7] The addition of acids with coordinating anions, like hydrochloric acid, lead partially to the destruction of the metallocene, forming cobalt salts, hydrogen and cyclopentadiene (Equation 27).

$$3\ CoCp_2 + 4\ HCl \longrightarrow 2[CoCp_2][CoCl_4] + H_2 + 2\ HCp \qquad \textbf{27}$$

The addition of acids with weakly coordinating anions, like acetic acid, sulfuric acid or hexafluorophosphoric acid, leads to hydrogen evolution (Equation 28).[7]

$$\textbf{28}$$
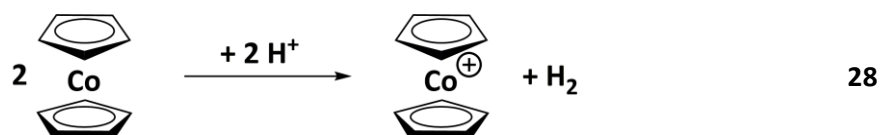
The mechanism of the reaction was unknown by then and highly discussed, due to different possible reaction pathways of ligand protonation, metal protonation and ligand-to-metal hydride migration.[7] Similar discussions are still ongoing for the protonation of ferrocene.[257,258]

Grätzel conducted different experiments to exclude possible mechanisms.[7] The results of protonation and deuteration experiments exclude mechanisms with protonated cyclopentadienyl ligands.[7]

In the residue mechanisms, one proton binds to the cobalt center, forming a hydride (Equation 29). Two hydridic complexes react with each other resulting in molecular hydrogen and cobaltocenium salt (A1). Otherwise, one cobaltocene reduces the hydridic complex (A2). Two neutral hydridic complexes react homolytically with each other to form hydrogen and cobaltocene (B1), which in turn can react in one of the previous steps again. Alternatively, the reaction of the neutral hydride with one proton forms molecular hydrogen and CcH^+ (B2).[7]
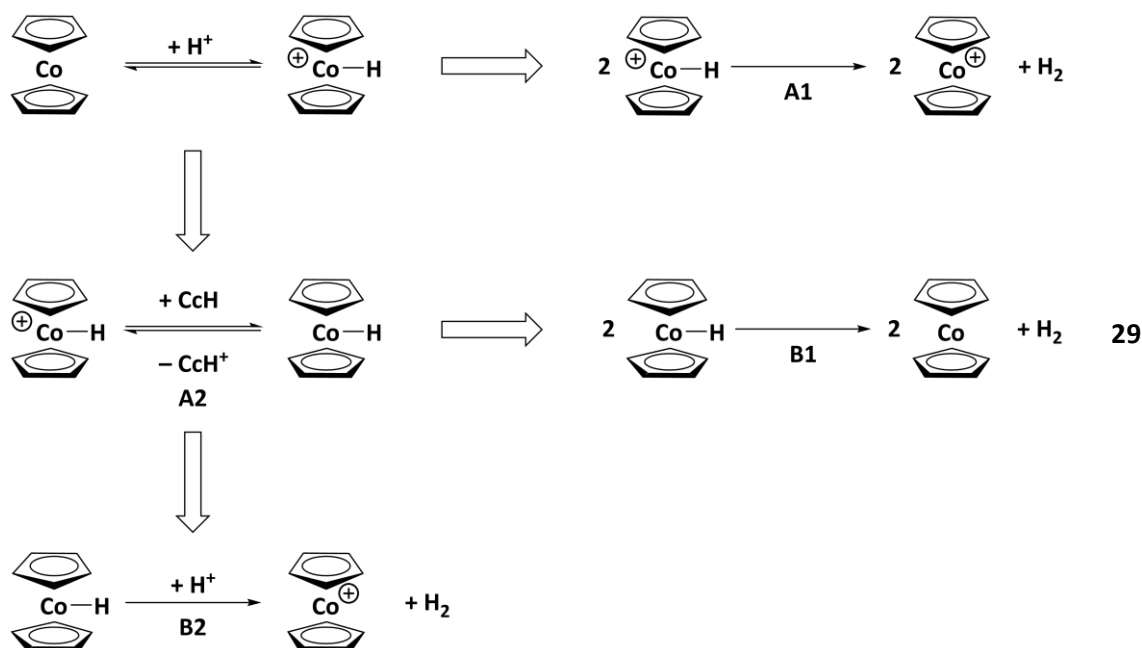
A closer look on the remaining possible mechanisms (Equation 29) was possible, considering the reaction rate constants. Pulsed radiolysis of a cobaltocenium chloride in aqueous sulfuric acid/isopropanol solution forms radicals, which reduce parts of the cobaltocenium chloride.[7] By this method, cobaltocene is formed without the influence of oxygen. The protonation of cobalt forming the metal hydride $[H-Co(C_5H_5)_2]^+$ is the rate determining step of the mechanism. The reduction of the charged hydride by an electron transfer from cobaltocene (route A2) possesses a low reorganization energy and is faster than the bimolecular reaction of two charged hydrides (route A1).[7] So, route A1 could be discarded. The author did not come to a decision, whether route B1 or B2 is faster, due to the poor availability of data. The concentration of protons is higher than the concentration of the neutral hydridic complex $[H-Co(C_5H_5)_2]$. Route B2 could be favored, because only one complex is needed for the reaction compared to the homolytic bimolecular reaction of route B1.[7]

1.5   References

[1]   Kaim, W., Schwederski, B., Klein, A., *Bioinorganic Chemistry: Inorganic Elements in the Chemistry of Life,* 2. Aufl., Wiley, Chichester, **2013**.

[2]   Deisenhofer, J., Michel, H., *Angew. Chem. Int. Ed. Engl.* **1989**, *28*, 829–847.

[3]   Hoff, A. J., Deisenhofer, J., *Phys. Rep.* **1997**, *287*, 1–247.

[4]   Deisenhofer, J., Michel, H., *Angew. Chem.* **1989**, *101*, 872–892.

[5]   Heinze, K., Lang, H., *Organometallics* **2013**, *32*, 5623–5625.

[6]   Astruc, D., *Eur. J. Inorg. Chem.* **2017**, 6–29.

[7]   Koelle, U., Infelta, P. P., Graetzel, M., *Inorg. Chem.* **1988**, *27*, 879–883.

[8]   Vanicek, S., Kopacka, H., Wurst, K., Müller, T., Schottenberger, H., Bildstein, B., *Organometallics* **2014**, *33*, 1152–1156.

[9]   Sheats, J. E., Rausch, M. D., *J. Org. Chem.* **1970**, *35*, 3245–3249.

[10] Melomedov, J., Wünsche von Leupoldt, A., Meister, M., Laquai, F., Heinze, K., *Dalton Trans.* **2013**, *42*, 9727–9739.

[11] Lang, P., Habermehl, J., Troyanov, S. I., Rau, S., Schwalbe, M., *Chem. Eur. J.* **2018**, *24*, 3225–3233.

[12] Fukuzumi, S. in *Progress in Inorganic Chemistry Vol. 56* (Kenneth D. Karlin (Ed.)), John Wiley, Hoboken, NJ, USA, **2009**, 49–154.

[13] Marcus, R. A., *Angew. Chem. Int. Ed. Engl.* **1993**, *32*, 1111–1121.

[14] Marcus, R. A., *Angew. Chem.* **1993**, *105*, 1161–1172.

[15] Marcus, R. A., *Annu. Rev. Phys. Chem.* **1964**, *15*, 155–196.

[16] Gryder, J. W., Dodson, R. W., *J. Am. Chem. Soc.* **1949**, *71*, 1894–1895.

[17] Thompson, R. C., *J. Am. Chem. Soc.* **1948**, *70*, 1045–1046.

[18] Seaborg, G. T., *Chem. Rev.* **1940**, *27*, 199–285.

[19] Varone, A., Ferrari, M., *Renew. Sustain. Energy Rev.* **2015**, *45*, 207–218.

[20] Marcus, R. A., *J. Chem. Phys.* **1956**, *24*, 966–978.

[21] Marcus, R. A., Siddarth, P. in *Photoprocesses in Transition Metal Complexes, Biosystems and other Molecules. Experiment and Theory* (E. Kochanski (Ed.)), Springer Netherlands, Dordrecht, **1992**, 49–88.

[22] Franck, J., Dymond, E. G., *Trans. Faraday Soc.* **1926**, *21*, 536.

[23] Condon, E., *Phys. Rev.* **1926**, *28*, 1182–1201.

[24] Condon, E. U., *Phys. Rev.* **1928**, *32*, 858–872.

[25] Meyer, T. J., *Acc. Chem. Res.* **1978**, *11*, 94–100.

[26] Hush, N. S., *Trans. Faraday Soc.* **1961**, *57*, 557.

[27] Hush, N. S., *Z. Elektrochem.* **1957**, *61*, 734–738.

[28] Brunschwig, B. S., Sutin, N., *Coord. Chem. Rev.* **1999**, *187*, 233–254.

[29] Heckmann, A., Lambert, C., *Angew. Chem. Int. Ed.* **2012**, *51*, 326–392.

[30] Heckmann, A., Lambert, C., *Angew. Chem.* **2012**, *124*, 334–404.

[31] Robin, M. B., Day, P., *Adv. Inorg. Chem.* **1968**, *10*, 247–422.

[32] Day, P., Hush, N. S., Clark, R. J. H., *Philos. Trans. Royal Soc. A* **2008**, *366*, 5–14.

[33] Parthey, M., Kaupp, M., *Chem. Soc. Rev.* **2014**, *43*, 5067–5088.

[34] Piero Zanello, *Inorganic Electrochemistry: Theory, Practice and Application*, Royal Society of Chemistry, Cambridge, **2003**.

[35] Allen, G. C., Hush, N. S. in *Prog. Inorg. Chem.* (F. A. Cotton (Ed.)), John Wiley, Hoboken, NJ, USA, **1967**, 391–444.

[36] Brunschwig, B. S., Sutin, N. in *Electron Transfer in Chemistry* (V. Balzani (Ed.)), Wiley-VCH, Weinheim, **2001**, 582–617.

[37] Szeghalmi, A. V., Erdmann, M., Engel, V., Schmitt, M., Amthor, S., Kriegisch, V., Nöll, G., Stahl, R., Lambert, C., Leusser, D., Stalke, D., Zabel, M., Popp, J., *J. Am. Chem. Soc.* **2004**, *126*, 7834–7845.

[38] Demadis, K. d., Hartshorn, C. M., Meyer, T. J., *Chem. Rev.* **2001**, *101*, 2655–2686.

[39] Cowan, D. O., Kaufman, F., *J. Am. Chem. Soc.* **1970**, *92*, 219–220.

[40] Hankache, J., Wenger, O. S., *Chem. Rev.* **2011**, *111*, 5138–5178.

[41] Lambert, C., Nöll, G., *J. Am. Chem. Soc.* **1999**, *121*, 8434–8442.

[42] Lahlil, K., Moradpour, A., Bowlas, C., Menou, F., Cassoux, P., Bonvoisin, J., Launay, J.-P., Dive, G., Dehareng, D., *J. Am. Chem. Soc.* **1995**, *117*, 9995–10002.

[43] Warratz, R., Peters, G., Studt, F., Römer, R.-H., Tuczek, F., *Inorg. Chem.* **2006**, *45*, 2531–2542.

[44] Wilkinson, G., *J. Am. Chem. Soc.* **1952**, *74*, 6148–6149.

[45] Zhu, L., Xiong, P., Mao, Z.-Y., Wang, Y.-H., Yan, X., Lu, X., Xu, H.-C., *Angew. Chem. Int. Ed.* **2016**, *55*, 2226–2229.

[46] Chernyak, N., Buchwald, S. L., *J. Am. Chem. Soc.* **2012**, *134*, 12466–12469.

[47] Zhu, L., Xiong, P., Mao, Z.-Y., Wang, Y.-H., Yan, X., Lu, X., Xu, H.-C., *Angew. Chem.* **2016**, *128*, 2266–2269.

[48] Alonso, B., Armada, P. G., Losada, J., Cuadrado, I., González, B., Casado, C. M., *Biosens. Bioelectron.* **2004**, *19*, 1617–1625.

[49] Casado, C. M., González, B., Cuadrado, I., Alonso, B., Morán, M., Losada, J., *Angew. Chem. Int. Ed.* **2000**, *39*, 2135–2138.

[50] Valério, C., Ruiz, J., Filiaux, J.-L., Astruc, D., *Comptes Rendus Acad. Sci. IIC* **1999**, *2*, 79–83.

[51] Casado, C. M., González, B., Cuadrado, I., Alonso, B., Morán, M., Losada, J., *Angew. Chem.* **2000**, *112*, 2219–2222.

[52] Koepp, H.-M., Wendt, H., Stkehlow, H., *Z. Elektrochem.* **1960**, *64*, 483–491.

[53] Connelly, N. G., Geiger, W. E., *Chem. Rev.* **1996**, *96*, 877–910.

[54] Waniek, S. D., Klett, J., Förster, C., Heinze, K., *Beilstein J. Org. Chem.* **2018**, *14*, 1004–1015.

[55] Ding, Y., Zhao, Y., Li, Y., Goodenough, J. B., Yu, G., *Energy Environ. Sci.* **2017**, *10*, 491–497.

[56] Hwang, B., Park, M.-S., Kim, K., *ChemSusChem* **2015**, *8*, 310–314.

[57] Veit, P., Volkert, C., Förster, C., Ksenofontov, V., Schlicher, S., Bauer, M., Heinze, K., *Chem. Commun.* **2019**, *55*, 4615–4618.

[58] Vanicek, S., Podewitz, M., Stubbe, J., Schulze, D., Kopacka, H., Wurst, K., Müller, T., Lippmann, P., Haslinger, S., Schottenberger, H., Liedl, K. R., Ott, I., Sarkar, B., Bildstein, B., *Chem. Eur. J.* **2018**, *24*, 3742–3753.

[59] Hettmanczyk, L., Suntrup, L., Klenk, S., Hoyer, C., Sarkar, B., *Chem. Eur. J.* **2017**, *23*, 576–585.

[60] Elschenbroich, C., *Organometallchemie,* 6. Aufl., Vieweg+Teubner, Wiesbaden, **2008**.

[61] Roginski, R. T., Moroz, A., Hendrickson, D. N., Drickamer, H. G., *J. Phys. Chem.* **1988**, *92*, 4319–4323.

[62] Ammeter, J. H., Swalen, J. D., *J. Chem. Phys.* **1972**, *57*, 678–698.

[63] Gray, H. B., Sohn, Y. S., Hendrickson, N., *J. Am. Chem. Soc.* **1971**, *93*, 3603–3612.

[64] Dunitz, J. D., Orgel, L. E., Rich, A., *Acta Cryst.* **1956**, *9*, 373–375.

[65] Scholz, S., Scheibitz, M., Schödel, F., Bolte, M., Wagner, M., Lerner, H.-W., *Inorg. Chim. Acta* **2007**, *360*, 3323–3329.

[66] Cotton, F. A., Daniels, L. M., Wilkinson, C. C., *Acta Cryst.* **2001**, *E57*, m529-m530.

[67] Bünder, W., Weiss, E., *J. Organomet. Chem.* **1975**, *92*, 65–68.

[68] Stahl, K.-P., Boche, G., Massa, W., *J. Organomet. Chem.* **1984**, *277*, 113–125.

[69] Petrov, A. R., Jess, K., Freytag, M., Jones, P. G., Tamm, M., *Organometallics* **2013**, *32*, 5946–5954.

[70] Butovskii, M. V., Englert, U., Herberich, G. E., Koelle, U., *Eur. J. Inorg. Chem.* **2005**, 971–980.

[71] Yamazaki, H., Wakatsuki, Y., *Bull. Chem. Soc. Jpn.* **1979**, *52*, 1239–1240.

[72] Turro, N. J., Hammond, G. S., *J. Am. Chem. Soc.* **1962**, *84*, 2841–2842.

[73] Ziegler, K., Froitzheim-Kühlhorn, H., Hafner, K., *Chem. Ber.* **1956**, *89*, 434–443.

[74] Bernheim, M., Boche, G., *Angew. Chem. Int. Ed. Engl.* **1980**, *19*, 1010–1011.

[75] Bernheim, M., Boche, G., *Angew. Chem.* **1980**, *92*, 1043–1044.

[76] Heinze, K., Schlenker, M., *Eur. J. Inorg. Chem.* **2004**, 2974–2988.

[77] Vanicek, S., Kopacka, H., Wurst, K., Müller, T., Hassenrück, C., Winter, R. F., Bildstein, B., *Organometallics* **2016**, *35*, 2101–2109.

[78] Jochriem, M., Bosch, D., Kopacka, H., Bildstein, B., *Organometallics* **2019**.

[79] Wolter-Steingrube, A., Cordsen, K., Heck, J., *Eur. J. Inorg. Chem.* **2017**, 1314–1319.

[80] Zhao, L., Liu, X., Zhang, L., Qiu, G., Astruc, D., Gu, H., *Coord. Chem. Rev.* **2017**, *337*, 34–79.

[81] Huesmann, H., Förster, C., Siebler, D., Gasi, T., Heinze, K., *Organometallics* **2011**, *31*, 413–427.

[82] Butler, I. R., Quayle, S. C., *J. Organomet. Chem.* **1998**, *552*, 63–68.

[83] Chowdhury, S., Schatte, G., Kraatz, H.-B., *Angew. Chem. Int. Ed.* **2006**, *45*, 6882–6884.

[84] Mahmoud, K. A., Kraatz, H.-B., *J. Inorg. Organomet. Polym.* **2006**, *16*, 201–210.

[85] Okamura, T.-a., Sakauye, K., Ueyama, N., Nakamura, A., *Inorg. Chem.* **1998**, *37*, 6731–6736.

[86] Chowdhury, S., Schatte, G., Kraatz, H.-B., *Angew. Chem.* **2006**, *118*, 7036–7038.

[87] Heinze, K., Siebler, D., *Z. Anorg. Allg. Chem.* **2007**, *633*, 2223–2233.

[88] Siebler, D., Förster, C., Heinze, K., *Dalton Trans.* **2011**, *40*, 3558–3575.

[89] Siebler, D., Linseis, M., Gasi, T., Carrella, L. M., Winter, R. F., Förster, C., Heinze, K., *Chem. Eur. J.* **2011**, *17*, 4540–4551.

[90] Siebler, D., Heinze, K., *J. Organomet. Chem.* **2016**, *821*, 19–24.

[91] Kovač, V., Radolović, K., Habuš, I., Siebler, D., Heinze, K., Rapić, V., *Eur. J. Inorg. Chem.* **2009**, 389–399.

[92] Piperberg, G., Wilner, O. I., Yehezkeli, O., Tel-Vered, R., Willner, I., *J. Am. Chem. Soc.* **2009**, *131*, 8724–8725.

[93] Beer, P. D., Drew, M. G. B., Hesek, D., Jagessar, R., *J. Chem. Soc., Chem. Commun.* **1995**, *65*, 1187–1189.

[94] Beer, P. D., Dickson, C. A. P., Fletcher, N., Goulden, A. J., Grieve, A., Hodacova, J., Wear, T., *J. Chem. Soc., Chem. Commun.* **1993**, 828–830.

[95] González, B., Cuadrado, I., Casado, C. M., Alonso, B., Pastor, C. J., *Organometallics* **2000**, *19*, 5518–5521.

[96] González, B., Cuadrado, I., Alonso, B., Casado, C. M., Morán, M., Kaifer, A. E., *Organometallics* **2002**, *21*, 3544–3551.

[97] Degrand, C., Limoges, B., Gautier, A., Blankespoor, R. L., *Appl. Organomet. Chem.* **1993**, *7*, 233–241.

[98] Chantson, J. T., Falzacappa, M. V. V., Crovella, S., Metzler-Nolte, N., *J. Organomet. Chem.* **2005**, *690*, 4564–4572.

[99] Yang, P., Pageni, P., Kabir, M. P., Zhu, T., Tang, C., *ACS Macro Lett.* **2016**, *5*, 1293–1300.

[100] Beer, P. D., *Chem. Commun.* **1996**, 689–696.

[101] Beer, P. D., Drew, M. G. B., Hodacova, J., Stokes, S. E., *J. Chem. Soc., Dalton Trans.* **1995**, 3447–3453.

[102] Beer, P. D., Hesek, D., Hodacova, J., Stokes, S. E., *J. Chem. Soc., Chem. Commun.* **1992**, 270–272.

[103] Beer, P. D., Chen, Z., Goulden, A. J., Graydon, A., Stokes, S. E., Wear, T., *J. Chem. Soc., Chem. Commun.* **1993**, 1834–1836.

[104] Beer, P. D., Drew, M. G. B., Hazlewood, C., Hesek, D., Hodacova, J., Stokes, S. E., *J. Chem. Soc., Chem. Commun.* **1993**, 229–231.

[105] Beer, P. D., Hazlewood, C., Hesek, D., Hodacova, J., Stokes, S. E., *J. Chem. Soc., Dalton Trans.* **1993**, 1327–1332.

[106] Beer, P. D., Hesek, D., Kingston, J. E., Smith, D. K., Stokes, S. E., Drew, M. G. B., *Organometallics* **1995**, *14*, 3288–3295.

[107] Beer, P. D., Szemes, F., *J. Chem. Soc., Chem. Commun.* **1995**, 2245–2247.

[108] Hunter, C. A., Sanders, J. K. M., *J. Am. Chem. Soc.* **1990**, *112*, 5525–5534.

[109] Gouterman, M., *J. Chem. Phys.* **1959**, *30*, 1139–1161.

[110] Moss, G. P., *Pure Appl. Chem.* **1987**, *59*, 779–832.

[111] Braun, J., Hasenfratz, C., Schwesinger, R., Limbach, H.-H., *Angew. Chem.* **1994**, *106*, 2302–2304.

[112] Braun, J., Hasenfratz, C., Schwesinger, R., Limbach, H.-H., *Angew. Chem. Int. Ed. Engl.* **1994**, *33*, 2215–2217.

[113] Falk, J. E., *Porphyrins and Metalloporphyrins,* 2. Aufl., Elsevier, Amsterdam, **1976**.

[114] Fulmer, G. R., Miller, A. J. M., Sherden, N. H., Gottlieb, H. E., Nudelman, A., Stoltz, B. M., Bercaw, J. E., Goldberg, K. I., *Organometallics* **2010**, *29*, 2176–2179.

[115] Melomedov, J., Ochsmann, J. R., Meister, M., Laquai, F., Heinze, K., *Eur. J. Inorg. Chem.* **2014**, 1984–2001.

[116] Rudine, A. B., DelFatti, B. D., Wamser, C. C., *J. Org. Chem.* **2013**, *78*, 6040–6049.

[117] Kadish, K. M., Smith, K. M., Guilard, R., *The Porphyrin Handbook Vol. 12: The Iron and Cobalt Pigments: Biosynthesis, Structure, and Degradation*, Academic Press, San Diego, CA, USA, **2003**.

[118] Kadish, K. M., Smith, K. M., Guilard, R., *The Porphyrin Handbook Vol. 13: Chlorophylls and Bilins: Biosynthesis, Synthesis, and Degradation*, Academic Press, San Diego, CA, USA, **2003**.

[119] Tame, J., Vallone, B., *Deoxy Human Hemoglobin*, **1998**.

[120] Tame, J. R. H., Vallone, B., *Acta Cryst.* **2000**, *D56*, 805–811.

[121] Rose, A. S., Bradley, A. R., Valasatava, Y., Duarte, J. M., Prlic, A., Rose, P. W., *Bioinformatics* **2018**, *34*, 3755–3758.

[122] Berman, H. M., Westbrook, J., Feng, Z., Gilliland, G., Bhat, T. N., Weissig, H., Shindyalov, I. N., Bourne, P. E., *Nucleic Acids Res.* **2000**, *28*, 235–242.

[123] Wei, X. P., Zhang, X. Z., Su, X. D., Cao, P., Liu, X. Y., Li, M., Chang, W. R., Liu, Z. F., *Cryo-EM structure of spinach PSII-LHCII supercomplex at 3.2 Angstrom resolution*, **2016**.

[124] Wei, X., Su, X., Cao, P., Liu, X., Chang, W., Li, M., Zhang, X., Liu, Z., *Nature* **2016**, *534*, 69–74.

[125] Berardi, S., Drouet, S., Francàs, L., Gimbert-Suriñach, C., Guttentag, M., Richmond, C., Stoll, T., Llobet, A., *Chem. Soc. Rev.* **2014**, *43*, 7501–7519.

[126] Nakamura, Y., Aratani, N., Osuka, A., *Chem. Soc. Rev.* **2007**, *36*, 831–845.

[127] Willner, I., Willner, B. in *Topics in Current Chemistry* (J. Mattay (Ed.)), Springer, Berlin, **1991**.

[128] Laible, P. D., Knox, R. S., Owens, T. G., *J. Phys. Chem. B* **1998**, *102*, 1641–1648.

[129] Shipman, L. L., Cotton, T. M., Norris, J. R., Katz, J. J., *Proc. Natl. Acad. Sci.* **1976**, *73*, 1791–1794.

[130] Govindjee, Shevela, D., Björn, L. O., *Photosynth. Res.* **2017**, *133*, 5–15.

[131] Blankenship, R. E., Prince, R. C., *Trends Biochem. Sci.* **1985**, *10*, 382–383.

[132] Blankenship, R. E., *Molecular Mechanisms of Photosynthesis,* 2. Aufl., Wiley Blackwell, Chichester, England, **2014**.

[133] Gerster, D., Reichert, J., Bi, H., Barth, J. V., Kaniber, S. M., Holleitner, A. W., Visoly-Fisher, I., Sergani, S., Carmeli, I., *Nat. Nanotechnol.* **2012**, *7*, 673–676.

[134] Kulik, L. V., Epel, B., Lubitz, W., Messinger, J., *J. Am. Chem. Soc.* **2007**, *129*, 13421–13435.

[135] Mukhopadhyay, S., Mandal, S. K., Bhaduri, S., Armstrong, W. H., *Chem. Rev.* **2004**, *104*, 3981–4026.

[136] Weinberg, D. R., Gagliardi, C. J., Hull, J. F., Murphy, C. F., Kent, C. A., Westlake, B. C., Paul, A., Ess, D. H., McCafferty, D. G., Meyer, T. J., *Chem. Rev.* **2012**, *112*, 4016–4093.

[137] Raux, E., Schubert, H. L., Warren, M. J., *Cell. Mol. Life Sci.* **2000**, *57*, 1880–1893.

[138] Rothemund, P., *J. Am. Chem. Soc.* **1935**, *57*, 2010–2011.

[139] Rothemund, P., *J. Am. Chem. Soc.* **1936**, *58*, 625–627.

[140] Rothemund, P., Menotti, A. R., *J. Am. Chem. Soc.* **1941**, *63*, 267–270.

[141] Heinze, K., Reinhart, A., *Dalton Trans.* **2008**, 469–480.

[142] Gouterman, M., *J. Mol. Spectrosc.* **1961**, *6*, 138–163.

[143] Gouterman, M., Wagnière, G. H., Snyder, L. C., *J. Mol. Spectrosc.* **1963**, *11*, 108–127.

[144] Rimington, C., Mason, S. F., Kennard, O., *Spectrochim. Acta* **1958**, *12*, 65–77.

[145] LeGourriérec, D., Andersson, M., Davidsson, J., Mukhtar, E., Sun, L., Hammarström, L., *J. Phys. Chem. A* **1999**, *103*, 557–559.

[146] McDermott, G., Prince, S. M., Freer, A. A., Hawthornthwaite-Lawless, A. M., Papiz, M. Z., Cogdell, R. J., Isaacs, N. W., *Nature* **1995**, *374*, 517–521.

[147] Deisenhofer, J., Epp, O., Miki, K., Huber, R., Michel, H., *J. Mol. Biol.* **1984**, *180*, 385–398.

[148] Breton, J., Verméglio, A., *The Photosynthetic Bacterial Reaction Center II. Structure, Spectroscopy and Dynamics*, Springer US, Boston, MA, USA, **1993**.

[149] Holten, D., Bocian, D. F., Lindsey, J. S., *Acc. Chem. Res.* **2002**, *35*, 57–69.

[150] Ladomenou, K., Natali, M., Iengo, E., Charalampidis, G., Scandola, F., Coutsolelos, A. G., *Coord. Chem. Rev.* **2015**, *304-305*, 38–54.

[151] Imahori, H., Sekiguchi, Y., Kashiwagi, Y., Sato, T., Araki, Y., Ito, O., Yamada, H., Fukuzumi, S., *Chem. Eur. J.* **2004**, *10*, 3184–3196.

[152] Fukuzumi, S., Okamoto, K., Yoshida, Y., Imahori, H., Araki, Y., Ito, O., *J. Am. Chem. Soc.* **2003**, *125*, 1007–1013.

[153] Winters, M. U., Dahlstedt, E., Blades, H. E., Wilson, C. J., Frampton, M. J., Anderson, H. L., Albinsson, B., *J. Am. Chem. Soc.* **2007**, *129*, 4291–4297.

[154] Gray, H. B., Winkler, J. R., *Proc. Natl. Acad. Sci. U.S.A.* **2005**, *102*, 3534–3539.

[155] Siddarth, P., Marcus, R. A., *J. Phys. Chem.* **1990**, *94*, 2985–2989.

[156] Das, S. K., Song, B., Mahler, A., Nesterov, V. N., Wilson, A. K., Ito, O., D'Souza, F., *J. Phys. Chem. C* **2014**, *118*, 3994–4006.

[157] Kadish, K. M., Smith, K. M., Guilard, R. (Ed.) *Handbook of Porphyrin Science Vol. 1: Supramolecular Chemistry*, World Scientific Publishing Company, Singapore, **2010**.

[158] Gust, D., Moore, T. A., Moore, A. L., *Acc. Chem. Res.* **1993**, *26*, 198–205.

[159] Burrell, A. K., Officer, D. L., Plieger, P. G., Reid, D. C. W., *Chem. Rev.* **2001**, *101*, 2751–2796.

[160] Natali, M., Campagna, S., Scandola, F., *Chem. Soc. Rev.* **2014**, *43*, 4005–4018.

[161] Luo, C., Guldi, D. M., Imahori, H., Tamaki, K., Sakata, Y., *J. Am. Chem. Soc.* **2000**, *122*, 6535–6551.

[162] Preiß, S., Päpcke, A., Burkhardt, L., Großmann, L., Lochbrunner, S., Bauer, M., Opatz, T., Heinze, K., *Chem. Eur. J.* **2019**, *25*, 5940–5949.

[163] Imahori, H., Tamaki, K., Araki, Y., Sekiguchi, Y., Ito, O., Sakata, Y., Fukuzumi, S., *J. Am. Chem. Soc.* **2002**, *124*, 5165–5174.

[164] Gust, D., Moore, T. A., Moore, A. L., Macpherson, A. N., Lopez, A., DeGraziano, J. M., Gouni, I., Bittersmann, E., Seely, G. R., *J. Am. Chem. Soc.* **1993**, *115*, 11141–11152.

[165] Imahori, H., Guldi, D. M., Tamaki, K., Yoshida, Y., Luo, C., Sakata, Y., Fukuzumi, S., *J. Am. Chem. Soc.* **2001**, *123*, 6617–6628.

[166] Fukuzumi, S., Okamoto, K., Imahori, H., *Angew. Chem.* **2002**, *114*, 642–644.

[167] Fukuzumi, S., Okamoto, K., Imahori, H., *Angew. Chem. Int. Ed.* **2002**, *41*, 620–622.

[168] Hiroshi, I., Kiyoshi, H., Tsuyoshi, A., Masanori, A., Seiji, T., Tadashi, O., Masahiro, S., Yoshiteru, S., *Chem. Phys. Lett.* **1996**, *263*, 545–550.

[169] Nurttila, S. S., Becker, R., Hessels, J., Woutersen, S., Reek, J. N. H., *Chem. Eur. J.* **2018**, *24*, 16395–16406.

[170] Wang, M., Chen, L., Li, X., Sun, L., *Dalton Trans.* **2011**, *40*, 12793–12800.

[171] Preiß, S., Melomedov, J., Wünsche von Leupoldt, A., Heinze, K., *Chem. Sci.* **2016**, *7*, 596–610.

[172] Fukuzumi, S., Okamoto, K., Gros, C. P., Guilard, R., *J. Am. Chem. Soc.* **2004**, *126*, 10441–10449.

[173] Fukuzumi, S., Ohkubo, K., Suenobu, T., *Acc. Chem. Res.* **2014**, *47*, 1455–1464.

[174] Melomedov, J., Ochsmann, J. R., Meister, M., Laquai, F., Heinze, K., *Eur. J. Inorg. Chem.* **2014**, 2902–2915.

[175] Esswein, A. J., Nocera, D. G., *Chem. Rev.* **2007**, *107*, 4022–4047.

[176] Álvarez, A., Bansode, A., Urakawa, A., Bavykina, A. V., Wezendonk, T. A., Makkee, M., Gascon, J., Kapteijn, F., *Chem. Rev.* **2017**, *117*, 9804–9838.

[177] Li, M. M.-J., Tsang, S. C. E., *Catal. Sci. Technol.* **2018**, *8*, 3450–3464.

[178] Nie, X., Jiang, X., Wang, H., Luo, W., Janik, M. J., Chen, Y., Guo, X., Song, C., *ACS Catal.* **2018**, *8*, 4873–4892.

[179] Holladay, J. D., Hu, J., King, D. L., Wang, Y., *Catal. Today* **2009**, *139*, 244–260.

[180] Cavell, A. C., Hartley, C. L., Liu, D., Tribble, C. S., McNamara, W. R., *Inorg. Chem.* **2015**, *54*, 3325–3330.

[181] Pregger, T., Graf, D., Krewitt, W., Sattler, C., Roeb, M., Möller, S., *Int. J. Hydrog. Energy* **2009**, *34*, 4256–4267.

[182] Grätzel, M., *Nature* **2001**, *414*, 338–344.

[183] May, M. M., Lewerenz, H.-J., Lackner, D., Dimroth, F., Hannappel, T., *Nat. Commun.* **2015**, *6*, 8286.

[184] Murdoch, M., Waterhouse, G. I. N., Nadeem, M. A., Metson, J. B., Keane, M. A., Howe, R. F., Llorca, J., Idriss, H., *Nat. Chem.* **2011**, *3*, 489–492.

[185] Abdi, F. F., Han, L., Smets, A. H. M., Zeman, M., Dam, B., van de Krol, R., *Nat. Commun.* **2013**, *4*, 2195.

[186] Kaufhold, S., D. Imanbaew, Riehn, C., Rau, S., *Sustain. Energ. Fuels* **2017**, *1*, 2066–2070.

[187] Pfeffer, M. G., Schäfer, B., Smolentsev, G., Uhlig, J., Nazarenko, E., Guthmuller, J., Kuhnt, C., Wächtler, M., Dietzek, B., Sundström, V., Rau, S., *Angew. Chem. Int. Ed.* **2015**, *54*, 5044–5048.

[188] Rommel, S. A., Sorsche, D., Schönweiz, S., Kübel, J., Rockstroh, N., Dietzek, B., Streb, C., Rau, S., *J. Organomet. Chem.* **2016**, *821*, 163–170.

[189] Pfeffer, M. G., Schäfer, B., Smolentsev, G., Uhlig, J., Nazarenko, E., Guthmuller, J., Kuhnt, C., Wächtler, M., Dietzek, B., Sundström, V., Rau, S., *Angew. Chem.* **2015**, *127*, 5132–5136.

[190] von Helmholtz, H., *J. Chem. Soc., Trans.* **1881**, *39*, 277–304.

[191] Lide, D. R., *CRC Handbook of Chemistry and Physics 84th Ed.*, CRC Press, Boca Raton, Florida, **2003**.

[192] Rossmeisl, J., Qu, Z.-W., Zhu, H., Kroes, G.-J., Nørskov, J. K., *J. Electroanal. Chem.* **2007**, *607*, 83–89.

[193] Tributsch, H. in *Energy and Environment Series* (S. D. Tilley, S. Lany, R. van de Krol (Ed.)), Royal Society of Chemistry, Cambridge, **2018**.

[194] Artrith, N., Sailuam, W., Limpijumnong, S., Kolpak, A. M., *Phys. Chem. Chem. Phys.* **2016**, *18*, 29561–29570.

[195] Dau, H., Limberg, C., Reier, T., Risch, M., Roggan, S., Strasser, P., *ChemCatChem* **2010**, *2*, 724–761.

[196] Cui, C., Gan, L., Heggen, M., Rudi, S., Strasser, P., *Nat. Mater.* **2013**, *12*, 765–771.

[197] Gupta, G., Slanac, D. A., Kumar, P., Wiggins-Camacho, J. D., Wang, X., Swinnea, S., More, K. L., Dai, S., Stevenson, K. J., Johnston, K. P., *Chem. Mater.* **2009**, *21*, 4515–4526.

[198] Ozawa, H., Yokoyama, Y., Haga, M.-a., Sakai, K., *Dalton Trans.* **2007**, 1197–1206.

[199] Tsuji, Y., Yamamoto, K., Yamauchi, K., Sakai, K., *Angew. Chem. Int. Ed.* **2018**, *57*, 208–212.

[200] Tsuji, Y., Yamamoto, K., Yamauchi, K., Sakai, K., *Angew. Chem.* **2018**, *130*, 214–218.

[201] Ozawa, H., Sakai, K., *Chem. Lett.* **2007**, *36*, 920–921.

[202] Miyaji, M., Kitamoto, K., Ozawa, H., Sakai, K., *Eur. J. Inorg. Chem.* **2017**, *2017*, 1237–1244.

[203] Tanaka, S., Nakazono, T., Yamauchi, K., Sakai, K., *Chem. Lett.* **2017**, *46*, 1573–1575.

[204] Yamauchi, K., Sakai, K., *Dalton Trans.* **2015**, *44*, 8685–8696.

[205] Goy, R., Bertini, L., Rudolph, T., Lin, S., Schulz, M., Zampella, G., Dietzek, B., Schacher, F. H., Gioia, L. de, Sakai, K., Weigand, W., *Chem. Eur. J.* **2017**, *23*, 334–345.

[206] Léger, C., Jones, A. K., Roseboom, W., Albracht, S. P. J., Armstrong, F. A., *Biochemistry* **2002**, *41*, 15736–15746.

[207] Madden, C., Vaughn, M. D., Díez-Pérez, I., Brown, K. A., King, P. W., Gust, D., Moore, A. L., Moore, T. A., *J. Am. Chem. Soc.* **2012**, *134*, 1577–1582.

[208] Frey, M., *ChemBioChem* **2002**, *3*, 153–160.

[209] Adams, M. W.W., Mortenson, L. E., Chen, J.-S., *Biochim. Biophys. Acta Rev. Bioenerg.* **1980**, *594*, 105–176.

[210] Yamaguchi, T., Masaoka, S., Sakai, K., *Chem. Lett.* **2009**, *38*, 434–435.

[211] Koshiba, K., Yamauchi, K., Sakai, K., *Angew. Chem. Int. Ed.* **2017**, *56*, 4247–4251.

[212] Koshiba, K., Yamauchi, K., Sakai, K., *Angew. Chem.* **2017**, *129*, 4311–4315.

[213] Aimoto, Y., Koshiba, K., Yamauchi, K., Sakai, K., *Chem. Commun.* **2018**, *54*, 12820–12823.

[214] Koshiba, K., Yamauchi, K., Sakai, K., *Dalton Trans.* **2019**, *48*, 635–640.

[215] Koshiba, K., Yamauchi, K., Sakai, K., *ChemElectroChem* **2019**, *6*, 2273–2281.

[216] Murakami, N., Tango, Y., Miyake, H., Tajima, T., Nishina, Y., Kurashige, W., Negishi, Y., Takaguchi, Y., *Sci. Rep.* **2017**, *7*, 43445 (1-7).

[217] Fan, X.-B., Yu, S., Hou, B., Kim, J. M., *Isr. J. Chem.* **2019**, *59*, 762–773.

[218] Rau, S., Schäfer, B., Gleich, D., Anders, E., Rudolph, M., Friedrich, M., Görls, H., Henry, W., Vos, J. G., *Angew. Chem.* **2006**, *118*, 6361–6364.

[219] Karnahl, M., Kuhnt, C., Ma, F., Yartsev, A., Schmitt, M., Dietzek, B., Rau, S., Popp, J., *ChemPhysChem* **2011**, *12*, 2101–2109.

[220] Rau, S., Schäfer, B., Gleich, D., Anders, E., Rudolph, M., Friedrich, M., Görls, H., Henry, W., Vos, J. G., *Angew. Chem. Int. Ed.* **2006**, *45*, 6215–6218.

[221] Pfeffer, M. G., Kowacs, T., Wächtler, M., Guthmuller, J., Dietzek, B., Vos, J. G., Rau, S., *Angew. Chem. Int. Ed.* **2015**, *54*, 6627–6631.

[222] Pfeffer, M. G., Kowacs, T., Wächtler, M., Guthmuller, J., Dietzek, B., Vos, J. G., Rau, S., *Angew. Chem.* **2015**, *127*, 6727–6731.

[223] Mengele, A. K., Kaufhold, S., Streb, C., Rau, S., *Dalton Trans.* **2016**, *45*, 6612–6618.

[224] Pan, Q., Freitag, L., Kowacs, T., Falgenhauer, J. C., Korterik, J. P., Schlettwein, D., Browne, W. R., Pryce, M. T., Rau, S., González, L., Vos, J. G., Huijser, A., *Chem. Commun.* **2016**, *52*, 9371–9374.

[225] Kowacs, T., O'Reilly, L., Pan, Q., Huijser, A., Lang, P., Rau, S., Browne, W. R., Pryce, M. T., Vos, J. G., *Inorg. Chem.* **2016**, *55*, 2685–2690.

[226] Habermehl, J., Nauroozi, D., Martynow, M., Vilk, Y. E., Beranek, R., Guthmuller, J., Rau, S., *Sustain. Energ. Fuels* **2019**, *107*, 4022.

[227] Call, A., Cibian, M., Yamamoto, K., Nakazono, T., Yamauchi, K., Sakai, K., *ACS Catal.* **2019**, *9*, 4867–4874.

[228] Zhang, W., Lai, W., Cao, R., *Chem. Rev.* **2017**, *117*, 3717–3797.

[229] Xu, L., Lei, H., Zhang, Z., Yao, Z., Li, J., Yu, Z., Cao, R., *Phys. Chem. Chem. Phys.* **2017**, *19*, 9755–9761.

[230] McNamara, W. R., Han, Z., Alperin, P. J., Brennessel, W. W., Holland, P. L., Eisenberg, R., *J. Am. Chem. Soc.* **2011**, *133*, 15368–15371.

[231] Tong, L., Kopecky, A., Zong, R., Gagnon, K. J., Ahlquist, M. S. G., Thummel, R. P., *Inorg. Chem.* **2015**, *54*, 7873–7884.

[232] Mandal, S., Shikano, S., Yamada, Y., Lee, Y.-M., Nam, W., Llobet, A., Fukuzumi, S., *J. Am. Chem. Soc.* **2013**, *135*, 15294–15297.

[233] Li, P., Zaffaroni, R., Bruin, B. de, Reek, J. N. H., *Chem. Eur. J.* **2015**, *21*, 4027–4038.

[234] Wang, J.-W., Yamauchi, K., Huang, H.-H., Sun, J.-K., Luo, Z.-M., Zhong, D.-C., Lu, T.-B., Sakai, K., *Angew. Chem. Int. Ed.* **2019**, *58*, 10923–10927.

[235] Wang, J.-W., Yamauchi, K., Huang, H.-H., Sun, J.-K., Luo, Z.-M., Zhong, D.-C., Lu, T.-B., Sakai, K., *Angew. Chem.* **2019**, *131*, 11039–11043.

[236] Kellett, R. M., Spiro, T. G., *Inorg. Chem.* **1985**, *24*, 2373–2377.

[237] Kielb, P., Horch, M., Wrzolek, P., Goetz, R., Ly, K. H., Kozuch, J., Schwalbe, M., Weidinger, I. M., *Catal. Sci. Technol.* **2018**, *8*, 1849–1857.

[238] Lee, C. H., Dogutan, D. K., Nocera, D. G., *J. Am. Chem. Soc.* **2011**, *133*, 8775–8777.

[239] Beyene, B. B., Mane, S. B., Hung, C.-H., *Chem. Commun.* **2015**, *51*, 15067–15070.

[240] Beyene, B. B., Mane, S. B., Hung, C.-H., *J. Electrochem. Soc.* **2018**, *165*, H481-H487.

[241] Dogutan, D. K., Bediako, D. K., Graham, D. J., Lemon, C. M., Nocera, D. G., *J. Porphyrins Phthalocyanines* **2015**, *19*, 1–8.

[242] Natali, M., Luisa, A., Iengo, E., Scandola, F., *Chem. Commun.* **2014**, *50*, 1842–1844.

[243] Gross, Z., Gray, H. B., *Comments Inorg. Chem.* **2006**, *27*, 61–72.

[244] Ganguly, S., Conradie, J., Bendix, J., Gagnon, K. J., McCormick, L. J., Ghosh, A., *J. Phys. Chem. A* **2017**, *121*, 9589–9598.

[245] Lei, H., Han, A., Li, F., Zhang, M., Han, Y., Du, P., Lai, W., Cao, R., *Phys. Chem. Chem. Phys.* **2014**, *16*, 1883–1893.

[246] Mondal, B., Sengupta, K., Rana, A., Mahammed, A., Botoshansky, M., Dey, S. G., Gross, Z., Dey, A., *Inorg. Chem.* **2013**, *52*, 3381–3387.

[247] Mahammed, A., Mondal, B., Rana, A., Dey, A., Gross, Z., *Chem. Commun.* **2014**, *50*, 2725–2727.

[248] Li, H., Li, X., Lei, H., Zhou, G., Zhang, W., Cao, R., *ChemSusChem* **2019**, *12*, 801–806.

[249] Jameson, D. L., Grzybowski, J. J., Hammels, D. E., Castellano, R. K., Hoke, M. E., Freed, K., Basquill, S., Mendel, A., Shoemaker, W. J., *J. Chem. Educ.* **1998**, *75*, 447.

[250] Siewert, I., *Chem. Eur. J.* **2015**, *21*, 15078–15091.

[251] Stubbert, B. D., Peters, J. C., Gray, H. B., *J. Am. Chem. Soc.* **2011**, *133*, 18070–18073.

[252] Hu, X., Brunschwig, B. S., Peters, J. C., *J. Am. Chem. Soc.* **2007**, *129*, 8988–8998.

[253] Baffert, C., Artero, V., Fontecave, M., *Inorg. Chem.* **2007**, *46*, 1817–1824.

[254] Fischer, E. O., Jira, R., *Z. Naturforsch. B* **1953**, *8*, 327–328.

[255] Kojima, H., Takahashi, S., Hagihara, N., *J. Chem. Soc., Chem. Commun.* **1973**, 230.

[256] van den Akker, M., Jellinek, F., *Recl. Trav. Chim. Pays-Bas* **1971**, *90*, 1101–1109.

[257] Malischewski, M., Seppelt, K., Sutter, J., Heinemann, F. W., Dittrich, B., Meyer, K., *Angew. Chem. Int. Ed.* **2017**, *56*, 13372–13376.

[258] Malischewski, M., Seppelt, K., Sutter, J., Heinemann, F. W., Dittrich, B., Meyer, K., *Angew. Chem.* **2017**, *129*, 13557–13561.

2   Aim of this Work

The aim of this work is the understanding and use of the electrochemical properties of cobaltocenium in bimetallocenes and metallocene-porphyrin amides.

The first part of this work covers to the synthesis and characterization of *N*-cobaltocenium amides. The synthesis of *C*-cobaltocenium amides (Figure 31) is well-known and the synthesis of *N*-cobaltocenium amides (Figure 31) allows the synthesis of cobaltocenium polypeptides. The possibilities to link cobaltocenium as substituent and to modify its redox properties open new fields of applications.
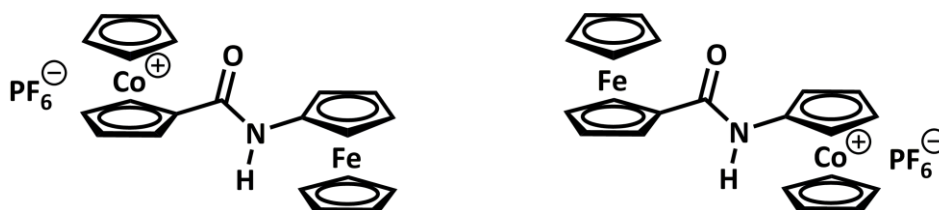
Figure 31. Known *C*-cobaltocenium-ferrocene amide (left side) and planed *N*-cobaltocenium-ferrocene amide (right side).

The second part of this work considers the synthesis and characterization of a cobaltocenium-porphyrin amide (Figure 32). Here, porphyrin should acts as biomimetic photosensitizer, which transfers a single electron after photoexcitation to a surrounding electron acceptor. Reduced cobaltocenium (cobaltocene) is known as a strong reductant, which reacts with protons. Linked to a porphyrin, cobaltocenium should be reduced after photoexcitation of the porphyrin and the following electron transfer. The overall process should be able to produce molecular hydrogen by photocatalysis
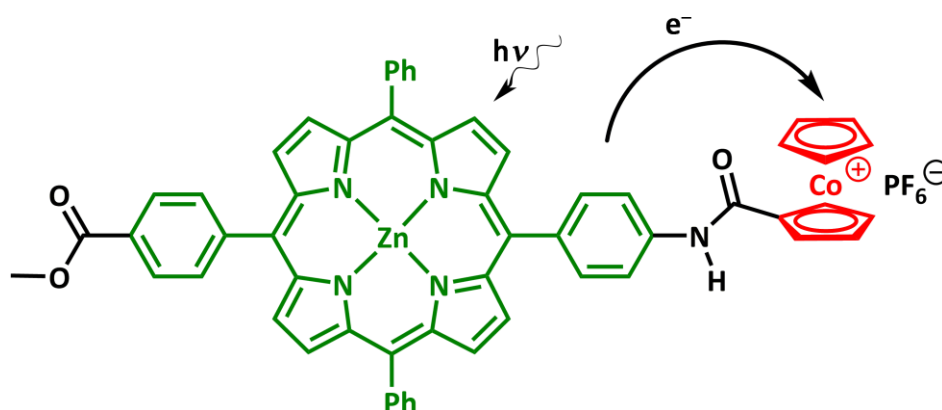
Figure 32. Planned cobaltocenium-porphyrin dyad including the assumed processes.

The final section of this work deals with the improvement of the first cobaltocenium-porphyrin amide (Figure 32). Ferrocene as electron donor should be linked to the porphyrin to reduce the porphyrin after photoexcitation (Figure 33). This should elongate the lifetime of the charge-shifted state with cobaltocene as catalytic active site, due to a larger distance of the electron acceptor (cobaltocenium) and the final electron donor (ferrocene instead of porphyrin).
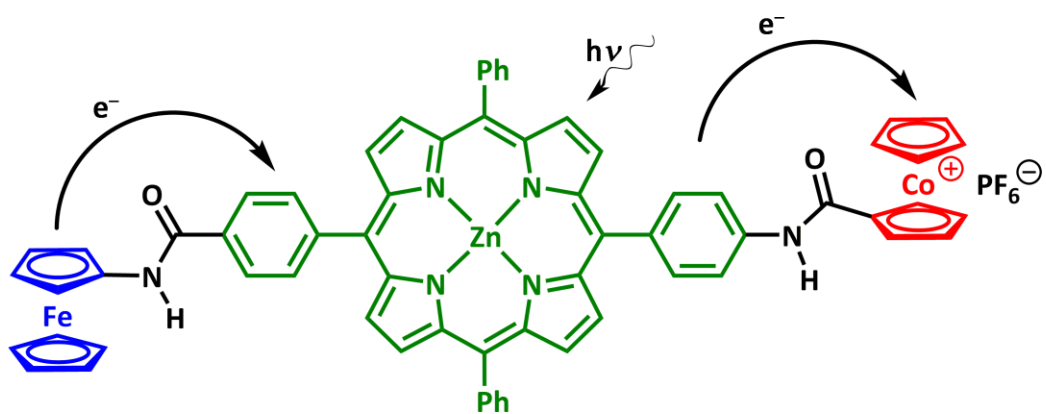
Figure 33. Planned ferrocene-porphyrin-cobaltocenium triad including the assumed processes.

3   Results and Discussion

The results of this work are summarized in two publications and one manuscript. These two articles have been published at the peer-reviewed Journals *Organometallics* and *Journal of Organometallic Chemistry* and are reprinted in this work. The permission does apply for uncommercial use only.

Chapter 3.1 was published as "*N*-Cobaltocenium Amide as Reactive Nucleophilic Reagent for Donor–Acceptor Bimetallocenes" in *Organometallics*. The article describes the synthesis and characterization of *N*-cobaltocenium amide as nucleophilic and uncharged reagent. The reaction with activated carboxylic acids yields organometallic charged *N*-cobaltocenium amides. The characterization, also via Hush analysis, allows deeper insights into electron transfer properties of metallocene amides.

Chapter 3.2 was published as "Cobaltocenium Substituents as Electron Acceptors in Photosynthetic Model Dyads" in *Journal of Organometallic Chemistry*. The article describes the synthesis and characterization of a cobaltocenium-porphyrin dyad, linked by an amide bridge. Spectroscopic characterization including time-resolved fluorescence and transient absorption pump–probe spectroscopy allows the understanding of the excited states properties of the dyad. Comparison of crystal structure and Density Functional Theory calculated geometries show the distribution of the electron density in excited states.

Chapter 3.3 possesses the working title "Lifetime Prolongation of the Charge-Shifted State: Cobaltocenium Substituents as Electron Acceptors in a Photosynthetic Model Triad" and is not published. The article describes several attempts to synthesize a triad consisting of peptide linked cobaltocenium, porphyrin and ferrocene, reporting both successful and unsuccessful attempts. The successful synthesis made partial characterization of the triad possible. Density Functional Theory calculations and literature research predict excited states properties and the distribution of the electron density in excited states.

3.1 *N*-Cobaltocenium Amide as Reactive Nucleophilic Reagent for Donor–Acceptor Bimetallocenes

Maximilian Lauck, Christoph Förster and Katja Heinze

Author Contributions

The synthesis as well as spectroscopical and analytical characterization of complexes **[H-1]**⁺, **1**, **2**⁺, **3**⁺ and **4**²⁺ and DFT calculations were performed by Maximilian Lauck. The crystal structures had been solved by Christoph Förster (group of Prof. Dr. Katja Heinze). The manuscript was written by Prof. Dr. Katja Heinze and Maximilian Lauck.

Supporting Information

The supporting information of this publication can be found in Chapter 5.1. The Cartesian coordinates of the DFT-optimized geometries, as well as of the crystal structures can be found online at https://pubs.acs.org/doi/10.1021/acs.organomet.7b00790.

Abstract

Deprotonation of the aminocobaltocenium ion [Cc-NH2]⁺ (**[H-1]**⁺) generates the nucleophilic imine CcNH (**1**). Reaction of **1** with acid chlorides R−COCl (R = Ph, Fc, and Cc⁺) yields the reference amide [Ph-CO-NH-Cc]⁺ (**2**⁺) and the amide-linked hetero- and homobimetallocenes [Fc-CO-NH-Cc]⁺ (**3**⁺) and [Cc-CO-NH-Cc]²⁺ (**4**²⁺), respectively.
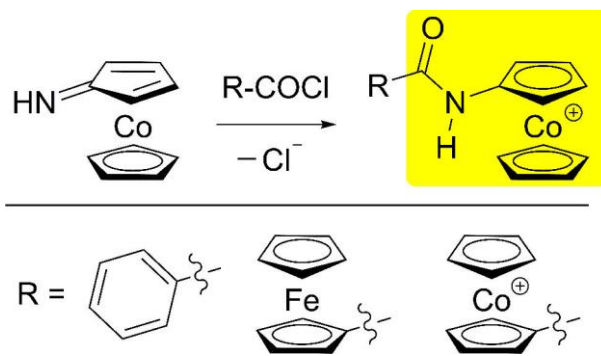
Cation−anion interactions of charged amides **2**⁺–**4**²⁺ in the solid state and in solution are probed by single crystal X-ray diffraction and NMR and IR spectroscopy. Intramolecular metal−metal interactions in donor−acceptor heterobimetallocene **3**⁺ and in mixed-valent homobimetallocene **4**⁺ (prepared electrochemically) are discussed within the Marcus−Hush framework aided by spectroelectrochemical experiments and time-dependent density functional theory calculations.

3.1.1 Introduction

The ferrocene/ferrocenium couple (FcH/FcH⁺) occupies an outstanding position in the metallocene series.[1–7] This central role in organometallic chemistry is based on its reversible redox behavior and its highly versatile substitution chemistry allowing for strongly electron-withdrawing and -donating substituents. The accessible potential range for the Fc/Fc⁺ redox process spans approximately 1.7 V based on substituent effects.[8–10] Furthermore, ferrocene can be conjugated to nearly every conceivable building block, including biomolecules, dyes or electrode surfaces for sensing applications.[1–7,11–32] Typically, Fc is introduced in the neutral form, thus acting as an electron-donating unit in photoinduced electron transfer (PET) systems[21–32] and in charge transfer (CT) complexes.[33–36]

Electron-poor metallocenes such as Cp₂Ti(CCR)₂[37] or [Cp₂Co]⁺ (CcH⁺)[36,38–48] were successfully incorporated as electron acceptors in CT systems. Compared to the ubiquitous Fc/Fc⁺ couple, the Cc/Cc⁺ couple has been less often employed in CT and PET schemes.[36,38–49] This underdeveloped attention is certainly due to the more difficult and less established substitution chemistry of CcH⁺.[50–55] Only in the last years have the groups of Bildstein and Heck put forward reliable routes toward important Cc⁺ key building blocks, such as [Cc-Br]⁺ [Cc-NO₂]⁺, [Cc-N₃]⁺, [Cc-COOH]⁺, or [Cc-NH₂]⁺.[56–59]

As our group and others have a strong interest in the development of redox-active oligoferrocene amide foldamers,[60–68] ferrocene-based redox switches involving classical NH···X and nonclassical NH···Fe hydrogen bonds,[69–73] ferrocene amide ion sensors,[74–76] amide-linked ferrocene-chromophore conjugates,[29,30,32,36] and redox-appended enzyme models,[77,78] we became strongly interested in the employment of charged cobaltocenium Cc⁺ building blocks in analogous isosteric systems. The positive charges in the parent systems and the expanded redox potential range toward more negative values are attractive assets in these applications.[8,56,57,59] The now good availability of [Cc-COOH]⁺[58] already allowed us to devise a porphyrin-cobaltocenium dyad [P-NHCO-Cc⁺]. This chromophore–acceptor system displays photoinduced charge separation after irradiation into the chromophore bands delivering a chargeshifted state with porphyrin radical cation–cobaltocene character [P⁺-NHCO-Cc].[49]

In contrast to Fc-NH₂ derivatives,[29,30,32–35,60–68,72,73,79] *N*-substituted Cc⁺ complexes which would constitute more electron-rich Cc⁺ building blocks are rare. In fact, only few reactions toward *N*-substituted Cc⁺ units are known so far. Starting from *N*-substituted lithium or sodium cyclopentadienides and CoCl₂ only 1,1'-disubstituted cobaltocenium ions are accessible after oxidation.[50,51,54] A unique isonitrile insertion into a cyclopentadienyl pentadienyl cobalt(III) complex gives the amino substituted sterically demanding [CpCo(η^5-C₅Me₄NH^{t}Bu)]⁺ complex.[55] Nucleophilic substitution of the nitro group of [Cc-NO₂]⁺ by *n*-butyl amine gives [Cc-NH^{n}Bu]⁺.[57] Heck reported the formation of the Boc-protected [Cp*Co(η^5-C₅H₄NHC(O)O^{t}Bu)]⁺ ion with one Cp* ligand starting from [Cp*Co(η^5-C₅H₄COCl)]⁺ and sodium azide, followed by a Curtius reaction in ^{t}BuOH.[56] Versatile key

building block $[Cc\text{-}NH_2]^+$ is obtained from $[Cc\text{-}COCl]^+$ and NaN_3 in an optimized procedure reported by Bildstein.[59] Thanks to the good availability of $[Cc\text{-}NH_2]^+$ we are now in the position to construct bimetallocene amides with $[Cc\text{-}NHCO\text{-}R]^+$ units.

Here we report a strategy to activate $[Cc\text{-}NH_2]^+$ toward acylation. After activation of $[Cc\text{-}NH_2]^+$, acid chlorides R-COCl were employed as acylating agents with R = Ph, Fc, and Cc^+. This gives access to $Cc\text{-}[NHCO\text{-}R]^+$ amides with the charged cobaltocenium ion connected to the *N*-side of the amide unit. The metal–metal interaction in the two novel homo- and heterometallic bimetallocenes $[Cc\text{-}CONH\text{-}Cc]^{2+/+}$ and $[Fc\text{-}CONH\text{-}Cc]^+$ via the amide unit is probed by optical spectroscopy and UV/vis/NIR spectroelectrochemistry (Scheme 1). The CT properties of the novel heterobimetallocene $[Fc\text{-}CONH\text{-}Cc]^+$ are compared to those of its $[Cc\text{-}CONH\text{-}Fc]^+$ isomer which shows strongly solvatochromic CT bands (Scheme 1).[36] The electronic interaction in novel d^6-/d^7-mixed-valent cation $[Cc\text{-}CONH\text{-}Cc]^+$ are contrasted to those of the d^5-/d^6-mixed-valent cation $[Fc\text{-}CONH\text{-}Fc]^+$.[63,64]
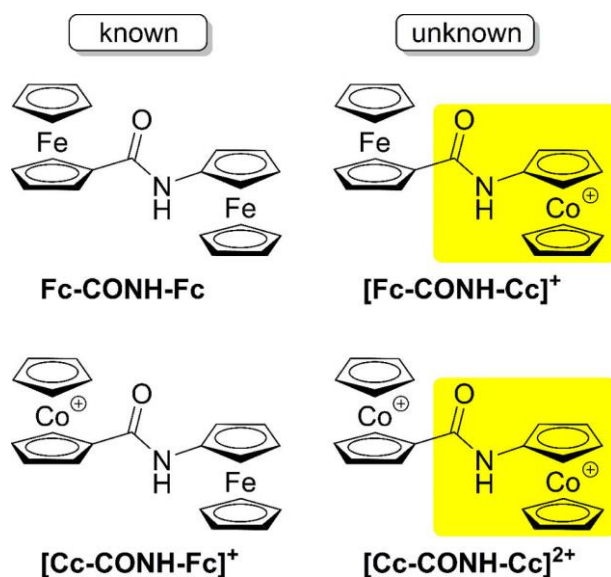
Scheme 1. Reported and unknown amide bridged bimetallocenes with Fc and Cc$^+$ building blocks.[36,63,64,68]

3.1.2 Results and discussion

The major challenge toward the introduction of $[Cc\text{-}NH]^+$ units into amides is the very low basicity and nucleophilicity of the $[Cc\text{-}NH_2]^+$ cation with a pK_b value of 15.6.[52] In fact, all conventional amide coupling formation reactions with $[Cc\text{-}NH_2]^+$ and strong electrophiles or potent coupling reagents failed in our hands. Reduction of positively charged poor nucleophile $[CcNH_2]^+$ to corresponding neutral amino cobaltocene $Cc\text{-}NH_2$ by KC_8 and subsequent acylation by R-COCl was unsuccessful as well due to competing decomposition side reactions. Deprotonation of $[Cc\text{-}NH_2]^+$ to CcNH by methyl lithium, potassium bis(trimethylsilyl)amide or *tert*-butylimino-tris(dimethylamino)phosphorane and subsequent acylation with R-COCl failed to give the desired pure products in isolable form due to the formation of side products. Finally, sodium hydride proved to be the ideal base for this propose.[80]

Preparation and Properties of CcNH (1). Aminocobaltocenium hexafluoridophosphate **[H-1][PF$_6$]** prepared according to the Bildstein procedure[59] was deprotonated by a slight excess of sodium hydride in THF (Scheme 2). After the color change from yellow to red within a few minutes (Figure 1), the solution was separated from the excess NaH by filtration. Prolonged reaction with NaH leads to decomposition according to the formation of a black insoluble precipitate (see the Experimental section). All attempts to crystallize neutral complex **1** were unsuccessful. Consequently, red cobalt complex **1** was investigated spectroscopically in solution and by density functional theory (DFT) calculations (B3LYP/def2-TZVP/PCM THF).
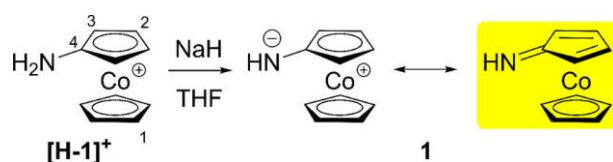
Scheme 2. Deprotonation of [H-1]$^+$ and resonance structures of 1. Atom numbering for NMR assignment.

Cobaltocenium hexafluoridophosphate exhibits absorption bands at 262, 301, and 404 nm in CH$_3$CN characteristic for many Cc$^+$ complexes (Figure S 1).[81,82] The latter two bands are clearly identified as spin-allowed ligand field transitions based on their weak intensity, while the high energy intense band has been assigned ligand-to-metal charge transfer (LMCT) character.[81] In THF, the amino substituent in **[H-1]$^+$** shifts all bands to lower energy, namely, 278, 358, and 414 nm. Deprotonation of **[H-1]$^+$** to **1** augments the shift to 280, 371, and 440 nm, respectively, and gives a new shoulder around 550 nm (Figure 1). The 440/550 nm bands of **1** account for its red color.

Time-dependent DFT (TD-DFT) calculations find composed bands at 317, 421, and 490 nm for **[H-1]$^+$** (Figure S 2). The energies are calculated as roughly 0.5 eV too low probably due to the failure of TD-DFT to describe these transitions properly in a quantitative sense. A very weak ligand field transition is calculated at 501 nm. All calculated bands for **[H-1]$^+$** display essentially ligand field character with the high-energy band at 317 nm featuring some LMCT contribution, originating from the nitrogen lone pair. Bands at 330, 426, 488, and 554 nm are calculated by TD-DFT for **1** (Figure S 2). Again, all bands are composed of ligand field transitions but with additional nitrogen lone pair → cobalt LMCT character (Figure 1). Although the numerical agreement is far from perfect, the batho- and hyperchromic effects experienced by the first three spin-allowed ligand field bands due to the increased LMCT character in **1** are reproduced well by the calculations (Figure 1 and Figure S 2).

The electronic structure of the aminocobaltocenium derivatives is best described with significant iminium ion character showing bond length alternation within the substituted C$_5$H$_5$NH$_2$ ring, short exocyclic C–N bond lengths of 1.340(4)–1.372(4) Å, and a tilted substituted ring with the *ipso* carbon atom being at a larger distance from the cobalt center (tilt angles 173.8(3)–175.7(4)°).[56,59,83] DFT

calculations on **[H-1]$^+$** reproduce these numbers reasonably well with a C–N bond length of 1.35 Å and a tilt angle of 173° (Figure S 3).

According to DFT calculations on **1**, the C–N distance shortens to 1.30 Å and the tilt angle reduces to 163°. Consequently, a description of the *N*-substituted C$_5$ ligand as 2,4-cyclopentadiene-1-imine coordinated to cobalt(I) is appropriate for **1** with only minor zwitterionic character (Scheme 2; Figure S 3).
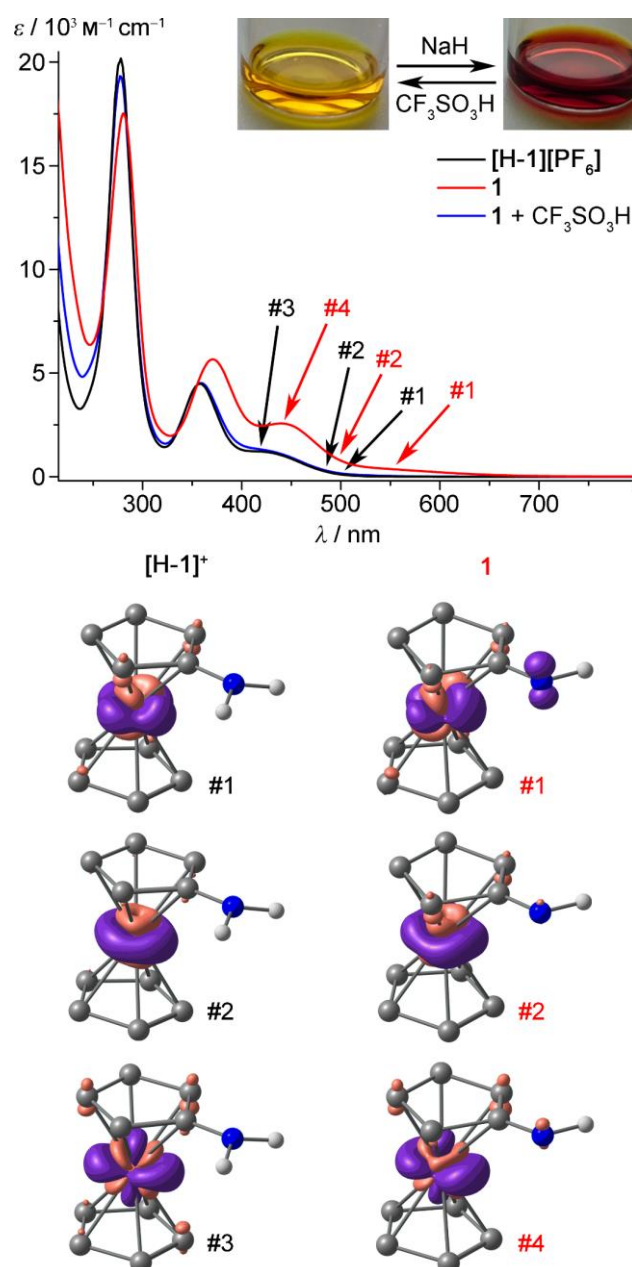

Figure 1. UV/vis spectra of [H-1][PF$_6$] (black), 1 (red), and 1 with CF$_3$SO$_3$H added (blue) in THF. TD-DFT calculated difference electron densities for relevant transitions of [H-1]$^+$ and a with contour values of 0.01 a.u.; purple = electron density depletion, orange = electron density gain. CH hydrogen atoms omitted for clarity.

Proton and carbon NMR shifts are substantially affected by deprotonation of **[H-1]$^+$** to **1** (Figure S 4– S 6). The proton resonances shift to higher field (Figure 2) by 0.88, 0.16, and 0.54 ppm (H$_3$, H$_2$, and NH).

Even the proton resonances of the unsubstituted Cp ring (H[1]) experience a strong shift by 0.51 ppm suggesting significant reorganization of the entire electronic structure. Similarly, the ^{13}C resonances for C_1, C_2, and C_3 shift to higher field, while the *ipso* carbon resonance (C_4) dramatically shifts by 26.5 ppm to lower field from 132.1 to 158.6 ppm. The latter value indicates $R_2\underline{C}$=NR' imine character.[84,85]
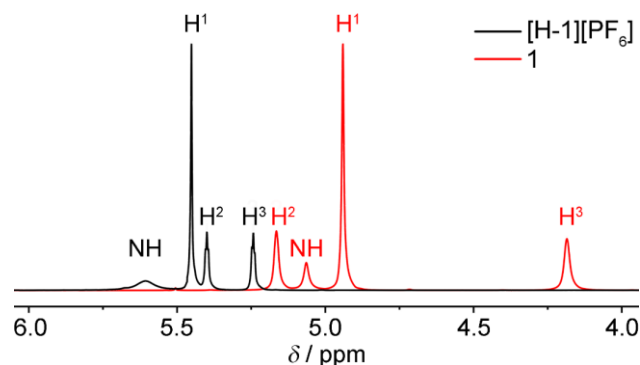
Figure 2. ^{1}H NMR spectra of [H-1][PF$_6$] (black) and 1 (red) in d$_8$-THF.

The change in electron density upon deprotonation should also affect the ^{59}Co NMR shift. Hence, attempts to observe ^{59}Co NMR resonances of **[H-1]$^+$** and **1** in THF were undertaken. The ^{59}Co NMR resonance of **[CcH]$^+$** has been reported at –2140 ppm,[86] while typical (cyclopentadienyl)-bis(olefine) cobalt(I) complexes display ^{59}Co NMR resonances in the range from –1100 to –1640 ppm (all referenced against K$_3$Co(CN)$_6$ in D$_2$O).[87] For **[H-1]$^+$**, a resonance at –2035 ppm could be found consistent with a cobaltocenium ion (Figure S 7). Unfortunately, no ^{59}Co NMR resonance could be detected for **1** under our conditions in the chemical shift range from –12 000 to +27 000 ppm.

Deprotonation of iminium ion **[H-1]$^+$** to imine 1 is fully reversible as addition of triflic acid restores the yellow color, the optical spectrum and the ^{1}H NMR spectrum of **[H-1]$^+$** (Figure 1 and Figure S 8–S 10).

The symmetric and antisymmetric NH stretching vibrations of **[H-1]$^+$** and the NH$_2$ deformation appear at 3444, 3334, and 1639 cm^{-1}, respectively, in the infrared spectrum in THF solution (Figure S 11–S 12). Expectedly, a single band for the NH stretching vibration is observed for **1** at 3283 cm^{-1}, while the NH$_2$ deformation band has vanished in THF. Numerical frequency calculations on the DFT level (B3LYP/def2-TZVP/PCM THF; scaled by 0.945) calculate these vibrational energies at 3476 and 3374 cm^{-1} (**[H-1]$^+$**) and at 3246 cm^{-1} (**1**) in reasonable agreement with the experiment lending credence to the imine description of **1** with minor contribution of the zwitterionic resonance structure (Scheme 2). We hypothesized that imine **1** should be nucleophilic enough for acylation reactions.

Preparation and Properties of [R-CONH-Cc]$^{n+}$ (2$^+$, 3$^+$, and 4^{2+}). Treatment of imine **1** with acid chlorides R-COCl (R = Ph, Fc, and Cc$^+$) yields corresponding amides **2[PF$_6$]**, **3[PF$_6$]**, and **4[PF$_6$]$_2$** in good yields of 62, 89, and 73 %, respectively (Scheme 3). In the reaction mixture of **1** with Ph-COCl, the doubly acylated amine [Cc-N(COPh)$_2$]$^+$ was detected by ESI$^+$ mass spectrometry, suggesting that smaller

electrophiles can attack the nitrogen atom even twice. No double substitution was observed for the larger metallocenyl acid chlorides. All amides were fully characterized by elemental analysis, ESI+ and HR-ESI+ mass spectrometry, and NMR and IR spectroscopy (Figure S 13–S 34). Optical and electrochemical properties of bimetallocences **3+** and **4²⁺** and reference cobaltocenium amide **2+** were probed by UV/vis/NIR spectroscopy, electrochemistry, and UV/vis/NIR spectroelectrochemistry. The solid state structures of **2[PF₆]** and **3[PF₆]** were ascertained by X-ray crystallography.
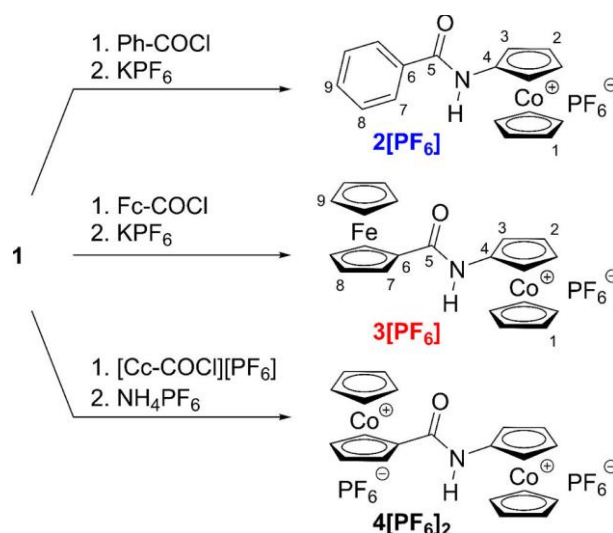
Scheme 3. Synthesis of [CcNH]+ amides 2[PF₆], 3[PF₆], and 4[PF₆]₂. Atom numbering for NMR assignment.

The ESI+ and HR-ESI+ mass spectra display peaks at mass-to-charge ratios appropriate for the cations **2+**, **3+**, and **[4-H]+** (see the Experimental section and Figure S 13–S 15).

In the multinuclear NMR spectra of **2[PF₆]**, **3[PF₆]**, and **4[PF₆]₂** (^{1}H, ^{13}C, ^{19}F, and ^{31}P; Figure S 16–S 33) all resonances have been assigned to corresponding nuclei. The ^{1}H (H^1, H^2, and H^3) and ^{13}C resonances (C^1, C^2, and C^3) of the Cc+ units of **2+**, **3+**, and **4²⁺** are negligibly affected by the R substituents. The resonance of the C^4 nuclei shifts to higher field from 114.4 and 113.8 to 111.0 ppm for R = Fc, Ph, and Cc+ with increasing electron-withdrawing nature of R. The same trend holds for the carbonyl resonances C^5 with δ = 170.8, 167.2, and 162.0 ppm for R = Fc, Ph, and Cc+, respectively. The NH proton resonance does not follow this trend with δ = 8.41, 9.17, and 8.96 ppm for R = Fc, Ph, and Cc+, suggesting other determining factors such as hydrogen bonding. In fact, small variations in the ^{19}F chemical shifts of the hexafluoridophosphate counterions display a similar trend with δ = −72.9, −73.2, and −73.1 ppm for R = Fc, Ph, and Cc+ which might be indicative of ion-pair formation via NH•••F hydrogen bonds in acetonitrile solution. Such ion-pair formation has been previously observed in positively charged ferrocenium and cobaltocenium amides, thioamides, ureas and thioureas.[36,49,65,73,88]

NH hydrogen bonding was further probed by IR spectroscopy (Figure S 34). In fact, absorption bands for NH stretching and amide I vibrations appear at $\tilde{\nu}_{NH}$ = 3264, 3394, and 3305 cm^{-1} and $\tilde{\nu}_{amideI}$ = 1654, 1678, and 1664 cm^{-1} for R = Fc, Ph, and Cc$^+$, respectively. These data suggest the strongest NH hydrogen bond for **3$^+$** (R = Fc) and the weakest one for **2$^+$** (R = Ph). Charging of the CO substituted metallocene in a formal Fc to Cc$^+$ isosteric replacement (**3$^+$ → 4^{2+}**) diminishes the NH hydrogen bond strength. Neutral diphenylamide Ph-CONH-Ph with $\tilde{\nu}_{NH}$ = 3345 cm^{-1} and $\tilde{\nu}_{amideI}$ = 1654 cm^{-1} only forms intermolecular NH•••OC hydrogen bonds due to the absence of counterions and is thus a poor reference compound for charged amides **2$^+$–4^{2+}**.[89]
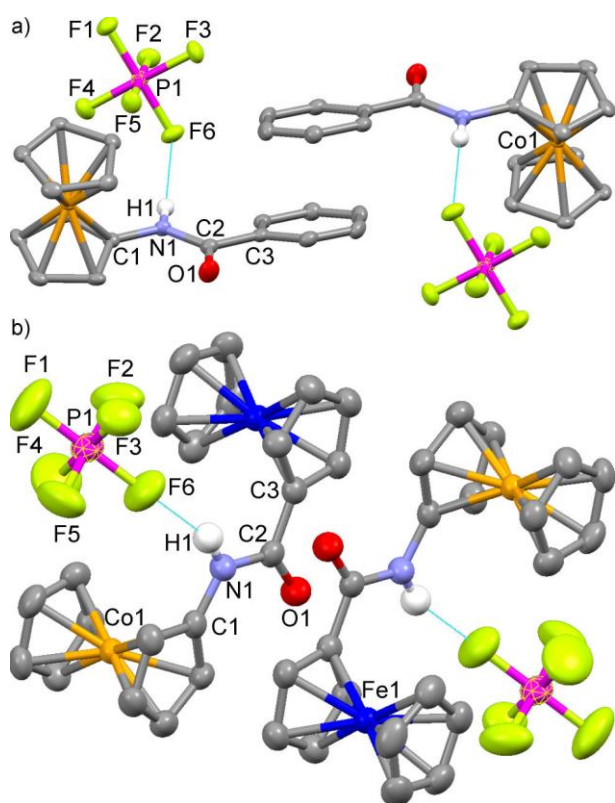
Figure 3. Molecular structures of a) 2[PF$_6$] and b) 3[PF$_6$] x ½C$_6$H$_6$ in the solid state including a nearest neighbor molecule and counterions (Thermal ellipsoids at 50 % probability. CH hydrogen atoms and solvent omitted; atom numbering modified with respect to the deposited data for clarity).

Table 1. Selected bond distances (Å) and angles (deg) of 2[PF$_6$] and 3[PF$_6$]. Cp denotes center of cyclopentadienyl rings; Ph denotes center of phenyl rings.

	2[PF$_6$]	3[PF$_6$]
Cp–Cp (Cc$^+$)	3.275(2)	3.281(3)
Cp–Cp (Fc)		3.303(3)
C1–N1	1.389(3)	1.386(4)
N1–C2	1.371(3)	1.374(4)
C2–O1	1.220(3)	1.223(4)
C2–C3	1.499(3)	1.474(5)
N•••F6	3.070(2)	2.920(19)
F6•••H1	2.23	2.19
N1–H1•••F6	160.3	140.0
Co1–Fe1		6.069(2)
Cp(Cc)–Cp(Fc) (intermolec.)		3.555(3)
Ph–Ph (intermolec.)	4.041(2)	
Cp–Co1–Cp	179.16(6)	178.95(10)
Cp–Fe1–Cp		177.66(10)
C1–N1–C2	124.13(17)	125.5(3)
N1–C2–C3	116.55(18)	115.0(3)
N1–C2–O1	121.86(19)	122.7(3)

Single crystals of **2[PF$_6$]** and **3[PF$_6$]** suitable for X-ray diffraction analysis were obtained (Figure 3a,b; Table 1). However, **4[PF$_6$]$_2$** crystallized under many attempted conditions only as heavily intergrown, sometimes very large crystallites which were unsuitable for single crystal diffraction (Figure S 34). The cation of **2$^+$** forms a NH•••F hydrogen bond to a PF$_6^-$ counterion with a N•••F distance of 3.070(2) Å (Figure 3a, Table 1). **3$^+$** forms a closer contact to its counterion with a shorter N•••F distance of 2.920(19) Å (Figure 3b, Table 1). Although not very pronounced, this difference fits to the results from the NMR and IR data with **3$^+$** (R = Fc) forming stronger hydrogen bonds than **2$^+$** (R = Ph). The contact ion pairs **2[PF$_6$]** and **3[PF$_6$]** pack via π stacking of the Ph substituents (center-to-center distance

4.041(2) Å; Figure 3a) or via Cp•••Cp contacts (center-to-center distance 3.555(3) Å; Figure 3b), respectively.

Similar to the well-explored FcH/FcH+ redox chemistry, the CcH/CcH+ redox potential can be tuned over a wide range, currently from −0.97 V to −2.37 V vs FcH/FcH+. Linear correlations with substituent properties apply as well.[8,36,57,59] The phenyl substituted reference amide **2+** is reversibly reduced to the cobaltocene **2** at −1.360 V in the cyclic voltammogram (Figure 4a, Table 2). At E_p = −2.265 V an irreversible Co^{II}/Co^I reduction wave[57] (likely associated with reductive deprotonation of the amide proton) appears, which gives rise to a follow-up product that is reoxidized at −1.825 V (Figure 4a). Spectroelectrochemical reduction of **2+** to **2** and reoxidation to **2+** is reversible as well, provided that the second irreversible reduction is not addressed (Figure S 35).

Replacing the Ph substituent in **2+** by the Fc substituent in **3+** barely affects the reversible Cc/Cc+ redox process ($E_{½}$ = −1.355 V) and the irreversible Co^{II}/Co^I reduction/follow-up reaction (E_p = −2.290 and −1.840 V), respectively (Figure 4b; Table 2). The reversible Fc/Fc+ oxidation of **3+** is observed in the expected range for CO substituted ferrocenes at 0.305 V.[8] Compared to the [Cc-CONH-Fc]+ isomer (Scheme 1) with an easy-to-reduce Cc+ unit ($E_{½}$ = −1.150 V) and an easy-to-oxidize Fc unit ($E_{½}$ = −0.015 V), the potential difference between the respective redox processes has increased by more than 0.5 V from 1.135 V in [Cc-CONH-Fc]+ to 1.660 V in **3+**.[36]

Table 2. Redox potentials (V) in CH$_3$CN/[^{n}Bu$_4$N][PF$_6$] vs. FcH/FcH+.

	2[PF$_6$]	3[PF$_6$]	4[PF$_6$]$_2$
$E_{½}$ (Fc/Fc+)		0.305	
$E_{½}$ (C–Cc/C–Cc+)			−1.020
$E_{½}$ (N–Cc/N–Cc+)	−1.360	−1.355	−1.420

Expectedly, the bicobaltocenium complex **4^{2+}** is reduced reversibly two times (Table 2, Figure 4c) and irreversibly at lower potential (E_p = −2.100 V) with an oxidation wave of the follow-up product at E_p = −1.570 V (Figure 4c, Table 2). The assignment of the Cc+ reduction waves to individual Cc+ units in **4^{2+}** is straightforward according to expected substituent effects, reference compounds (**2+** and reported [Cc-COR]+ derivatives), and DFT calculations (Figure 4c).[8,36,49,59]

For the prototypical symmetric [Cc-Cc]$^{2+}$ bimetallocenium, the potential difference between the reductions has been reported by Weaver as 0.395 V.[90,91] The potential difference of **4^{2+}** is with 0.400 V accidentally similar due to compensating Co•••Co distance and substituent effects.
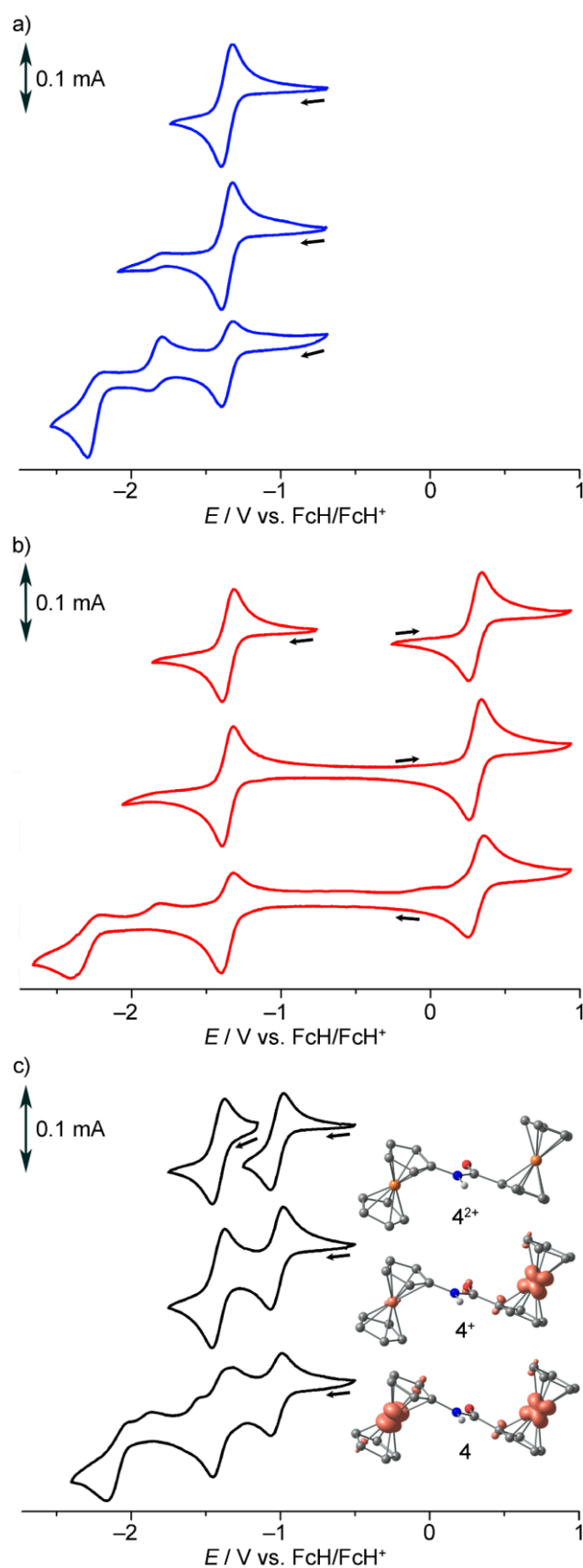
Figure 4. Cyclic voltammograms of a) 2[PF$_6$], b) 3[PF$_6$], and c) 4[PF$_6$]$_2$ in CH$_3$CN/[^{n}Bu$_4$N][PF$_6$] (scan rate 100 mV s^{-1}). DFT calculated spin densities of 4$^+$ and 4 with contour values of 0.01 a.u.; CH hydrogen atoms omitted for clarity.

The electronic spectrum of **2[PF$_6$]** in CH$_3$CN (Figure 5a) shows a prominent LMCT maximum at 280 nm, a less intense band at 347 nm, and a shoulder at 406 nm. This pattern is characteristic for

cobaltocenium ions (see above).[81,82] The bicobaltocenium ion 4_{2+} displays essentially the same pattern (λ = 271, 346, 406 nm), yet with higher intensity (Figure 5a, Experimental section).
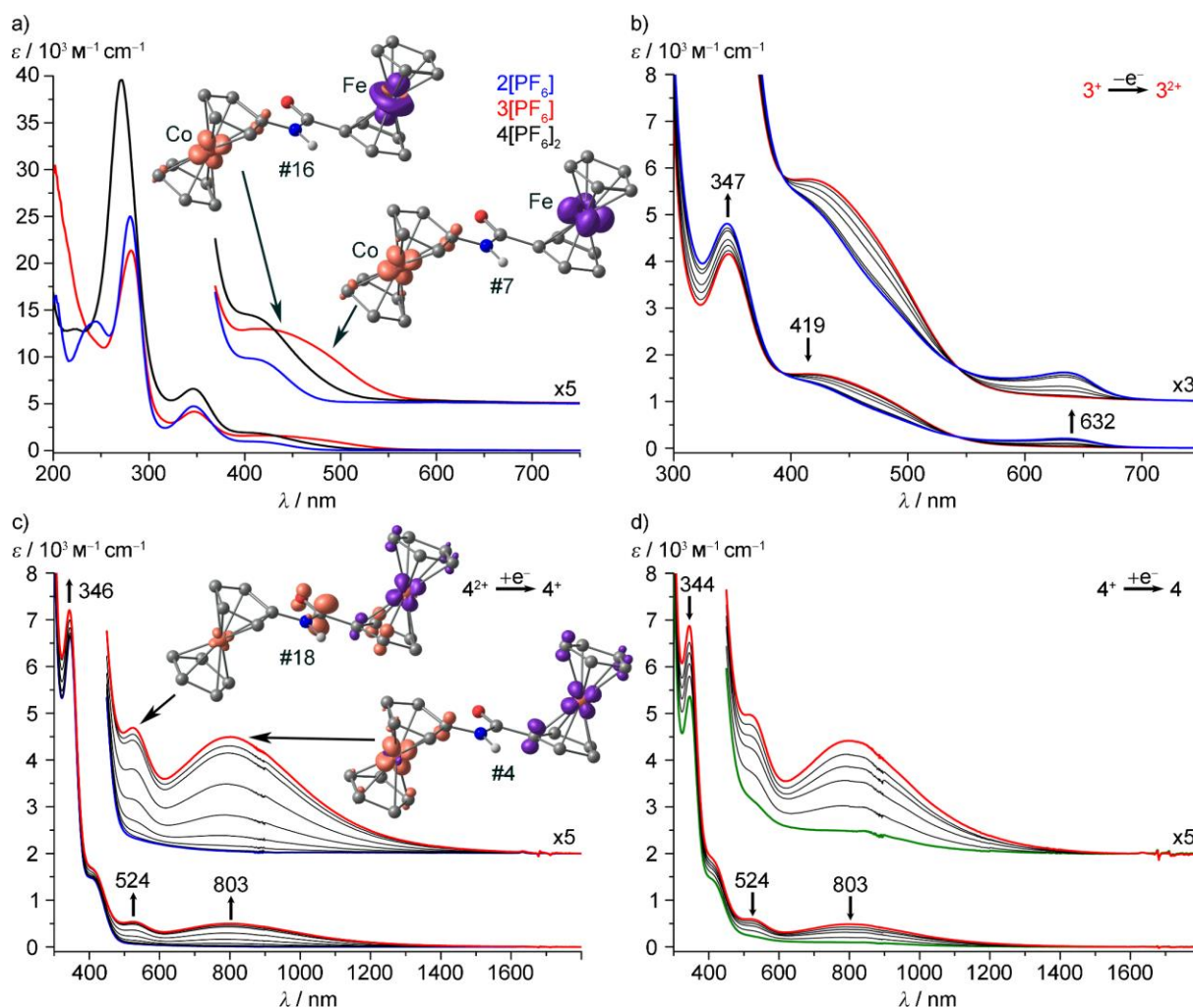
Figure 5. a) UV/vis spectra of 2[PF$_6$], 3[PF$_6$], and 4[PF$_6$]$_2$ in CH$_3$CN. Changes in the UV/vis/NIR spectra in the course of redox events in CH$_3$CN/[^{n}Bu$_4$N][PF$_6$] during OTTLE spectroelectrochemistry: b) oxidation of 3$^+$ → 3^{2+}, c) reduction of 4^{2+} → 4$^+$, and d) reduction of 4$^+$ → 4. TD-DFT calculated difference electron densities with contour values of 0.01 a.u.: purple = electron density depletion, orange = electron density gain. CH hydrogen atoms omitted for clarity.

In the heterobimetallic complex **3$^+$** the ferrocene can act as donor moiety, similar to its [Cc-CONH-Fc]$^+$ isomer (Scheme 1).[36] The latter isomer with the smaller redox potential gap (and consequently a smaller HOMO−LUMO gap), features a solvatochromic absorption band with MM'CT character at 534 nm in CH$_3$CN.[36] For **3$^+$**, the cobaltocenium ligand field band around 406 nm is indeed considerably broadened on the lower energy side. According to TD-DFT calculations on **3$^+$**, these absorptions represent MM'CT transitions from iron to cobalt (Figure 5a). To distinguish the MM'CT from the normal Cc$^+$ and Fc absorption pattern, the Cc$^+$ pattern of the spectrum of **2$^+$** and the spectrum of Fc-COOMe were subtracted from the composed spectrum of **3$^+$** (Figure S 36). This procedure yields an approximate absorption band for the MM'CT transition in **3$^+$** at 471 nm. This MM'CT occurs at considerably higher energy in **3$^+$** (by 2500 cm^{-1}) as compared to the MM'CT of the [Cc-CONH-Fc]$^+$ isomer which fits well to the electrochemical data (see above).[36] Hush analysis with the modified Hush

formula for closed-shell donor–acceptor systems[38] $H_{AB} = 2.05 \times 10^{-2} (0.5\varepsilon_{max}\Delta\tilde{v}_{1/2}\tilde{v}_{max})^{1/2} / r$ gives the electronic coupling matrix element $H_{AB} = 584$ cm^{-1} for the closed-shell mixed-metal system **3$^+$** (Table 3).

Further proof that the MM'CT assignment of **3$^+$** is correct comes from spectroelectrochemistry. Oxidation of **3$^+$** to the cobaltocenium–ferrocenium complex **3^{2+}** bleaches the MM'CT band around 471 nm, while the characteristic ferrocenium absorption of [Fc–C(O)R]$^+$ units at 632 nm grows (Figure 5b and Figure S 37).[81,92] Likewise, reduction of **3$^+$** to **3** bleaches the MM'CT band as the Cc$^+$ electron acceptor is reduced to cobaltocene (Figure S 37). No distinct new bands grow in similar to the reduction of **2$^+$** to **2** (Figure S 35). The overall reduction of **3$^+$** to **3** is spectroscopically more complicated involving three individual steps with distinct isosbestic points (Figure S 37). We also note some precipitation during electrolysis. However, the overall process **3$^+$** → **3** → **3$^+$** is reversible (Figure S 37).

Reduction of **4^{2+}** to **4$^+$** yields the redox-asymmetric d^7-Co^{II}/d^6-Co^{III} mixed-valence system with the [CcCO]$^+$ unit reduced to the cobaltocene moiety (Figure 4c). Spectroelectrochemical reduction delivers a new prominent band at 524 nm and a very broad band at 803 nm (Figure 5c). Both bands bleach upon reoxidation to **4^{2+}** and upon further reduction of **4$^+$** to the Co^{II}Co^{II} complex **4** (Figure S 38 and Figure 5d). These findings suggest that these bands are associated with the uncharged [Cc-CO] cobaltocene moiety. Indeed, TD-DFT calculations on **4$^+$** assign the band at 524 nm to a metal-to-ligand charge transfer (MLCT) from the electron-rich [Cc-CO] cobaltocene moiety to the carbonyl group of the bridge and importantly describe the band at 803 nm as an intervalence charge transfer (IVCT) transition from the electron-rich [Cc-CO] cobaltocene to the electron-deficient [Cc-NH]$^+$ cobaltocenium unit.

Table 3. Results of the Hush analysis of the MM'CT (IVCT) bands of several bimetallocenes composed of Fc, Fc$^+$, Cc, and Cc$^+$ moieties. ^{a}Average distances of the two metal centers as estimated by DFT calculations. ^{b}In CH$_3$CN. ^{c}In CH$_2$Cl$_2$. ^{d}In THF.

	$\tilde{v}$ (cm^{-1}) (ε (M^{-1} cm^{-1}))	$\Delta\tilde{v}_{1/2}$ (cm^{-1})	ΔG^0 (cm^{-1})	r (Å)^a	H_{AB} (cm^{-1})	α	λ (cm^{-1})
[Fc-Fc]$^+$ [90]b	5680 (750)	3620	2541	5.0	509	0.090	3139
[Cc-Fc]$^+$ [38, 44]b	18115 (2480)	4176	12752	5.0	1256	0.069	5363
[Cc-Cc]$^+$ [90]b	6580 (3500)	3900	3186	5.0	1229	0.187	3394
[Fc-CH=CH-Fc]$^+$ [91]c	4910 (1340)	4360	1371	6.9	503	0.102	3539
[Fc-CONH-Fc]$^+$ [63, 64]d	9556 (95)	2443	3388	6.9	140	0.015	6168
[Cc-CONH-Fc]$^+$ [36]b	18736 (347)	5584	9154	6.9	400	0.021	9582
[Fc-CONH-Cc]$^+$ **3$^+$** ^{b}	21240 (886)	4113	13389	6.9	584	0.028	7851
[Cc-CONH-Cc]$^+$ **4$^+$** ^{b}	12475 (505)	5436	3226	6.9	550	0.044	9249

Gaussian deconvolution of the absorption spectrum of **4$^+$** yields the IVCT absorption band data (Table 3; Figure S 39). With an (averaged) Co•••Co distance of $r = 6.9$ Å, Hush's formula[93] delivers the

electronic coupling matrix element $H_{AB} = 2.05 \times 10^{-2} \, (\varepsilon_{max}\Delta\tilde{v}_{1/2}\tilde{v}_{max})^{1/2} / r = 550 \text{ cm}^{-1}$ for the open-shell system $\mathbf{4^+}$. This is less than half of H_{AB} obtained for the redox-symmetric bimetallocene $[Cc\text{-}Cc]^+$ lacking the amide unit (Table 3). This decrease is likely due to the redox asymmetry, the larger metal–metal distance, and the less conjugated amide bridge in $\mathbf{4^+}$ dramatically decreasing the transition dipole moment for the IVCT transition.

Compared to the $d^6\text{-}Fe^{II}/d^5\text{-}Fe^{III}$ mixed-valent system $[Fc\text{-}CONH\text{-}Fc]^+$, H_{AB} of $\mathbf{4^+}$ is approximately four times larger.[64] The same trend holds for the electronic mixing coefficients $\alpha = H_{AB}/\tilde{v}_{max}$ (Table 3). Clearly, orbital symmetry plays a major role with the mainly iron-centered e orbitals with local δ symmetry interacting only weakly. However, the redox orbitals in the $d^7\text{-}Co^{II}/d^6\text{-}Co^{III}$ system both feature π^* character with both *ipso* carbon atoms involved. Such a symmetry of the redox orbitals enables electronic interaction via the amide bridge (see Figure 5c).

In the heterometallic isomeric bimetallocenes $[Cc\text{-}CONHFc]^+$ and $[Fc\text{-}CONH\text{-}Cc]^+$ ($\mathbf{3^+}$), the electronic mixing coefficient α is larger than that in $[Fc\text{-}CONH\text{-}Fc]^+$ due to the extended Cc^+ acceptor π system (Figure 5a) but smaller than that in $[Cc\text{-}CONH\text{-}Cc]^+$ ($\mathbf{4^+}$) due to the very localized Fc donor system in the heterometallics (Figure 5a). The electronic mixing coefficient α increases in the series $[Fc\text{-}CONH\text{-}Fc]^+$, $[Cc\text{-}CONH\text{-}Fc]^+$, $[Fc\text{-}CONH\text{-}Cc]^+$, and $[Cc\text{-}CONH\text{-}Cc]^+$ (Table 3).

All amide-bridged bimetallocenes $[Mc\text{-}NHCO\text{-}Mc]^+$ (Mc = Fc and Cc) display MM'CT or IVCT transitions albeit with different intensities due to the different orbital symmetry and all belong clearly to class II of the Robin/Day system. They all exhibit similar nuclear reorganization energies $\lambda = \tilde{v}_{max} - \Delta G^0$ (Table 3) which has been discussed before for other linked bimetallocenes based on the similar bond length and vibrational data of the involved metallocenes.[90] However, the reorganization energy λ of the amide-bridged bimetallocenes $[Mc\text{-}NHCO\text{-}Mc]^+$ is significantly larger than the reorganization energy of $[Fc\text{-}Fc]^+$, $[Fc\text{-}Cc]^+$, and $[Cc\text{-}Cc]^+$ with a direct link (Table 3). It is also larger than estimated for the vinylene bridged biferrocene $[Fc\text{-}CH\text{=}CH\text{-}Fc]^+$ with a similar metal–metal distance.[91] It is tempting to attribute this extra effect to the connecting amide unit and especially the hydrogen bonds of counterions to the NH group. Charge transfer across the amide unit and the hydrogen-bonded counterion certainly affects the NH•••X bonding situation and contributes to the inner-sphere reorganization energy (if one ascribes the hydrogen-bonded counterion to the inner sphere). More systematic studies on solvent and counter ion effects in amidelinked metallocenes are clearly warranted and will be conducted in the future.

3.1.3 Conclusion

The poor nucleophile $[Cc\text{-}NH_2]^+$ **[H-1]$^+$** has been successfully activated by deprotonation to the imine CcNH **1** by NaH. Acylation of **1** by R-COCl gave the cobaltocenium amides $[R\text{-}CONH\text{-}Cc]^+$ **2$^+$**, **3$^+$**, and **4^{2+}**

(R = Ph, Fc, and Cc$^+$). They form contact ion pairs with hexafluoridophosphate counterions in solution (**2$^+$**, **3$^+$**, and **4^{2+}**) and in the solid state (**2$^+$**, **3$^+$**, and likely **4^{2+}**) via NH•••F hydrogen bonds. Both the donor–acceptor heterobimetallocene **3$^+$** and the mixed-valent Co^{III}/Co^{II} complex **4$^+$** (prepared by spectroelectrochemistry) are Robin/Day class II systems with similar nuclear reorganization energies but different electronic mixing coefficients α. The electronic coupling in the mixed-valent Co^{III}/Co^{II} complex **4$^+$** is 4-fold higher than that of the mixed-valent Fe^{III}/Fe^{II} complex [Fc-CONH-Fc]$^+$ due to the more favorable π symmetry of the redox orbitals in **4$^+$**. The reorganization energies λ of the amidebridged bimetallocences are increased by the hydrogen-bonded counterions relative to those of bimetallocenes with a direct link.

On the basis of the availability of suitably substituted aminocobaltocenium complexes and the here developed amide-coupling chemistry, conducting peptidic molecular wires with cobaltocene/cobaltocenium units in the main chain are now within reach. The development of molecular wires, as well as sensing and charge-separating systems with amino-substituted cobaltocenium electron acceptor units as building blocks is now actively pursued.

3.1.4   Experimental section

Instrumentation. NMR spectra were recorded on a Bruker Avance DRX 400 spectrometer at 400.31 MHz (^{1}H), 100.05 MHz (^{13}C{^{1}H}), 376.67 MHz (^{19}F), and 162.05 MHz (^{31}P) and on a Bruker Avance DSX 400 spectrometer at 94.88 MHz (^{59}Co). Chemical shifts are reported on the δ scale in ppm relative to the solvent signal as an internal standard (CD$_3$CN (^{1}H: δ = 1.94 ppm; ^{13}C: δ = 118.26 ppm), d^8-THF (^{1}H: δ = 3.58 ppm; ^{13}C: δ = 67.57 ppm))[94] or relative to an external standard (^{19}F: CFCl$_3$, ^{31}P: H$_3$PO$_4$, ^{59}Co: 1.0 M K$_3$[Co(CN)$_6$] in H$_2$O); s = singlet, d = doublet, and t = triplet. IR spectra were recorded with a Thermo Nicolet 5700 FT-IR as ATR and with a Bruker ALPHA FT-IR spectrometer as KBr disk, and in THF, with signal intensities: s = strong, m = medium, w = weak. ESI$^+$ and HR ESI$^+$ mass spectra were recorded on a Micromass Q-TOF-Ultima spectrometer and a Waters Q-Tof Ultima 3 spectrometer, respectively. Cyclic voltammetric measurements were carried out with a BioLogic SP-50 voltammetric analyzer in CH$_3$CN containing 0.1 M [^{n}Bu$_4$N][PF$_6$] as supporting electrolyte at a platinum working electrode, a platinum wire as counter electrode, and a 0.01 M Ag/AgNO$_3$ electrode as the reference electrode. All cyclic voltammetric measurements were recorded at 100 mV s^{-1} scan rate. Ferrocene or decamethylferrocene were employed as an internal reference redox system. (rev.) = reversible, (irrev.) = irreversible redox process. Spectroelectrochemical experiments were performed using a Specac omni-cell liquid transmission cell with CaF$_2$ windows equipped with a Pt gauze working electrode, a Pt counter electrode, and a Ag pseudoreference electrode, melt-sealed in a polyethylene spacer (path length 0.7 mm).[95] UV/vis/NIR absorption spectra were measured on a Varian Cary 5000 spectrometer in 1.0 cm cells (Hellma, Suprasil); sh = shoulder.

Density Functional Calculations. Calculations were carried out with the ORCA 4.0.1/DFT series of programs.[96] The B3LYP formulation of density functional theory was used for geometry optimizations and numerical frequency calculations employing the ZORA-Def2-TZVP basis set,[97,98] the RIJCOSX approximation,[99,100] the zeroth order regular approximation (ZORA),[101,102] and the KDIIS algorithm[103] at GRID5. No symmetry constraints were imposed on the molecules. Solvent modeling was done employing the conductor-like continuum polarization model (CPCM CH_3CN, and THF).[104]

Crystal Structure Determinations. Intensity data were collected with a STOE IPDS-2T diffractometer using Mo K_α radiation (λ = 0.71073 Å). The diffraction frames were integrated using the STOE X-red package and most were corrected for absorption with MULABS of the PLATON software package.[105–107] The structure was solved by direct methods and refined by the full-matrix method based on F^2 using the SHELX software package.[108,109] All non-hydrogen atoms were refined anisotropically, while the positions of all hydrogen atoms were generated with appropriate geometric constraints and allowed to ride on their respective parent carbon atoms with fixed isotropic thermal parameters.

Crystallographic Data of 2[PF$_6$]. $C_{17}H_{15}CoF_6NOP$ (453.20); triclinic, $P\bar{1}$; a = 7.6178(15) Å, b = 9.4454(19) Å, c = 12.203(2) Å, α = 73.80(3)°, β = 85.77(3)°, γ = 81.08(3)°, V = 832.6(3) Å^3, Z = 2; density, calcd. = 1.808 g cm^{-3}, T = 100 K, μ = 1.198 mm^{-1}; $F(000)$ = 456; crystal size 0.140 x 0.117 x 0.090 mm^3; ϑ = 2.268–28.127°; $-10 \leq h \leq 10$, $-10 \leq k \leq 12$, $-16 \leq l \leq 16$; rfln collected = 8491; rfln unique = 4049 [R(int) = 0.0383]; completeness to ϑ = 25.242° = 99.7 %; semiempirical absorption correction from equivalents; max. and min transmission 1.19124 and 0.90255; data 4049; restraints 0; parameters 244; goodness-of-fit on F^2 = 1.053; final indices [$I > 2\sigma(I)$] R_1 = 0.0323. wR_2 = 0.0736; R indices (all data) R_1 = 0.0411, wR_2 = 0.0791; largest diff. peak and hole 0.478 and −0.429 e Å^{-3}.

Crystallographic Data of 3[PF$_6$] × ½C$_6$H$_6$. $C_{24}H_{22}CoF_6FeNOP$ (600.17); monoclinic, $P2_1$/c; a = 7.5786(15) Å, b = 19.480(4) Å, c = 15.757(3) Å, α = 90°, β = 102.42(3)°, γ = 90°, V = 2271.8(8) Å^3, Z = 4; density, calcd. = 1.755 g cm^{-3}, T = 193 K, μ = 1.507 mm^{-1}; $F(000)$ = 1212; crystal size 0.460 x 0.287 x 0.120 mm^3; ϑ = 2.091–28.337°; $-10 \leq h \leq 10$, $-25 \leq k \leq 25$, $-19 \leq l \leq 20$; rfln collected = 13 537; rfln unique = 5541 [R(int) = 0.0466]; completeness to ϑ = 25.242° = 99.4 %; semiempirical absorption correction from equivalents; max and min transmission 1.31360 and 0.81612; data 5541; restraints 126; parameters 379; goodness-of-fit on F^2 = 1.052; final indices [$I > 2\sigma(I)$] R_1 = 0.0472. wR_2 = 0.1121; R indices (all data) R_1 = 0.0719, wR_2 = 0.1323; largest diff. peak and hole 0.636 and −0.393 e Å^{-3}. The hexafluoridophosphate counterion is disordered over two positions. CCDC 1581720 and 1581721 contain the supplementary crystallographic data for this paper. These data can be obtained free of charge from Cambridge Crystallographic Data Center via www.ccdc.cam.ac.uk/data_request/cif.

Materials. Unless otherwise noted, all chemical reagents were used without any further purification as received from suppliers (Sigma-Aldrich, Acros, Alfa Aesar). Tetrahydrofuran was freshly distilled from potassium, CH_3CN from calcium hydride. For the characterization experiments of 1, the sodium hydride was freed from mineral oil prior the reaction by washing with absolute THF. CcH[PF$_6$],[58] **[H-1][PF$_6$]**,[59] [Cc-COOH][PF$_6$],[58] and Fc-COOH[110] were prepared according to literature procedures.

General Procedures. All preparations (until quenching with water) were performed under an inert atmosphere of argon, using an M. Braun glovebox and absolute solvents.

CcH[PF$_6$]. UV/vis (CH_3CN): λ [nm] (ε [M^{-1} cm^{-1}]) = 262 (36 140), 301 (1140), 404 (230) consistent with CcH[ClO$_4$]: UV/vis (H$_2$O): λ [nm] (ε [M^{-1} cm^{-1}]) = 263 (38 000), 300 (1200), 407 (220).[81]

[H-1][PF$_6$]. ^{1}H NMR (d$_8$-THF): δ [ppm] = 5.24 (t, 2H, $^3J_{HH}$ = 1.9 Hz, H^3), 5.40 (t, 2H, $^3J_{HH}$ = 1.9 Hz, H^2), 5.45 (s, 5H, H^1), 5.61 (s, 2H, H^{NH}). ^{13}C {1H} NMR (d$_8$-THF): δ [ppm] = 66.4 (C^3), 79.1 (C^2), 84.9 (C^1), 132.1 (C^4). ^{59}Co NMR (THF): δ [ppm] = –2035. UV/vis (THF): λ [nm] (ε [M^{-1} cm^{-1}]) = 278 (20 180), 358 (4480), 414 (sh, 1220). IR (KBr): $\tilde{\nu}$ [cm^{-1}] = 3503 (s, NH$_{asym}$), 3402 (s, NH$_{sym}$), 3244 (s, CH), 3124 (s, CH), 1633 (s, CN), 1538 (s, CN), 1414 (m, C = C), 831 (m, PF), 638, 557 (m, FPF$_{def}$), 452. IR (THF): $\tilde{\nu}$ [cm^{-1}] = 3444 (s, NH$_{asym}$), 3334 (s, NH$_{sym}$), 1639 (s, NH$_{2,def}$), 1542 (s, CN), 559 (s, PF$_{2,def}$).

Synthesis of 1. Aminocobaltocenium hexafluoridophosphate **[H-1][PF$_6$]** (10 mg, 29 μmol, 1 equiv) was dissolved in THF (5 mL) and NaH (1.4 mg, 58 μmol, 2 equiv) was added. The solution was stirred and the color changed from orange to red. After 5 min, the solution was filtered through a 0.2 μm PTFE syringe filter. Prolonged reactions times (ca. 20 min) lead to the formation of a black precipitate, decreasing the yield of **1**.

^{1}H NMR (d$_8$-THF): δ [ppm] = 4.19 (s, 2H, H^3), 4.94 (s, 5H, H^1), 5.07 (s, 1H, H^{NH}), 5.17 (s, 2H, H^2). ^{13}C {1H} NMR (d$_8$-THF): δ [ppm] = 60.2 (C^3), 76.6 (C^2), 81.7 (C^1), 158.6 (C^4). UV/vis (THF): λ [nm] (ε [M^{-1} cm^{-1}]) = 280 (17 515), 371 (5660), 440 (2565). IR (THF): $\tilde{\nu}$ [cm^{-1}] = 3283 (m, NH), 1565 (s, CN).

Synthesis of 2[PF$_6$]. Aminocobaltocenium hexafluoridophosphate **[H-1][PF$_6$]** (187.6 mg, 537 μmol, 1.0 equiv) was dissolved in THF (25 mL) and NaH (150 mg, 3.75 mmol, 7.0 equiv, 60 % dispersion in mineral oil) was added. The solution was stirred and the color shifted from orange to red. After 10 min, CcNH the solution was filtered through a 0.2 μm PTFE syringe filter.

Benzoyl chloride (80 μL, 694 μmol, 1.3 equiv) was dissolved in THF (15 mL) and added dropwise to the CcNH solution over 5 min. The solution was stirred for 3 h at room temperature. Water (80 mL), acetic acid (0.5 mL), and potassium hexafluoridophosphate (500 mg, 2.71 mmol, 5.1 equiv) were added. After 12 h of stirring, the THF was removed under reduced pressure and the solution was extracted with dichloromethane (3 x 50 mL). The solvent was removed under reduced pressure. The solid was washed on a short alumina column with hexane/acetic acid (100:5) and with ethanol. On a second

alumina column, the product was washed with THF:H$_2$O (85:15) and eluted with THF. The solvent was removed under reduced pressure. The solid and potassium hexafluoridophosphate (500 mg, 2.71 mmol, 5.1 equiv) were dissolved in acetone (50 mL) and stirred for 5 h. Water (250 mL) was added, and the solution was extracted with dichloromethane (5 x 30 mL). The organic phase was dried over sodium sulfate. The solvent was removed under reduced pressure yielding a yellow glassy solid. Yield 151 mg (0.333 µmol, 62 %). For further purification, the solid was recrystallized from a benzene solution at 6°C. These crystals were suitable for X-ray diffraction analysis.

MS (ESI$^+$, CH$_3$CN): m/z (%) = 308.05 (100) [M − PF$_6$]$^+$. HR MS (ESI$^+$, CH$_3$CN): obs. m/z = 308.0477; calcd. for [M − PF6]$^+$ = 308.0486. ^{1}H NMR (CD$_3$CN): δ [ppm] = 5.54 (t, 2H, $^3J_{HH}$ = 2.0 Hz, H^2), 5.62 (s, 5H, H^1), 6.16 (t, 2H, $^3J_{HH}$ = 2.0 Hz, H^3), 7.59 (t, 2H, $^3J_{HH}$ = 7.6 Hz, H^8), 7.69 (t, 1H, $^3J_{HH}$ = 7.4 Hz, H^9), 7.98 (d, 2H, $^3J_{HH}$ = 7.3 Hz, H^7), 9.17 (s, 1H, H^{NH}). ^{13}C {^{1}H} NMR (CD$_3$CN): δ [ppm] = 74.4 (C^3), 80.8 (C^2), 85.8 (C^1), 113.8 (C^4), 128.7 (C^7), 129.7 (C^8), 133.9 (C^9), 133.8 (C^6), 167.2 (C^5). ^{19}F NMR (CD$_3$CN): δ [ppm] = −73.2 (d, 6F, $^1J_{PF}$ = 706 Hz, F^{PF_6}). ^{31}P NMR (CD$_3$CN): δ [ppm] = −143.5 (sept, 1P, $^1J_{PF}$ = 706 Hz, P^{PF_6}). IR (ATR): $\tilde{v}$ [cm^{-1}] = 3394 (s, NH), 3122 (s, CH), 3100 (s, CH), 1678 (s, CO), 1530 (s, NC), 1498, 1485, 1413, 1393, 1361, 1336, 1259 (s), 1099, 820 (m, PF), 704, 651, 553 (m, FPF$_{def}$), 459. UV/vis (CH$_3$CN): λ [nm] (ε [M^{-1} cm^{-1}]) = 244 (13 90), 280 (25 000), 347 (4720), 406 (sh, 970). CV (FcH/ FcH$^+$, 100 mV^{-1}, CH$_3$CN, 0.1 M [^{n}Bu$_4$N][PF$_6$]): $E_{½}$ [V] = −1.360 (rev.), −1.825 (irrev. ox.), −2.265 (irrev.). Elemental analysis: Anal. Calcd. for C$_{17}$H$_{15}$NOCoPF$_6$ (453.23): C, 45.05; H, 3.34; N, 3.09. Found: C, 44.81; H, 3.65; N, 3.31.

Synthesis of 3[PF$_6$]. Aminocobaltocenium hexafluoridophosphate **[H-1][PF$_6$]** (564 mg, 1.62 mmol, 1.1 equiv) was dissolved in THF (100 mL) and NaH (250 mg, 6.25 mmol, 4.1 equiv, 60 % dispersion in mineral oil) was added. The solution was stirred, and the color shifted orange to red. After 90 min, the CcNH solution was filtered through a 0.2 µm PTFE syringe filter. Carboxyferrocene (344 mg, 1.50 mmol, 1.0 equiv) and Ghosez's reagent (0.7 mL, 5.29 mmol, 3.5 equiv) were dissolved in dichloromethane (100 mL), and the solution was refluxed for 18 h. The solvent was removed under reduced pressure, the solid was washed with dichloromethane (50 mL), and the solvent was removed under reduced pressure. The solid was suspended in THF (50 mL), and the CcNH solution was added dropwise over 10 min to the Fc-COCl solution. The mixture was stirred for 24 h at room temperature and terminated by adding water (1 mL). The solvent was removed under reduced pressure, and the resulting oil was washed on an alumina column with ethyl acetate and with ethanol. The solution was filtered through a 0.2 µm PTFE filter, and the solvent was removed under reduced pressure. The solid was dissolved in acetone (30 mL), and potassium hexafluoridophosphate (1.00 g, 5.42 mmol, 3.4 equiv) was added. The solution was stirred for 3 h. Water (250 mL) was added, the solution extracted with dichloromethane (5 x 50 mL), and the organic phase washed with water (3 x 50 mL). The organic phase was dried over sodium sulfate. The solvent was removed under reduced pressure yielding a red powder. Yield 751 mg (1.33 mmol, 89 %). For further purification, the product was recrystallized by diffusing diethyl ether in

an acetonitrile solution. Crystals suitable for X-ray diffraction analysis were obtained by recrystallization from a benzene solution at 6°C.

MS (ESI$^+$, CH$_3$CN): m/z (%) = 416.03 (100) [M − PF$_6$]$^+$, 977.04 (7) [2xM − PF$_6$]$^+$. HR MS (ESI$^+$, CH$_3$CN): obs. m/z = 416.0139; calcd for [M − PF$_6$]$^+$ = 416.0148. ^{1}H NMR (CD$_3$CN): δ [ppm] = 4.25 (s, 5H, H^9), 4.54 (t, 2H, $^3J_{HH}$ = 1.6 Hz, H^8), 4.86 (t, 2H, $^3J_{HH}$ = 1.6 Hz, H^7), 5.49 (t, 2H, $^3J_{HH}$ = 1.9 Hz, H^2), 5.55 (s, 5H, H^1), 6.08 (t, 2H, $^3J_{HH}$ = 1.9 Hz, H^3), 8.41 (s, 1H, H^{NH}). ^{13}C {^{1}H} NMR (CD$_3$CN): δ [ppm] = 69.7 (C^7), 70.9 (C^9), 72.8 (C^8), 73.6 (C^3), 74.8 (C^6), 80.5 (C^2), 85.6 (C^1), 114.4 (C^4), 170.8 (C^5). ^{19}F NMR (CD$_3$CN): δ [ppm] = −72.8 (d, 6F, $^1J_{PF}$ = 707 Hz, F^{PF_6}). ^{31}P NMR (CD$_3$CN): δ [ppm] = −143.4 (sept, 1P, $^1J_{PF}$ = 707 Hz, P^{PF_6}). IR (ATR): $\tilde{v}$ [cm^{-1}] = 3364 (s, NH), 3188 (s, CH$_{Fc}$), 3121 (s, CH), 3100 (s, CH), 1654 (s, amide I), 1533 (s, NC), 1498, 1449, 1418, 1379, 1283 (s), 1139, 823 (m, PF), 644, 555 (m, FPF$_{def}$), 468. UV/vis (CH$_3$CN): λ [nm] (ε [M^{-1} cm^{-1}]) = 281 (21 370), 347 (4160), 419 (1600). CV (FcH/FcH$^+$, 100 mV^{-1}, CH$_3$CN, 0.1 M [^{n}Bu$_4$N][PF$_6$]): $E_{½}$ [V] = 0.305 (rev.), −1.355 (rev.), −1.840 (irrev. ox.), −2.290 (irrev.). Elemental analysis: Anal. Calcd. for C$_{21}$H$_{19}$NOFeCoPF$_6$ (561.13) x ½H$_2$O: C, 44.24; H, 3.54; N, 2.46. Found: C, 44.45; H, 3.88; N, 2.51. The water content was confirmed by ^{1}H NMR spectroscopy.

Synthesis of 4[PF$_6$]$_2$. Amino cobaltocenium hexafluoridophosphate **[H-1][PF$_6$]** (106 mg, 304 µmol, 1.0 equiv) was dissolved in THF (15 mL) and NaH (100 mg, 2.50 mmol, 8.2 equiv, 60 % dispersion in mineral oil) was added. The solution was stirred, and the color shifted from orange to red. After 30 min, the CcNH solution was filtered through a 0.2 µm PTFE syringe filter. Carboxycobaltocenium hexafluoridophosphate (116 mg, 307 µmol, 1.0 equiv) and Ghosez's reagent (0.2 µL, 1.51 mmol; 4.97 equiv) were dissolved in dichloromethane (50 mL), and the solution was refluxed for 18 h. The solvent was removed under reduced pressure, the solid was washed with dichloromethane (30 mL). The solvent was removed under reduced pressure. The solid was suspended in acetonitrile (25 mL), and the CcNH solution was added dropwise over 2 min. The mixture was stirred for 6 h at room temperature. Ammonium hexafluoridophosphate (330 mg, 2.02 mmol; 6.6 equiv) was added, and the solution was stirred for 14 h. The solvent was removed under reduced pressure, and the solid was washed on a short alumina column with ethyl acetate, ethyl acetate/ethanol (1:2), and acetone. The product was dissolved in acetonitrile (50 mL) and filtered through a 0.2 µm PTFE filter. The solvent was removed under reduced pressure yielding a yellow powder. Yield 158 mg (223 µmol, 73 %). For further purification, the product was recrystallized by diffusing diethyl ether in an acetonitrile solution.

MS (ESI$^+$, CH$_3$CN): m/z (%) = 209.52 (97) [M − 2xPF$_6$]$^{2+}$, 418.04 (100) [M − H − 2xPF$_6$]$^+$, 564.01 (34) [M − PF$_6$]$^+$, 1273.03 (16) [2M − PF$_6$]$^+$. HR MS (ESI$^+$, CH$_3$CN): obs. m/z = 418.0054; calcd. for [M − H − 2xPF$_6$]$^+$ = 418.0052. ^{1}H NMR (CD$_3$CN): δ [ppm] = 5.55 (t, 2H, $^3J_{HH}$ = 2.1 Hz, H^2), 5.63 (s, 5H, H^1), 5.76 (s, 5H, H^9), 5.86 (t, 2H, $^3J_{HH}$ = 2.0 Hz, H^8), 6.09 (t, 2H, $^3J_{HH}$ = 2.1 Hz, H^3), 6.19 (t, 2H, $^3J_{HH}$ = 2.0 Hz, H^7), 8.96 (s, 1H, H^{NH}). ^{13}C {^{1}H} NMR (CD$_3$CN): δ [ppm] = 74.7 (C^3), 80.8 (C^2), 84.8 (C^7), 85.7 (C^1), 87.0 (C^9), 87.1

(C[8]), 92.7 (C[6]), 111.0 (C[4]), 162.0 (C[5]). ^{19}F NMR (CD$_3$CN): δ [ppm] = −73.1 (d, 6F, ^{1}J$_{PF}$ = 706 Hz, F^{PF_6}). ^{31}P NMR (CD$_3$CN): δ [ppm] = −143.5 (sept, 1P, ^{1}J$_{PF}$ = 706 Hz, P^{PF_6}). IR (ATR): $\tilde{v}$ [cm^{-1}] = 3305 (s, NH), 3220 (s, CH$_{Cc(C)}$), 3129 (s, CH), 3104 (s, CH), 1664 (s, amide I), 1557 (s, NC), 1494, 1464, 1421, 1384, 1384, 1286 (s), 1160, 816 (m, PF), 640, 554 (m, FPF$_{def}$), 456. UV/vis (CH$_3$CN): λ [nm] (ε [M^{-1} cm^{-1}]) = 221 (12 980), 271 (39 570), 346 (6590), 406 (sh, 1900). CV (FcH/FcH$^+$, 100 mV^{-1}, CH$_3$CN, 0.1 M [^{n}Bu$_4$N][PF$_6$]): $E_{\frac{1}{2}}$ [V] = −1.020 (rev.), −1.420 (rev.), −1.570 (irrev. ox.), −1.900 (irrev. ox.), −2.100 (irrev.). Elemental analysis: Anal. Calcd. for C$_{21}$H$_{19}$NOCo$_2$P$_2$F$_{12}$ (709.21) x ¼CH$_3$CN: C, 35.89; H, 2.77; N, 2.43. Found: C, 35.89; H, 2.77; N, 2.46. The CH$_3$CN content was confirmed by ^{1}H NMR spectroscopy.

Acknowledgements

3.1.5   References

[1]   Štěpnička, P., *Eur. J. Inorg. Chem.* **2017**, *2017*, 215–216.

[2]   Heinze, K., Lang, H., *Organometallics* **2013**, *32*, 5623–5625.

[3]   Štěpnička, P. (Ed.) *Ferrocenes*. *Ligands, materials and biomolecules*, Wiley-VCH, Chichester, England, Hoboken, NJ, **2008**.

[4]   Togni, A., Hayashi, T. (Ed.) *Ferrocenes*. *Homogeneous Catalysis, Organic Synthesis, Materials Science*, Wiley-VCH, Weinheim, **2008**.

[5]   Hailes, R. L. N., Oliver, A. M., Gwyther, J., Whittell, G. R., Manners, I., *Chem. Soc. Rev.* **2016**, *45*, 5358–5407.

[6]   Astruc, D., *Eur. J. Inorg. Chem.* **2017**, 6–29.

[7]   Molina, P., Tárraga, A., Alfonso, M., *Dalton Trans.* **2014**, *43*, 18–29.

[8]   Lu, S., Strelets, V. V., Ryan, M. F., Pietro, W. J., Lever, A. B. P., *Inorg. Chem.* **1996**, *35*, 1013–1023.

[9]   Khobragade, D. A., Mahamulkar, S. G., Pospíšil, L., Císařová, I., Rulíšek, L., Jahn, U., *Chem. Eur. J.* **2012**, *18*, 12267–12277.

[10]   Shafir, A., Power, M. P., Whitener, G. D., Arnold, J., *Organometallics* **2000**, *19*, 3978–3982.

[11]   Kraatz, H.-B., Lusztyk, J., Enright, G. D., *Inorg. Chem.* **1997**, *36*, 2400–2405.

[12]   Brosch, O., Weyhermüller, T., Metzler-Nolte, N., *Inorg. Chem.* **1999**, *38*, 5308–5313.

[13]   van Staveren, D. R., Metzler-Nolte, N., *Chem. Rev.* **2004**, *104*, 5931–5985.

[14]   Moriuchi, T., Hirao, T., *Chem. Soc. Rev.* **2004**, *33*, 294–301.

[15]   Heinze, K., Beckmann, M., *Eur. J. Inorg. Chem.* **2005**, *2005*, 3450–3457.

[16] Heinze, K., Wild, U., Beckmann, M., *Eur. J. Inorg. Chem.* **2007**, *2007*, 617–623.

[17] Djaković, S., Siebler, D., Semenčić, M. Č., Heinze, K., Rapić, V., *Organometallics* **2008**, *27*, 1447–1453.

[18] Lataifeh, A., Beheshti, S., Kraatz, H.-B., *Eur. J. Inorg. Chem.* **2009**, 3205–3218.

[19] Semenčić, M. Č., Siebler, D., Heinze, K., Rapić, V., *Organometallics* **2009**, *28*, 2028–2037.

[20] Förster, C., Kovačević, M., Barišić, L., Rapić, V., Heinze, K., *Organometallics* **2012**, *31*, 3683–3694.

[21] Mansour, H., El-Khouly, M. E., Shaban, S. Y., Ito, O., Jux, N., *J. Porphyrins Phthalocyanines* **2007**, *11*, 719–728.

[22] Poddutoori, P. K., Sandanayaka, A. S. D., Hasobe, T., Ito, O., van der Est, A., *J. Phys. Chem. B* **2010**, *114*, 14348–14357.

[23] Bakar, M. A., Sergeeva, N. N., Juillard, T., Senge, M. O., *Organometallics* **2011**, *30*, 3225–3228.

[24] Suijkerbuijk, B. M. J. M., Klein Gebbink, R. J. M., *Angew. Chem. Int. Ed.* **2008**, *47*, 7396–7421.

[25] Suijkerbuijk, B. M. J. M., Klein Gebbink, R. J. M., *Angew. Chem.* **2008**, *120*, 7506–7532.

[26] Dammer, S. J., Solntsev, P. V., Sabin, J. R., Nemykin, V. N., *Inorg. Chem.* **2013**, *52*, 9496–9510.

[27] Vecchi, A., Gatto, E., Floris, B., Conte, V., Venanzi, M., Nemykin, V. N., Galloni, P., *Chem. Commun.* **2012**, *48*, 5145–5147.

[28] Nemykin, V. N., Rohde, G. T., Barrett, C. D., Hadt, R. G., Bizzarri, C., Galloni, P., Floris, B., Nowik, I., Herber, R. H., Marrani, A. G., Zanoni, R., Loim, N. M., *J. Am. Chem. Soc.* **2009**, *131*, 14969–14978.

[29] Melomedov, J., Ochsmann, J. R., Meister, M., Laquai, F., Heinze, K., *Eur. J. Inorg. Chem.* **2014**, 1984–2001.

[30] Melomedov, J., Ochsmann, J. R., Meister, M., Laquai, F., Heinze, K., *Eur. J. Inorg. Chem.* **2014**, 2902–2915.

[31] Siemeling, U., Vor der Brüggen, J., Vorfeld, U., Neumann, B., Stammler, A., Stammler, H.-G., Brockhinke, A., Plessow, R., Zanello, P., Laschi, F., Fabrizi de Biani, F., Fontani, M., Steenken, S., Stapper, M., Gurzadyan, G., *Chem. Eur. J.* **2003**, *9*, 2819–2833.

[32] Heinze, K., Hempel, K., Beckmann, M., *Eur. J. Inorg. Chem.* **2006**, 2040–2050.

[33] Neidlinger, A., Ksenofontov, V., Heinze, K., *Organometallics* **2013**, *32*, 5955–5965.

[34] Neidlinger, A., Förster, C., Heinze, K., *Eur. J. Inorg. Chem.* **2016**, 1274–1286.

[35] Neidlinger, A., Förster, C., Heinze, K., *Eur. J. Org. Chem.* **2016**, 4852–4864.

[36] Huesmann, H., Förster, C., Siebler, D., Gasi, T., Heinze, K., *Organometallics* **2011**, *31*, 413–427.

[37] Turlington, M. D., Pienkos, J. A., Carlton, E. S., Wroblewski, K. N., Myers, A. R., Trindle, C. O., Altun, Z., Rack, J. J., Wagenknecht, P. S., *Inorg. Chem.* **2016**, *55*, 2200–2211.

[38] Schwarzhans, K.-E., Stolz, W., *Monatsh. Chem.* **1987**, *118*, 875–878.

[39] Beer, P. D., Chen, Z., Goulden, A. J., Graydon, A., Stokes, S. E., Wear, T., *J. Chem. Soc., Chem. Commun.* **1993**, 1834–1836.

[40] Casado, C. M., González, B., Cuadrado, I., Alonso, B., Morán, M., Losada, J., *Angew. Chem.* **2000**, *112*, 2219–2222.

[41] Casado, C. M., González, B., Cuadrado, I., Alonso, B., Morán, M., Losada, J., *Angew. Chem. Int. Ed.* **2000**, *39*, 2135–2138.

[42] Barlow, S., *Inorg. Chem.* **2001**, *40*, 7047–7053.

[43] Laus, G., Strasser, C. E., Holzer, M., Wurst, K., Pürstinger, G., Ongania, K.-H., Rauch, M., Bonn, G., Schottenberger, H., *Organometallics* **2005**, *24*, 6085–6093.

[44] Warratz, R., Peters, G., Studt, F., Römer, R.-H., Tuczek, F., *Inorg. Chem.* **2006**, *45*, 2531–2542.

[45] Ornelas, C., Ruiz, J., Astruc, D., *Organometallics* **2009**, *28*, 2716–2723.

[46] Astruc, D., Ornelas, C., Ruiz, J., *Chem. Eur. J.* **2009**, *15*, 8936–8944.

[47] Gilroy, J. B., Patra, S. K., Mitchels, J. M., Winnik, M. A., Manners, I., *Angew. Chem. Int. Ed.* **2011**, *50*, 5851–5855.

[48] Gilroy, J. B., Patra, S. K., Mitchels, J. M., Winnik, M. A., Manners, I., *Angew. Chem.* **2011**, *123*, 5973–5977.

[49] Lauck, M., Förster, C., Gehrig, D., Heinze, K., *J. Organomet. Chem.* **2017**, *847*, 33–40.

[50] Knox, G. R., Munro, J. D., Pauson, P. L., Smith, G. H., Watts, W. E., *J. Chem. Soc.* **1961**, 4619–4624.

[51] Pauson, P. L., Knox, G. R.; U.S. Patent 3278514, **1966**.

[52] Sheats, J. E., Rausch, M. D., *J. Org. Chem.* **1970**, *35*, 3245–3249.

[53] Yamazaki, H., Wakatsuki, Y., *Bull. Chem. Soc. Jpn.* **1979**, *52*, 1239–1240.

[54] Stahl, K.-P., Boche, G., Massa, W., *J. Organomet. Chem.* **1984**, *277*, 113–125.

[55] Butovskii, M. V., Englert, U., Herberich, G. E., Koelle, U., *Eur. J. Inorg. Chem.* **2005**, 971–980.

[56] Wolter-Steingrube, A., Bugenhagen, B. E. C., Herrmann, C., Heck, J., *Eur. J. Inorg. Chem.* **2014**, 4115–4122.

[57] Wolter-Steingrube, A., Cordsen, K., Heck, J., *Eur. J. Inorg. Chem.* **2017**, 1314–1319.

[58] Vanicek, S., Kopacka, H., Wurst, K., Müller, T., Schottenberger, H., Bildstein, B., *Organometallics* **2014**, *33*, 1152–1156.

[59] Vanicek, S., Kopacka, H., Wurst, K., Müller, T., Hassenrück, C., Winter, R. F., Bildstein, B., *Organometallics* **2016**, *35*, 2101–2109.

[60] Heinze, K., Schlenker, M., *Eur. J. Inorg. Chem.* **2004**, 2974–2988.

[61] Chowdhury, S., Schatte, G., Kraatz, H.-B., *Angew. Chem.* **2006**, *118*, 7036–7038.

[62] Chowdhury, S., Schatte, G., Kraatz, H.-B., *Angew. Chem. Int. Ed.* **2006**, *45*, 6882–6884.

[63] Heinze, K., Siebler, D., *Z. Anorg. Allg. Chem.* **2007**, *633*, 2223–2233.

[64]   Siebler, D., Linseis, M., Gasi, T., Carrella, L. M., Winter, R. F., Förster, C., Heinze, K., *Chem. Eur. J.* **2011**, *17*, 4540–4551.

[65]   Siebler, D., Förster, C., Heinze, K., *Dalton Trans.* **2011**, *40*, 3558–3575.

[66]   Siebler, D., Förster, C., Gasi, T., Heinze, K., *Organometallics* **2011**, *30*, 313–327.

[67]   Siebler, D., Heinze, K., *J. Organomet. Chem.* **2016**, *821*, 19–24.

[68]   Acton, E. M., Silverstein, R. M., *J. Org. Chem.* **1959**, *24*, 1487–1490.

[69]   Förster, C., Veit, P., Ksenofontov, V., Heinze, K., *Chem. Commun.* **2015**, *51*, 1514–1516.

[70]   Veit, P., Förster, C., Seibert, S., Heinze, K., *Z. Anorg. Allg. Chem.* **2015**, *641*, 2083–2092.

[71]   Veit, P., Prantl, E., Förster, C., Heinze, K., *Organometallics* **2016**, *35*, 249–257.

[72]   Kienz, T., Förster, C., Heinze, K., *Organometallics* **2016**, *35*, 3681–3691.

[73]   Hanauer, K., Pham, M. T., Förster, C., Heinze, K., *Eur. J. Inorg. Chem.* **2017**, 433–445.

[74]   Heinze, K., Schlenker, M., *Eur. J. Inorg. Chem.* **2005**, *2005*, 66–71.

[75]   Molina, P., Tárraga, A., Caballero, A., *Eur. J. Inorg. Chem.* **2008**, *2008*, 3401–3417.

[76]   Siebler, D., Förster, C., Heinze, K., *Eur. J. Inorg. Chem.* **2010**, 523–527.

[77]   Camara, J. M., Rauchfuss, T. B., *Nat. Chem.* **2011**, *4*, 26–30.

[78]   Hüttinger, K., Förster, C., Heinze, K., *Chem. Commun.* **2014**, *50*, 4285–4288.

[79]   Sethi, S., Das, P. K., Behera, N., *J. Organomet. Chem.* **2016**, *824*, 140–165.

[80]   Enk, B., Kopacka, H., Wurst, K., Müller, T., Bildstein, B., *Organometallics* **2009**, *28*, 5575–5586.

[81]   Gray, H. B., Sohn, Y. S., Hendrickson, N., *J. Am. Chem. Soc.* **1971**, *93*, 3603–3612.

[82]   El Murr, N., *J. Organomet. Chem.* **1976**, *112*, 189–199.

[83]   Inyushin, S., Shafir, A., Sheats, J. E., Minihane, M., Whitten, C. E., Arnold, J., *Polyhedron* **2004**, *23*, 2937–2942.

[84]   Lee, J. H., Gupta, S., Jeong, W., Rhee, Y. H., Park, J., *Angew. Chem.* **2012**, *124*, 11009–11013.

[85]   Lee, J. H., Gupta, S., Jeong, W., Rhee, Y. H., Park, J., *Angew. Chem. Int. Ed.* **2012**, *51*, 10851–10855.

[86]   Lucken, E. A. C., Noack, K., Williams, D. F., *J. Chem. Soc., A* **1967**, 148–154.

[87]   Benn, R., Cibura, K., Hofmann, P., Jonas, K., Rufinska, A., *Organometallics* **1985**, *4*, 2214–2221.

[88]   Kienz, T., Förster, C., Heinze, K., *Organometallics* **2014**, *33*, 4803–4812.

[89]   Gockel, S. N., Hull, K. L., *Org. Lett.* **2015**, *17*, 3236–3239.

[90]   McManis, G. E., Nielson, R. M., Weaver, M. J., *Inorg. Chem.* **1988**, *27*, 1827–1829.

[91]   Ribou, A.-C., Launay, J.-P., Sachtleben, M. L., Li, H., Spangler, C. W., *Inorg. Chem.* **1996**, *35*, 3735–3740.

[92]   Siebler, D., Förster, C., Heinze, K., *Eur. J. Inorg. Chem.* **2010**, 3986–3992.

[93]   Hush, N. S. in *Prog. Inorg. Chem.* (F. A. Cotton (Ed.)), John Wiley & Sons, Inc, Hoboken, NJ, USA, **1967**, 391–444.

[94] Fulmer, G. R., Miller, A. J. M., Sherden, N. H., Gottlieb, H. E., Nudelman, A., Stoltz, B. M., Bercaw, J. E., Goldberg, K. I., *Organometallics* **2010**, *29*, 2176–2179.

[95] Krejčik, M., Daněk, M., Hartl, F., *J. Electroanal. Chem. Interfacial Electrochem.* **1991**, *317*, 179–187.

[96] Neese, F., *WIREs Comput Mol Sci* **2012**, *2*, 73–78.

[97] Weigend, F., Ahlrichs, R., *Phys. Chem. Chem. Phys.* **2005**, *7*, 3297–3305.

[98] Weigend, F., *Phys. Chem. Chem. Phys.* **2006**, *8*, 1057–1065.

[99] Neese, F., Wennmohs, F., Hansen, A., Becker, U., *Chem. Phys.* **2009**, *356*, 98–109.

[100] Izsák, R., Neese, F., *J. Chem. Phys.* **2011**, *135*, 144105.

[101] van Lenthe, E., Baerends, E. J., Snijders, J. G., *J. Chem. Phys.* **1993**, *99*, 4597–4610.

[102] van Wüllen, C., *J. Chem. Phys.* **1998**, *109*, 392–399.

[103] Kollmar, C., *J. Chem. Phys.* **1996**, *105*, 8204–8212.

[104] Barone, V., Cossi, M., *J. Phys. Chem. A* **1998**, *102*, 1995–2001.

[105] Stoe & Cie, *X-red*, Stoe & Cie, Darmstadt, Germany, **2002**.

[106] Blessing, R. H., *Acta Cryst.* **1995**, *A51*, 33–38.

[107] Spek, A. L., *Acta Cryst.* **2009**, *D65*, 148–155.

[108] Sheldrick, G. M., *Acta Cryst.* **2015**, *C71*, 3–8.

[109] Sheldrick, G. M., *SHELXL-2014/7*, Universität Göttingen, Göttingen, Germany, **2014**.

[110] Rausch, M. D., Ciappenelli, D. J., *J. Organomet. Chem.* **1967**, *10*, 127–136.

3.2 Cobaltocenium Substituents as Electron Acceptors in Photosynthetic Model Dyads

Maximilian Lauck, Christoph Förster, Dominik Gehrig and Katja Heinze

Author Contributions

The synthesis as well as spectroscopical and analytical characterization of complex **[Zn-1][PF$_6$]** and DFT calculations were performed by Maximilian Lauck. The crystal structure had been solved by Christoph Förster (group of Prof. Dr. Katja Heinze). The excited state lifetime measurements had been carried out by Dominik Gehrig at the Max Planck Institute for Polymer Research in Mainz, Germany. The manuscript was written by Prof. Dr. Katja Heinze and Maximilian Lauck.

Supporting Information

The supporting information of this publication can be found in Chapter 5.2. The Cartesian coordinates of the DFT-optimized geometries, as well as of the crystal structure can be found online at https://doi.org/10.1016/j.jorganchem.2017.02.026.

Abstract

Cobaltocenium carboxylic acid hexafluoride-phosphate has been attached to a zinc(II) *meso*-tetraphenyl porphyrin chromophore via an amide linkage. Optical and electrochemical studies reveal that the metallocene and the porphyrin interact only negligibly in the ground state of the dyad. Photoinduced charge-shift from the zinc porphyrin to the cobaltocenium substituent to give the zinc porphyrin radical cation and the cobaltocene occurs upon exciting the porphyrin with light. Steady state emission, time-resolved fluorescence and transient absorption pump–probe spectroscopy in addition to density functional theory calculations suggest that the charge shift to the cobaltocenium substituent can occur from several excited states of the porphyrin, namely from the S$_2$, S$_1$ and T$_1$ states. The triplet states of the cobaltocenium substituent ($^3E_{1g}$) and the triplet state of the zinc porphyrin (T$_1$) are higher in energy than the charge-shifted state. This energy sequence of states of the dyad is beneficial for photoinduced charge-shift reactions.
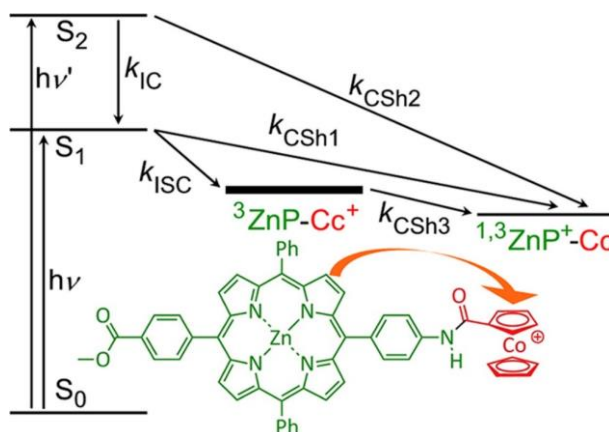
3.2.1 Introduction

Due to its reversible redox chemistry, its suitable redox potential and the ease of functionalization,[1–3] ferrocene FcH [Fe(η^5-C$_5$H$_5$)$_2$] has been frequently employed in Fc-chromophor dyads[4–7] Fc-acceptor dyads and Fc-P-acceptor triads with porphyrins P as chromophores to mimic the initial charge separating step of photosynthesis.[8–17] Fullerene C$_{60}$,[8–12] quinones[14–16] or electron deficient porphyrins such as gold(III) porphyrins[17–19] often act as electron acceptors in these model systems with typical reduction potentials of $E_{½} = -1.0$ to $E_{½} = -1.2$ V vs. ferrocene.[16,19–21] Furthermore, in cleverly designed donor-Q-donor triads, the quinone can even accept two electrons after absorption of two photons by the donors.[22,23]

Interestingly, reduction of the organometallic 18 ve cobaltocenium ion [Co(η^5-C$_5$H$_5$)$_2$]$^+$ (CcH$^+$) to the 19 ve complex cobaltocene CcH occurs at a similarly suited redox potential[24] which can even be tuned by the substituents, e.g. [Co(η^5-C$_5$H$_5$)(η^5-C$_5$H$_4$-CONH-Bu)]$^{+/0}$ features $E_{½} = -1.1$ V vs. ferrocene.[25] Furthermore, Cc$^+$ has been coupled to ferrocene and the resulting dyads possess intense solvatochromic charge-transfer bands.[26–29] Using amides as connecting units in [Fc-NHCO-Cc$^+$], the charge-shifted state [Fc$^+$-NHCO-Cc] is around 1.1 eV and directly accessible by visible light irradiation.[29] Much to our surprise, Cc$^+$ has not yet been employed as electron acceptor in photosynthetic models using porphyrins as chromophores,[30–32] in spite of its suitable redox properties. A single study of P. D. Beer reported a tetra cobaltocenium free-base porphyrin as anion sensor with electrochemical sensing.[33–35] Yet, photophysical properties or photoinduced electron transfer (PET) reactions from an electronically excited porphyrin to a covalently attached cobaltocenium ion have not been reported.[33–35] The lack of cobaltocenium ions in covalent photosynthetic models might be associated with its less developed substitution chemistry compared to ferrocene and the difficulty of purification of the cobaltocenium cations.[36] Recently, a reliable, high-yield route to cobaltocenium carboxylic acid hexafluoridophosphate has been provided by Bildstein.[37] This will expand the use of cobaltocenium ions in various areas including photosynthesis.

Here, we describe the preparation of an amide-linked zinc(II) porphyrin-cobaltocenium dyad **[Zn-1]$^+$** and report its photophysical properties with respect to modeling the first step of photosynthesis using the organometallic electron acceptor Cc$^+$.

3.2.2 Results and discussion

The electron acceptor cobaltocenium carboxylic acid hexafluoridophosphate[37] was coupled to a *meso*-tetraphenyl porphyrin amino acid methyl ester[38] using Ghosez's reagent[39] (Scheme 1a). After metallation of the porphyrin with zinc(II) acetate and counter ion exchange in one step, the final dyad **[Zn-1][PF$_6$]** was isolated in 88 % overall yield as a red-purple powder (Scheme 1a). NMR, IR and ESI$^+$ mass spectra are fully consistent with the proposed structure (Supporting Information). The most

significant differences to the reference porphyrin MeOOC-ZnP-NHCO-Me **Zn-2** lacking the cobaltocenium substituent (Scheme 1b),[16] are observed for the ^{13}C NMR resonance of the CO_{amide} unit (168.7/154.3 ppm), the C=O stretching vibration of the CO_{amide} group (1650/1661 cm^{-1}) and the proton resonance of the NH_{amide} group (9.41/10.34 ppm), i.e. close the charged Cc^+ substituent. The latter difference (δ_{NH}) might also be due to the different solvent employed (d$_8$-THF/d$_6$-acetone) which are able to bind to the amide NH group via hydrogen bonds.

In the electronic spectrum, **[Zn-1]$^+$** shows the characteristic Soret and Q bands of a zinc porphyrin at energies essentially unperturbed by the charged substituent compared to the reference porphyrin **Zn-2** (see 3.2.4 Experimental section).[16] Changing the solvent from CH_2Cl_2 to acetone, slightly shifts the porphyrin absorption bands due to coordination of the solvent at the zinc(II) ion. The absorption of the Cc^+ substituent of **[Zn-1]$^+$** is too weak compared to the intense porphyrin absorptions (λ_{max} = 420 nm, ε > 24 x 10^4 M^{-1} cm^{-1}) to be discernible in either solvent (c.f. λ_{max} = 409 nm, ε = 260 M^{-1} cm^{-1} for [Co(η^5-C$_5$H$_5$)(η^5-C$_5$H$_4$-COO-Me)]$^+$.[40]
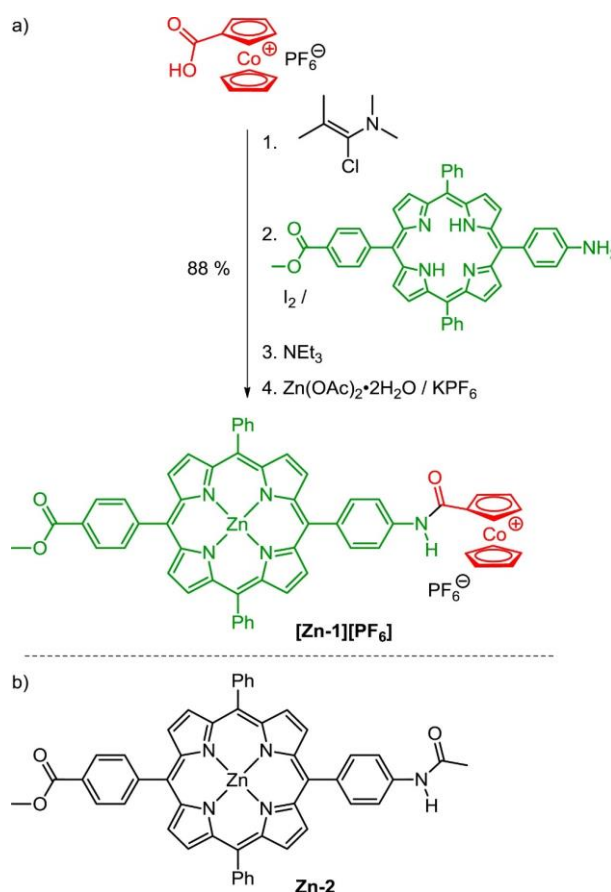
Scheme 1. a) Synthesis of the ZnP-Cc$^+$ dyad [Zn-1][PF$_6$] and b) structure of the reference porphyrin Zn-2.

Electrochemical events of the dyad proved to be reversible in CH_2Cl_2 using the non-coordinating salt [^{n}Bu$_4$N][B(C$_6$F$_5$)$_4$] as electrolyte (Figure 1a, see 3.2.4 Experimental section). Under these conditions, the cobaltocenium-to-cobaltocene reduction is found at −1.05 V and the oxidation of the porphyrin to its radical cation at 0.36 V vs. ferrocene. A further porphyrin oxidation occurs at 0.77 V and two porphyrin

reductions are found at −1.84 and −2.22 V, respectively. These values are not significantly different from those of the individual components[16,25] suggesting the absence of ground state interactions between the porphyrin chromophore and the cobaltocenium acceptor.

Spectroelectrochemical reduction from **[Zn-1]+** to **Zn-1** induces a shift of the Soret and Q bands from 420, 548 and 588 nm to 437, 565 and 608 nm, respectively. However, full recovery of the bands of **[Zn-1]+** of upon re-oxidation is not achieved, suggesting a follow-up reaction of **Zn-1** on the time scale of the spectroelectrochemical experiment (Figure 1b). This reaction might be associated with an internal proton transfer from the amide NH to a cyclopentadienyl ring upon reduction of the appended cobaltocenium ion to cobaltocene giving a $[Co^{II}(\eta^5-C_5H_5)(\eta^5-C_5H_4-R)]^+$ substituent[41,42] and a deprotonated amide. Proton transfer after electron transfer would also be consistent with the observed significant shift of the Soret band, while a simple reduction of the Cc^+ substituent should not significantly affect the Soret band. Indeed, deprotonation of **[Zn-1]+** by the phosphazene base $P_1{}^t$Bu (*tert*-butyliminotris(dimethylamino)phosphorane) in CH_2Cl_2 results in a similar shift of the Soret band (Supporting Information). According to Grätzel, proton transfer to cobaltocene is feasible, yet slow.[41,42] It might even be followed by hydrogen evolution[41,42] suggesting future applications of chromophore-substituted cobaltocenium ions as photocatalysts for hydrogen-evolution.

Spectroelectrochemical oxidation of **[Zn-1]+** to access the spectral properties of the zinc(II) porphyrin radical cation **[Zn-1]2+** revealed characteristic bands at wavelengths above 600 nm, namely at approximately 631 and 685 nm (Figure 1c). Upon re-reduction of **[Zn-1]2+** to **[Zn-1]+**, the absorption bands of **[Zn-1]+** are fully recovered (Figure 1c). Hence, the **[Zn-1]+**/**[Zn-1]2+** oxidation is fully reversible on the time scale of the spectroelectrochemical experiment in spite of the increased charge (Figure 1c). This reversible redox behavior is consistent with literature precedence for the Zn(TPP)/[Zn(TPP)]+ couple (TPP^{2-} = *meso*-tetraphenylporphyrinato(2–)).[43]

From the electrochemical data, the energy of the charge shifted (CSh) state ZnP^+-Cc of **[Zn-1]+** is estimated as 1.41 eV relative to the ground state according to the Rehm-Weller equation[43,44] (neglecting the Coulomb term, as no charge separation has occurred) (Figure 2). The energies of the porphyrin's excited singlet states S_2 and S_1 have been determined by time-resolved and static emission spectroscopy as 438 and 615 nm ($h\nu_2$ = 2.83 eV and $h\nu_1$ = 2.01 eV) after excitation with a 400 nm pulse in acetonitrile (Figure 3a). The energies of both states are well above the energy of the charge-shifted states ^{1,3}CSh. A significant energy difference between ^{1}CSh and ^{3}CSh states is not
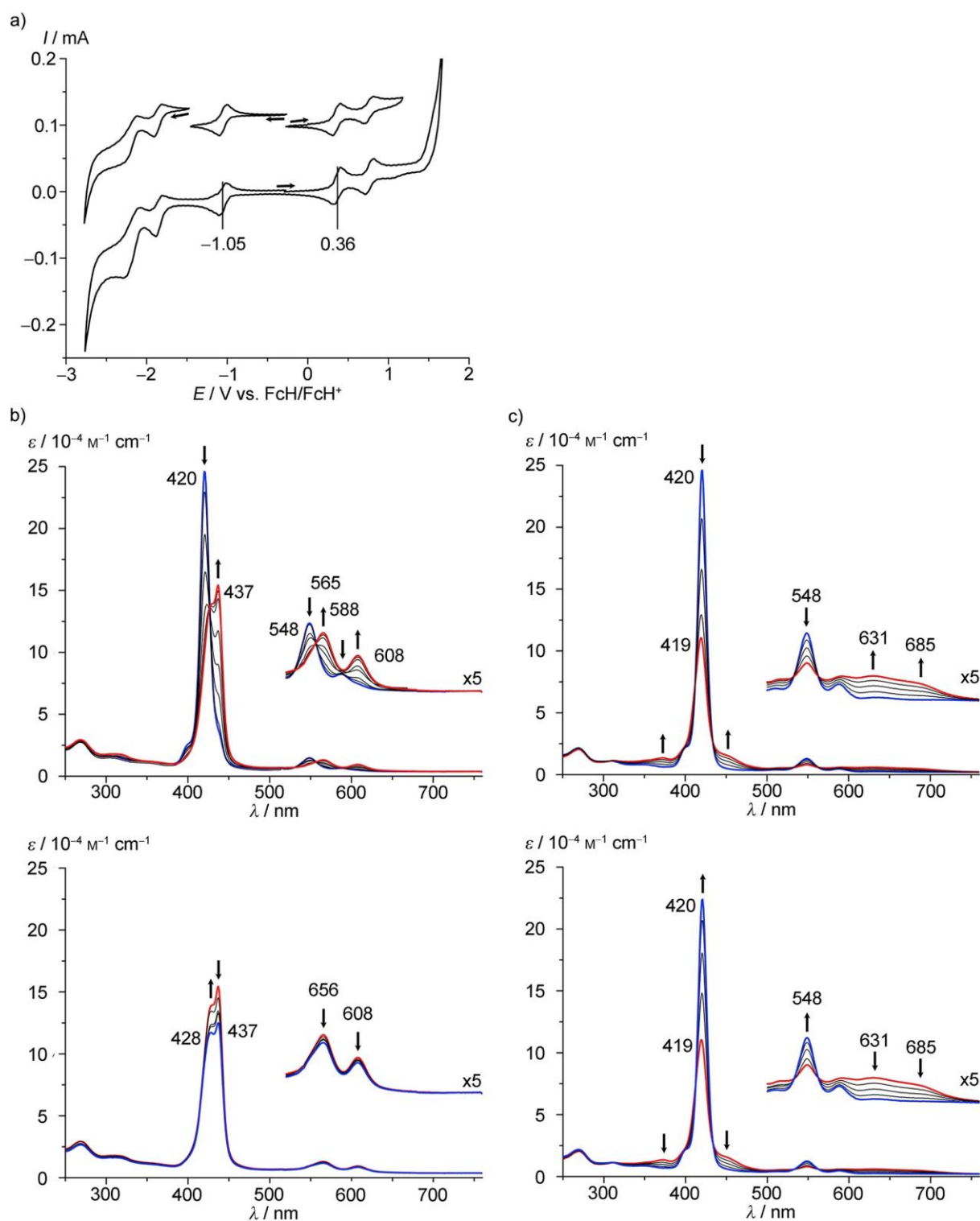
Figure 1. a) Cyclic voltammogram of [Zn-1][PF$_6$] in CH$_2$Cl$_2$/[^{n}Bu$_4$N][B(C$_6$F$_5$)$_4$] (scan rate 50 mV s^{-1}), **b)** spectroelectrochemical reduction and re-oxidation of [Zn-1][PF$_6$] and **c)** spectroelectrochemical oxidation and re-reduction of [Zn-1][PF$_6$] in CH$_2$Cl$_2$/[^{n}Bu$_4$N][PF$_6$].

expected due to the large distance of the spin centers and a facile ISC between ^{1}CSh and ^{3}CSh due to the spin-orbit coupling provided by the cobalt ion. Hence, photoinduced electron transfer to give ^{1,3}CSh states is thermodynamically feasible from both excited singlet states of the porphyrin with $\Delta G_{ET}(S_2)$ = -1.42 eV and $\Delta G_{ET}(S_1)$ = -0.60 eV (Figure 2). The rate constants for these PET reactions from the S$_2$ and S$_1$ states are denoted as k_{CSh2} and k_{CSh1}, respectively (Figure 2).
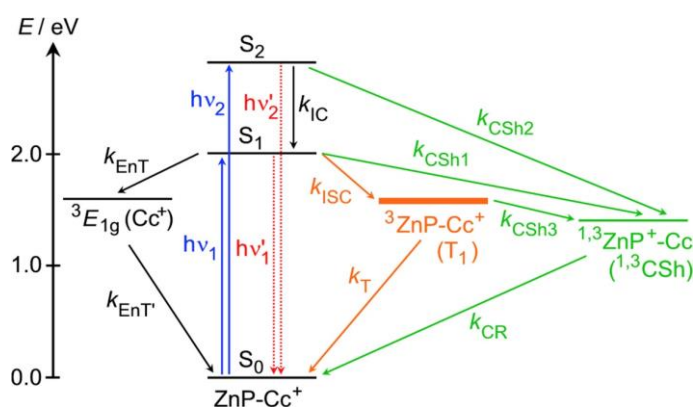
Figure 2. Jablonski diagram depicting the photochemical events occurring in the [Zn-1]+ dyad upon photoexcitation leading to the formation of the charge-separated state. Abbreviations: CSh = charge shift, EnT = energy transfer, CR = charge recombination, IC = internal conversion, ISC = intersystem crossing, T = triplet recombination.

The triplet energy of tetraphenylporphyrinato zinc(II) complexes has been reported around 1.61 ± 0.20 eV (T_1), slightly depending on the *meso*-substituents and the solvent which can coordinate to the central Zn^{II} ion.[20,21,45] This places the $^3ZnP-Cc^+$ (T_1) state above the $^{1,3}CSh$ states by ca. 0.2 eV (Figure 2). Hence, we expect only minor $^3ZnP-Cc^+$ formation from the $^{1,3}CSh$ states. Similarly, the lowest electronically excited state of the cobaltocenium ion (the $^3E_{1g}$ ligand field state with an $(e_{2g})^4(a_{1g})^1(e_{1g})^1$ electron configuration) is around 1.61 eV.[46] The corresponding excited singlet state $^1E_{1g}$ is too high in energy to be of relevance (3.0 eV).[46] The energy transfer efficiency from the porphyrin's S_1 state to give the Cc^+ $^3E_{1g}$ state (k_{EnT}) should be rather low due to its spin- and dipole-forbidden nature. We therefore neglect this k_{EnT} pathway and the $^3E_{1g}$ ligand field state of Cc^+ (Figure 2) in the following discussion.
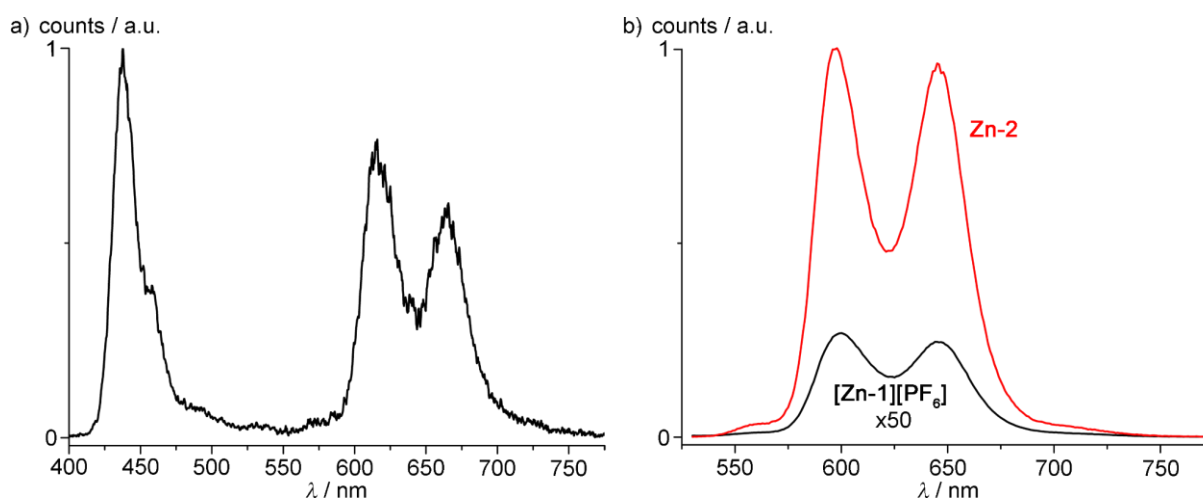
Figure 3. a) Emission spectrum of [Zn-1][PF$_6$] in acetonitrile directly after a 400 nm laser pulse and b) static emission spectra of isoabsorptive solutions of [Zn-1][PF$_6$] (black) and Zn-2 (red) in CH$_2$Cl$_2$ after excitation at 420 nm (note the 50x scaling for the spectrum of [Zn-1][PF$_6$]).

Upon excitation with 400 nm, we observe residual S_2 fluorescence ($h\nu'_2$) at 438 nm with a lifetime of < 100 ps, which is within our instrument's response function (Figure 3a). The S_2 lifetime of a

trimesityl(4-methoxycarbonylphenyl) substituted *meso*-porphyrin has been reported as 1.6 ps.[47] Attachment of a Re(bpy)(CO)$_3$Cl electron acceptor reduced this lifetime to 0.53 ps (bpy = 2,2'-bipyridine). The driving force for PET in this porphyrin-rhenium dyad amounts to 0.73 eV.[47]
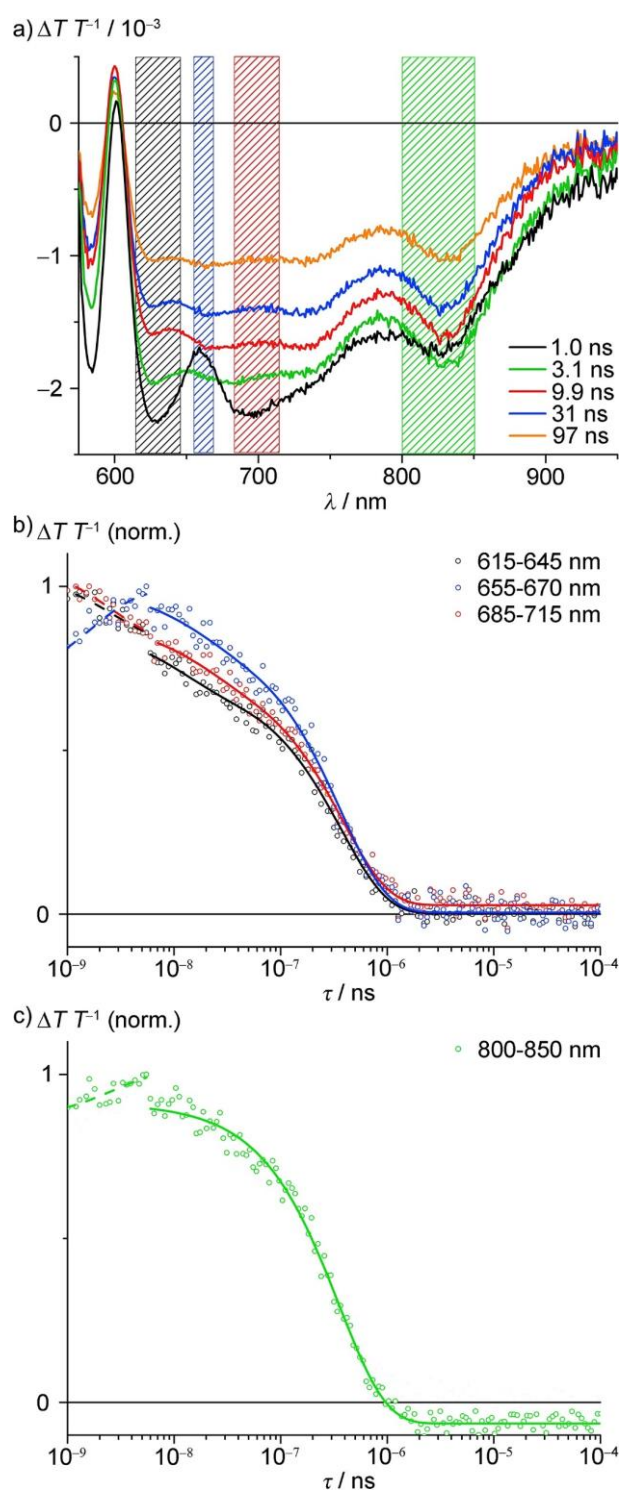
Figure 4. a) ns TA spectra after excitation with 546 nm; highlighted areas correspond to wavelength regions at which the dynamics were monitored by integration, b) decay dynamics extracted at 615–645 nm (black, biexponential fit), 655–670 (blue, biexponential fit) and 685–715 nm (red, biexponential fit) and c) 800–850 nm (green, monoexponential fit) and the fast initial signal evolution (dashed lines).

For the S_2 state of [Zn-1]$^+$, the driving force to give the CSh state is more than twice as high, possibly placing this PET already in the Marcus inverted region.[48,49] Due to instrument limitations, we cannot access the efficiency of PET from the S_2 state. Yet, we suppose that internal conversion to the S_1 state (k_{IC}) significantly competes with the PET (k_{CSh2}) as fluorescence from the S_1 state is observed as well after excitation of the S_2 state (hv'_1, Figure 2; Figure 3a).

According to static fluorescence spectroscopy, the S_1 fluorescence of [Zn-1]$^+$ is significantly reduced (by 99.6 %) compared to the reference porphyrin Zn-2 (Figure 3b). In agreement with this observation, the decay of the S_1 state of [Zn-1]$^+$ prepared by excitation at 556 nm and monitored by time-resolved photoluminescence follows a biexponential rate law. Two components are extracted with τ_1 = 2.1 ns (53 %) and τ_2 = 0.16 ns (47 %). The first one matches the lifetime of the S_1 state of the reference porphyrin Zn-2 and we assign this to the typical decay of singlet excitons.[7] As we consider k_{EnT} to give the $^3E_{1g}$ excited state of Cc$^+$ to be negligible, we associate τ_2 to the remaining decay path of the S_1 state, namely the oxidative PET giving the CSh state (Figure 2). The rate constant for this PET is then estimated according to k_{CSh1} = $1/\tau_2 - 1/\tau_1$ = 5.8 x 10^9 s^{-1}.

In order to track the evolution of the non-emissive states (T_1: ^{3}ZnP-Cc$^+$; ^{1,3}CSh: ^{1,3}ZnP$^+$-Cc), pump-probe transient absorption (TA) spectroscopy was employed in the ns–ms time regime. The TA spectra 1–97 ns after excitation with a 546 nm pulse are depicted in Figure 4a. The TA spectrum 1 ns after the 546 nm pulse shows three characteristic features at 629, 696 and 830 nm. The bands at 629 and 696 nm match the absorption bands of the radical cation [Zn-1]$^{2+}$ (Figure 1c) and are hence assigned to the ZnP$^+$-Cc CSh state. The band at 830 nm is a clear marker for zinc porphyrin triplet states[50,51] and is thus assigned to the ^{3}ZnP-Cc$^+$ T_1 state. Obviously, both states are populated after excitation. At 97 ns after the pulse, only features of the T_1 state are clearly visible in the TA spectrum. Hence, the CSh state decays faster than the T_1 state. After the initial fast kinetics with τ_1 = 2.6(0.5) ns (corresponding to the fluorescence lifetime of Zn-2) the integrated intensity at spectral regions where both the T_1 and the CSh state absorb (λ < 715 nm; black, blue and red regions indicated in Figure 4a) can be fitted to biexponential rate laws with τ_2 = 14(3) ns and τ_3 = 373(6) ns (Figure 4b). In the spectral region 800–815 nm (green region, Figure 4a), where only the T_1 state absorbs, the data can be fit to a monoexponetial decay with τ_3 = 356 ns (Figure 4c). Hence, we assign τ_3 = 373(6) ns to the decay of the T_1 state and τ_2 = 14(3) ns to the faster recombination of the CSh state. As typical lifetimes of ^{3}ZnTPP T_1 states are in the millisecond range,[51] the significantly reduced lifetime τ_3 suggests an efficient alternate decay path for the T_1 state. As the energy of the CSh state of dyad [Zn-1]$^+$ is below the energy of the T_1 state, the latter could also evolve into the CSh state (Figure 2, k_{CSh3}). With this interpretation given, we assign τ_3 = 373(6) ns to the charge shift from the T_1 state to the ^{3}CSh state (k_{CSh3}). In summary, after excitation to the porphyrin's S_1 state, both ISC to the T_1 state and PET to give the CSh state occur. The CSh state recombines to the ground state (τ_2 = 14(3) ns) while the T_1 state (τ_3 = 373(6) ns) decays via the CSh

state. Although the lifetime of the CSh state is only a few nanoseconds, this state is fed from the longer lived porphyrin T_1 state.
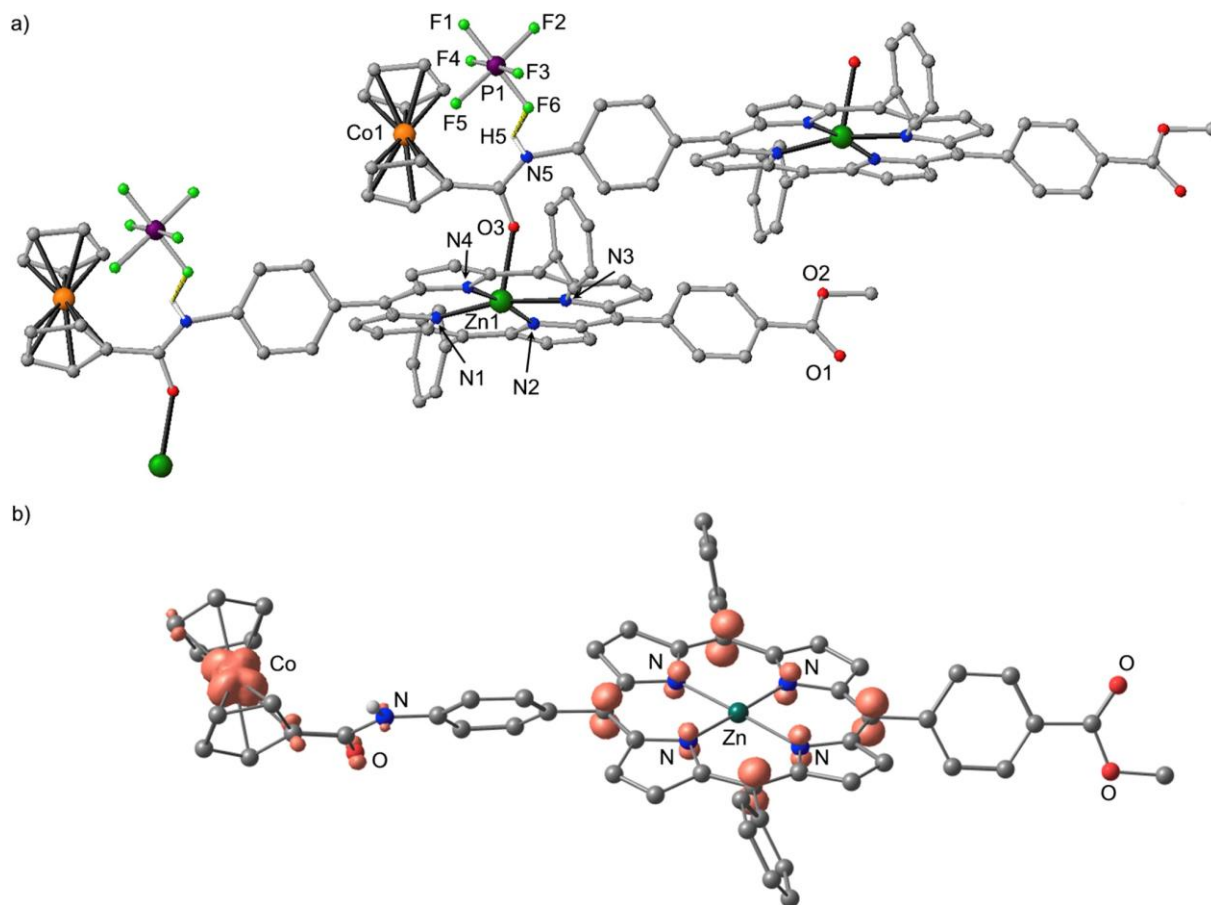
Figure 5. a) Molecular structure of [Zn-1][PF$_6$] in the solid state including connectivity to neighbouring molecules and counter ions and b) DFT optimized geometry and calculated spin density of the ^{3}CSh state of [Zn-1]$^+$ in orange (isosurface value at 0.01 a.u.; CH hydrogen atoms omitted).

To confirm the excited state ordering (**Figure 2**), density functional theory (DFT, B3LYP/def2-SV(P), ZORA) calculations have been conducted on the ground and the ^{3}CSh state of **[Zn-1]$^+$** and on **Zn-2** in its singlet and triplet state to obtain the respective relative state energies. The metrical data of **[Zn-1]$^+$** calculated by DFT and experimentally determined by X-ray diffraction on a single crystal of **[Zn-1][PF6]** are in reasonable agreement (**Figure 5**a). In the solid state of **[Zn-1][PF6]**, an intermolecular interaction between the Zn^{2+} ion and an amide carbonyl oxygen atom of an adjacent molecule is present [Zn1-O 2.2323(47) Å] resulting in a square-pyramidal coordination of Zn^{2+} with the metal ion 0.1773(23) Å above the N$_4$ mean plane (**Figure 5**a). The NH group of the amide is hydrogen-bonded to the hexafluoridophosphate counter ion with an N5···F6 distance of 2.9949(70) Å. In dilute solution, however, such interactions (Zn···O; NH···F) are likely absent.

The level ordering as shown in Figure 2 is qualitatively reproduced by the DFT calculations with the ^{3}CSh state below the T_1 state. Compared to the **[Zn-1]$^+$** ground state with a 18 ve cobaltocenium ion,

the Co-C bond lengths increase in the ^{3}CSh state with a 19 ve cobaltocene from 2.058 to 2.126 Å (averaged distances), consistent with the reduction of cobalt(III) to cobalt(II).[52,53] The ^{3}CSh state features spin density in the π system of the zinc porphyrin, at the cobalt ion and in the π system of the connecting η^5-C$_5$H$_4$ ring, especially at the *ipso* carbon atom (Figure 5b). The spin density at the cobalt ion fits to a $(e_{2g})^4(a_{1g})^2(e_{1g})^1$ electron configuration expected for a 19 ve cobaltocene, while the spin density at the zinc porphyrin fits to a π radical cation with large coefficients at the *meso* carbon atoms. Both connecting atoms, namely the *meso* carbon atom of the porphyrin and the *ipso* carbon atom of the η^5-C$_5$H$_4$ ligand, are involved. This orbital symmetry suggests that electron transfer is facile through the π system of the η^5-C$_5$H$_4$-CONH-C$_5$H$_4$ bridging unit and could be mediated by the bridge.

3.2.3 Conclusion

Cobaltocenium carboxylic acid hexafluoridophosphate is easily functionalized with a zinc(II) porphyrin chromophore to give the organometallic chromophor-acceptor dyad [ZnP-Cc$^+$][PF$_6$] **[Zn-1] [PF$_6$]**. The redox potentials of zinc(II) porphyrins and cobaltocenium ions place the charge-shifted state ZnP$^+$-Cc (CSh) at an energy of 1.41 eV relative to the ground state. This CSh state is below all triplet states, namely the high-energy triplet state of cobaltocenium ions and the T$_1$ state of the zinc(II) porphyrin. Furthermore, the CSh state can be populated from the porphyrin's S$_2$, S$_1$ and T$_1$ states with energies of 2.83, 2.01 and 1.61 eV, respectively. Electron transfer from the zinc porphyrin's π system to the cobaltocenium's Cp π system is allowed by symmetry. Hence, cobaltocenium ions are ideal candidates as primary electron acceptors in bioinspired organometallic models of the photosystem.

3.2.4 Experimental section

Instrumentation. NMR spectra were recorded on a Bruker Avance DRX 400 spectrometer at 400.31 MHz (^{1}H) and 100.05 MHz (^{13}C{^{1}H}). Chemical shifts are reported on the δ scale in ppm relative to the solvent signal as an internal standard: d$_6$-acetone (^{1}H: δ = 2.05 ppm; ^{13}C: δ = 29.84 ppm), CD$_2$Cl$_2$ (^{1}H: δ = 5.32 ppm); (s) = singlet, (d) = doublet, (m) = multiplet. IR spectra were recorded with a BioRad Excalibur FTS 3100 spectrometer as KBr disks with signal intensity: (br) = broad, (s) = strong, (m) = medium, (w) = weak. ESI and HR ESI mass spectra were recorded on a Micromass Q-TOF-Ultima spectrometer. Cyclic and square wave voltammetric measurements were carried out with a BioLogic SP-50 voltammetric analyzer in CH$_2$Cl$_2$ or CH$_3$CN containing 0.1 M [^{n}Bu$_4$N][B(C$_6$F$_5$)$_4$] or [^{n}Bu$_4$N][PF$_6$] as supporting electrolytes at a platinum working electrode, a platinum wire as the counter electrode and a 0.01 M Ag/AgNO$_3$ electrode as the reference electrode. All cyclic voltammetric measurements were recorded at 50 or 100 mV s^{-1} scan rate. Ferrocene was employed as an internal reference redox system. rev. = reversible, qrev. = quasireversible, irrev. = irreversible redox process. Spectroelectrochemical experiments were performed using a thin layer (CaF$_2$; path length 1 mm) cell kit (GAMEC Analysentechnik, Illingen, Germany) equipped with a Pt gauze working electrode, a Pt

counter electrode and a Ag reference electrode. UV/vis/NIR absorption spectra were measured on a Varian Cary 5000 spectrometer in 1.0 cm cells (Hellma, suprasil). Steady-state emission spectra were recorded on a Varian Cary Eclipse spectrometer in 1.0 cm cells (Hellma, suprasil). Quantum yields Φ were determined by comparing the areas under the emission spectra on an energy scale [cm^{-1}] recorded for optically matched solutions (absorption intensity below 0.05) of the samples and the reference (Φ(H$_2$TPP) = 0.13 in benzene)[54] using the equation[55] $\Phi = \Phi_{ref}$ x I/I_{ref} x $\eta 2/\eta 2_{ref}$ with η(benzene) = 1.5011, η(CH$_2$Cl$_2$) = 1.4242; experimental uncertainty 15 %. Fluorescence decay and transient absorption spectroscopic measurements were performed under inert conditions as described elsewhere.[7,16]

Density functional calculations were carried out with the ORCA 3.0.2/DFT series of programs.[56] For geometry optimizations and energy calculations, the B3LYP formulation of density functional theory was used employing the def2-SV(P) basis set,[57,58] the RIJCOSX approximation,[59,60] the zeroth order regular approximation (ZORA),[61,62] and the KDIIS algorithm[63] at GRID5. No symmetry constraints were imposed on the molecules. The approximate free energies at 298 K were obtained through thermochemical analysis of the numerical frequency calculation, using the thermal correction to Gibbs free energy as reported by ORCA 3.0.2.

Crystal structure determination. Intensity data were collected with a STOE IPDS-2T diffractometer using Mo-K$_\alpha$ radiation (λ = 0.71073 Å) and were corrected for absorption and other effects. The diffraction frames were integrated using the STOE X-RED package and most were corrected for absorption with MULABS of the PLATON software package.[64–66] The structure was solved by direct methods and refined by the full-matrix method based on F^2 using the SHELX software package.[67,68] The PLATON SQUEEZE procedure has been used to calculate the contribution of disordered solvent to the calculated structure factor.[69] All non-hydrogen atoms were refined anisotropically while the positions of all hydrogen atoms were generated with appropriate geometric constraints and allowed to ride on their respective parent carbon atoms with fixed isotropic thermal parameters.

Crystallographic Data of **[Zn-1][PF$_6$]**: C$_{57}$H$_{39}$CoF$_6$N$_5$O$_3$PZn (1111.22); triclinic; $P\bar{1}$; a = 10.783(2) Å, b = 10.848(2) Å, c = 25.150(5) Å, α = 79.29(3)°, β = 83.46(3)°, γ = 78.65(3)°, V = 2824.9(11) Å^3; Z = 2; density, calcd. = 1.306 g cm^{-3}, T = 193 K, μ = 0.812 mm^{-1}; F(000) = 1132; crystal size 0.700 x 0.310 x 0.010 mm; ϑ = 2.330–28.412 deg.; -14 = $\leq$ $\leq$ 14, $-14 \leq k \leq 13$, $-33 \leq l \leq 33$; rfln collected = 29974; rfln unique = 14066 [R(int) = 0.0941]; completeness to ϑ = 25.242 deg. = 99.8 %; semi empirical absorption correction from equivalents; max. and min. transmission 1.10085 and 0.92822; data 14066; restraints 1168, parameters 823; goodness-of-fit on F^2 = 0.983; final indices [$I > 2\sigma$(I)] R_1 = 0.0768, wR_2 = 0.1922; R indices (all data) R_1 = 0.1641, wR_2 = 0.2508; extinction coefficient 0.0030(8); largest diff. peak and hole 1.514 and -0.989 e Å^{-3}. Voids in the crystal structure

contain disordered solvent molecules, which were handled using SQUEEZE. The hexafluoridophosphate counter ion is disordered over two positions. The [Cc-CONH] unit is disordered over two positions. CCDC-1522073 contains the supplementary crystallographic data for this paper. These data can be obtained free of charge from the Cambridge Crystallographic Data Centre via www.ccdc.cam.ac.uk/data_request/cif.

Materials. Unless otherwise noted, all chemical reagents were used without any further purification as received from suppliers (Sigma Aldrich, Acros, Alfa Aesar, Merck). CH_2Cl_2 was freshly distilled from calcium hydride. Carboxycobaltocenium hexafluoridophosphate,[37] 15-(4-methoxycarbonylphenyl)-5-(4-aminophenyl)-10,20-diphenylporphyrin[38] and **Zn-2**[16] were prepared according to literature procedures.

Synthesis of [Zn-1][PF$_6$]. Carboxycobaltocenium hexafluoridophosphate (113 mg, 298 mmol) was suspended in anhydrous dichloromethane (50 mL) and Ghosez's reagent (0.3 mL, 2.27 mmol) was added. The suspension was refluxed for 13 h resulting in a yellow/brownish solution. The solvent and excess of Ghosez's reagent were removed under reduced pressure. The residue was dissolved in dichloromethane (50 mL) and iodine (46 mg, 181 mmol) and 15-(4-methoxycarbonylphenyl)-5-(4-aminophenyl)-10,20-diphenylporphyrin (135 mg, 196 mmol) were added resulting in a green solution. The solution was stirred under argon at room temperature until all amino porphyrine was consumed (TLC control after 6 h). Trimethylamine (1 mL) was added resulting in a color change from green to red. The solvent was removed under reduced pressure. The solid was dissolved in a mixture of dichloromethane (20 mL), ethanol (5 mL) and water (5 mL) and potassium hexafluoridophosphate (1 g, 5.41 mmol) and zinc acetate dihydrate (1 g, 4.56 mmol) were added. The suspension was stirred at room temperature for 48 h. The water phase was removed, the organic layer was washed with water (2 x 15 mL), dried over sodium sulfate and the solvent was removed under reduced pressure. The crude product was suspended in pentane (30 mL) and sonicated in an ultrasonic bath. The product was isolated by filtration and dried under reduced pressure giving a purple-red powder. Yield 199 mg (179 mmol, 88 %). Crystals suitable for X-ray diffraction were obtained by recrystallization from a CH2Cl2 solution layered with hexanes. For atom numbering see Scheme 2.
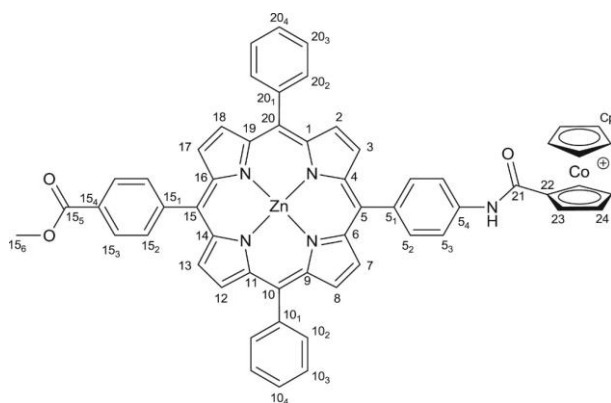
Scheme 2. Atom numbering of [Zn-1]+ for NMR assignment.

^{1}H NMR (d_6-acetone): δ [ppm] = 4.08 (s, 3H, $H^{15.6}$), 6.17 (s, 5H, H^{Cp}), 6.19 (pt, 2H, $^3J_{HH}$ = 1.9 Hz, H^{24}), 6.68 (pt, 2H, 3J$_{HH}$ = 1.9 Hz, H^{23}), 7.78–7.85 (m, 6H, $H^{10.3,10.4,20.3,20.4}$), 8.19–8.27 (m, 8H, $H^{5.2,5.3,10.2,20.2}$), 8.35 (d, 2H, $^3J_{HH}$ = 8.1 Hz, $H^{15.2}$), 8.44 (d, 2H, $^3J_{HH}$ = 8.2 Hz, $H^{15.3}$), 8.84 (d, 2H, $^3J_{HH}$ = 4.6 Hz), 8.86 (d, 4H, $^3J_{HH}$ = 4.2 Hz), 8.90 (d, 2H, $^3J_{HH}$ = 4.6 Hz ($H^{2,3,7,8,12,13,17,18}$)), 10.34 (s, 1H, H^{NH}). ^{1}H NMR (CD_2Cl_2): δ [ppm] = 4.07 (s, 3H, $H^{15.6}$), 5.84 (s, 2H, H^{24}), 5.89 (s, 5H, H^{Cp}), 6.55 (s, 2H, H^{23}), 7.74–7.82 (m, 6H, $H^{10.3,10.4,20.3,20.4}$), 8.13–8.27 (m, 8H, $H^{5.2,5.3,10.2,20.2}$), 8.32 (d, 2H, $^3J_{HH}$ = 8.0 Hz, $H^{15.2}$), 8.41 (d, 2H, $^3J_{HH}$ = 7.9 Hz, $H^{15.3}$), 8.82 (s, 1H, H^{NH}), 8.91 (d, 2H, $^3J_{HH}$ = 4.6 Hz), 8.96 (d, 2H, $^3J_{HH}$ = 4.6 Hz), 8.97 (d, 2H, $^3J_{HH}$ = 4.6 Hz), 9.01 (d, 2H, $^3J_{HH}$ = 4.6 Hz ($H^{2,3,7,8,12,13,17,18}$)). ^{13}C {^{1}H} NMR (d_6-acetone): δ [ppm] = 52.6 ($C^{15.6}$), 85.5 (C^{23}), 87.0 (C^{24}), 87.5 (C^{Cp}), 97.0 (C^{22}), 119.3 ($C^{15.5,3}$), 121.0 (C^5), 121.6 ($C^{10,20}$), 127.4 ($C^{10.3,20.3}$), 128.3 ($C^{15.3,10.4,20.4}$), 130.2 ($C^{15.4}$), 132.1, 132.3, 132.4, 132.7 ($C^{2,3,7,8,12,13,17,18}$), 135.2 ($C^{10.2,20.2}$), 135.4 ($C^{15.2}$), 135.6 ($C^{5.2}$), 138.7 ($C^{5.1}$), 140.8 ($C^{5.4}$), 144.2 ($C^{10.1,20.1}$), 149.2 ($C^{15.1}$), 150.4, 150.9, 150.9, 151.1 ($C^{1,4,6,9,11,14,16,19}$), 154.3 (C^{21}), 167.6 ($C^{15.5}$). IR(KBr): $\tilde{\nu}$ [cm^{-1}] = 3362 (br, NH), 3198 (br, CH_{Cc}), 2961 (s, CH), 2924 (s, CH), 2855 (s, CH), 1720 (s, CO_{ester}), 1661 (s, CO_{amide}), 1527 (m), 1566 (m), 1412 (w),1261 (s, COC_{def}),1097 (s),1022 (s), 843 (m, PF), 802 (s), 704 (m), 559 (m, FPF_{def}). MS (ESI$^+$): m/z (%) = 964.16 (100) [M − PF$_6$]$^+$. HR-MS (ESI$^+$, MeOH): obs. m/z (%) = 964.1675; calcd for [M − PF$_6$]$^+$: 964.1677. UV/vis (CH_2Cl_2): λ [nm] (ε [10^4 M^{-1}cm^{-1}]) = 420 (24.60), 512 (0.18), 548 (1.04), 588 (0.23). UV/vis (acetone): λ [nm] (ε [10^4 M^{-1}cm^{-1}]) = 423 (25.30), 518 (0.16), 556 (0.95), 597 (0.38). Fluorescence (λ_{exc} = 420 nm, CH_2Cl_2): λ [nm] (rel. intensity) = 599 (1.00), 647 (0.94). Fluorescence (λ_{exc} = 423 nm, acetone): λ [nm] (rel. intensity) = 605 (1.00), 654 (0.63). Quantum yield (λ_{exc} = 421 nm, CH_2Cl_2): Φ = 0.0006. CV (FcH/FcH$^+$, 50 mV^{-1}, CH_2Cl_2, 0.1 M [^{n}Bu$_4$N][B(C$_6$F$_5$)$_4$]): $E_{1/2}$ [V] = 0.77 (rev.), 0.36 (rev.), −1.05 (rev.), −1.84 (rev.), −2.22 (rev.). CV (FcH/FcH$^+$, 50 mV^{-1}, CH_2Cl_2, 0.1 M [^{n}Bu$_4$N][PF$_6$]): $E_{1/2}$ [V] = 0.74 (rev.), 0.37 (rev.), −1.16 (rev.), −1.88 (rev.), −2.23 (irrev.). CV (FcH/FcH$^+$, 50 mV^{-1}, CH_3CN, 0.1 M [^{n}Bu$_4$N][B(C$_6$F$_5$)$_4$]): $E_{1/2}$ [V] = 0.76 (rev.), 0.40 (rev.), −1.14 (qrev.), −1.80 (rev.), −2.13 (irrev.). CV (FcH/FcH$^+$, 100 mV^{-1}, CH_3CN, 0.1 M [^{n}Bu$_4$N][PF$_6$]): $E_{1/2}$ [V] = 0.74 (rev.), 0.41 (rev.), −1.16 (qrev.), −1.78 (rev.), −2.18 (irrev.).

3.2.5   References

[1]   Heinze, K., Lang, H., *Organometallics* **2013**, *32*, 5623–5625.

[2]   Štěpnička, P. (Ed.) *Ferrocenes*. *Ligands, materials and biomolecules*, Wiley-VCH, Chichester, England, Hoboken, NJ, **2008**.

[3]   Togni, A., Hayashi, T. (Ed.) *Ferrocenes*. *Homogeneous Catalysis, Organic Synthesis, Materials Science*, Wiley-VCH, Weinheim, **2008**.

[4]   Mansour, H., El-Khouly, M. E., Shaban, S. Y., Ito, O., Jux, N., *J. Porphyrins Phthalocyanines* **2007**, *11*, 719–728.

[5]   Thornton, N. B., Wojtowicz, H., Netzel, T., Dixon, D. W., *J. Phys. Chem. B* **1998**, *102*, 2101–2110.

[6]   Kubo, M., Mori, Y., Otani, M., Murakami, M., Ishibashi, Y., Yasuda, M., Hosomizu, K., Miyasaka, H., Imahori, H., Nakashima, S., *Chem. Phys. Lett.* **2006**, *429*, 91–96.

[7]   Melomedov, J., Ochsmann, J. R., Meister, M., Laquai, F., Heinze, K., *Eur. J. Inorg. Chem.* **2014**, 2902–2915.

[8]   Imahori, H., Guldi, D. M., Tamaki, K., Yoshida, Y., Luo, C., Sakata, Y., Fukuzumi, S., *J. Am. Chem. Soc.* **2001**, *123*, 6617–6628.

[9]   Imahori, H., Tamaki, K., Araki, Y., Sekiguchi, Y., Ito, O., Sakata, Y., Fukuzumi, S., *J. Am. Chem. Soc.* **2002**, *124*, 5165–5174.

[10]   Imahori, H., Sekiguchi, Y., Kashiwagi, Y., Sato, T., Araki, Y., Ito, O., Yamada, H., Fukuzumi, S., *Chem. Eur. J.* **2004**, *10*, 3184–3196.

[11]   Winters, M. U., Dahlstedt, E., Blades, H. E., Wilson, C. J., Frampton, M. J., Anderson, H. L., Albinsson, B., *J. Am. Chem. Soc.* **2007**, *129*, 4291–4297.

[12]   Wijesinghe, C. A., El-Khouly, M. E., Zandler, M. E., Fukuzumi, S., D'Souza, F., *Chem. Eur. J.* **2013**, *19*, 9629–9638.

[13]   Fukuzumi, S., Okamoto, K., Imahori, H., *Angew. Chem.* **2002**, *114*, 642–644.

[14]   Fukuzumi, S., Okamoto, K., Imahori, H., *Angew. Chem. Int. Ed.* **2002**, *41*, 620–622.

[15]   Fukuzumi, S., Okamoto, K., Yoshida, Y., Imahori, H., Araki, Y., Ito, O., *J. Am. Chem. Soc.* **2003**, *125*, 1007–1013.

[16] Melomedov, J., Ochsmann, J. R., Meister, M., Laquai, F., Heinze, K., *Eur. J. Inorg. Chem.* **2014**, 1984–2001.

[17] Göransson, E., Boixel, J., Fortage, J., Jacquemin, D., Becker, H.-C., Blart, E., Hammarström, L., Odobel, F., *Inorg. Chem.* **2012**, *51*, 11500–11512.

[18] Fukuzumi, S., Ohkubo, K., E, W., Ou, Z., Shao, J., Kadish, K. M., Hutchison, J. A., Ghiggino, K. P., Sintic, P. J., Crossley, M. J., *J. Am. Chem. Soc.* **2003**, *125*, 14984–14985.

[19] Preiß, S., Melomedov, J., Wünsche von Leupoldt, A., Heinze, K., *Chem. Sci.* **2016**, *7*, 596–610.

[20] Lim, G. N., Obondi, C. O., D'Souza, F., *Angew. Chem.* **2016**, *128*, 11689–11693.

[21] Lim, G. N., Obondi, C. O., D'Souza, F., *Angew. Chem. Int. Ed.* **2016**, *55*, 11517–11521.

[22] Orazietti, M., Kuss-Petermann, M., Hamm, P., Wenger, O. S., *Angew. Chem.* **2016**, *128*, 9553–9556.

[23] Orazietti, M., Kuss-Petermann, M., Hamm, P., Wenger, O. S., *Angew. Chem. Int. Ed.* **2016**, *55*, 9407–9410.

[24] Connelly, N. G., Geiger, W. E., *Chem. Rev.* **1996**, *96*, 877–910.

[25] Beer, P. D., Hesek, D., Hodacova, J., Stokes, S. E., *J. Chem. Soc., Chem. Commun.* **1992**, 270–272.

[26] Warratz, R., Peters, G., Studt, F., Römer, R.-H., Tuczek, F., *Inorg. Chem.* **2006**, *45*, 2531–2542.

[27] Laus, G., Strasser, C. E., Holzer, M., Wurst, K., Pürstinger, G., Ongania, K.-H., Rauch, M., Bonn, G., Schottenberger, H., *Organometallics* **2005**, *24*, 6085–6093.

[28] Barlow, S., *Inorg. Chem.* **2001**, *40*, 7047–7053.

[29] Huesmann, H., Förster, C., Siebler, D., Gasi, T., Heinze, K., *Organometallics* **2011**, *31*, 413–427.

[30] Vecchi, A., Galloni, P., Floris, B., Dudkin, S. V., Nemykin, V. N., *Coord. Chem. Rev.* **2015**, *291*, 95–171.

[31] Suijkerbuijk, B. M. J. M., Klein Gebbink, R. J. M., *Angew. Chem.* **2008**, *120*, 7506–7532.

[32] Suijkerbuijk, B. M. J. M., Klein Gebbink, R. J. M., *Angew. Chem. Int. Ed.* **2008**, *47*, 7396–7421.

[33] Beer, P. D., Drew, M. G. B., Hesek, D., Jagessar, R., *J. Chem. Soc., Chem. Commun.* **1995**, *65*, 1187–1189.

[34] Beer, P. D., *Chem. Commun.* **1996**, 689–696.

[35] Beer, P. D., Hayes, E. J., *Coord. Chem. Rev.* **2003**, *240*, 167–189.

[36] Sheats, J. E., Rausch, M. D., *J. Org. Chem.* **1970**, *35*, 3245–3249.

[37] Vanicek, S., Kopacka, H., Wurst, K., Müller, T., Schottenberger, H., Bildstein, B., *Organometallics* **2014**, *33*, 1152–1156.

[38] Heinze, K., Reinhart, A., *Dalton Trans.* **2008**, 469–480.

[39] Devos, A., Remion, J., Frisque-Hesbain, A.-M., Colens, A., Ghosez, L., *J. Chem. Soc., Chem. Commun.* **1979**, 1180–1181.

[40] El Murr, N., *J. Organomet. Chem.* **1976**, *112*, 189–199.

[41] Koelle, U., Infelta, P. P., Graetzel, M., *Inorg. Chem.* **1988**, *27*, 879–883.

[42] El Murr, N., Laviron, E., *Tetrahedron Letters* **1975**, *11*, 875–878.

[43] Rehm, D., Weller, A., *Isr. J. Chem.* **1970**, *8*, 259–271.

[44] Weller, A., *Z. Phys. Chem.* **1982**, *133*, 93–98.

[45] Walters, V. A., Paula, J. C. de, Jackson, B., Nutaitis, C., Hall, K., Lind, J., Cardozo, K., Chandran, K., Raible, D., Phillips, C. M., *J. Phys. Chem.* **1995**, *99*, 1166–1171.

[46] Roginski, R. T., Moroz, A., Hendrickson, D. N., Drickamer, H. G., *J. Phys. Chem.* **1988**, *92*, 4319–4323.

[47] Kiyosawa, K., Shiraishi, N., Shimada, T., Masui, D., Tachibana, H., Takagi, S., Ishitani, O., Tryk, D. A., Inoue, H., *J. Phys. Chem. C* **2009**, *113*, 11667–11673.

[48] Marcus, R. A., *Angew. Chem.* **1993**, *105*, 1161–1172.

[49] Marcus, R. A., *Angew. Chem. Int. Ed. Engl.* **1993**, *32*, 1111–1121.

[50] Nojiri, T., Watanabe, A., Ito, O., *J. Phys. Chem. A* **1998**, *102*, 5215–5219.

[51] Brookfield, R. L., Ellul, H., Harriman, A., *Faraday Trans. 2* **1985**, *81*, 1837–1848.

[52] Braga, D., Scaccianoce, L., Grepioni, F., Draper, S. M., *Organometallics* **1996**, *15*, 4675–4677.

[53] Bünder, W., Weiss, E., *J. Organomet. Chem.* **1975**, *92*, 65–68.

[54] Rosa, A., Ricciardi, G., Baerends, E. J., Romeo, A., Monsù Scolaro, L., *J. Phys. Chem. A* **2003**, *107*, 11468–11482.

[55] Lakowicz, J. R., *Principles of Fluorescence Spectroscopy, 3. Ed.*, Springer, New York, **2006**.

[56] Neese, F., *WIREs Comput Mol Sci* **2012**, *2*, 73–78.

[57] Schäfer, A., Horn, H., Ahlrichs, R., *J. Chem. Phys.* **1992**, *97*, 2571–2577.

[58] Schäfer, A., Huber, C., Ahlrichs, R., *J. Chem. Phys.* **1994**, *100*, 5829–5835.

[59] Neese, F., Wennmohs, F., Hansen, A., Becker, U., *Chem. Phys.* **2009**, *356*, 98–109.

[60] Izsák, R., Neese, F., *J. Chem. Phys.* **2011**, *135*, 144105.

[61] van Lenthe, E., Baerends, E. J., Snijders, J. G., *J. Chem. Phys.* **1993**, *99*, 4597–4610.

[62] van Wüllen, C., *J. Chem. Phys.* **1998**, *109*, 392–399.

[63] Kollmar, C., *J. Chem. Phys.* **1996**, *105*, 8204–8212.

[64] Stoe & Cie, *X-red*, Stoe & Cie, Darmstadt, Germany, **2002**.

[65] Blessing, R. H., *Acta Cryst.* **1995**, *A51*, 33–38.

[66] Spek, A. L., *Acta Cryst.* **2009**, *D65*, 148–155.

[67] Sheldrick, G. M., *Acta Cryst.* **2015**, *C71*, 3–8.

[68] Sheldrick, G. M., *SHELXL-2014/7*, Universität Göttingen, Göttingen, Germany, **2014**.

[69] Spek, A. L., *Acta Cryst.* **2015**, *C71*, 9–18.

3.3 Lifetime Prolongation of the Charge-Shifted State: Cobaltocenium Substituents as Electron Acceptors in a Photosynthetic Model Triad

Since the early 1950s, Ferrocene has been well described due to the reversible electrochemical properties of the ferrocene/ferrocenium (FcH/FcH$^+$) couple and the broad adjustability of the substitution pattern.[1–6] Therefore, the use as electron donor in artificial photosynthesis models,[7–15] in further biomimetic model applications[16–20] and for electron transfer studies[21–23] was possible. The cobaltocene/cobaltocenium (CcH/CcH$^+$) couple shows reversible electrochemical properties as well,[22,24,25] whereby the electronically stable 18 e$^-$ homologue of ferrocene CcH$^+$ possesses one positive charge. Cobaltocenium is a well-known electron acceptor[22,26] and in the reduced state – in opposite to ferrocene – able to reduce protons to elemental hydrogen.[25,27] On the contrary to the ferrocene couple, the width of the substitution pattern of the cobaltocene couple is shortened due to the high reduction potential of cobaltocene[28] on the one hand and the cation character of cobaltocenium[29,30] on the other hand. Ferrocene-cobaltocenium amides have shown, that electron transfer from ferrocene to cobaltocenium is possible and leads to ferrocenium-cobaltocene intermediates.[21,22] Cobaltocene can be re-oxidized by ferrocenium to form the starting complex, otherwise it can transfer the electron to a surrounding electron acceptor, like protons.[25,26] Unfortunately the quenching of the reactive state by ferrocenium is faster, and thereby the use as hydrogen evolution catalyst is not yet possible.
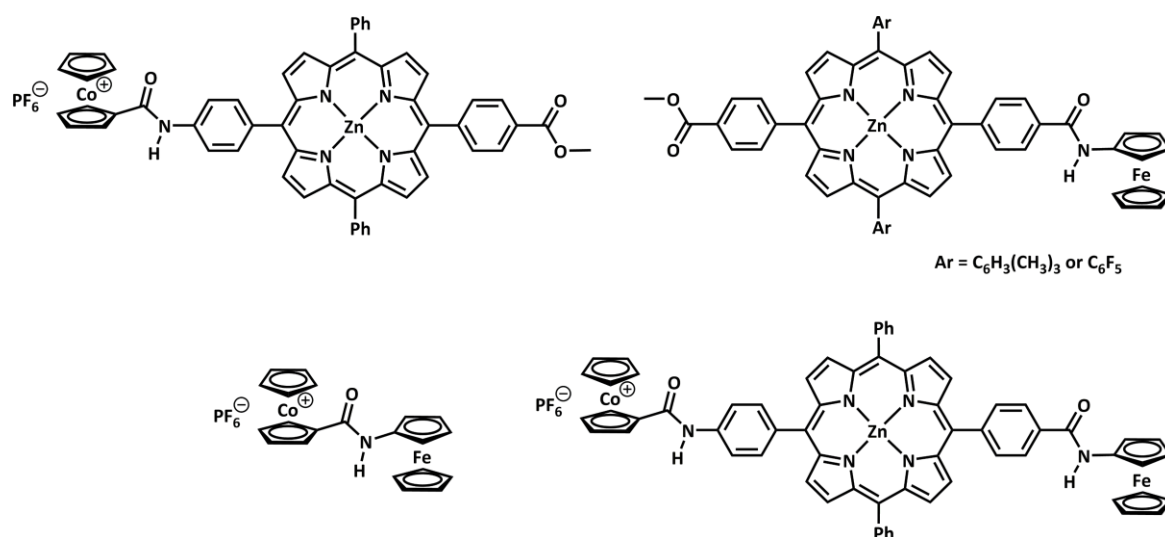
Figure 1. Reported metallocene-porphyrin dyads[9,26] (top), bimetallocene dyad (bottom left side) and novel bimetallocene-porphyrin triad (bottom right side).

As previously shown (Chapter 3.2), cobaltocenium can accept electrons from porphyrins due to PET.[26] The reactivity of the amide linked cobaltocene is verified, due to the reduction of the close-by bonded amide proton in absolute solvents.[26] In here, the cobaltocene can interact with the porphyrin cation (back-ET) or undergo further reactions with protons.[26] Both possibilities depend on the lifetime of the

charge-shifted state. A short lifetime leads to the restored ground state, a long-lived intermediate increases the chance for the further reaction.

A triad consisting of an amide linked cobaltocenium, porphyrin and ferrocene was synthesized (Figure 1) and partially characterized (^{1}H NMR spectroscopy). The porphyin acts as chromophore for the photoinduced electron transfer from porphyrin to cobaltocenium to form reactive cobaltocene, and the ferrocene can restore the porphyrin ground state. Furthermore, after charge separation the porphyrin acts as a spacer and should extend the lifetime of the charge-shifted state[31] with cobaltocene on the one side, and ferrocenium on the other side.

3.3.1 Electron Transfer, Kinetics and Density Functional Theory

Irradiation of a porphyrin leads to the excitation of one electron out of the porphyrin ground state. For the following photoinduced charge separation and electron transfer cascade of the triad, several deactivation pathways have to be considered (Figure 2).

In the first step, the porphyrin is excited by photon induction ($h\nu_1$ or $h\nu_2$) to the S_1 or S_2 state. The energy of the excited states of zinc porphyrins can be observed at 2.0-2.1 eV for the S_1[9,10] and 2.8-2.9 eV for the S_2[26,32] state. After excitation, the following deactivation pathways are conceivable:
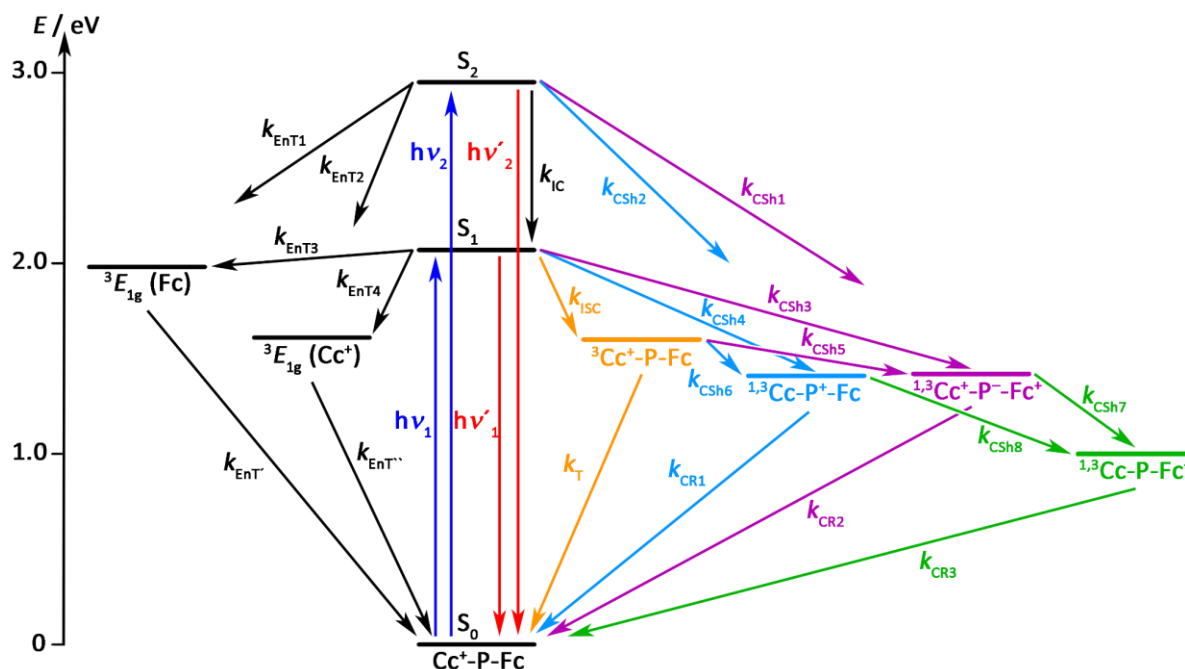
Figure 2. Jablonski diagram showing possible photochemical processes occurring in the bimetallocene-porphyrin triad [Cc-P(Zn)-Fc]⁺. Abbreviations: CR = charge recombination, CSh = charge shift, EnT = energy transfer, IC = internal conversion, ISC = intersystem crossing, P = P(Zn), T = triplet recombination.

1. Via radiative relaxation ($h\nu'_1$ and $h\nu'_2$; Figure 2), to the S_0 ground state/recombination under light emission (fluorescence). The attachment of a cobaltocenium substituent to a porphyrin shows an effective quenching of the fluorescence by 99.6 %,[10,26] a ferrocene substituent yields in an effective quenching of 92.9 to 99.2 %, depending on the *meso* substitution of the porphyrin.[9,33] Cobaltocenium

acts as effective electron acceptor and ferrocene as effective electron donor, hence fluorescence can be neglected for the following discussion.

2. Via energy transfer (EnT), the lowest electronically excited state ($^1A_{1g}$ → a^3E_{1g}, $(e_{2g})^4(a_{1g})^1(e_{1g})^1$)) of cobaltocenium (1.61 eV) and ferrocene (1.98 eV) can be populated (Figure 2).[34] The EnT from the porphyrin excited states to these metallocene orbitals is spin- and dipole-forbidden, therefore the efficiency is low and the EnT can be disregarded for this discussion.[26] The population of the singlet $^1E_{1g}$ state of the metallocenes is also possible, but for cobaltocenium irrelevant (3.0 eV).[34] For ferrocene, the $^1E_{1g}$ state owns an energy of around 2.6 eV[34] (not depicted) and is in principle accessible from the S_2 state. A radiationless-relaxation via EnT via ferrocene is feasible.[35–37]

3. Via electron transfer (CSh1/CSh3/CSh5; Figure 2) from ferrocene to the porphyrin, ferrocenium and a porphyrinato radical anion are formed.[9] The porphyrinato radical anion is able to reduce the cobaltocenium cation (CSh7),[26] resulting in the charge shifted product Cc-P(Zn)-Fc$^+$. The Cc$^+$-P(Zn)$^-$-Fc$^+$ state can be placed between 1.37 and 1.48 eV depending on the substitution pattern.[9,10] Charge recombination (CR2) to give the ground state is possible.[9]

4. Via electron transfer (CSh2/CSh4/CSh6; Figure 2) from the porphyrin S_1/S_2 state to cobaltocenium, cobaltocene and a porphyrin radical cation are formed.[26] The porphyrin radical cation can be reduced by ferrocene (CSh8),[9] resulting in the charge shifted product Cc-P(Zn)-Fc$^+$. The Cc-P(Zn)$^+$-Fc state can be placed at 1.41 eV.[26] Also in here, charge recombination (CR1) to give the ground state is possible.[26]

5.Via intersystem crossing (ISC; Figure 2), the porphyrin triplet state can be populated at around 1.6 eV.[38–40] From this point the charge-shifted/charge-separated states ^{3}[Cc-P(Zn)$^+$-Fc] and ^{3}[Cc$^+$-P(Zn)$^-$-Fc$^+$] are available. For the charge-shifted/charge-separated triplet states, the interactions of the spin centers can be neglected due to their large distance, so the energy is similar to those of the corresponding singlet states.

Due to the Rehm-Weller equation,[41,42] the energy of the charge shifted states relative to the ground state can be calculated from the redox potentials. Using −0.08 eV for the ferrocene/ferrocenium substituent[10] and −1.05 eV for the cobaltocene/cobaltocenium couple,[26] the energy of the charge shifted state Cc-P(Zn)-Fc$^+$ can be placed at 0.97 eV. In this calculation, the Coulomb term can be neglected due to a charge shift instead of a charge separation. Equally, the energy of the charge-separated state Cc$^+$-P(Zn)$^-$-Fc$^+$ can be calculated. By adding the coulomb term $-e_0^2/[4\pi\varepsilon_0\varepsilon(CH_2Cl_2)r]$ (0.126 eV) with $\varepsilon(CH_2Cl_2)$ = 8.934[43] and r_{Zn-Fe} = 12.8 Å (estimated by DFT calculations see Figure 4), the

energy of the charge-separated state Cc$^+$-P(Zn)$^-$-Fc$^+$ can be calculated as 1.37 eV and 1.48 eV, depending on the substitution pattern.[9,10]

Which excited state is populated first, Cc-P(Zn)$^+$-Fc or Cc$^+$-P(Zn)$^-$-Fc$^+$, is given by comparison of the excited states properties of the dyads Cc$^+$-P(Zn) and P(Zn)-Fc. The rate constant for the PET from P(Zn) to Cc$^+$ (k_{CSh4}) is calculated as 5.8 x 10^9 s^{-1} for a phenyl substituted zinc porphyrin.[26] For the P(Zn)-Fc dyad, the rate constant of the PET (k_{CSh3}) from Fc to P(Zn) is given as 6.80 x 10^9 s^{-1} for a mesityl substituted porphyrin and 76.41 x 10^9 s^{-1} for a pentafluoridophenyl substituted porphyrin.[9] Regardless of the porphyrin substitution pattern, the reductive quenching by ferrocene is faster than the reduction of the cobaltocenium (Figure 3). Therefore, the electron transfer cascade via CSh3 and CSh7 should be favored over the CSh4 and CSh8 path.
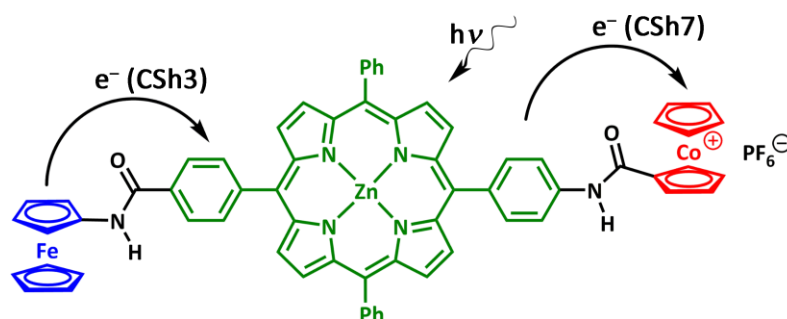
Figure 3. Biomimetic triad with ferrocene as electron donor, zinc(II) porphyrin as chromophore and spacer, cobaltocenium hexafluoridophosphate as electron acceptor and amide bridging ligands.

DFT calculations (Figure 4) show for a cobaltocenium-porphyrin dyad a cobalt to zinc distance of 12.9 Å, which is comparable to the distance of 12.5 Å determined from a crystal structure.[26] For the cobaltocenium-porphyrin-ferrocene triad, an iron to zinc distance of 13.0 Å, a cobalt to zinc distance of 13.0 Å and a cobalt to iron distance of 25.9 Å were calculated. The use of porphyrin as a spacer doubles the overall ET distance between the electron donor and acceptor. Additionally, the DFT calculated spin densities of the charge-shifted triplet state (Figure 4) show for the cobaltocenium-porphyrin dyad spin density localized on the *meso* carbon atoms of the porphyrin. Thus the distance, which has to be overcome for a charge recombination, is drastically reduced compared to the final charge shifted state of the triad (Cc-P(Zn)-Fc$^+$). So the lifetime of the charge shifted state should be prolonged resulting in a higher chance of a further reaction.
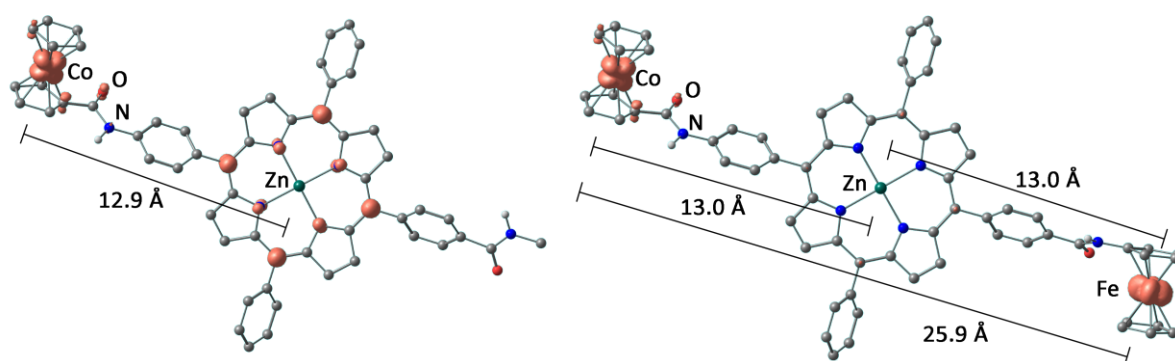
Figure 4. DFT optimized geometry and calculated spin density of the ³CSh state of a cobaltocenium-porphyrin dyad (left) and a cobaltocenium-porphyrin-ferrocene triad (right) in orange (isosurface value at 0.01 a.u.); CH hydrogen atoms omitted; B3LYP/ZORA-def2-SV(P). The measurements of the distances start/end from/at the center of the subunit.

The bimetallocene porphyrin triad [Cc-CONH-P(Zn)-CONH-Fc][PF₆] has not yet been fully characterized. Therefore, unsuccessful syntheses and incomplete characterization data of all intermediate products are described here. Experimental details are given in the supplemental information (Chapter 5.3). [Cc-CONH-P(Zn)-CONH-Fc][PF₆] will be named as "triad" **1[PF₆]** in the following.

3.3.2   Attempted Synthesis via Ester Cleavage

The synthesis of the triad **1[PF₆]** (Figure 5) started from the cobaltocenium-porphyrin dyad [Cc-CONH-P(Zn)-COOCH₃][PF₆] **A[PF₆]**.[26] The ester group should be cleaved to form the free carboxylic acid [Cc-CONH-P(Zn)-COOH][PF₆] **B[PF₆]**. After activation of the carboxylic acid by formation of acyl chloride **C[PF₆]**, [Cc-CONH-P(Zn)-CONH-Fc][PF₆] **1[PF₆]** should be formed by coupling with aminoferrocene.
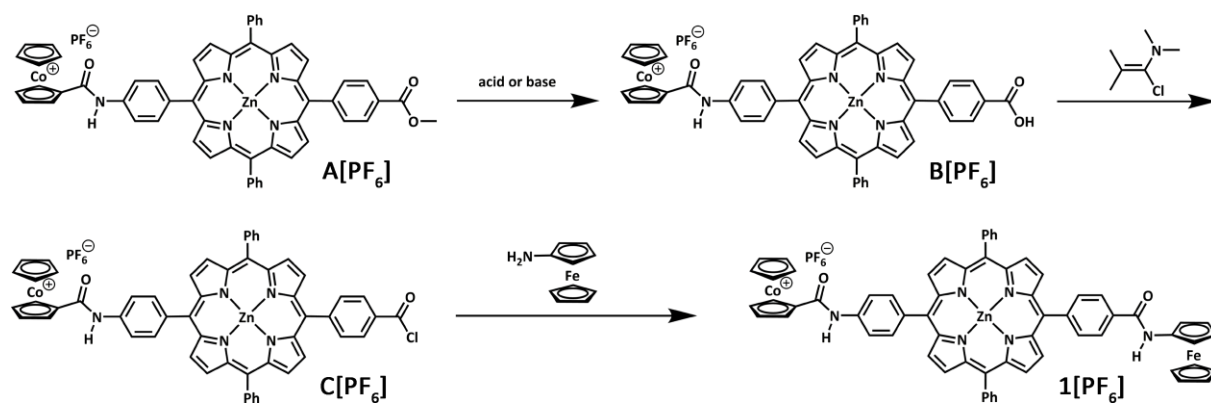
Figure 5. Attempts to synthesize the cobaltocenium-ferrocene-porphyrin triad via ester cleavage.

The cleavage of the ester group of **A⁺** was attempted with potassium hydroxide in methanol at room temperature (r.t.), and sulfuric acid in dimethyl sulfoxide at 95 °C. In both cases, ¹H NMR spectroscopy of the products showed a decreased intensity ratio between the resonances of the Cc⁺ group and the porphyrin core, whereby the intensity ratio between the resonances of the porphyrin core and the methyl group remained unperturbed. Using sulfuric acid in methanol at 50 °C, ¹H NMR spectroscopy of the product showed an unperturbed ratio between the porphyrin core and the methyl group. In all

cases the amide bond was cleaved instead of the ester group, or the starting material A^+ remained unreacted (Chapter 5.3.1) The splitting of the amide bond between Cc^+ and the porphyrin is favored over the ester cleavage due to the negative inductive effect of the cobaltocenium cation.

3.3.3 Attempted Synthesis via Boc Protection

The deprotection of the carboxylic acid **A[PF$_6$]** following the attachment of the cobaltocenium amide to the porphyrin was not successful. Therefore, the synthesis of the triad was started from amino porphyrin H$_2$N-P(Zn)-COOCH$_3$ **D**. The use of porphyrin amino acid H$_2$N-P(Zn)-COOH without protection of the amino group would lead to a reaction of the amino and the activated carboxylic acid group, resulting in an oligopolymerization. So the amino group should be protected via a *tert*-butyloxycarbonyl (Boc) group, which is stable against bases, but labile against acids. After protecting the amino group of the porphyrin to give **E1/E2**, the ester should be cleaved (**F1/F2**) and the ferrocene substituent should be attached, forming **G1/G2**. In the final steps, the Boc group should be cleaved (**H**), the cobaltocenium substituent be attached to the porphyrin and metalation of the porphyrin and anion exchange yields in **1[PF$_6$]**.
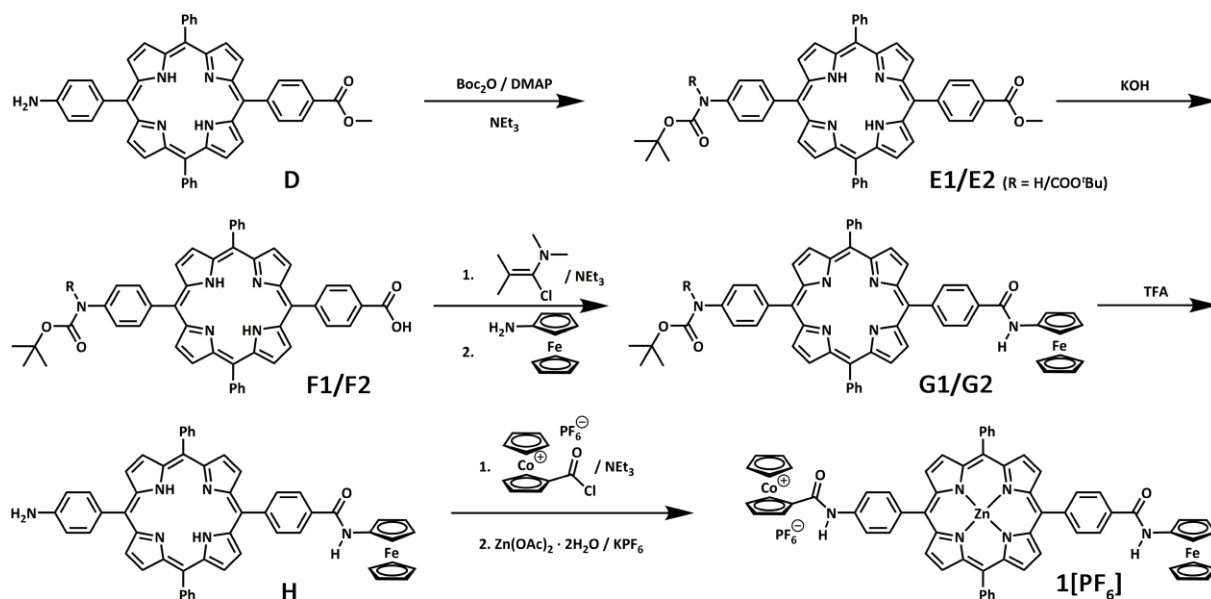
Figure 6. Attempts to synthesize the cobaltocenium-ferrocene-porphyrin triad via Boc protection.

The initial route was started from H$_2$N-P(2H)-COOH. In three different attempts, di-*tert*-butyl carbonate and base were added and the solution was sonicated or heated, respectively.[44] In one case, mass spectrometry of the crude solution showed peaks for the Boc (Boc-NH-P(2H)-COOH) protected porphyrin. Mass spectrometry after purification did only show peaks for the isocyano (OCN-P(2H)-COOH) protected porphyrin. An isocyano group is the decomposition product of a Boc protection group. In all cases, no product could be isolated in the end. So the synthesis was started from H$_2$N-P(2H)COOCH$_3$ **D** (Figure 6). In tetrahydrofuran, di-*tert*-butyl carbonate and triethylamine were added and the solution was heated at 45 °C. The reaction was not successful. Hence, the excess of the

carbonate was increased from 1.3 to 24 equivalents (eq) and the solution was heated up 66 °C (reflux). TLC control showed a mixture of product **E1/E2** and starting material **D**, so 4-(dimethylamino)pyridine was added as a catalyst. After full consumption of **D**, the product **E1/E2** was purified by column chromatography. A purple powder with a yield of 82 % was obtained. ^{1}H NMR resonances could be assigned to the doubly Boc protected product Boc$_2$N-P(2H)-COOMe **E2** (Chapter 5.3.2). Nevertheless it should be considered that the activation conditions (-COOH to -COCl) during the ongoing procedure could be too acidic for the withstand of the protection group, so that the Boc groups of **F1/F2** will be cleaved. The reaction scheme was discarded.

3.3.4 Attempted Synthesis via Benzyl Protection

Starting from H$_2$N-P(2H)-COOMe **D**, the amino group should be protected by a benzyl protection group (Bn) to form Bn-HN-P(2H)-COOMe **I1**.[45] After the cleavage of the ester (**J1**), the ferrocene substituent should be attached (**K1**) and the benzyl group removed via reduction (**H**). Finally, the cobaltocenium should be added via amide bonding (Figure 7).
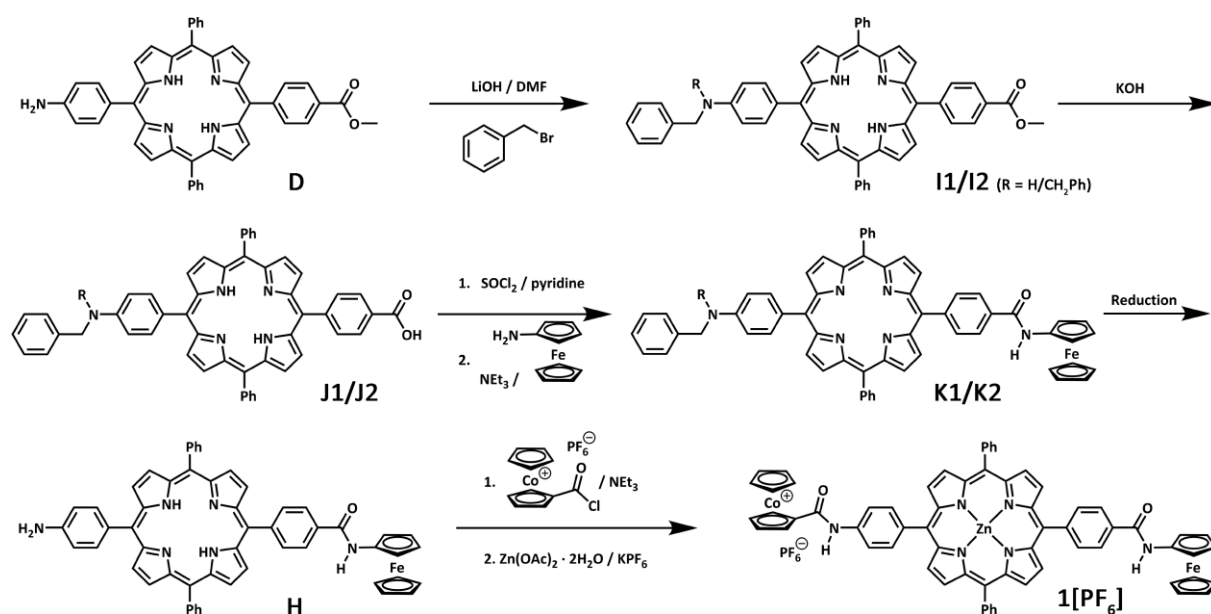
Figure 7. Attempts to synthesize the cobaltocenium-ferrocene-porphyrin triad via benzyl protection group.

H$_2$N-P(2H)-COOCH$_3$ **D** was added to a suspension of lithium hydroxide, molecular sieve and dimethylformamide. After dissolution of the porphyrin – benzyl bromide was added. When TLC control showed full consumption of the porphyrin **D**, the reaction was stopped and the products **I1/I2** were purified by column chromatography. The synthesis of the benzyl protected aminoporphyrin Bn-NH-P(2H)-COOMe **I1** was successful with a yield of 9.7 %. In a side reaction, the second amino hydrogen was also removed by another benzyl group (**I2**). Bn$_2$N-P(2H)-COOCH$_3$ **I2** was obtained with a yield of 44 %. Both products were characterized by ^{1}H NMR spectroscopy and FD mass spectrometry (Chapter 5.3.3). The ^{1}H NMR spectra show four main differences from mono to doubly benzylation. The resonances of the two different protons next to the amino group shifted to lower field by 0.33 ppm

(H^{22}) and 0.08 ppm ($H^{5.3}$). Additionally two separated resonances for the benzyl group merged together forming a multiplet and the amino proton resonance vanished.

In the next step, Bn-NH-P(2H)-COOMe **I1** and Bn_2N-P(2H)-COOMe **I2** were separately dissolved in tetrahydrofuran and potassium hydroxide was added. The solutions were heated to 66 °C until TLC control showed no remaining starting material. To yield the benzyl protected porphyrin amino acids Bn-NH-P(2H)-COOH **J1** and Bn_2N-P(2H)-COOH **J2** (66 %), the solutions were acidified with acetic acid and extracted with dichloromethane. **J1** and **J2** were characterized by ^{1}H NMR spectroscopy and ESI$^+$ mass spectrometry (Chapter 5.3.3). The ^{1}H NMR spectra did not show considerable changes, except the vanishing of the resonance of the cleaved methyl group.

For the coupling of porphyrin with aminoferrocene, the carboxylic acid group was transformed to the acid chloride. Bn-NH-P(2H)-COOH **J1**, pyridine and thionyl chloride were dissolved in toluene. After around 4 hours, the solvents were removed under reduced pressure. The remaining solid was dissolved in toluene, triethylamine and aminoferrocene were added. After 18 hours, the product was purified by column chromatography, resulting in a purple powder (>20 % yield). Bn-NH-P(2H)-CONH-Fc **K1** was characterized by ^{1}H NMR spectroscopy and FD mass spectrometry (Chapter 5.3.3). The resonances for the amidoferrocene protons are given at 4.15, 4.30, 4.87 and 7.63 ppm (H^{23}, H^{24}, H^{25}, amide), respectively.

For the deprotection of the amino group, the benzyl group should be removed by reduction with H_2 on palladium. Bn-NH-P(2H)-CONH-Fc **K1** and palladium on activated carbon were dissolved/suspended in methanol. The solution was degassed by "freeze pumping" and the evacuated flask was filled with hydrogen. TLC control showed a new spot, so the activated carbon was removed by filtration. ESI$^+$ mass spectrometry showed a signal intensity of 1.3 % for H_2N-P(2H)-CONH-Fc **H**. More prominent, signals for Bn-NH-P(2H)-CH(OH)NH_2 were observed with an intensity of 100 % (Figure S 12, Chapter 5.3.3), the product of the hydrogenation of the amide bond. The reduction of the amide bond is clearly favored over the cleavage of the benzyl group. No product was isolated.

In another attempt, hydrogen as reducing agent was exchanged with formic acid. The formic acid was added to the porphyrin **K1**/palladium suspension and immediately, the color changed from purple to green (porphyrin protonation) and 5 seconds later to yellow/red. The palladium was filtered off and the mass spectrometry showed mainly Bn-NH-P(2H)-CH(OH)NH_2 and several unidentified byproducts.

The introduction of the benzyl protection group worked well. Yet, difficulties in the deprotection of the porphyrin **K1** forbid the use of the complex for further reactions. The reduction of the amide bond is preferred towards the cleavage of the benzyl protection group.

3.3.5 Synthesis of the Triad via Fmoc Protection

Starting from porphyrin amino acid H_2N-P(2H)-COOH **L**, the amino group should be protected by a fluorenylmethyloxycarbonyl (Fmoc) group (**M**).[46–48] This group is stable against acids and weak bases, but labile against secondary amines such as piperidine. Following the protection of the amino group, aminoferrocene can be connected by amide coupling and the Fmoc group can be cleaved by the addition of piperidine (**H**). Carboxycobaltocenium hexafluoridophosphate can be inserted as acid chloride. Metalation of the porphyrin and anion exchange complete the scheme (**1[PF$_6$]**) (Figure 8).
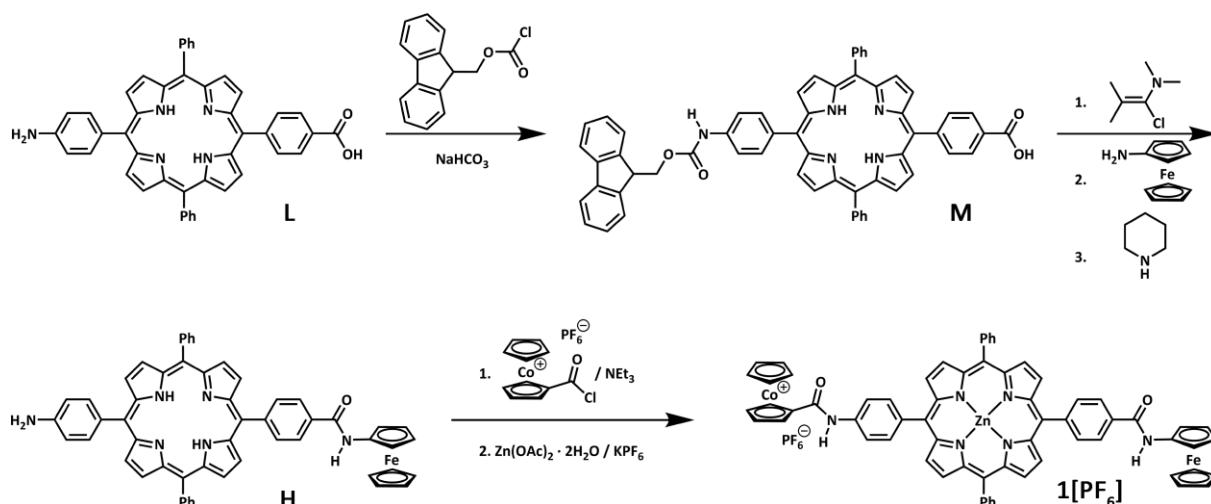
Figure 8. Synthesis of the cobaltocenium-ferrocene-porphyrin triad via Fmoc protection group.

Porphyrin amino acid **L** was dissolved in absolute dioxane, sodium bicarbonate and Fmoc-Cl were added and after one hour, water was added. The weak base was added to deprotonate the carboxylic acid to prevent additional side reactions of this group. After all starting material was consumed (TLC control), the solvent was removed, the product **M** dissolved in dichloromethane and washed with a water/acetic acid mixture. The crude product **M** was purified by column chromatography. This purification procedure on a silica column is sensitive to protonation/deprotonation. By adding triethylamine, the product is deprotonated and sticks on the column material. Excess of acetic acid lead to the protonation of the porphyrin backbone observed by a drastic color change into green of the solution. Additionally, by switching from triethylamine as additive in the solvent to acetic acid, an ionic liquid ([HNEt$_3$][OAc]) is formed, resulting in a mixing of the different components on the column. The product solution has to be washed with water to remove the ionic liquid, resulting in a purple powder with a yield of 63 % The product **M** was characterized by HR-ESI[+], ^{1}H NMR, ^{13}C NMR, ^{1}H^{1}H COSY and ^{1}H^{13}C HMBC (Chapter 5.3.4.1).

For the activation of the carboxylic acid as acid chloride, Fmoc protected porphyrin **M** was dissolved in absolute dichloromethane and Ghosez's reagent was added. The solution was refluxed and the solvent removed under reduced pressure. The solid was washed with absolute dichloromethane and the solvent was again removed to clear remaining Ghosez's reagent. The solid was dissolved in

dichloromethane and aminoferrocene was added. After the porphyrin was consumed (TLC control), piperidine was added in situ to cleave the Fmoc protection group. After consumption of the intermediate product **M**, acetic acid was added to neutralize the base and to protect the peptide bond. The solvent was removed, the product **H** dissolved in dichloromethane and washed with water. The crude product **H** was purified by column chromatography resulting in a yield of 98 %. **H** was characterized by HR-ESI[+], ^{1}H NMR and ^{13}C NMR (Chapter 5.3.4.2).

Carboxycobaltocenium hexafluoridophosphate and Ghosez's reagent were dissolved in absolute dichloromethane for the activation of the carboxylic acid group of Cc[+]. The solvent was removed under reduced pressure. The solid was suspended in dichloromethane, triethylamine and porphyrin-ferrocene dyad **H** were added. ESI[+] mass spectrometry verified the formation of [Cc-CONH-P(2H)-CONH-Fc][+] (*m/z*: obs. 1071.29; calcd. 1071.25). The solution was washed with water to remove cobaltocenium salts, potassium hexafluoridophosphate and zinc acetate were added to metalate the porphyrin and exchange the counter ion. Via UV/vis spectroscopy, the successful metalation of the porphyrin forming **1[PF$_6$]** was verified due to the absence of free base porphyrin. ^{1}H NMR spectroscopy showed resonances for several different porphyrins. Column chromatography on silica or alumina oxide was not successful due to decomposition or sticking on the column material. By using Supelite DAX-8 polymer beads, the separation of the porphyrins was achieved. Using nonpolar solvents such as toluene, the charged triad **1[PF$_6$]** remains on the column material and can be eluted with methanol (yield: 35 %; 35 mg). ^{1}H NMR spectroscopy (Figure 9) showed a "clean porphyrin area", but still remaining impurities in the aliphatic region. Ferrocene shows resonances at 4.06 (H[23]), 4.25 (H[24]) and 4.97 ppm (H[22]), respectively. These values are typical for zinc porphyrin bonded ferrocene dyads in deuterated tetrahydrofuran[9], just varying by 0.02 ppm.
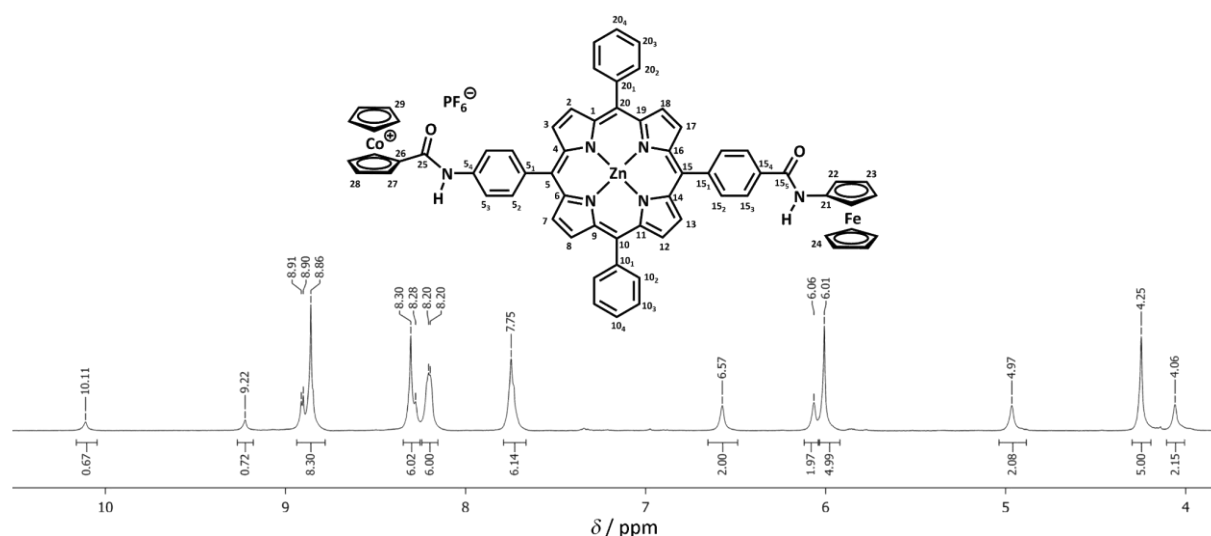
Figure 9. ^{1}H NMR spectrum of the triad [Cc-CONH-P(Zn)-CONH-Fc][PF$_6$] 1[PF$_6$] in *d$_8$*-tetrahydrofuran.

The resonances for the cobaltocenium substituent are given at 6.01 (H[29]), 6.06 (H[28]) and 6.57 ppm (H[27]). The known zinc(II) porphyrin-cobaltocenium dyad displays resonances at 5.84 (H[28]), 5.89 (H[29]), and 6.55 ppm (H[27]) for the cobaltocenium substituent in deuterated dichloromethane and 6.17 (H[29]), 6.19 (H[28]) and 6.68 ppm (H[27]) in deuterated acetone, respectively.[26] The resonances of the cobaltocenium substituent of the triad shows values, which are between the resonances of the two dyad measurements. This is feasible, because tetrahydrofuran has a polarity between acetone and dichloromethane[43] resulting in minor shifts. Resonances of the amide protons are shown at 9.22 ppm for the ferrocene amide and at 10.11 ppm for the cobaltocenium amide. Both resonances are in accord with those of the reference dyads at 9.22 and 10.32 ppm, respectively.[9,26] To be mentioned, at 10.87 ppm, an unknown resonance was observed with an integral of 0.11 ppm. Possibly a special hydrogen bond is formed in here, which is different from the amide-hexafluoridophosphate NH•••F ion-pairs known from the cobaltocenium porphyrin dyad.[26] Additional ^{31}P NMR spectroscopy was used to confirm the presence of the hexafluoride counter ion. The phosphorus resonance was detected at 144.0 ppm.

To remove the remaining impurities, the purple solid **1[PF₆]** was sonicated in pentane and the solvent including the impurities was removed by filtration. Unfortunately, the proton NMR spectrum (Figure 10) showed the removal of the ferrocene resonances. Due to the destruction of the triad, a further characterization was not possible.
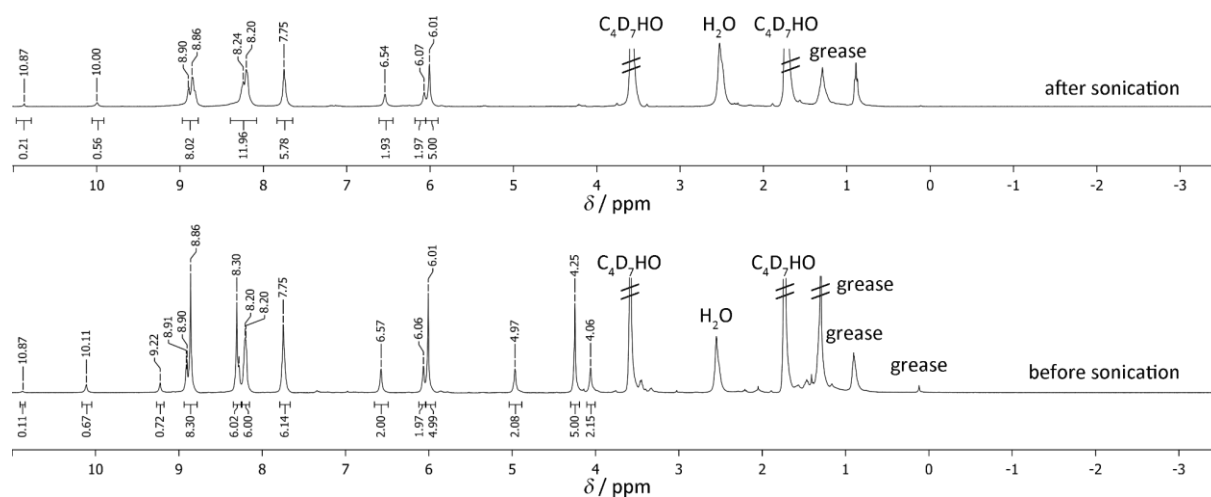
Figure 10. ¹H NMR of the triad [Cc-CONH-P(Zn)-CONH-Fc][PF₆] 1[PF₆] before and after sonication, in *d₈*-tetrahydrofuran.

3.3.6 Conclusion and Outlook

The synthesis of the triad [Cc-CONH-P(Zn)-CONH-Fc][PF₆] **1[PF₆]** was successful using fluorenylmethyl-oxycarbonyl as protection group. The usage of polymer beads for column chromatography allows the purification of the triad **1[PF₆]**, whereby the triad has to be handled carefully. DFT calculations and excited state properties of model dyads predict a ferrocene to porphyrin electron transfer (reductive

quenching), followed by the reduction of the cobaltocenium substituent. This should yield the reactive charge-shifted intermediate Cc-CONH-P(Zn)-CONH-Fc$^+$ **1[PF$_6$]** with an elongated lifetime.

The synthesis of the triad will allow to determine their properties, for example via time-resolved fluorescence, steady state emission, transient absorption pump-probe spectroscopy and cyclic voltammetry. Further, hydrogen-evolving experiments by electrocatalysis or photocatalysis should be possible.

3.3.7   References

[1]   Kealy, T. J., Pauson, P. L., *Nature* **1951**, *168*, 1039–1040.

[2]   Miller, S. A., Tebboth, J. A., Tremaine, J. F., *J. Chem. Soc.* **1952**, 632–635.

[3]   Astruc, D., *Eur. J. Inorg. Chem.* **2017**, 6–29.

[4]   Heinze, K., Lang, H., *Organometallics* **2013**, *32*, 5623–5625.

[5]   Okuda, J., *Eur. J. Inorg. Chem.* **2017**, *2017*, 217–219.

[6]   Štěpnička, P., *Eur. J. Inorg. Chem.* **2017**, *2017*, 215–216.

[7]   Thornton, N. B., Wojtowicz, H., Netzel, T., Dixon, D. W., *J. Phys. Chem. B* **1998**, *102*, 2101–2110.

[8]   Kubo, M., Mori, Y., Otani, M., Murakami, M., Ishibashi, Y., Yasuda, M., Hosomizu, K., Miyasaka, H., Imahori, H., Nakashima, S., *Chem. Phys. Lett.* **2006**, *429*, 91–96.

[9]   Melomedov, J., Ochsmann, J. R., Meister, M., Laquai, F., Heinze, K., *Eur. J. Inorg. Chem.* **2014**, 2902–2915.

[10]   Melomedov, J., Ochsmann, J. R., Meister, M., Laquai, F., Heinze, K., *Eur. J. Inorg. Chem.* **2014**, 1984–2001.

[11]   Imahori, H., Guldi, D. M., Tamaki, K., Yoshida, Y., Luo, C., Sakata, Y., Fukuzumi, S., *J. Am. Chem. Soc.* **2001**, *123*, 6617–6628.

[12]   Imahori, H., Tamaki, K., Araki, Y., Sekiguchi, Y., Ito, O., Sakata, Y., Fukuzumi, S., *J. Am. Chem. Soc.* **2002**, *124*, 5165–5174.

[13]   Imahori, H., Sekiguchi, Y., Kashiwagi, Y., Sato, T., Araki, Y., Ito, O., Yamada, H., Fukuzumi, S., *Chem. Eur. J.* **2004**, *10*, 3184–3196.

[14]   Winters, M. U., Dahlstedt, E., Blades, H. E., Wilson, C. J., Frampton, M. J., Anderson, H. L., Albinsson, B., *J. Am. Chem. Soc.* **2007**, *129*, 4291–4297.

[15]   Wijesinghe, C. A., El-Khouly, M. E., Zandler, M. E., Fukuzumi, S., D'Souza, F., *Chem. Eur. J.* **2013**, *19*, 9629–9638.

[16]   Hanauer, K., Förster, C., Heinze, K., *Eur. J. Inorg. Chem.* **2018**, *31*, 3537-3547.

[17]   Hüttinger, K., Förster, C., Heinze, K., *Chem. Commun.* **2014**, *50*, 4285–4288.

[18]   Camara, J. M., Rauchfuss, T. B., *Nat. Chem.* **2011**, *4*, 26–30.

[19] Hatten, X. de, Bothe, E., Merz, K., Huc, I., Metzler-Nolte, N., *Eur. J. Inorg. Chem.* **2008**, 4530–4537.

[20] Correia-Ledo, D., Arnold, A. A., Mauzeroll, J., *J. Am. Chem. Soc.* **2010**, *132*, 15120–15123.

[21] Huesmann, H., Förster, C., Siebler, D., Gasi, T., Heinze, K., *Organometallics* **2011**, *31*, 413–427.

[22] Lauck, M., Förster, C., Heinze, K., *Organometallics* **2017**, *36*, 4968–4978.

[23] Siebler, D., Förster, C., Heinze, K., *Dalton Trans.* **2011**, *40*, 3558–3575.

[24] Gubin, S. P., Smirnova, S. A., Denisovich, L. I., *J. Organomet. Chem.* **1971**, *30*, 257–265.

[25] El Murr, N., Dabard, R., Laviron, E., *J. Organomet. Chem.* **1973**, *47*, C13-C16.

[26] Lauck, M., Förster, C., Gehrig, D., Heinze, K., *J. Organomet. Chem.* **2017**, *847*, 33–40.

[27] Koelle, U., Infelta, P. P., Graetzel, M., *Inorg. Chem.* **1988**, *27*, 879–883.

[28] Connelly, N. G., Geiger, W. E., *Chem. Rev.* **1996**, *96*, 877–910.

[29] Sheats, J. E., Rausch, M. D., *J. Org. Chem.* **1970**, *35*, 3245–3249.

[30] Knox, G. R., Munro, J. D., Pauson, P. L., Smith, G. H., Watts, W. E., *J. Chem. Soc.* **1961**, 4619–4624.

[31] Imahori, H., Tamaki, K., Guldi, D. M., Luo, C., Fujitsuka, M., Ito, O., Sakata, Y., Fukuzumi, S., *J. Am. Chem. Soc.* **2001**, *123*, 2607–2617.

[32] Kiyosawa, K., Shiraishi, N., Shimada, T., Masui, D., Tachibana, H., Takagi, S., Ishitani, O., Tryk, D. A., Inoue, H., *J. Phys. Chem. C* **2009**, *113*, 11667–11673.

[33] Melomedov, J., Wünsche von Leupoldt, A., Meister, M., Laquai, F., Heinze, K., *Dalton Trans.* **2013**, *42*, 9727–9739.

[34] Roginski, R. T., Moroz, A., Hendrickson, D. N., Drickamer, H. G., *J. Phys. Chem.* **1988**, *92*, 4319–4323.

[35] Araki, Y., Yasumura, Y., Ito, O., *J. Phys. Chem. B* **2005**, *109*, 9843–9848.

[36] Mansour, H., El-Khouly, M. E., Shaban, S. Y., Ito, O., Jux, N., *J. Porphyrins Phthalocyanines* **2007**, *11*, 719–728.

[37] Giasson, R., Lee, E. J., Zhao, X., Wrighton, M. S., *J. Phys. Chem.* **1993**, *97*, 2596–2601.

[38] Walters, V. A., Paula, J. C. de, Jackson, B., Nutaitis, C., Hall, K., Lind, J., Cardozo, K., Chandran, K., Raible, D., Phillips, C. M., *J. Phys. Chem.* **1995**, *99*, 1166–1171.

[39] Lim, G. N., Obondi, C. O., D'Souza, F., *Angew. Chem. Int. Ed.* **2016**, *55*, 11517–11521.

[40] Lim, G. N., Obondi, C. O., D'Souza, F., *Angew. Chem.* **2016**, *128*, 11689–11693.

[41] Rehm, D., Weller, A., *Isr. J. Chem.* **1970**, *8*, 259–271.

[42] Weller, A., *Z. Phys. Chem.* **1982**, *133*, 93–98.

[43] Lide, D. R., *CRC Handbook of Chemistry and Physics 84th Ed.*, CRC Press, Boca Raton, Florida, **2003**.

[44] Einhorn, J., Einhorn, C., Luche, J.-L., *Synlett* **1991**, 37–38.

[45] Cho, J. H., Kim, B.M., *Tetrahedron Letters* **2002**, *43*, 1273–1276.

[46] Reinhart, A., *trans-AB2C-Porphyrine : Synthese in Lösung und an der Festphase, Verkettung und photophysikalische Eigenschaften*. Dissertation, Universität Heidelberg, **2008**.

[47] Carpino, L. A., Han, G. Y., *J. Org. Chem.* **1972**, *37*, 3404–3409.

[48] Chang, C.-D., Waki, M., Ahmad, M., Meienhofer, J., Lundell, E. O., Haug, J. D., *Int. J. Peptide Protein Res.* **1980**, *15*, 59–66.

4   Summary and Outlook

The synthesis of *N*-cobaltocenium amides [Cc-NHCO-R]$^+$ of R = phenyl, ferrocenyl and cobaltoceniumyl was successful using cobaltocene amide [Cc-NH] as reactive agent. By electrochemical oxidation and reduction, respectively, different charged states of the amides were accessible and intervalence charge transfer bands for [Cc-CONH-Cc]$^+$ and [Fc-CONH-Cc]$^+$ observable. Hush analysis of the IVCT bands made the calculation of the electronic coupling element H_{AB} and a comparison with the homo- and heterobimetallocenes [Fc-CONH-Fc]$^+$ and [Cc-CONH-Fc]$^+$ possible. The four complexes belong to the Robin-Day class II and show similar reorganization energies λ. The electronic coupling α increases with the exchange of ferrocene by cobaltocene, due to a more beneficial orbital symmetry of the redox orbitals of cobaltocene. DFT calculations, NMR spectroscopy and crystal structures of the peptides prove the existence of hydrogen bonds between the amide proton and the counterion (NH•••F) in liquid and solid state. These hydrogen bonds are responsible for higher reorganization energies of the bimetallocene amides compared to bimetallocenes without amide bridge.

The reactive molecule cobaltocene amide [Cc-NH] was synthesized by deprotonation of cobaltocenium amine hexafluoridophosphate [CcNH$_2$][PF$_6$] with sodium hydride. Titration experiments prove the reversibility of the reaction and the temporary stability of the amide. NMR and infrared spectroscopy show a switch of the electronic structure from a zwitterionic amide to a neutral imine. Time-dependent DFT calculations indicate transitions with high LMCT character, which arise from the imino functional group and explain the intense red color of the compound.

The amide coupling of cobaltocenium carboxylic acid with a functionalized zinc(II) tetraphenylporphyrin ([Cc-CONH-P(Zn)][PF$_6$]) has been successful. The solid state structure shows a typical NH•••F hydrogen bonded contact ion pair. The porphyrin acts as biomimetic light harvesting pigment, which transfers one electron to the cobaltocenium substituent, observable via transient absorption spectroscopy. The energy of the charge-shifted state Cc-CONH-P(Zn)$^+$ was calculated from the redox potentials at 1.41 eV above the ground state Cc$^+$-CONH-P(Zn). The analysis of the transient absorption pump-probe spectroscopy also places other deactivation pathways, like the triplet states of the porphyrin or cobaltocenium, above the charge-shifted state. Therefore, population of the charge-shifted state is possible from the S$_1$, S$_2$ and T$_1$ states of the porphyrin, which rises the efficiency of the electron transfer and the lifetime of the charge-shifted state.

The synthesis of the amide-bridged triad ([Cc-CONH-P(Zn)-CONH-Fc][PF$_6$]), consisting of cobaltocenium as electron acceptor, zinc(II) porphyrin as chromophore and ferrocene as electron donor, was successful using the Fmoc protection group strategy. After the introduction of fluorenylmethyloxycarbonyl as amino protection group, the tetraphenylporphyrin "amino acid" was

linked with aminoferrocene. After cleavage of the protection group, cobaltocenium carboxylic acid hexafluoridophosphate was attached to the porphyrin. Metallation of the porphyrin with zinc(II) finalizes the synthesis. The usage of a polymer resin in column chromatography allowed the purification of the photosynthetic model complex.

In the future, the new substitution pattern of *N*-cobaltocenium peptides makes the preparation of homo cobaltocenium (Figure 34) and hetero cobaltocenium-metallocene oligopeptides possible. These foldamers are of high interest in applications like switchable redox-active foldameres and as conducting molecular wires. The electrochemical switch from an assumed rod conformation to a *zigzag* conformation by reduction of the cobaltocenium subunits enables the use as artificial muscles or molecular switches. Other applications are conceivable in the fields of sensing and ion separation, both relying on ionic interactions. Furthermore, these oligopeptides can help to determine the secondary structure of paramagnetic ferrocenium foldamers due to their diamagnetic properties in the oxidized state.
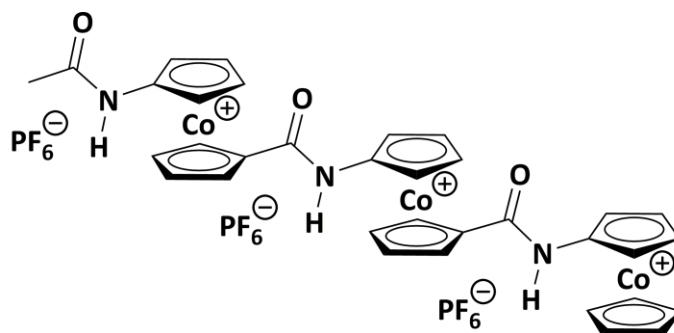
Figure 34. Peptide-bridged cobaltocenium peptide.

Considering redox-active polymers with linked cobaltocenium units, only minor changes for the adjustment of the redoxpotential are possible. Through the exchange of carboxycobaltocenium (ester or amide linkage) by aminocobaltocenium substituents (amide or amine linkage), the variability of the applicable redox potentials increases significantly (Figure 35).

The deprotonation of amino cobaltocenium hexafluoridophosphate yields a reactive cobaltocenium species, which acts as nucleophile. The nucleophilic substitution reactions with organic and organometallic nitro compounds or halides leads to secondary and tertiary amines. This allows the synthesis of substituted cobaltocenium compounds with fine-tuned redox potentials. Moreover, the synthesis of a dicobaltoceniumamine $[Cc_2N-R]^{2+}$ group is possible, which can act as electron trap or as bulky electron-withdrawing group (Figure 35).
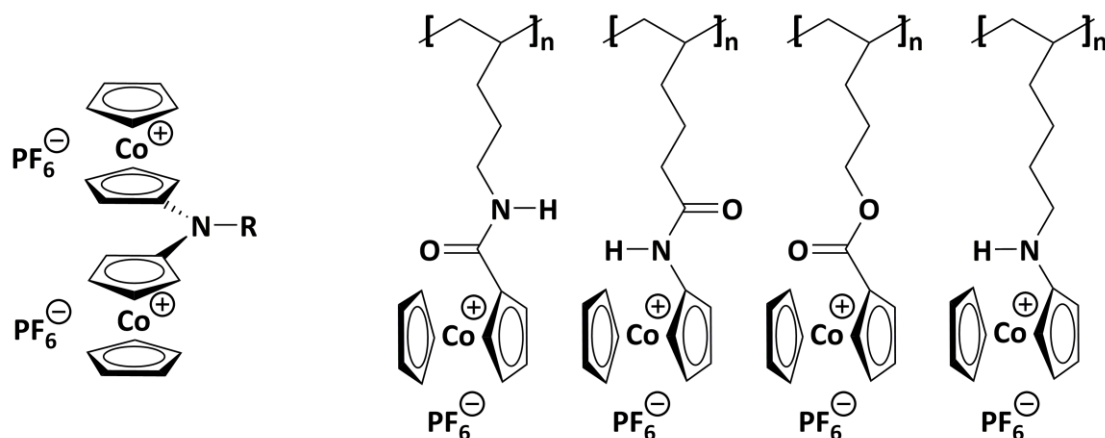
Figure 35. Dicobalteceniumamino group (left) and peptides with different cobaltoceniumsubstituents (right).

The characterization of the cobaltocenium-porphyrin peptide showed, that the photoinduced reduction of cobaltocenium by a porphyrin chromophore is successful. The exchange of the acidic amide-proton by methylation (Figure 36) of the nitrogen atom of the peptide bridge will lower the intramolecular reactivity and prevent reactions with cobaltocene. An electron-donating group, ferrocene, was amended to the cobaltocenium-chromophore dyad. The synthesis of the peptide-bridged triad was successful. DFT calculations and excited state properties of other model dyads allow to predict excited states properties of the biomimetic model complex. After excitation of the porphyrin, ferrocene transfers an electron to the porphyrin, filling the electron hole. Followed by the reduction of the cobaltocenium substituent, whereby cobaltocene as reactive intermediate is formed. The lifetime of this excited state will be prolonged compared to the previously synthesized dyads. The comparison of the triplet and singlet excited states will make the verification of the developed Jablonski diagram possible.
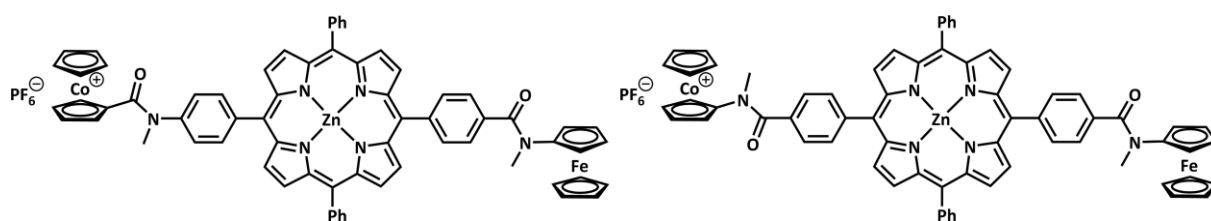
Figure 36. Biomimetic model complexes with directing methylated peptide bridges (left) and with inverse peptide bond (right).

An inversion of the peptide bridge between the cobaltocenium substituent and the porphyrin of the biomimetic model triad ([Cc-NHCO-P(Zn)-CONH-Fc][PF$_6$]), will significantly change the redox potential of the catalytically active substituent. Using cobaltocenium amide [CcNH], the synthesis of the inverse amide bridging direction is now within reach (Figure 36). The lowering of the redox potential of the cobaltocenium will increase the gap between the charge shifted state and the ground state of the model complex. This rises the reactivity of the cobaltocene and therefore the amount of achievable reactions. By adding a second chromophore to cobaltocenium, two electrons can be transferred to the

cobaltocenium subunit (Figure 37). By transferring two electrons to one reactive center, no second molecule is needed for a two-electron reaction. Additionally, it doubles the chance for the photoexcitation of at least one porphyrin.

All these improvements will make a photoinduced hydrogen evolution more probable.
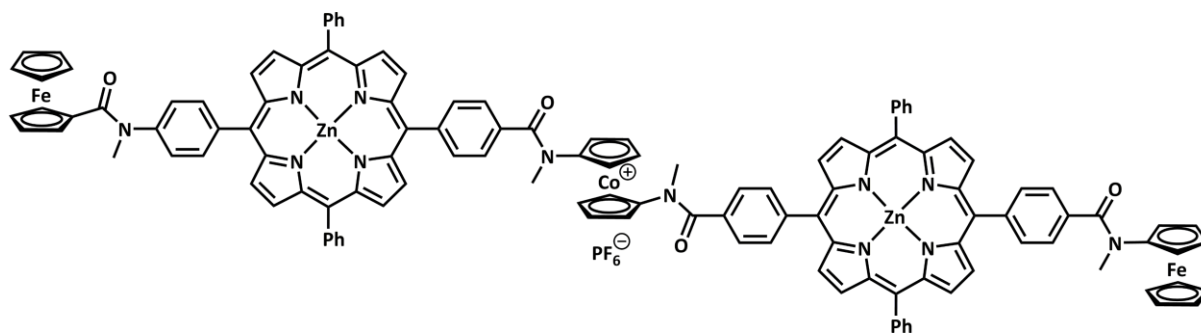
Figure 37. Photosynthesis model pentade with two chromophores.

5   Supporting Information

5.1   Supporting Information to Chapter 3.1: *N*-Cobaltocenium Amide as Reactive Nucleophilic Reagent for Donor-Acceptor Bimetallocenes

Maximilian Lauck, Christoph Förster and Katja Heinze

Organometallics **2017**, *36*, 4968–4978. Supporting Information
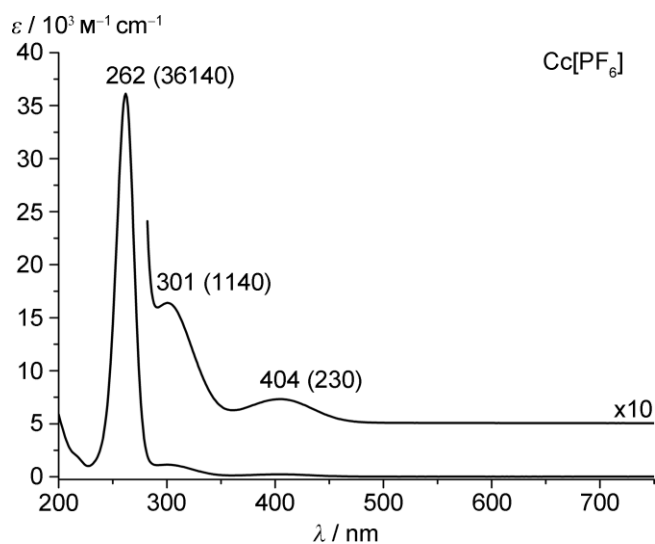
Figure S 1. Electronic spectrum of CcH[PF$_6$] in acetonitrile, maxima λ_{max} (ε) in nm (M^{-1} cm^{-1}).
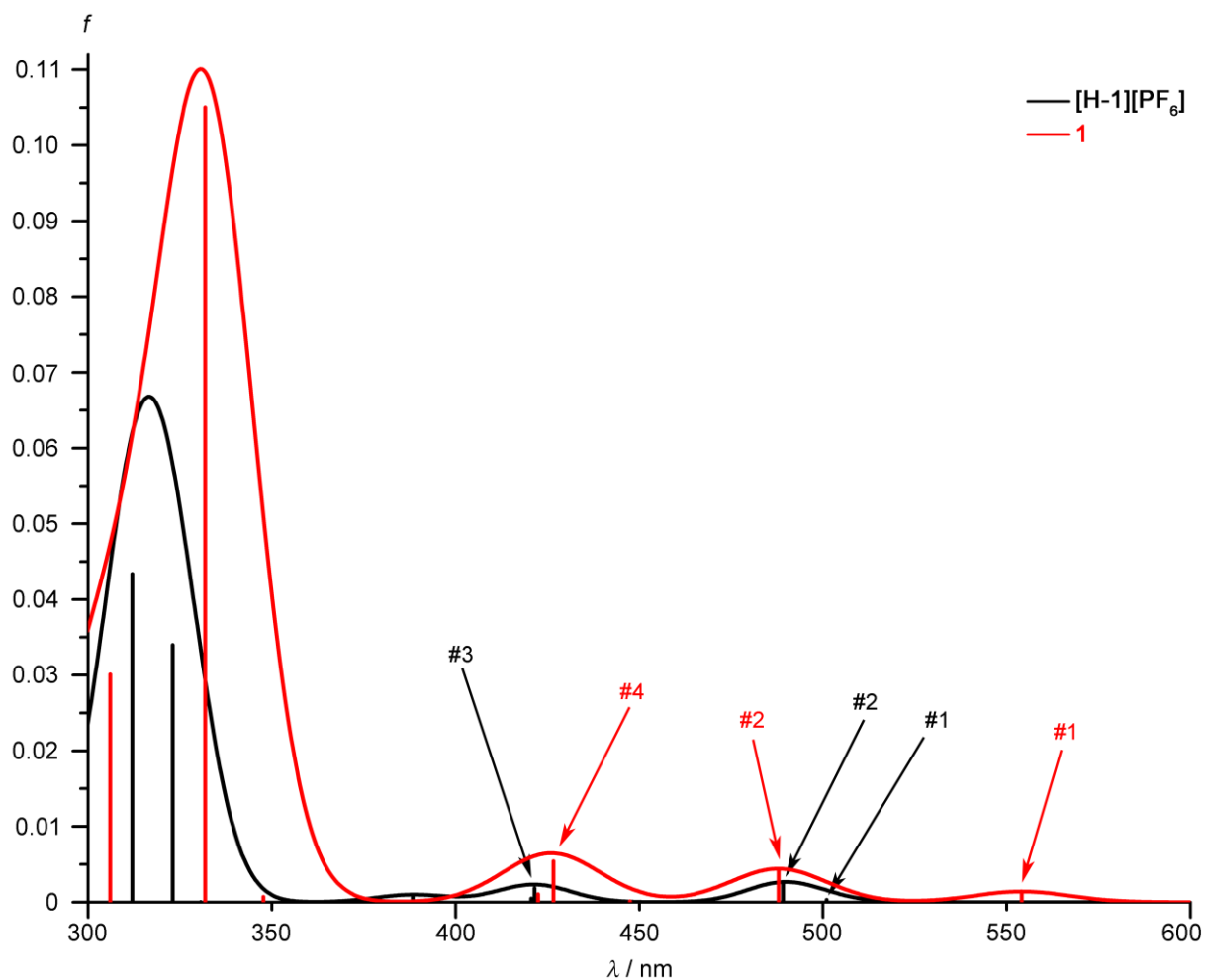
Figure S 2. TD-DFT calculated UV/vis spectra of [H-1]$^+$ (black) and 1 (red) (Gaussian line broadening).
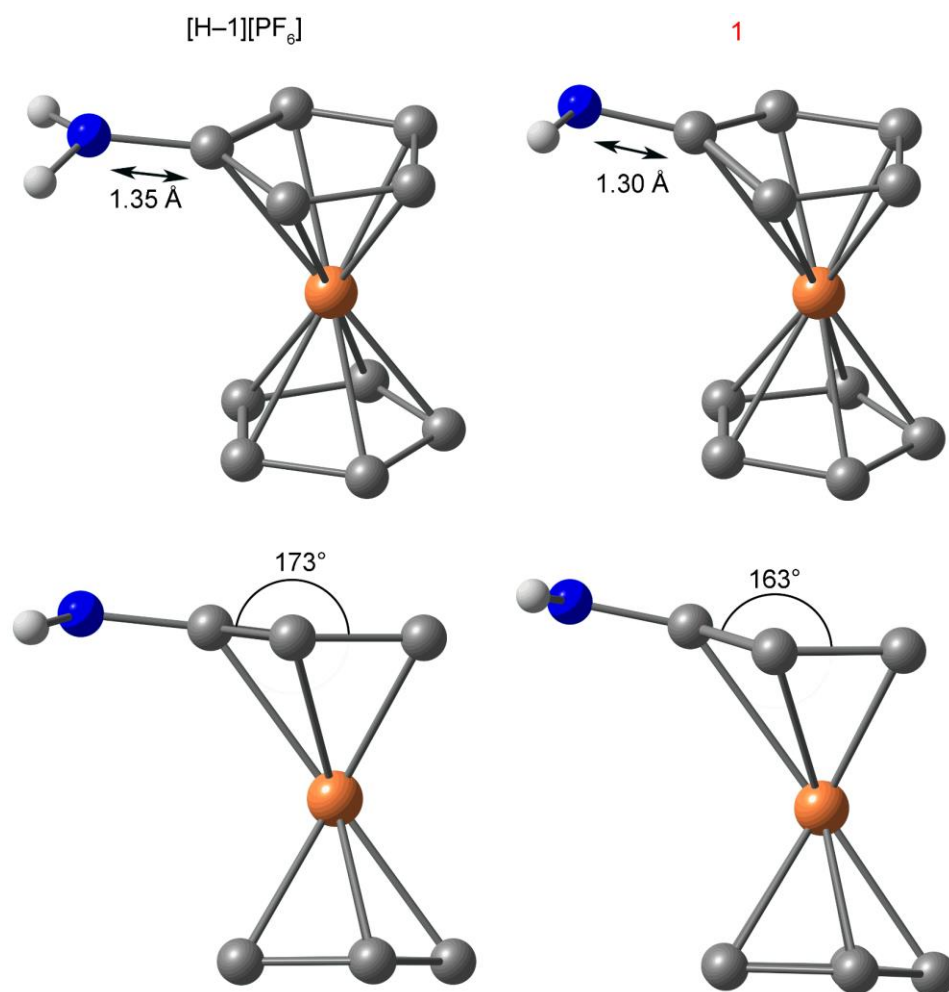
Figure S 3. DFT optimized structures of [H–1]+ and **1** (bottom: side view).
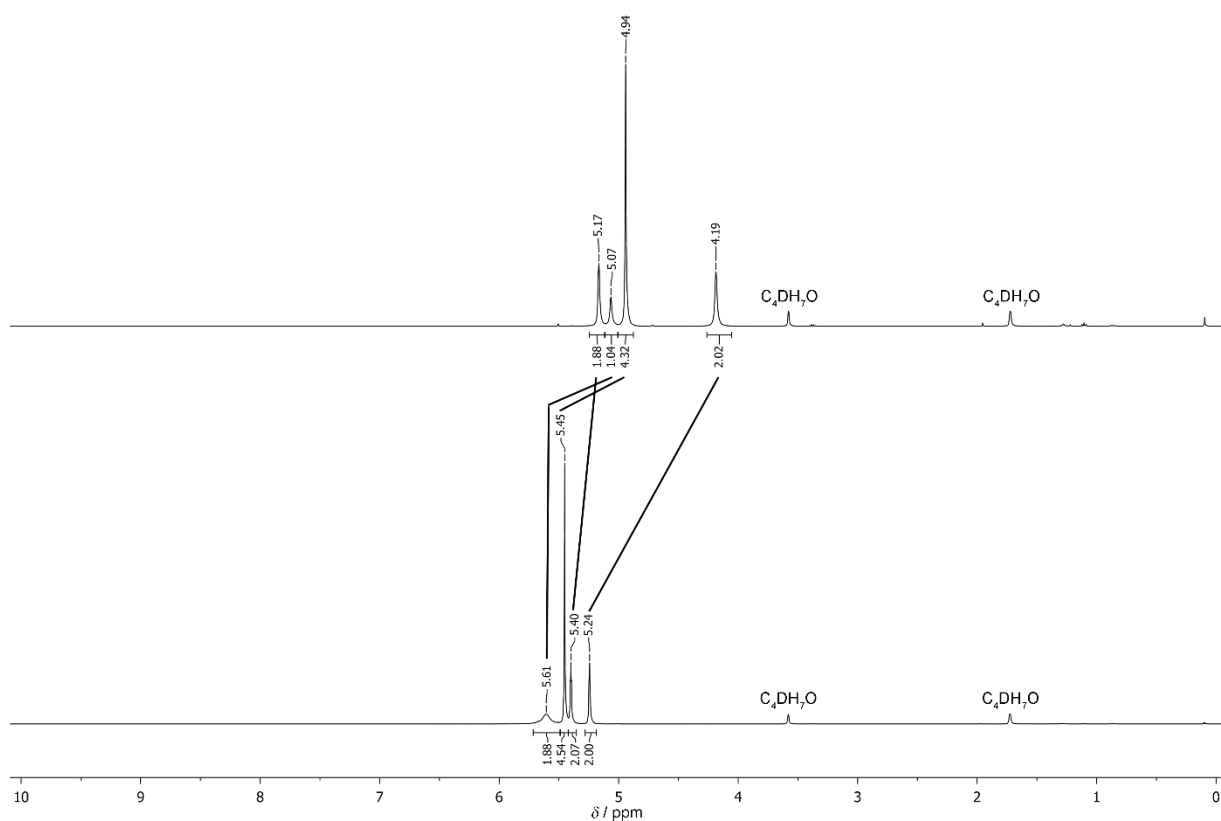
Figure S 4. ^{1}H NMR spectrum of [H-1][PF$_6$] (bottom) and 1 (top) in d$_8$-tetrahydrofuran.
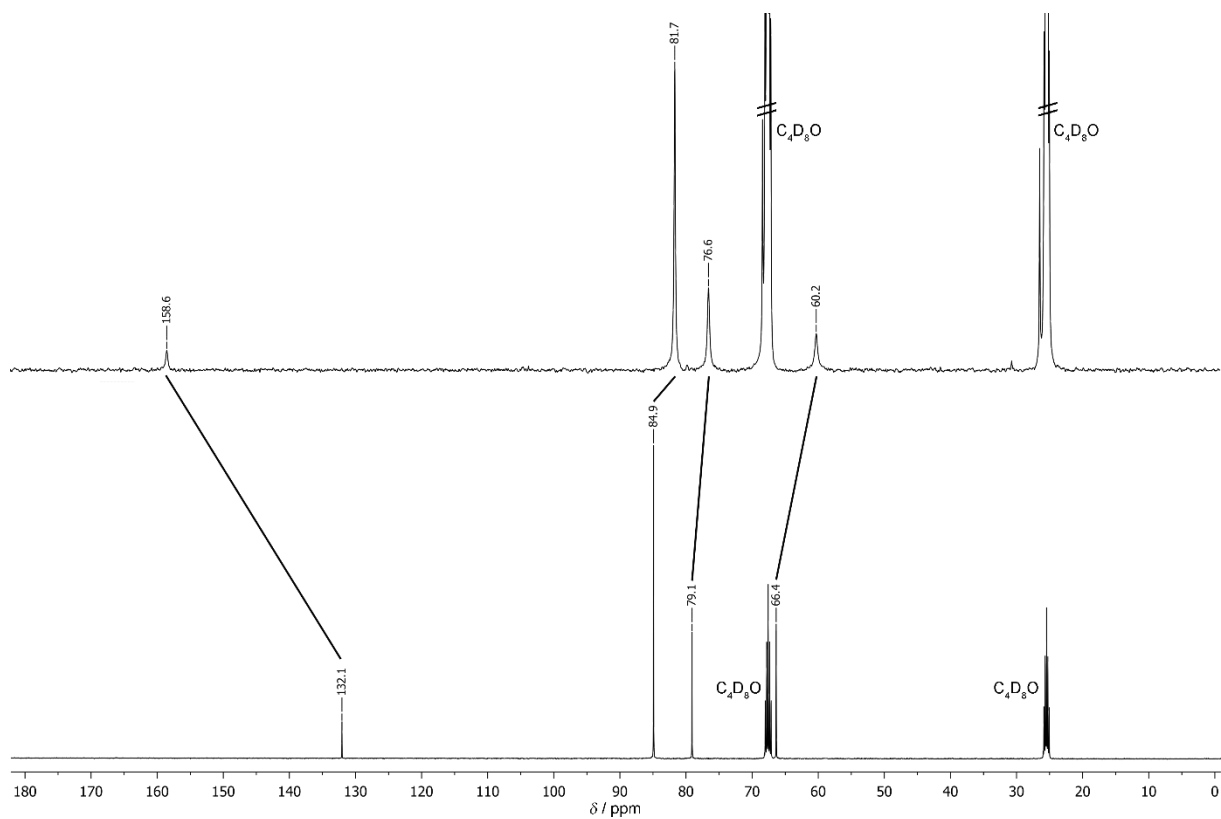
Figure S 5. ^{13}C NMR spectrum of [H-1][PF$_6$] (bottom) and 1 (top) in d$_8$-tetrahydrofuran.
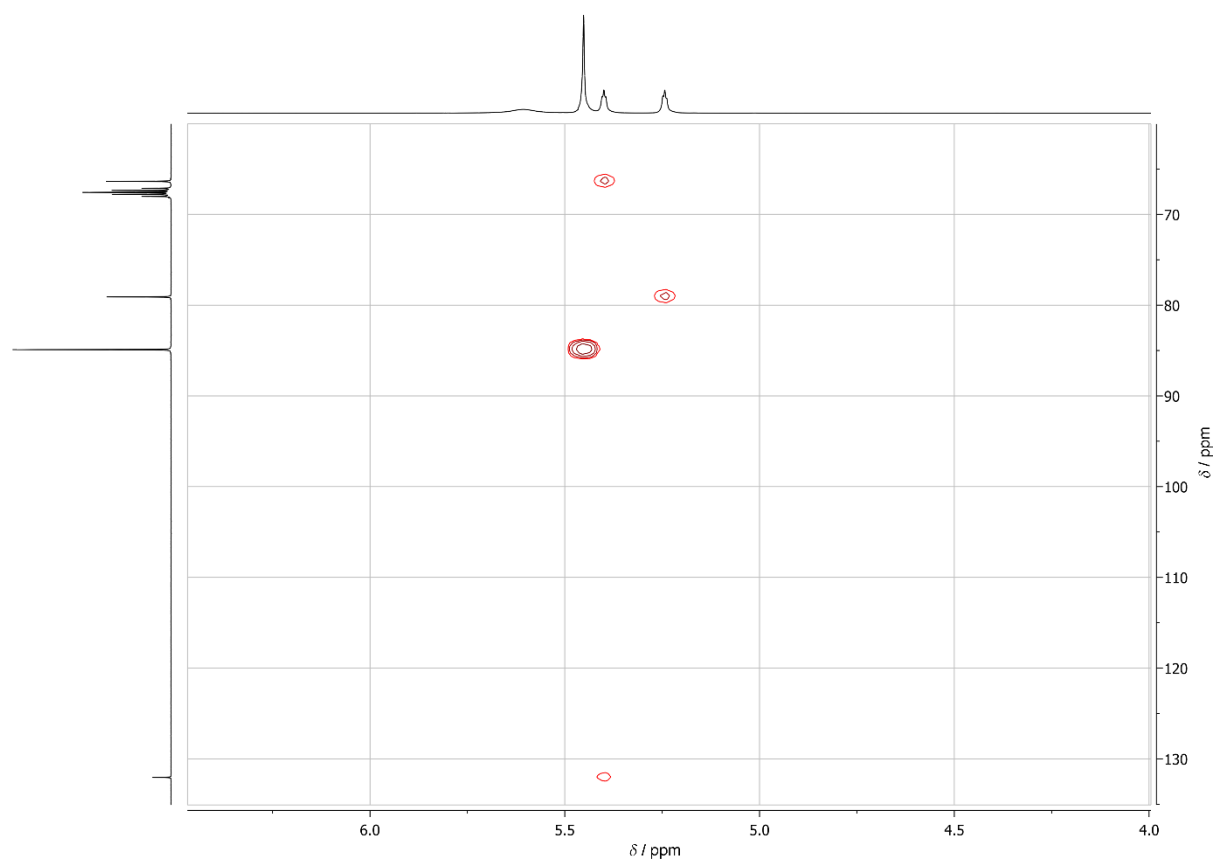
Figure S 6. $^1H^{13}C$ HMBC spectrum of [H-1][PF$_6$] in d$_8$-tetrahydrofuran.
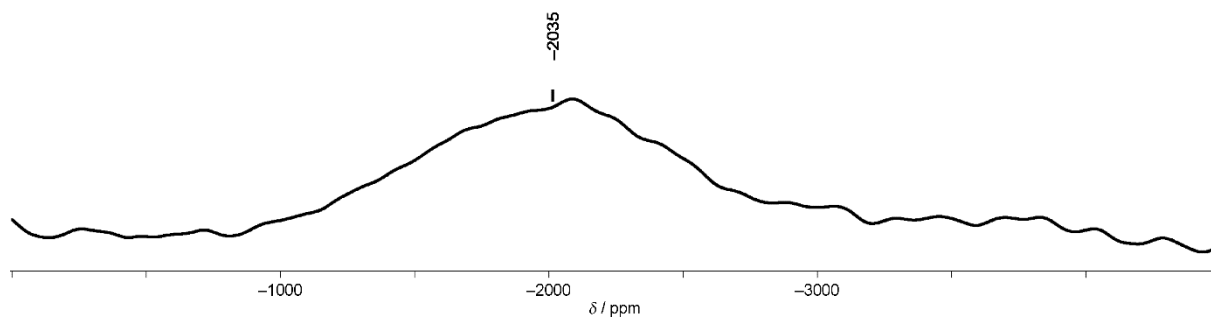
Figure S 7. ^{59}Co NMR spectrum of [H-1][PF$_6$] in d$_8$-tetrahydrofuran, full width at half height 116 kHz at 2035 ppm.
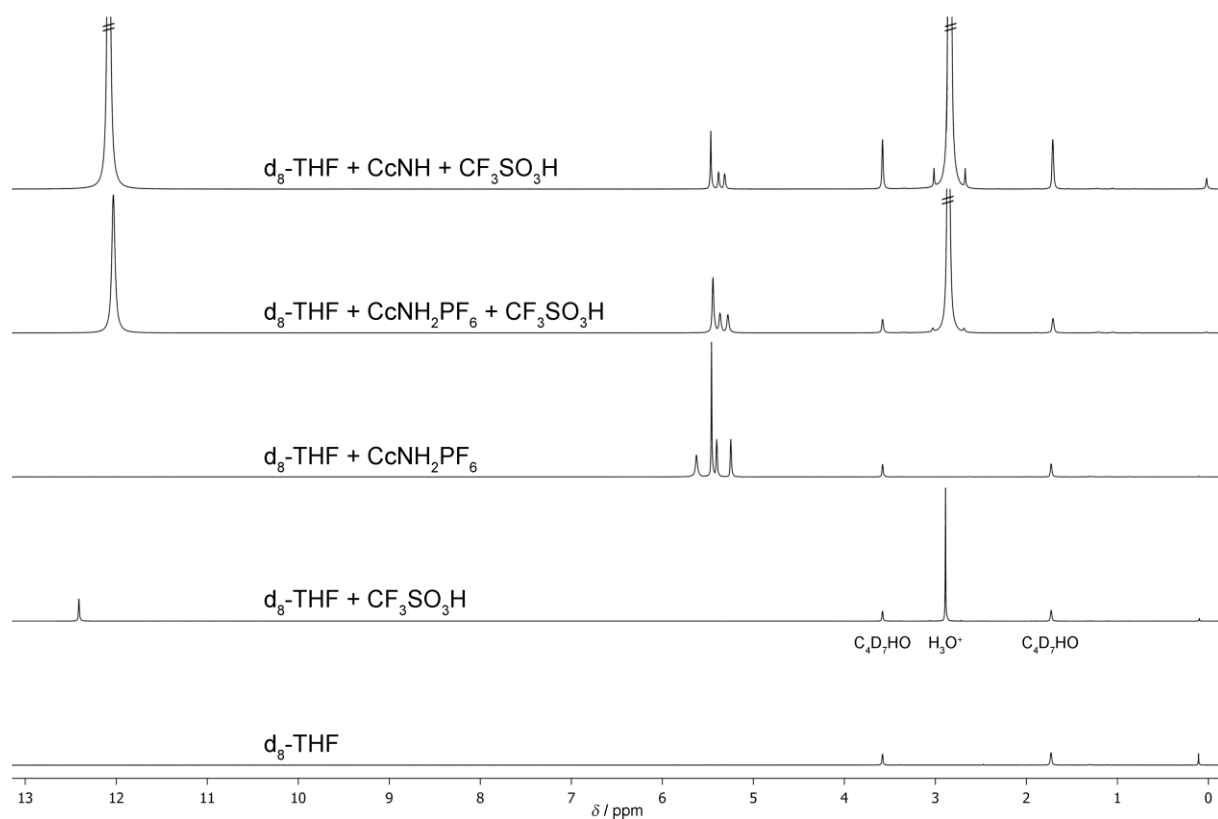
Figure S 8. ^{1}H NMR spectra before and after titration with CF$_3$SO$_3$H in d$_8$-tetrahydrofuran.
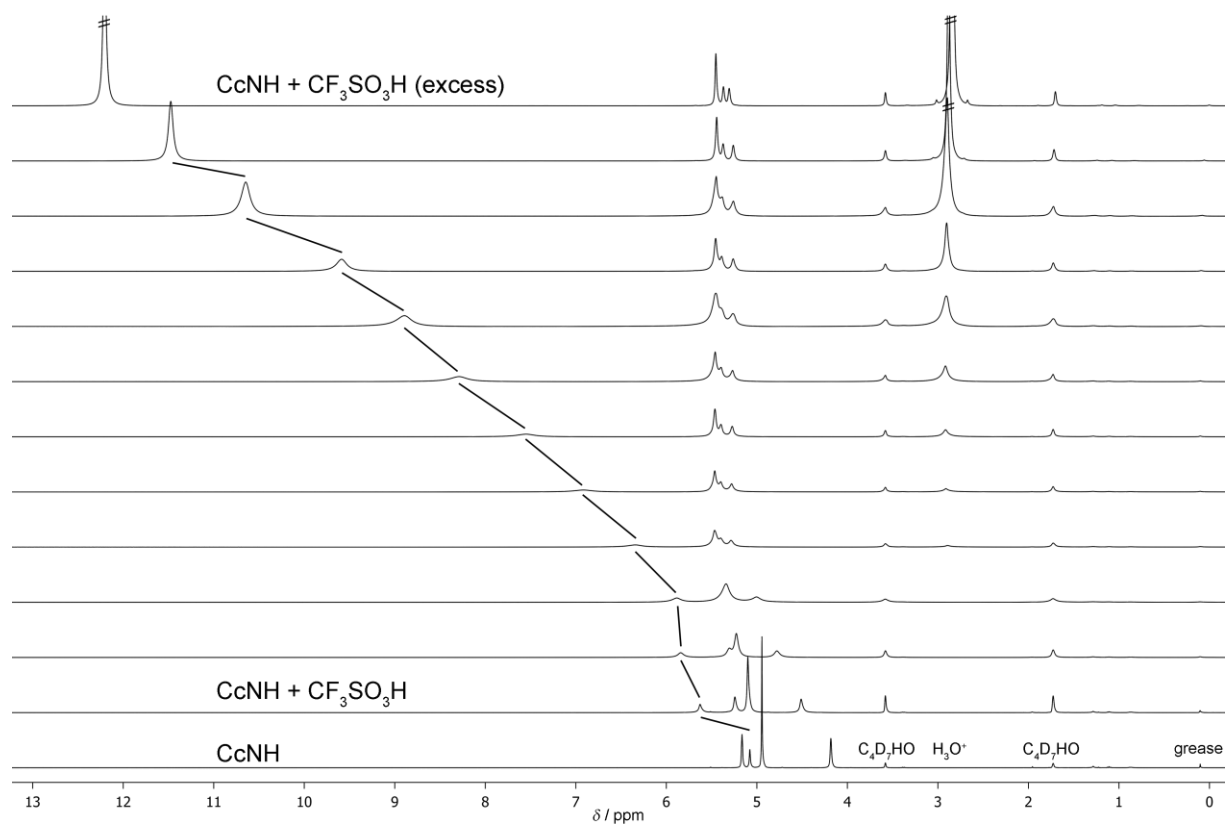
Figure S 9. ^{1}H NMR spectra, titration of 1 with CF$_3$SO$_3$H in d$_8$-tetrahydrofuran.
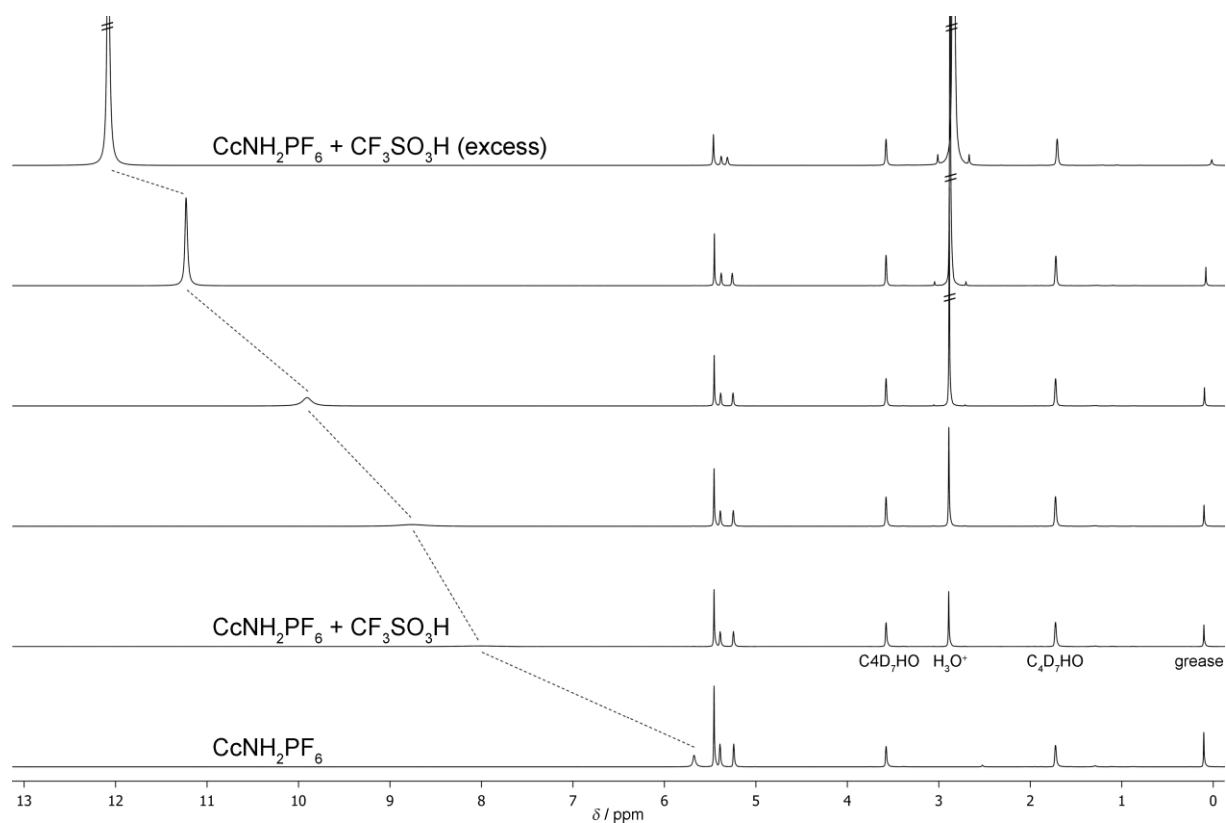
Figure S 10. ^{1}H NMR spectra, titration of [H-1][PF$_6$] with CF$_3$SO$_3$H in d$_8$-tetrahydrofuran.
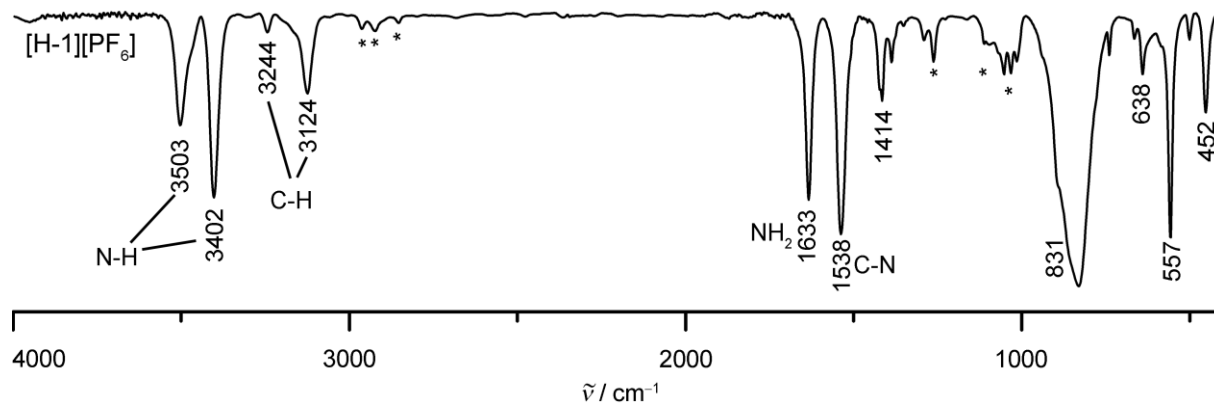
Figure S 11. IR spectrum of [H-1][PF$_6$] as KBr disc. * marks residual bands of tetrahydrofuran.
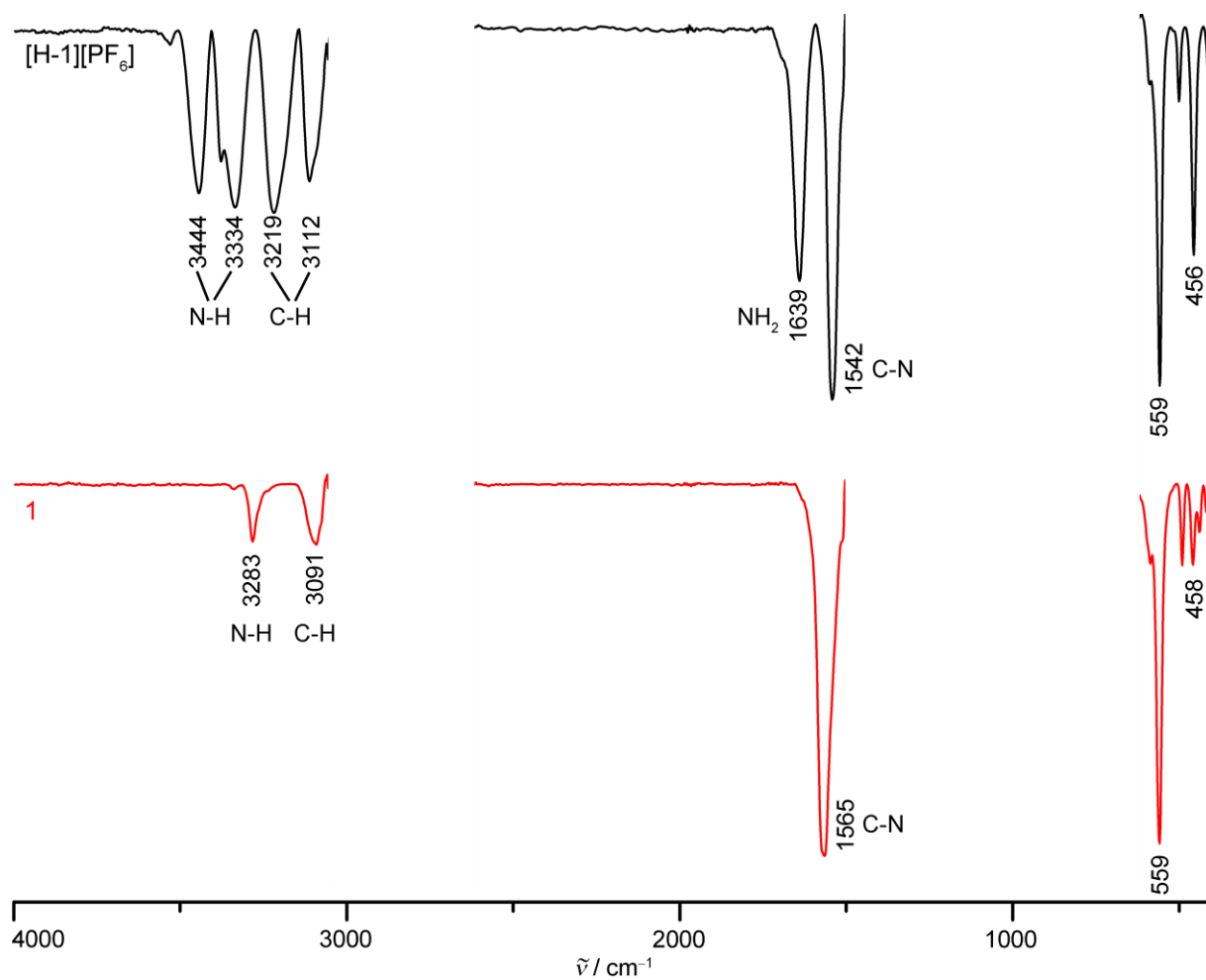
Figure S 12. IR spectra of a solution of [H-1][PF$_6$] (top) and 1 (bottom), respectively, in tetrahydrofuran. In the bleached areas, transmission was not possible due to the solvent.
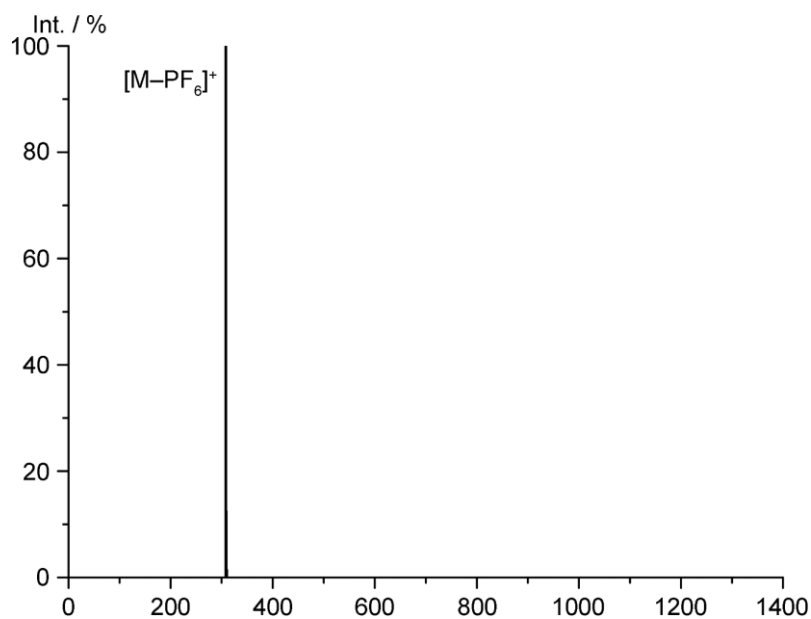
Figure S 13. ESI$^+$ mass spectrum of 2[PF$_6$] in acetonitrile.
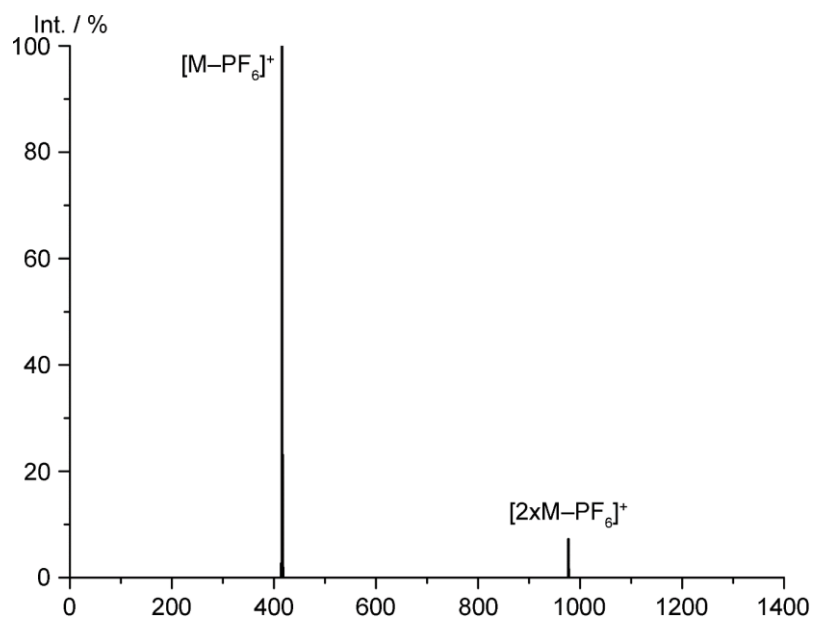
Figure S 14. ESI$^+$ mass spectrum of 3[PF$_6$] in acetonitrile.
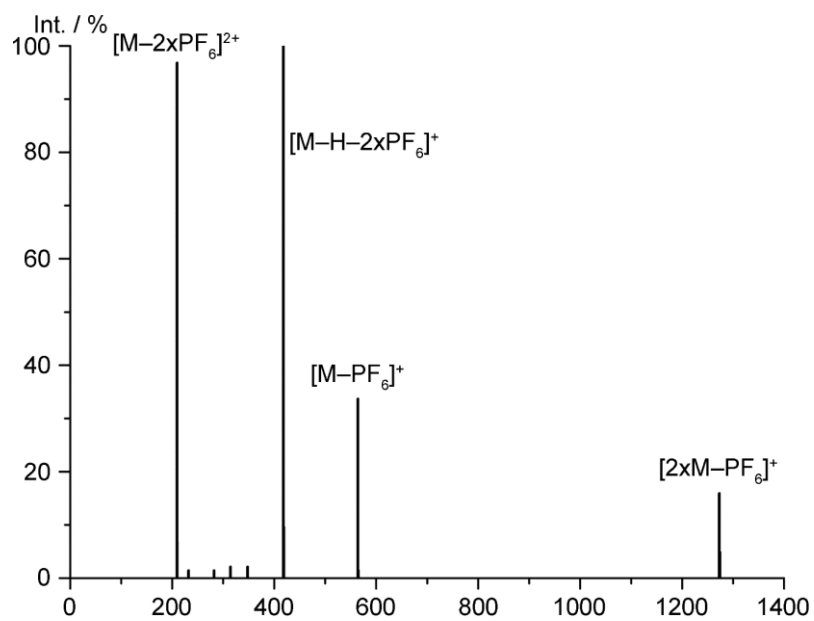
Figure S 15. ESI$^+$ mass spectrum of 4[PF$_6$]$_2$ in acetonitrile.
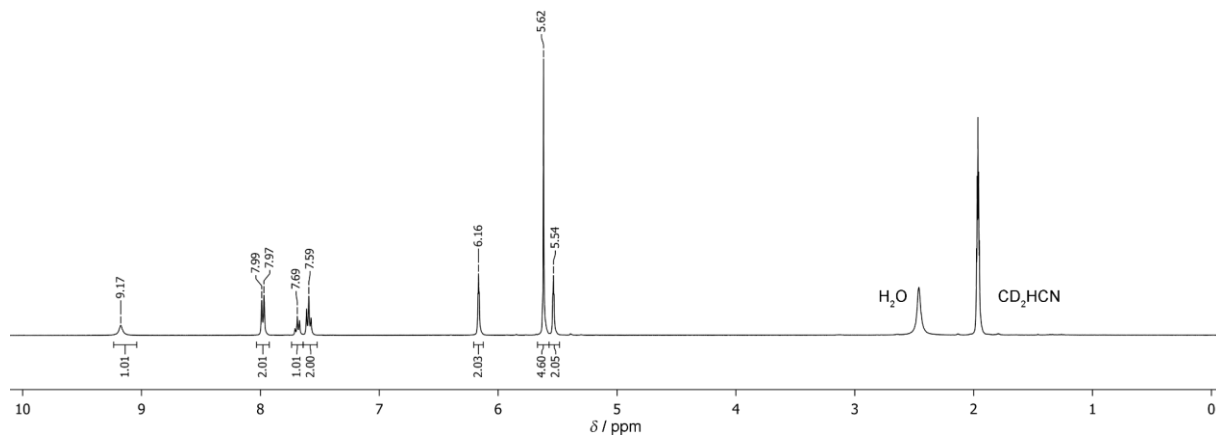
Figure S 16. ^{1}H NMR spectrum of 2[PF$_6$] in d$_3$-acetonitrile.
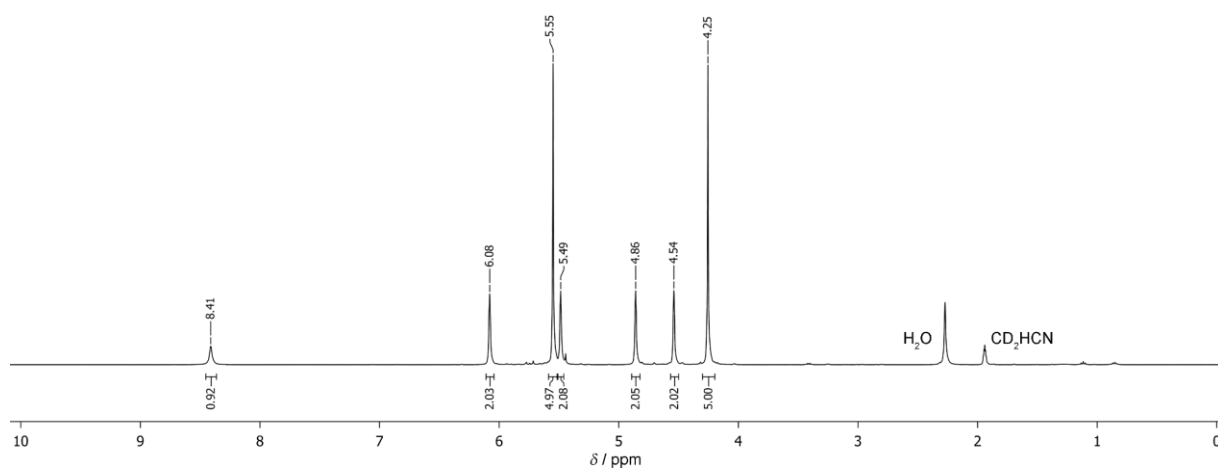
Figure S 17. ^{1}H NMR spectrum of 3[PF$_6$] in d$_3$-acetonitrile.
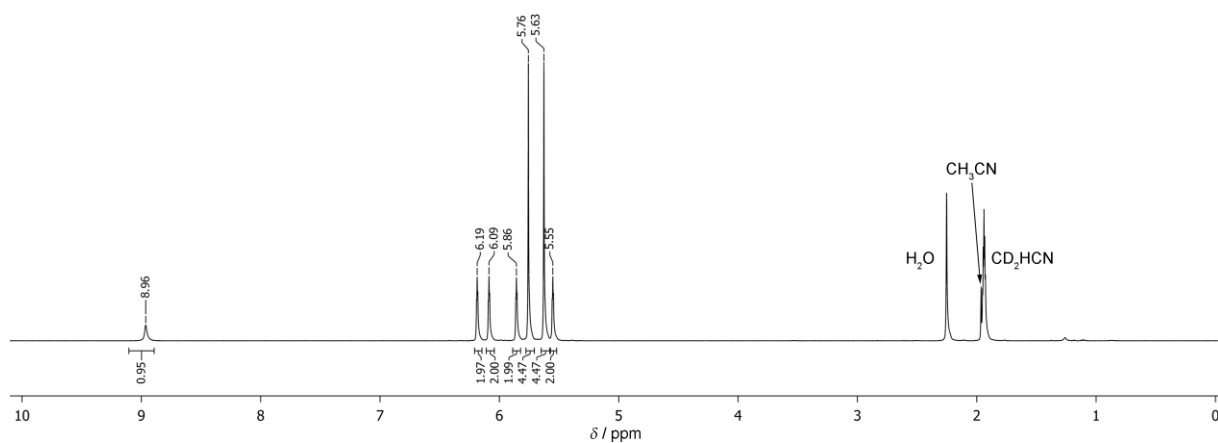
Figure S 18. ^{1}H NMR spectrum of 4[PF$_6$]$_2$ in d$_3$-acetonitrile.
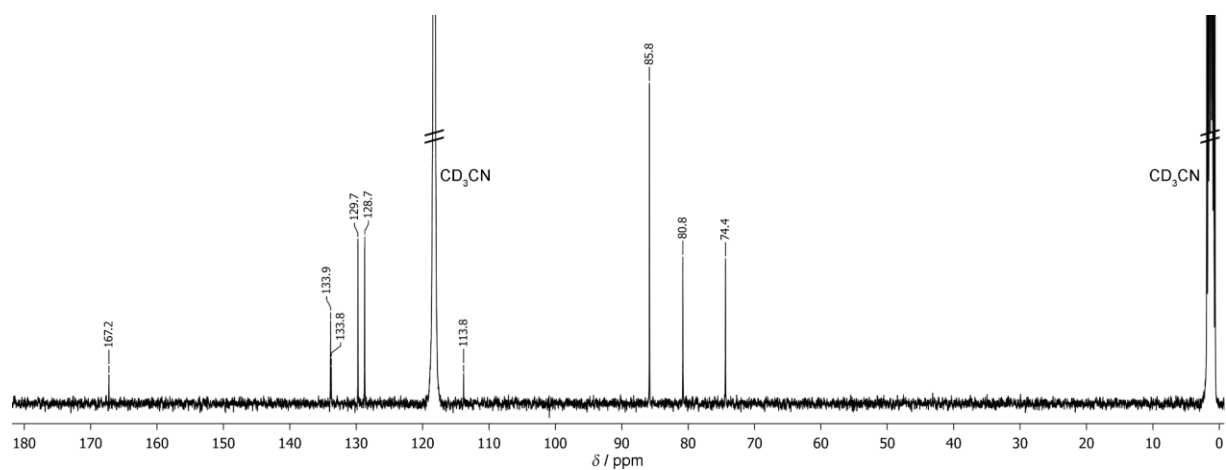
Figure S 19. ^{13}C NMR spectrum of 2[PF$_6$] in d$_3$-acetonitrile.
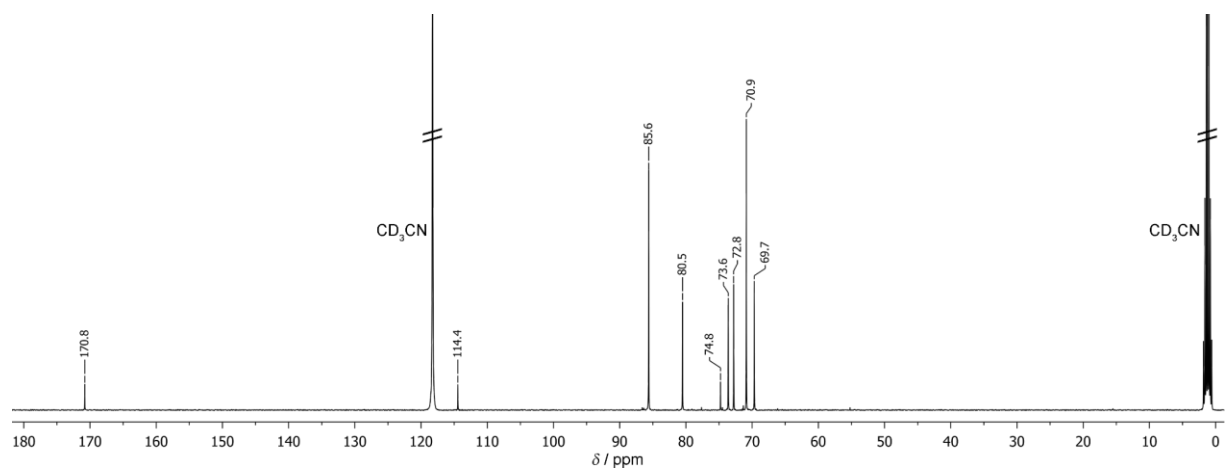
Figure S 20. ^{13}C NMR spectrum of 3[PF$_6$] in d$_3$-acetonitrile.
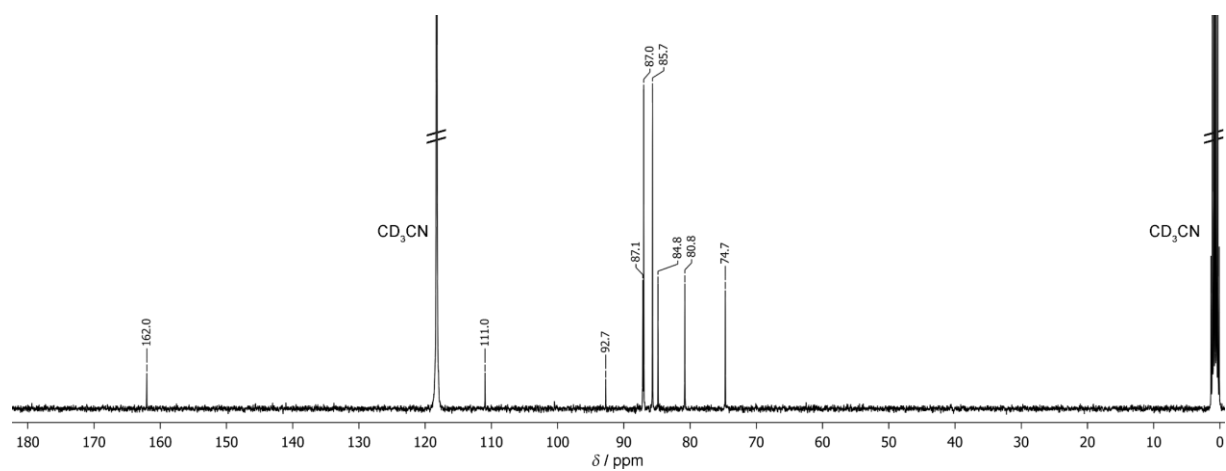
Figure S 21. ^{13}C NMR spectrum of 4[PF$_6$]$_2$ in d$_3$-acetonitrile.
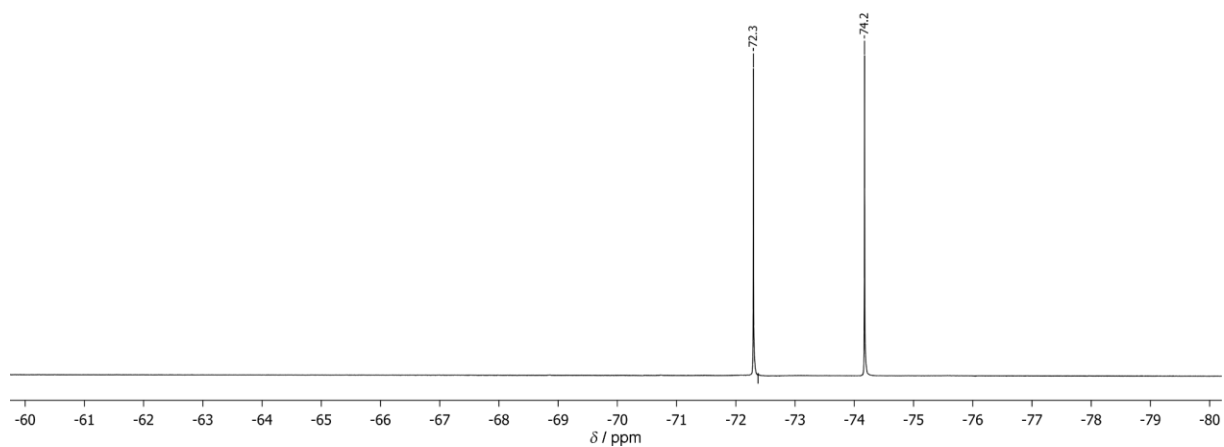
Figure S 22. ^{19}F NMR spectrum of 2[PF$_6$] in d$_3$-acetonitrile.
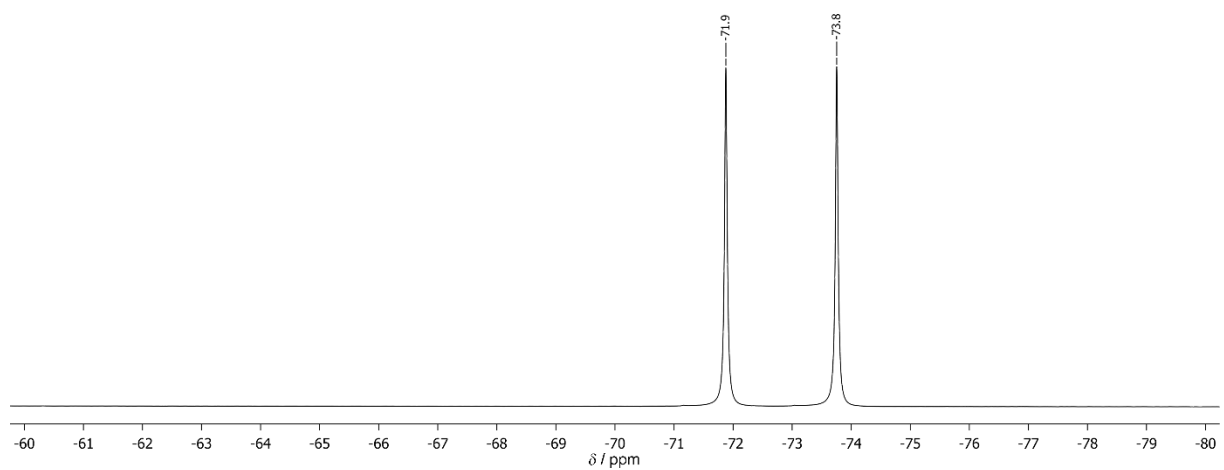
Figure S 23. ^{19}F NMR spectrum of 3[PF$_6$] in d$_3$-acetonitrile.
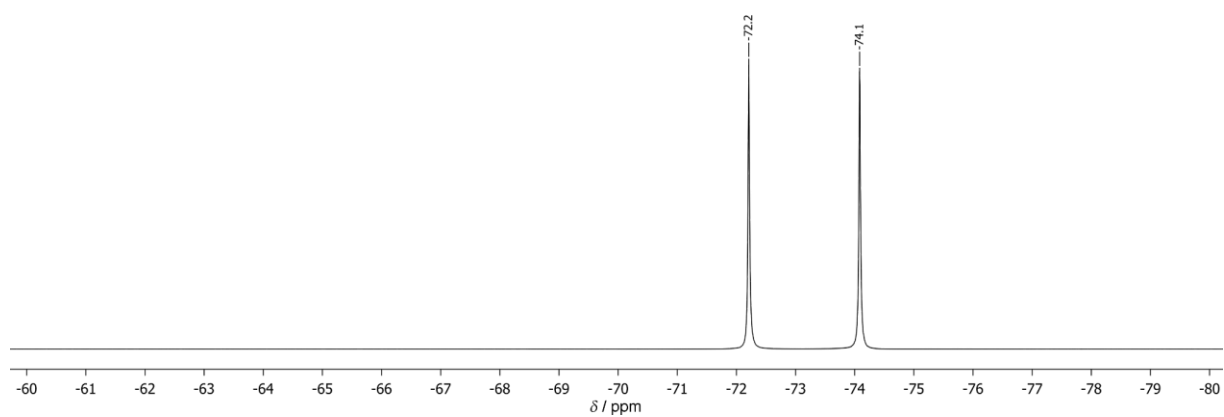
Figure S 24. ^{19}F NMR spectrum of 4[PF$_6$]$_2$ in d$_3$-acetonitrile.
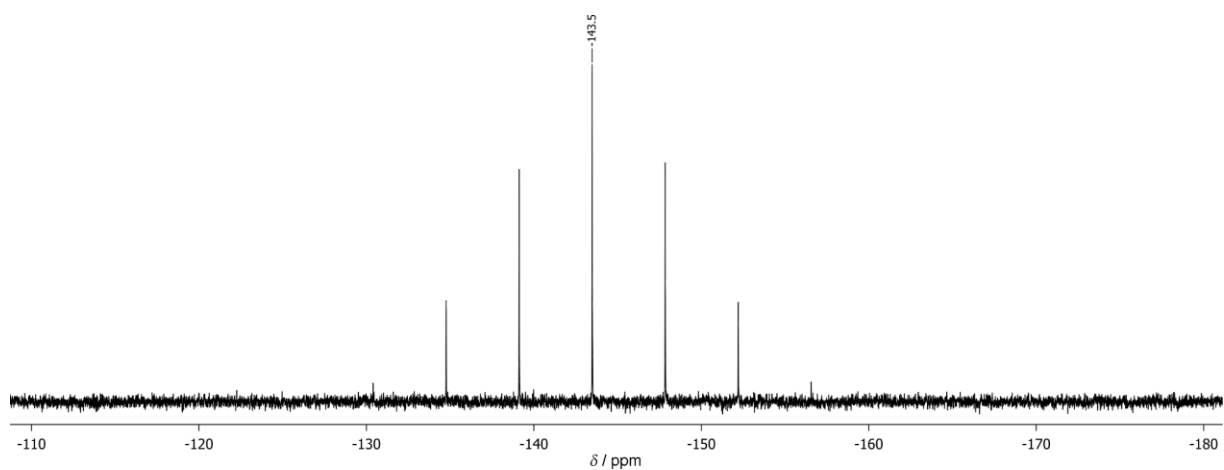
Figure S 25. ^{31}P NMR spectrum of 2[PF$_6$] in d$_3$-acetonitrile.
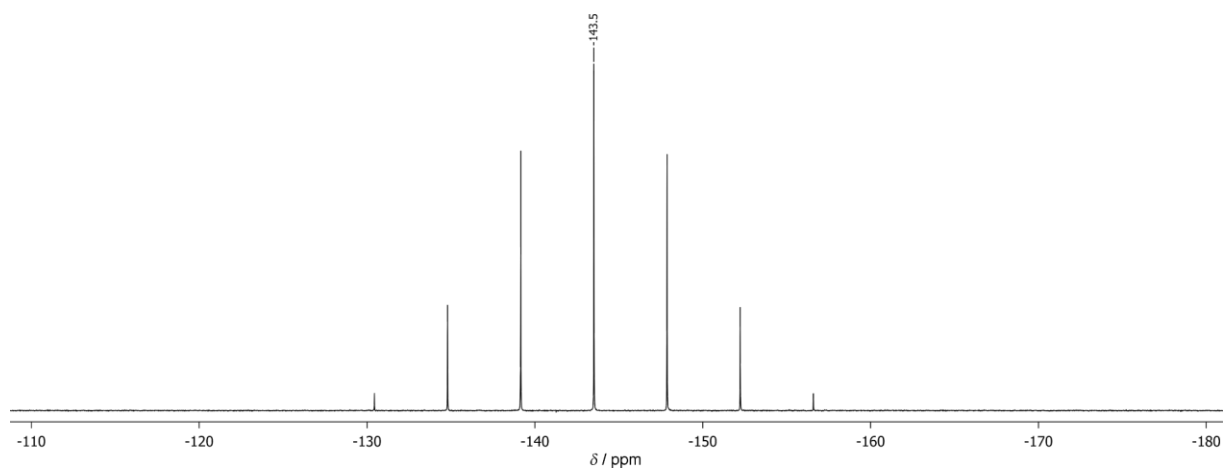
Figure S 26. ^{31}P NMR spectrum of 3[PF$_6$] in d$_3$-acetonitrile.
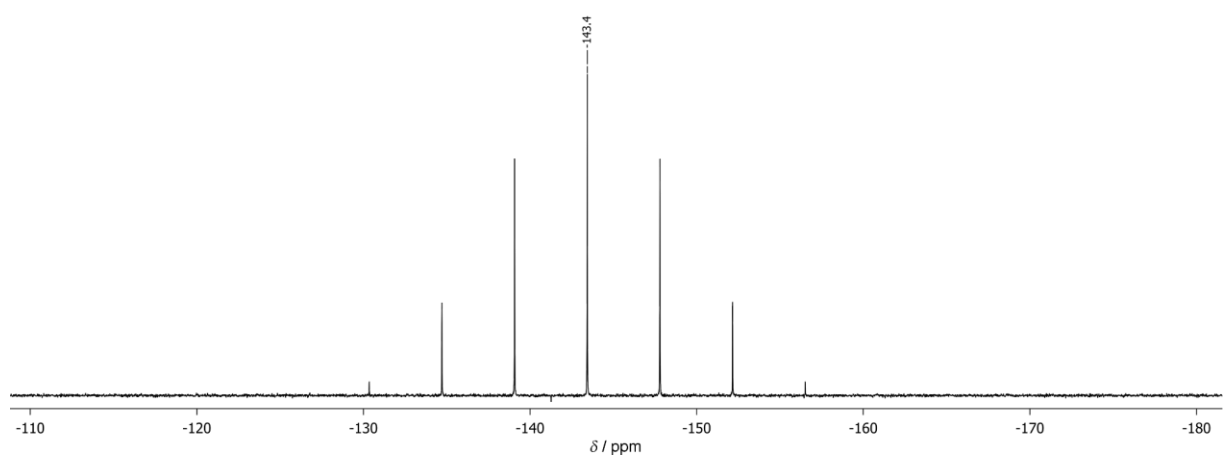
Figure S 27. ^{31}P NMR spectrum of 4[PF$_6$]$_2$ in d$_3$-acetonitrile.
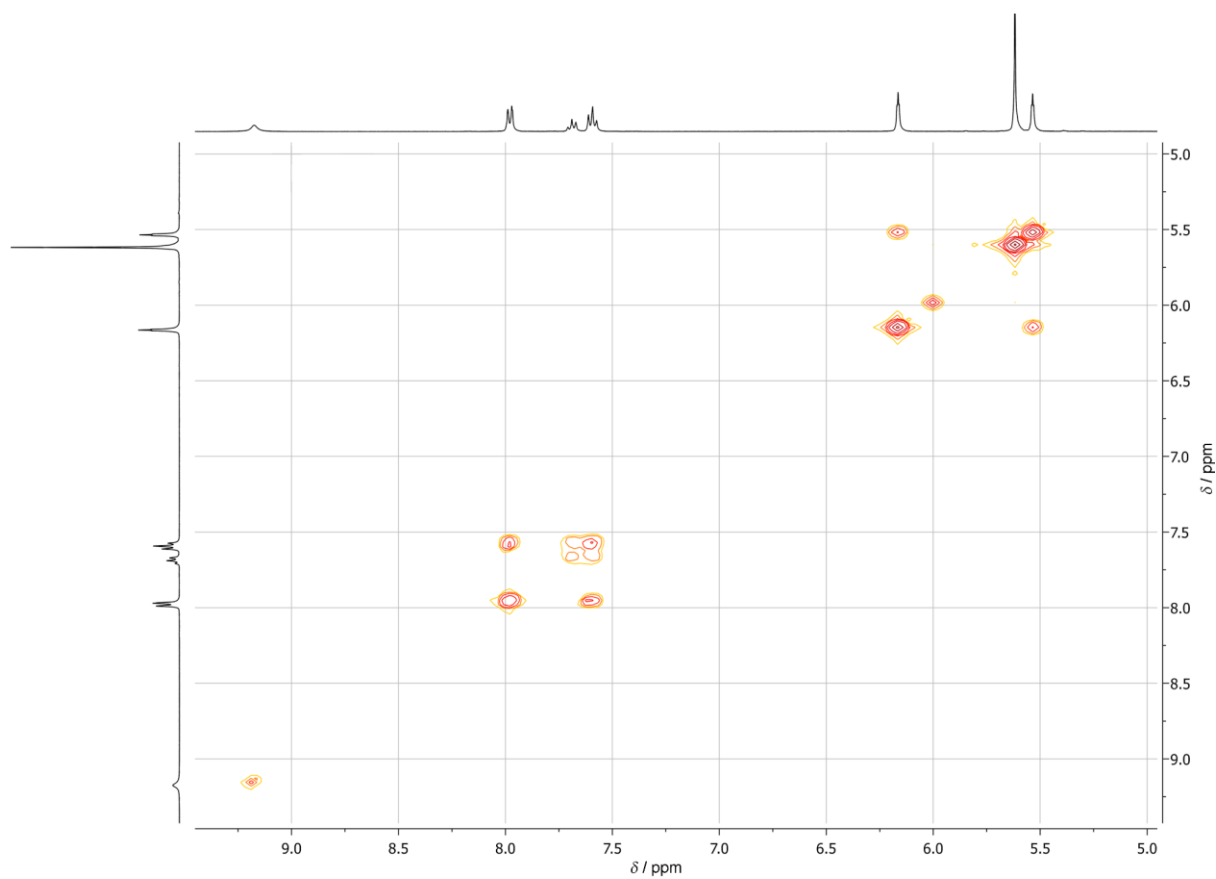
Figure S 28. $^1H^1H$ COSY spectrum of 2[PF$_6$] in d$_3$-acetonitrile.
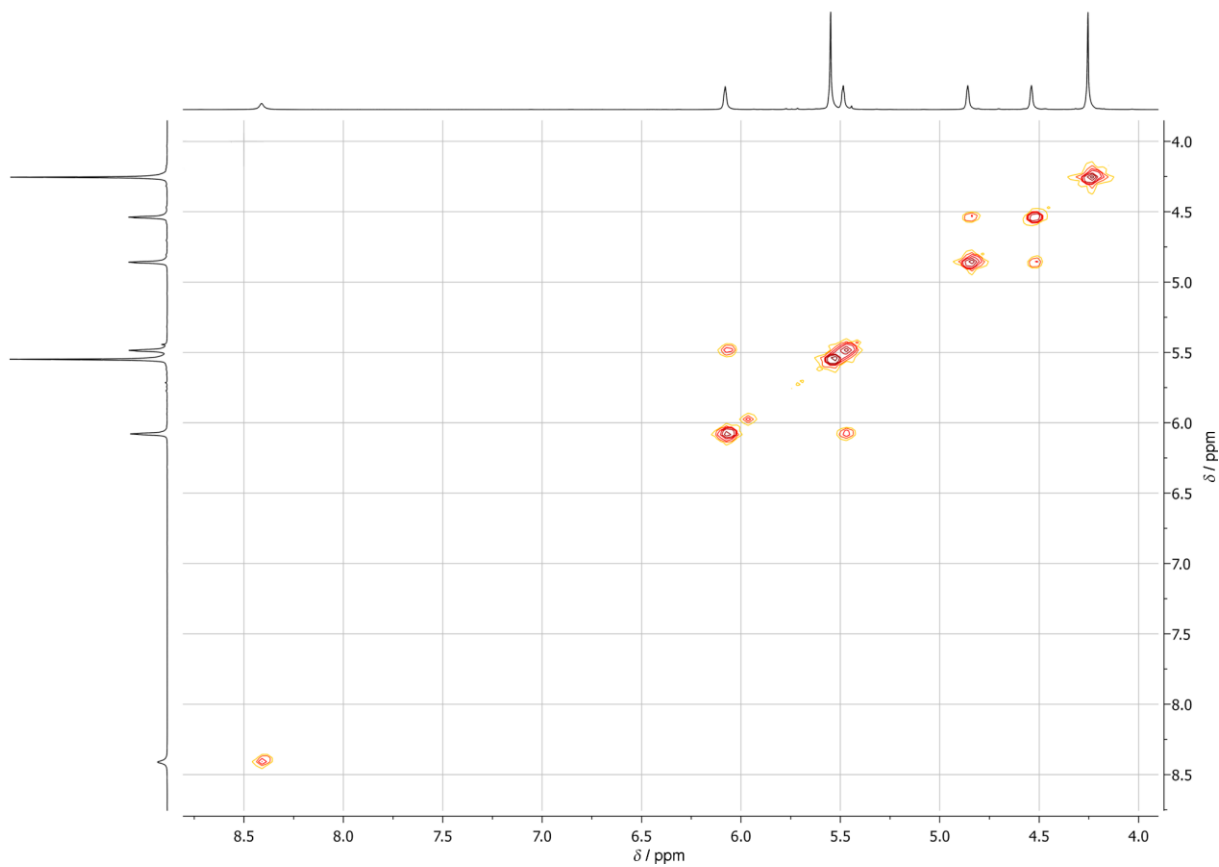
Figure S 29. $^1H^1H$ COSY spectrum of 3[PF$_6$] in d$_3$-acetonitrile.
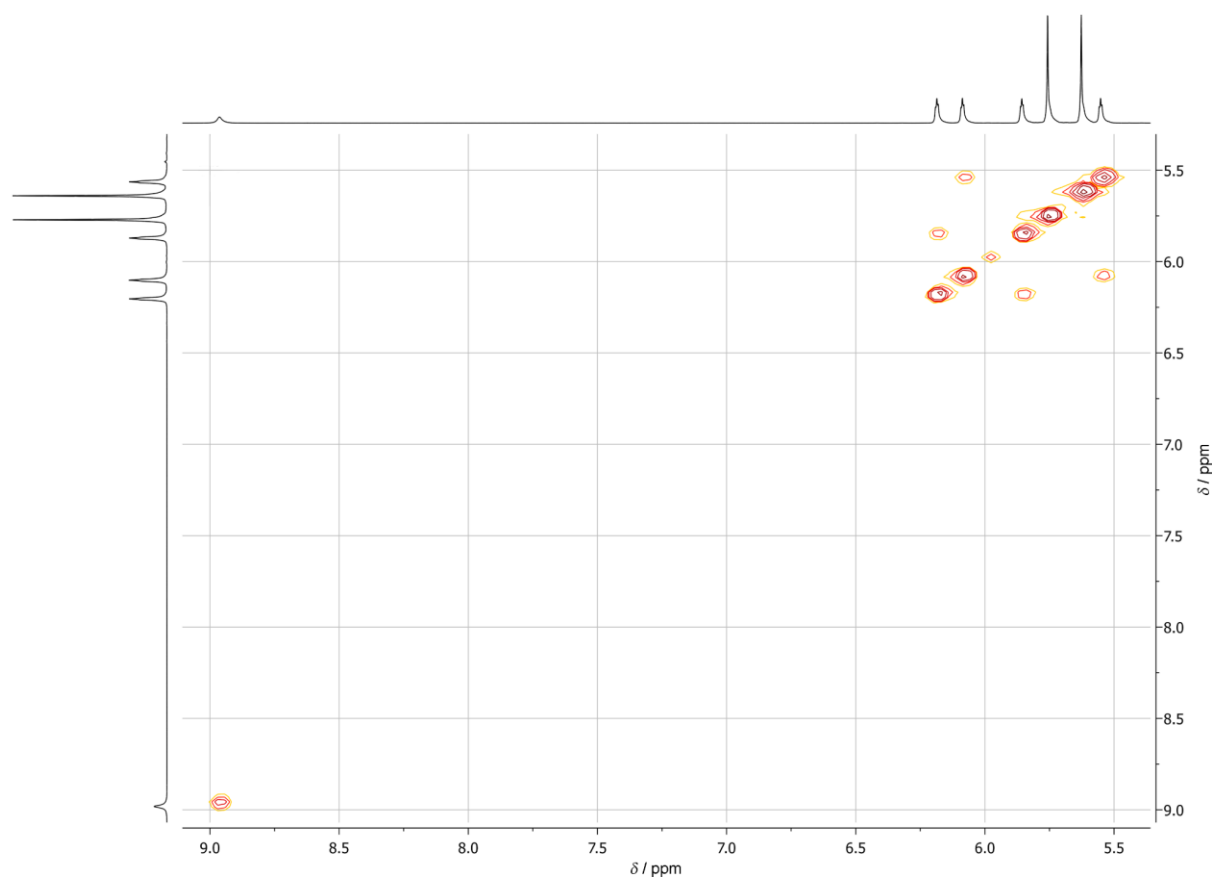
Figure S 30. $^1H^1H$ COSY spectrum of 4[PF$_6$]$_2$ in d$_3$-acetonitrile.
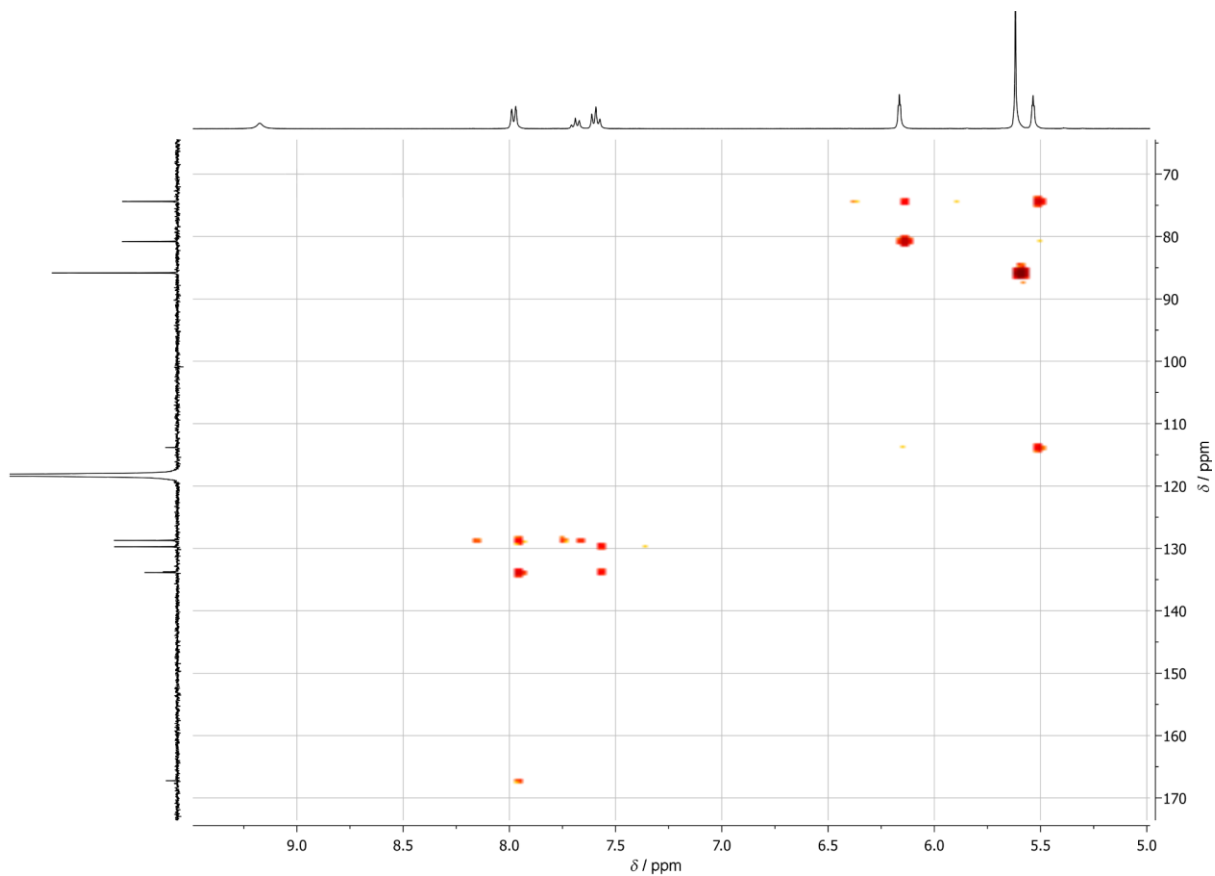
Figure S 31. $^1H^{13}C$ HMBC spectrum of 2[PF$_6$] in d$_3$-acetonitrile.
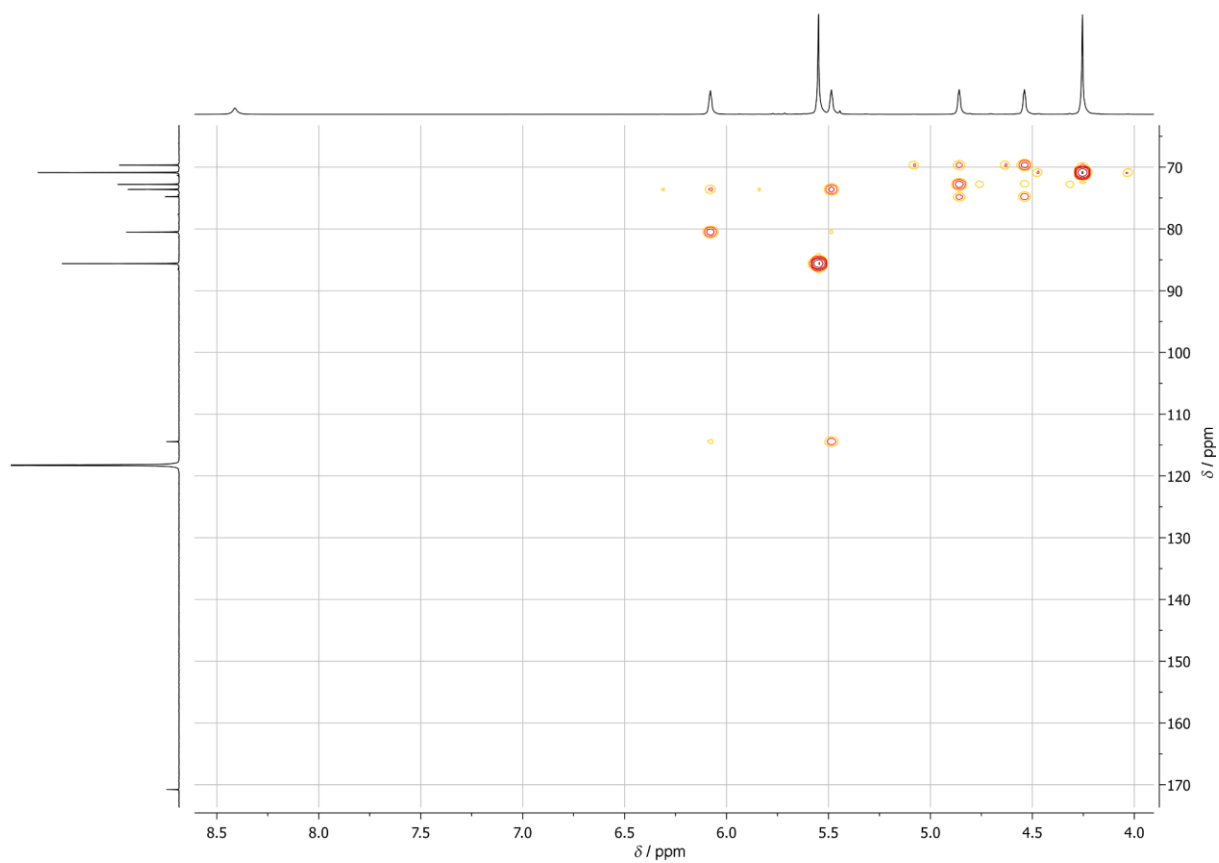
Figure S 32. $^1H^{13}C$ HMBC spectrum of **3**[PF$_6$] in d$_3$-acetonitrile.
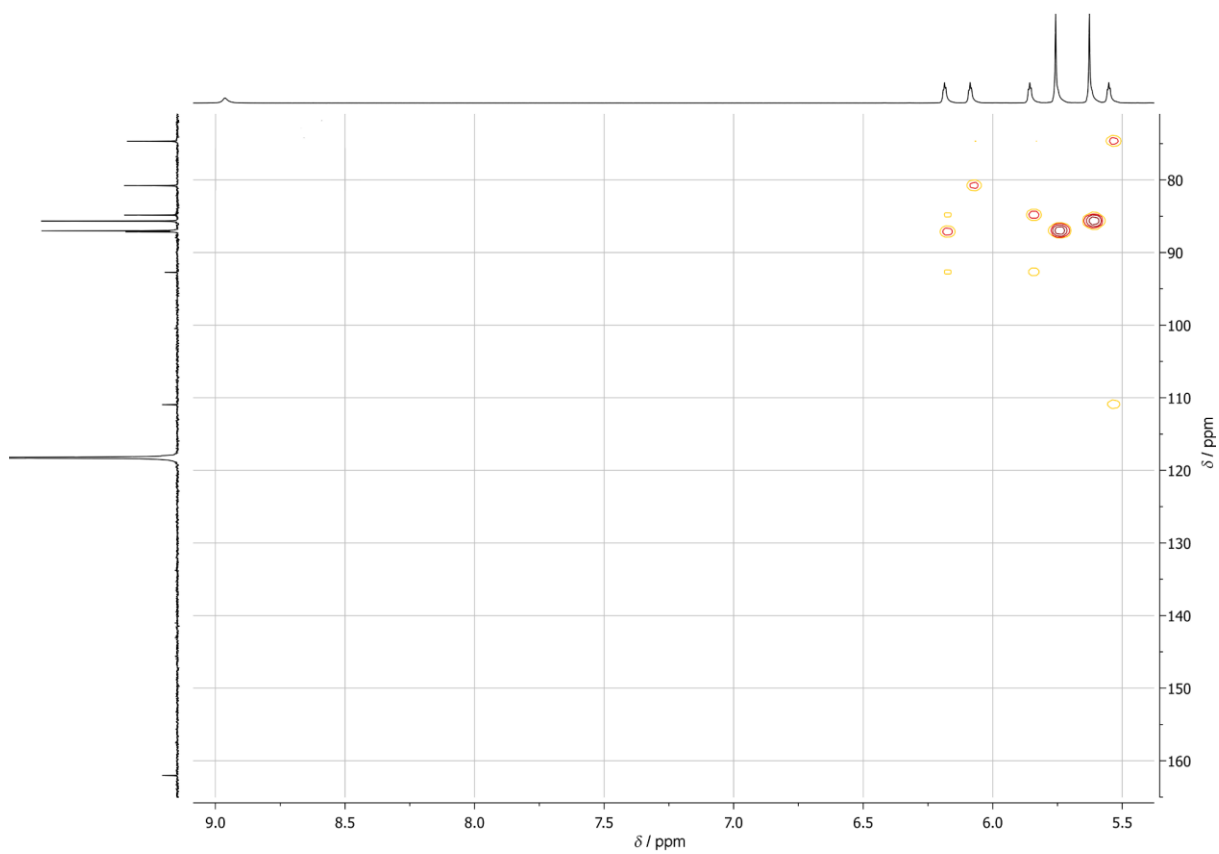
Figure S 33. $^1H^{13}C$ HMBC spectrum of **4**[PF$_6$]$_2$ in d$_3$-acetonitrile.
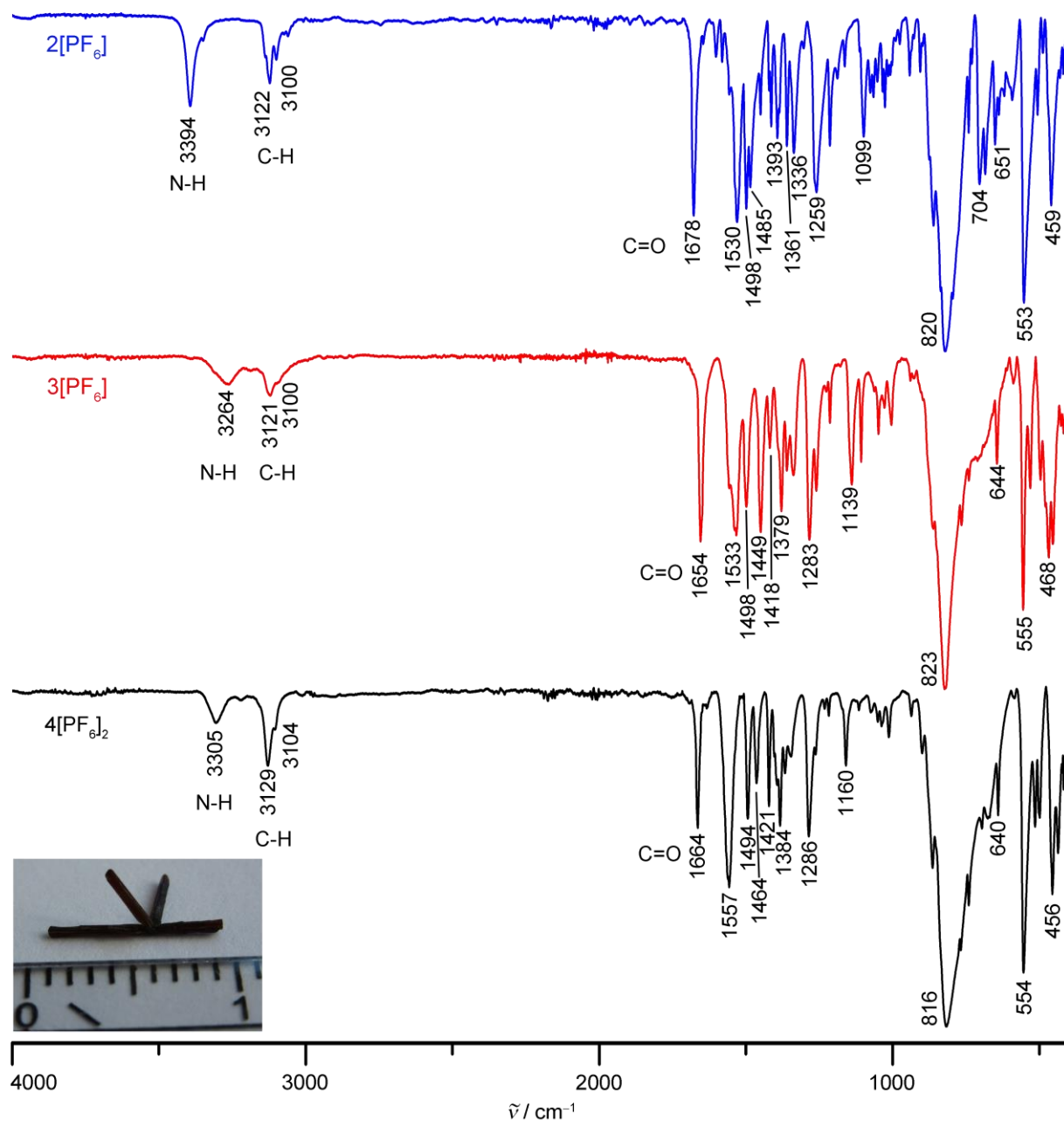
Figure S 34. IR spectra (ATR) of 2[PF$_6$] (top), 3[PF$_6$] (center) and 4[PF$_6$]$_2$ (bottom). Photograph of the large intergrown crystals of 4[PF$_6$]$_2$ x CH$_3$CN (scale in cm).
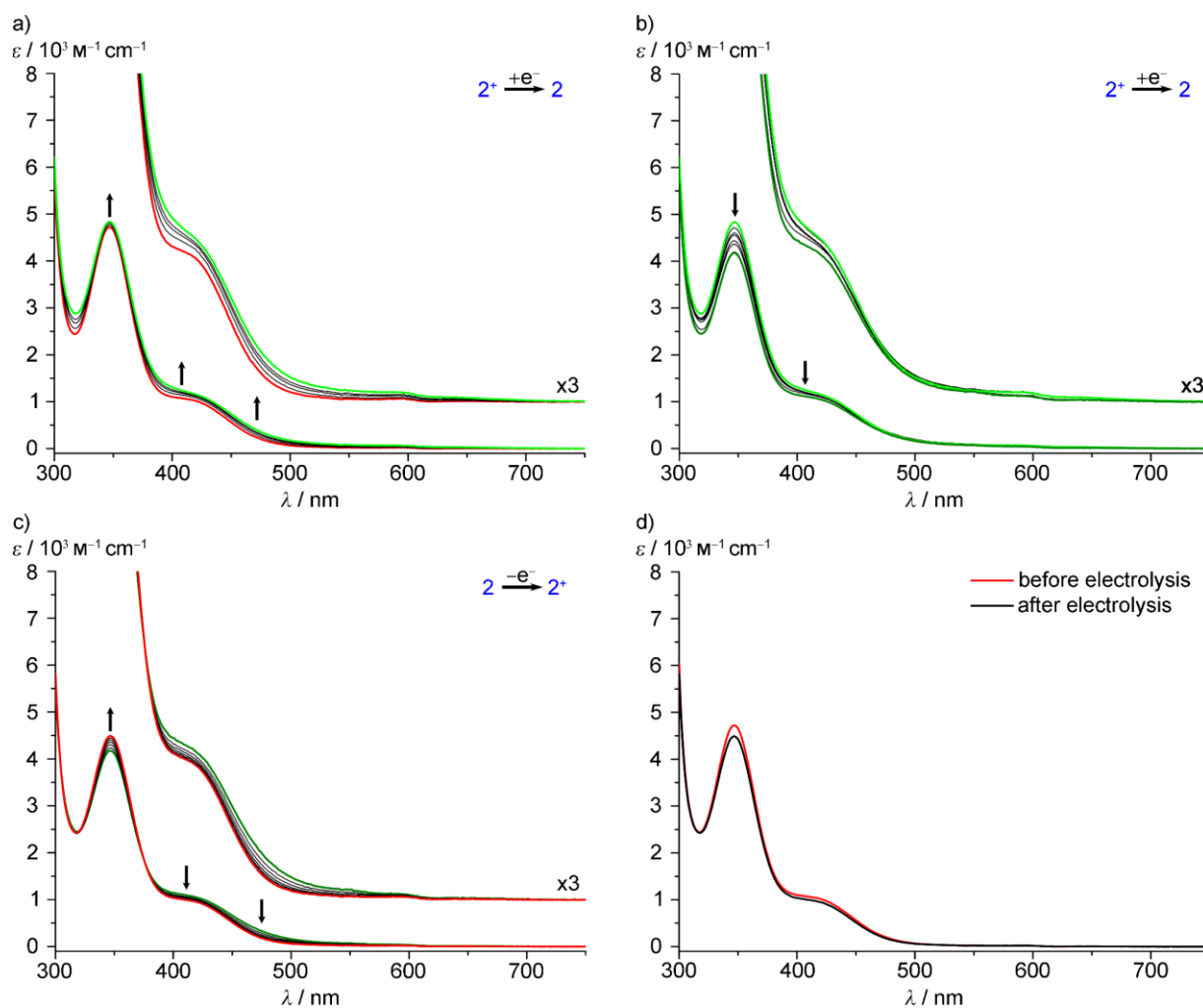
Figure S 35. Changes in the UV/vis spectra in the course of redox events in $CH_3CN/[^nBu_4N][PF_6]$ during OTTLE spectroelectrochemistry: a) and b) reduction of $2^+ \rightarrow 2$ in two steps, c) re-oxidation of $2 \rightarrow 2^+$, d) Comparison of spectra before reduction of $2^+ \rightarrow 2$ (red) and after re-oxidation of $2 \rightarrow 2^+$ (black).
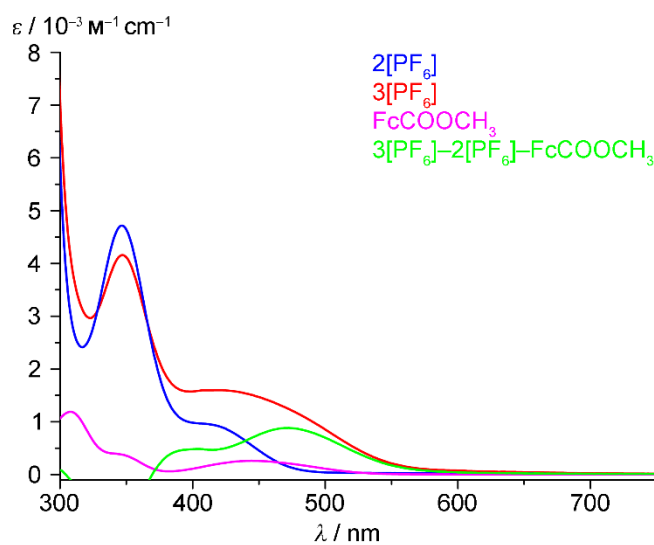
Figure S 36. UV/vis spectra of $2[PF_6]$ (blue), $3[PF_6]$ (red), Fc-COOCH$_3$ (purple) in acetonitrile and UV/vis difference spectrum of "$3[PF_6]$ minus $2[PF_6]$ minus Fc-COOCH$_3$".
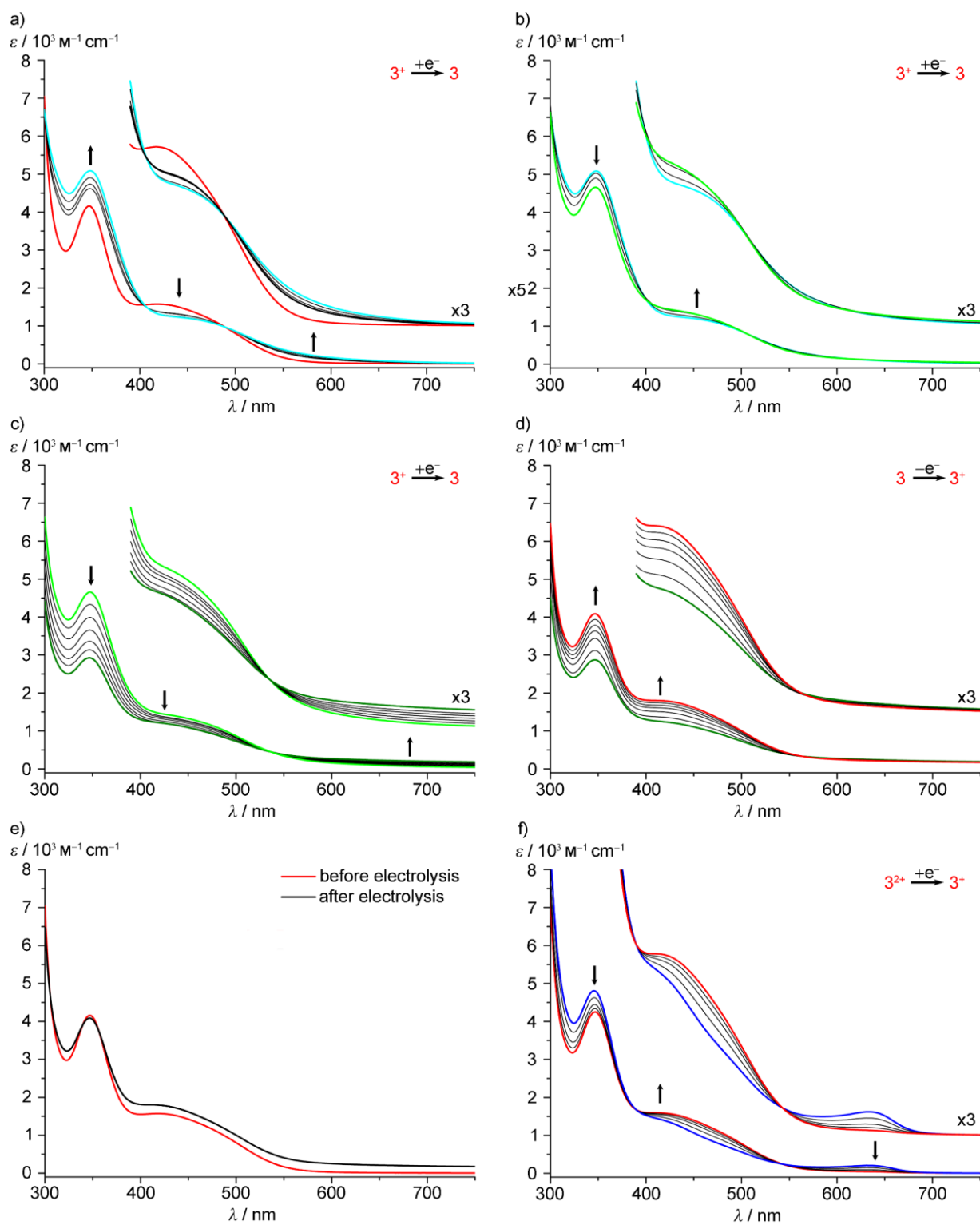
Figure S 37. Changes in the UV/vis spectra in the course of redox events in CH$_3$CN/[^{n}Bu$_4$N][PF$_6$] during OTTLE spectroelectrochemistry: a-c) reduction of 3$^+$ → 3 in three steps, d) re-oxidation of 3 → 3$^+$, e) Comparison of spectra before reduction of 3$^+$ → 3 (red) and after re-oxidation of 3 → 3$^+$ (black), f) re-reduction of 3^{2+} → 3$^+$.
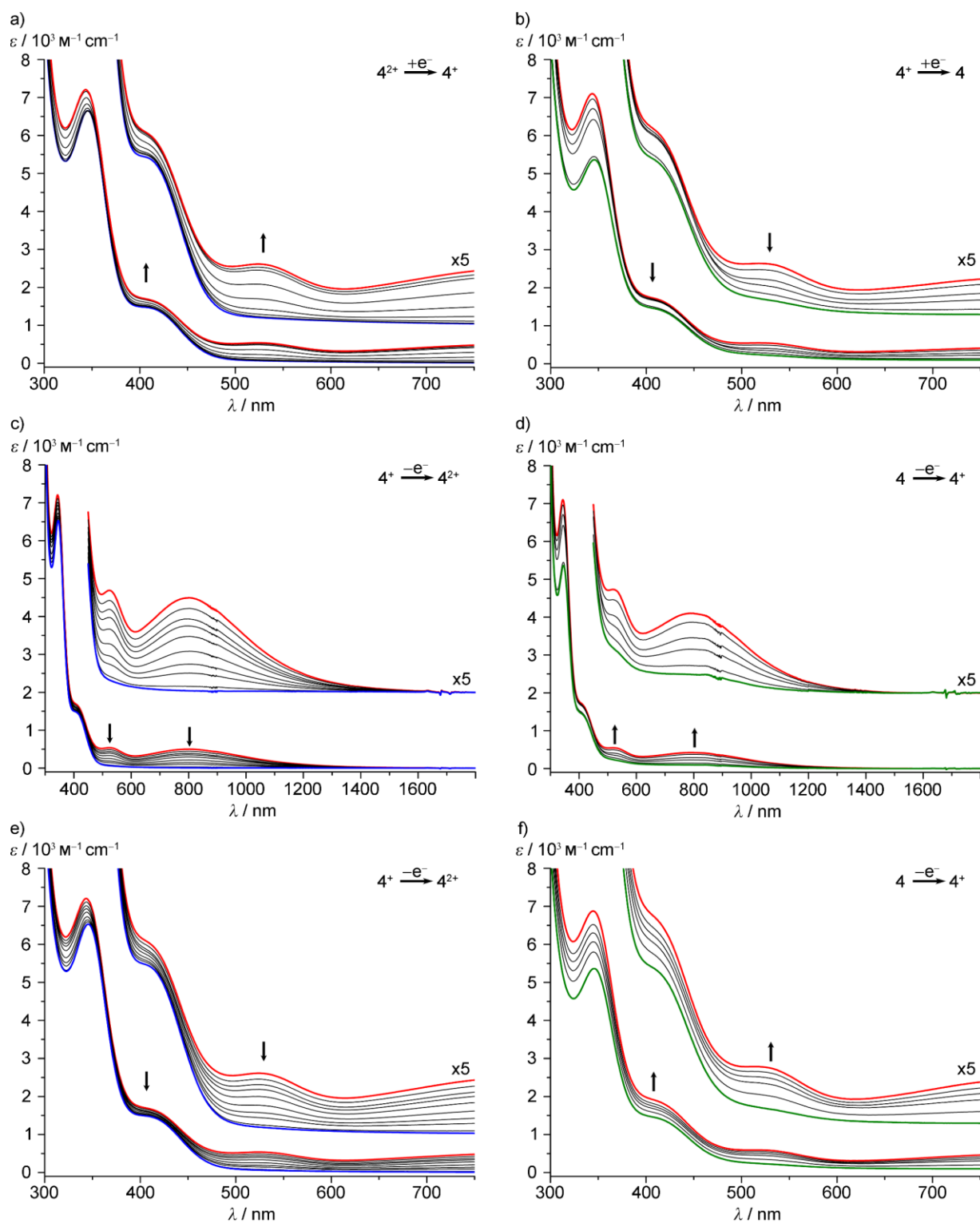
Figure S 38. Changes in the UV/vis/NIR spectra in the course of redox events in $CH_3CN/[^nBu_4N][PF_6]$ during OTTLE spectroelectrochemistry: a) reduction of $4^{2+} \rightarrow 4^+$, b) reduction of $4^+ \rightarrow 4$, c) and e) re-oxidation of $4^+ \rightarrow 4^{2+}$, d) and f) re-oxidation of $4^+ \rightarrow 4^{2+}$.
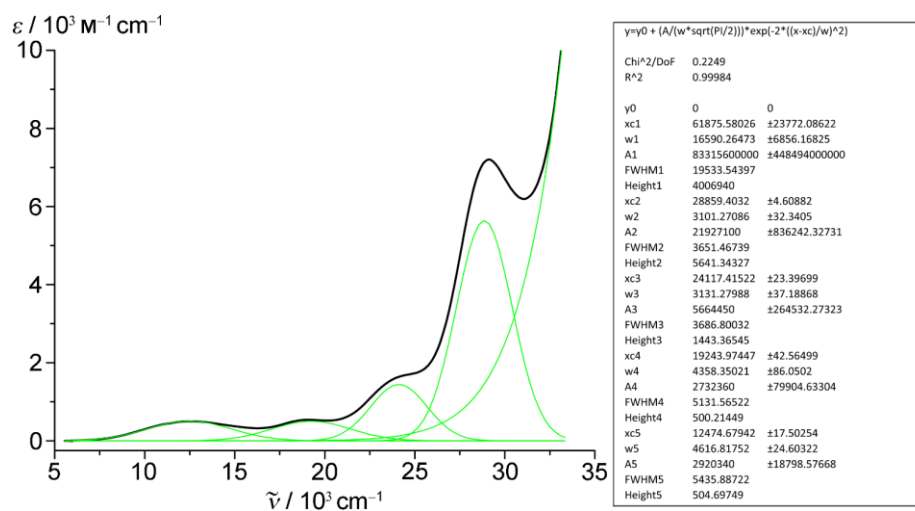
Figure S 39. UV/vis spectrum of **4+** in acetonitrile (reduced from **4[PF$_6$]$_2$** by electrochemical reduction (OTTLE)) with deconvolution into Gaussian bands.
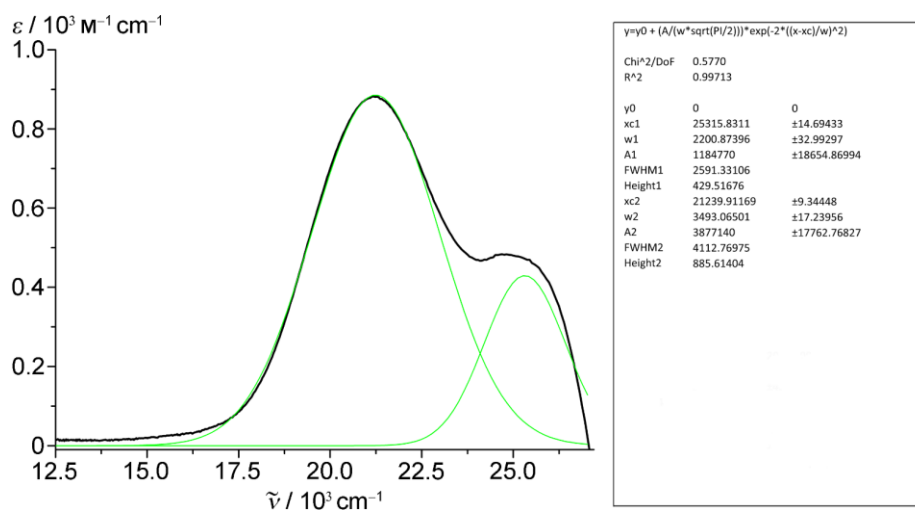
Figure S 40. UV/vis difference spectrum of "3[PF$_6$] minus 2[PF$_6$] minus Fc-COOCH$_3$" in acetonitrile with deconvolution into Gaussian bands.

5.2 Supporting Information to Chapter 3.2: Cobaltocenium Substituents as Electron Acceptors in Photosynthetic Model Dyads

Maximilian Lauck, Christoph Förster, Dominik Gehrig and Katja Heinze
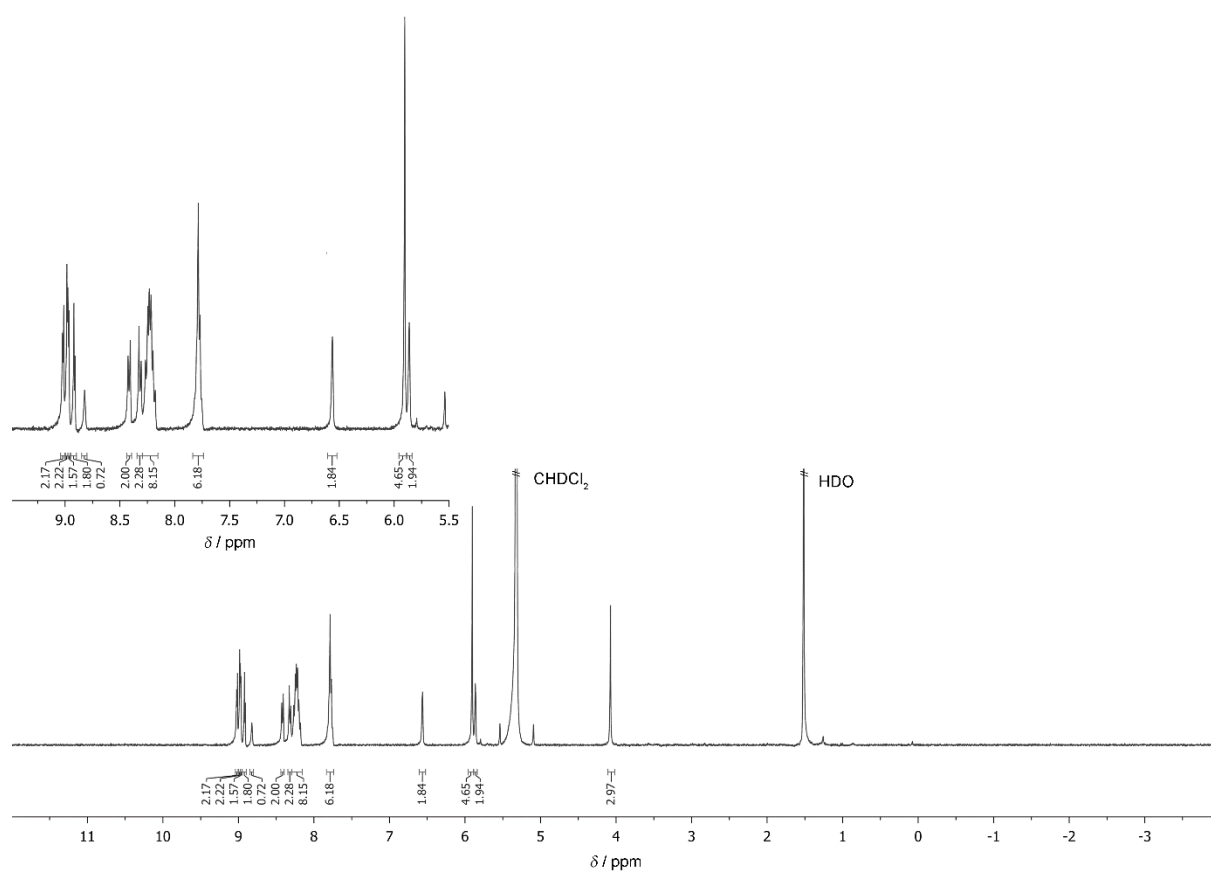
Figure S 1. ^{1}H NMR spectrum of [Zn-1][PF$_6$] in CD$_2$Cl$_2$.
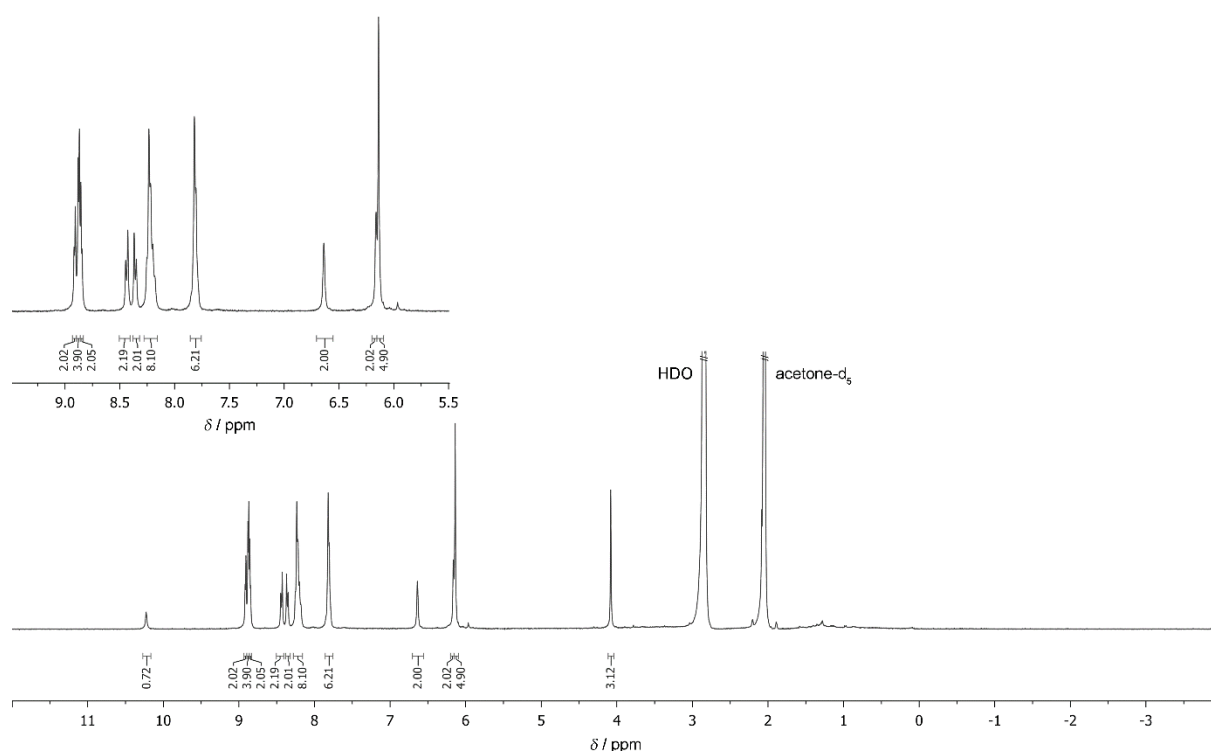
Figure S 2. ^{1}H NMR spectrum of [Zn-1][PF$_6$] in d$_6$-acetone.
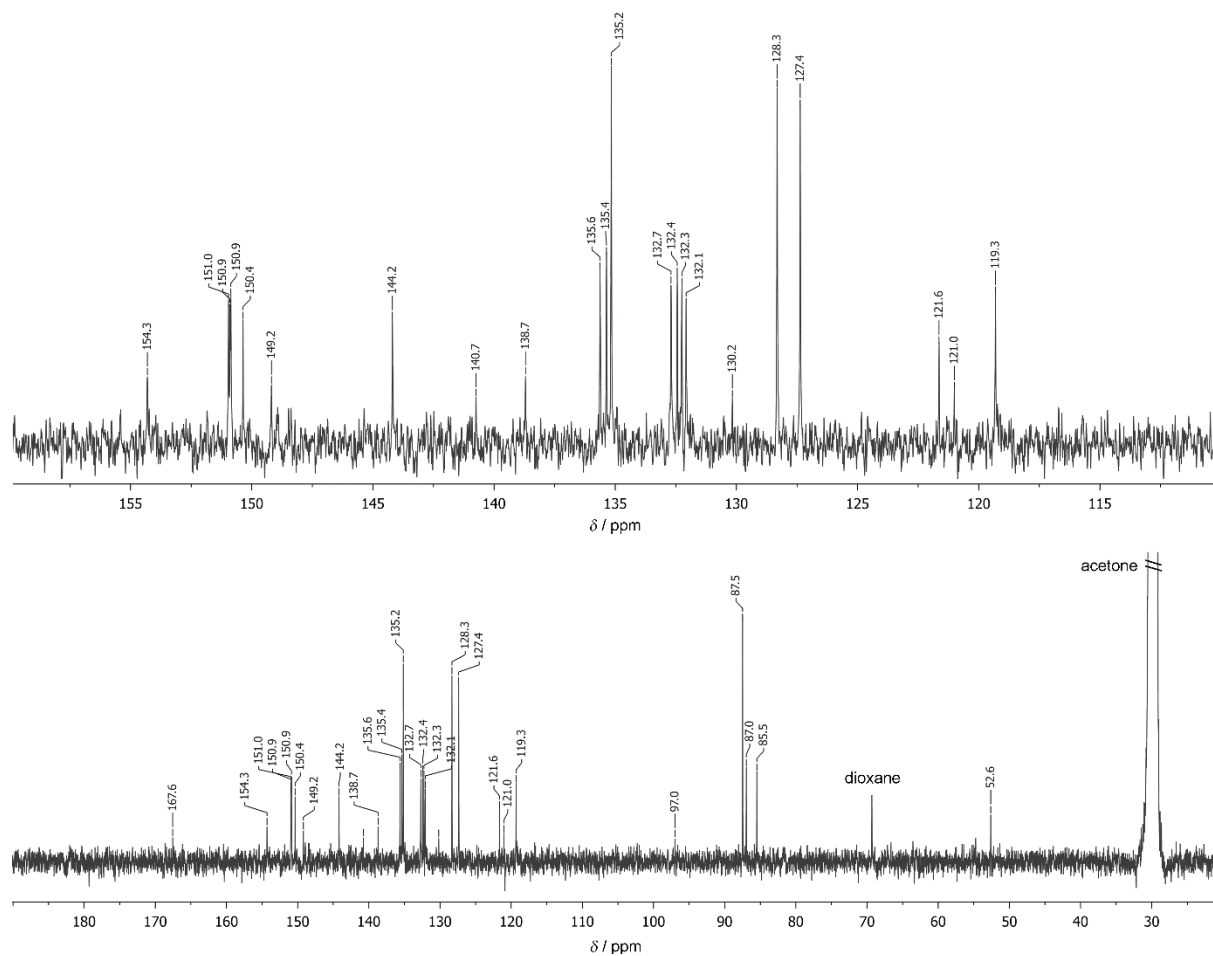
Figure S 3. ^{13}C{^{1}H} NMR spectrum of [Zn-1][PF$_6$] in d$_6$-acetone.
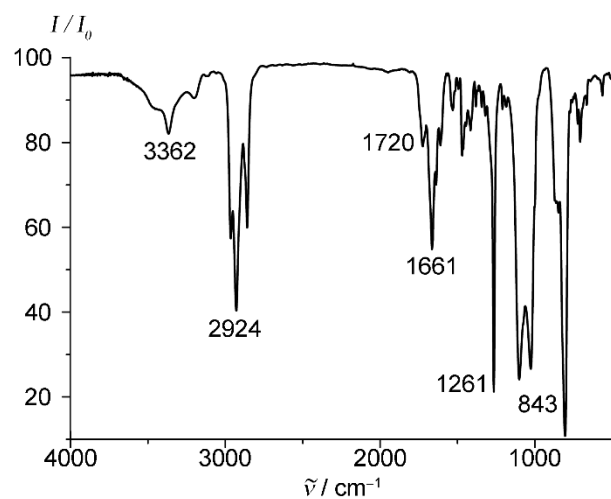
Figure S 4. IR spectrum of [Zn-1][PF$_6$] in KBr.

ε / 10^{-4} M^{-1} cm^{-1}
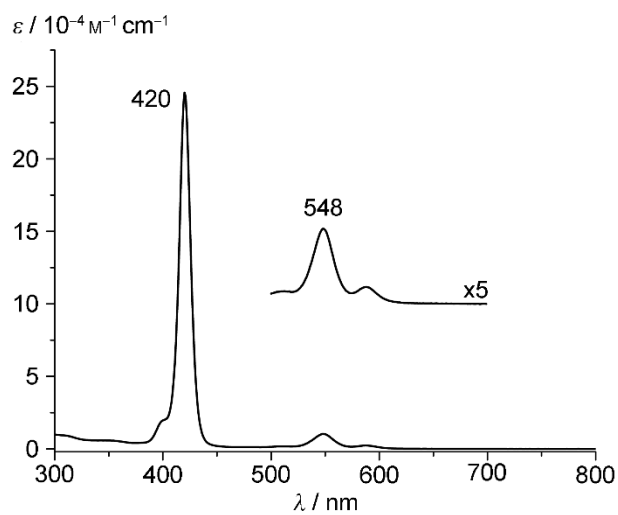
Figure S 5. UV/vis spectrum of [Zn-1][PF$_6$] in CH$_2$Cl$_2$.

ε / 10^{-4} M^{-1} cm^{-1}
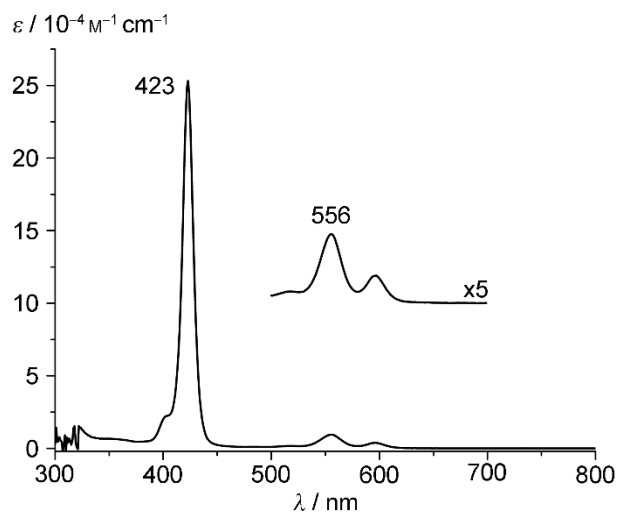
Figure S 6. UV/vis spectrum of [Zn-1][PF$_6$] in acetone.

emission / a.u.
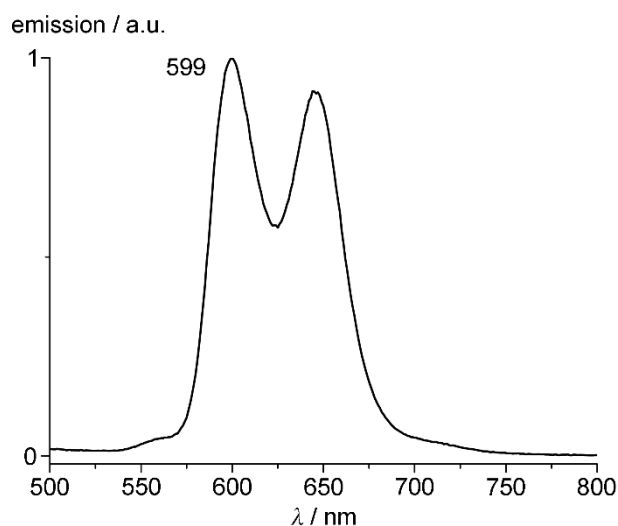
Figure S 7. Fluorescence spectrum of [Zn-1][PF$_6$] in CH$_2$Cl$_2$ (λ_{exc} = 420 nm).

emission / a.u.
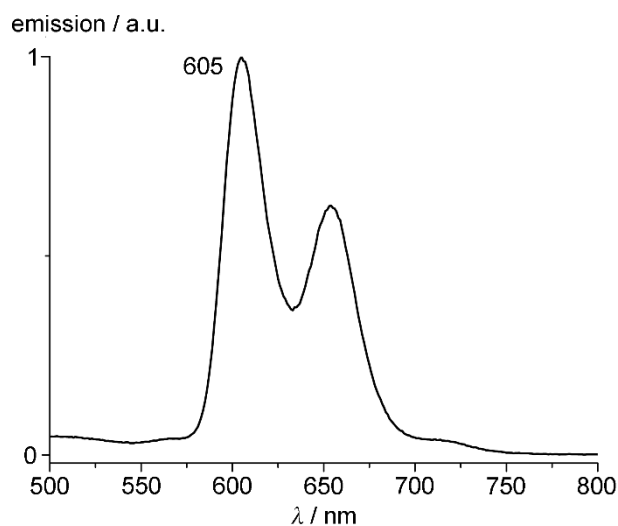
Figure S 8. Fluorescence spectrum of [Zn-1][PF$_6$] in acetone (λ_{exc} = 423 nm).
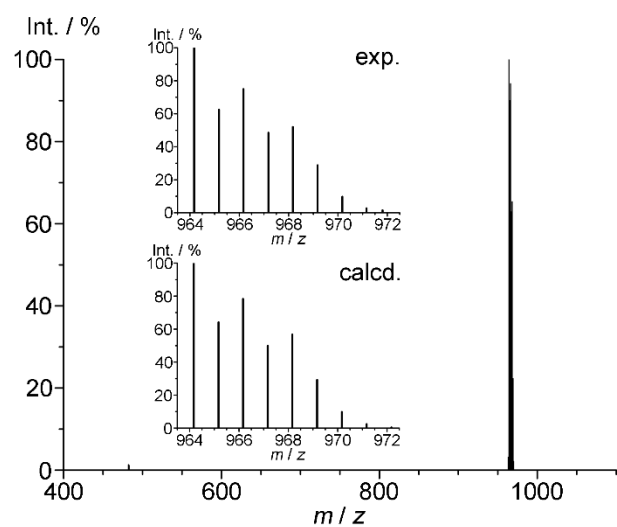
Figure S 9. ESI$^+$ mass spectrum of [Zn-1][PF$_6$] in MeOH and experimental and calculated isotopic pattern of the molecular ion peak.
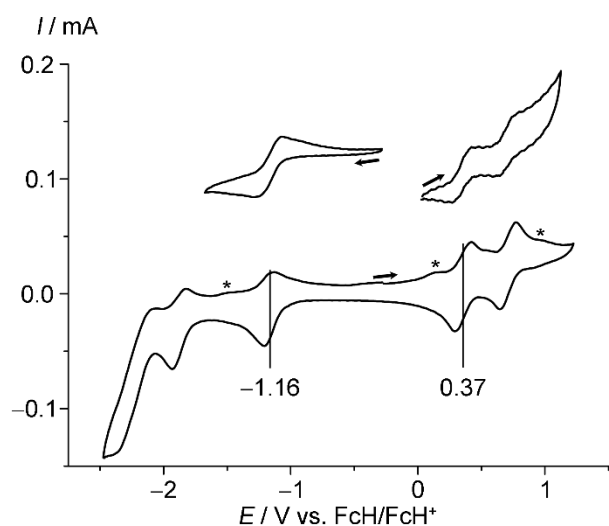
Figure S 10. Cyclic voltammogram of [Zn-1][PF$_6$] in CH$_2$Cl$_2$/[^{n}Bu$_4$N][PF$_6$] (scan rate 50 mV s^{-1}). * denote waves of a follow-up product formed after scanning to −2 V.
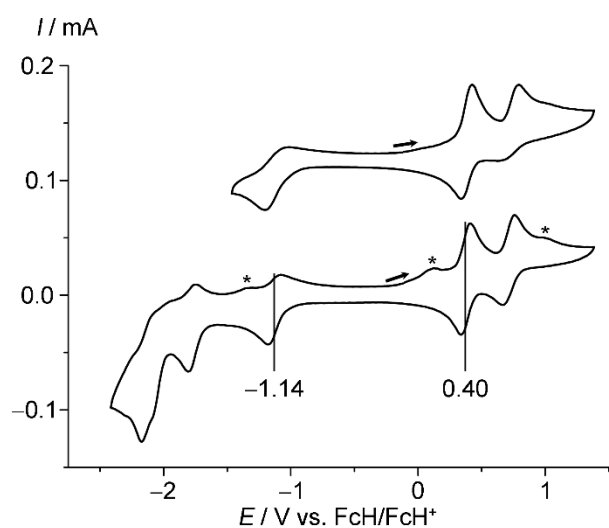
Figure S 11. Cyclic voltammogram of [Zn-1][PF$_6$] in CH$_3$CN/[^{n}Bu$_4$N][B(C$_6$F$_5$)$_4$] (scan rate 50 mV s^{-1}). * denote waves of a follow-up product formed after scanning to −2 V.
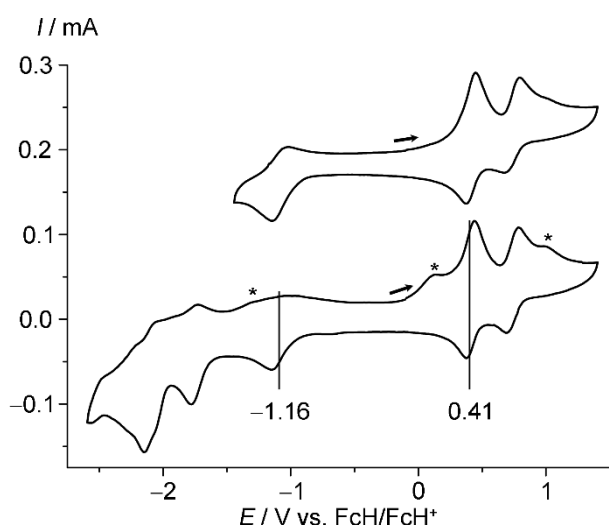
Figure S 12. Cyclic voltammogram of [Zn-1][PF$_6$] in CH$_3$CN/[^{n}Bu$_4$N][PF$_6$] (scan rate 100 mV s^{-1}). * denote waves of a follow-up product formed after scanning to −2 V.
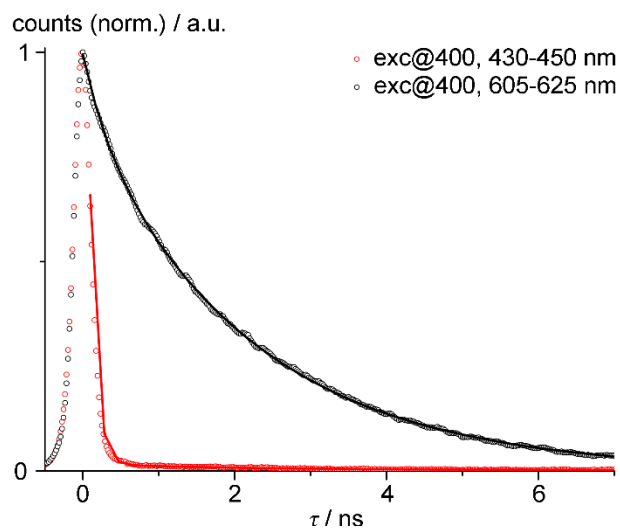
Figure S 13. Photoluminescence decay after excitation with 400 nm tracked from 430–450 nm (red, S$_2$ emission; biexponential fit τ = 0.1/2.2 ns) and 605–625 nm (black, S$_1$ emission; biexponential fit τ = 0.3/2.2 ns) and the corresponding fits (solid lines).
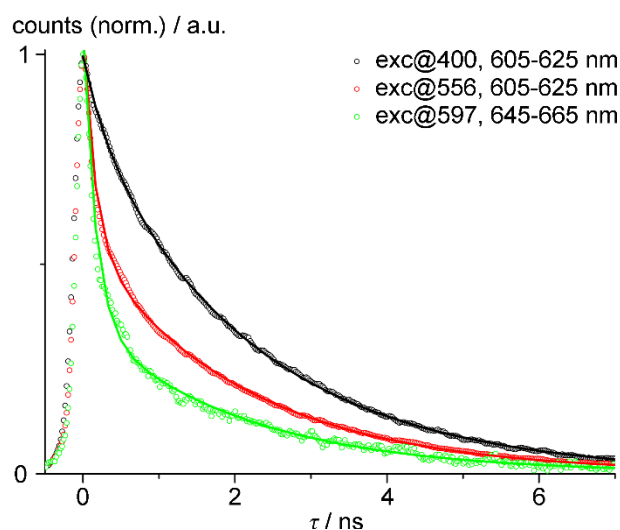
Figure S 14. Photoluminescence decay of the Q band emission after excitation with 400 nm (black; biexponential fit τ = 0.31/2.2 ns), 556 nm (red; biexponential fit τ = 0.16/2.1 ns) and 597 nm (green; biexponential fit τ = 0.17/2.1 ns) with corresponding biexponential fits (solid lines).
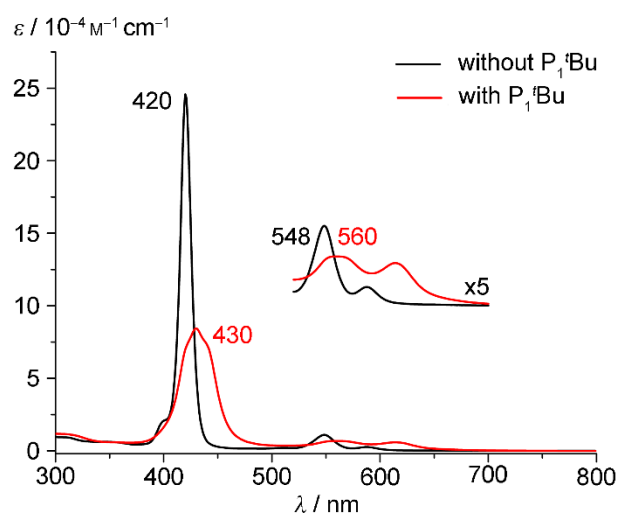
Figure S 15. UV/vis absorption spectra of [Zn-1][PF$_6$] in the absence and presence of 1 eq P$_1$^{t}Bu in CH$_2$Cl$_2$.

5.3 Supporting Information to Chapter 3.3: Prolongation of the Charge-Shifted State: Cobaltocenium Substituents as Electron Acceptors in a Photosynthetic Model Triad

Abbreviations: P(2H) = free base tetraphenylporphyrin; P(Zn) = zinc tetraphenylporphyrin

5.3.1 Experimental Section to Chapter 3.3.2

ML-56: [Cc-NHCO-P(Zn)-COOMe][PF$_6$] **A[PF$_6$]** (43.6 mg, 39.2 µmol, 1.0 eq) and 10 % aqueous potassium hydroxide solution (1 mL, 168 µmol, 4.3 eq) were dissolved in methanol (15 mL). The solution was stirred under argon atmosphere for 20 h. Water (30 mL) was added and the mixture extracted with dichloromethane (40 mL) and the solvent removed under reduced pressure. ^{1}H NMR spectroscopy measured in CD$_2$Cl$_2$ showed a decrease of the intensity ratio of the cobaltocenium and porphyrin core resonances due to the splitting of the dyad, supported by the yellow colored water phase (cleaved cobaltocenium). The intensity ratio between the resonances of the methyl group and the porphyrin core remained unperturbed. The amide bond was cleaved rather than the ester group.

ML-57-01: [Cc-NHCO-P(Zn)-COOMe][PF$_6$] **A[PF$_6$]** (4.5 mg, 4.05 µmol, 1.0 eq), water (2 mL, 111 mmol,) and concentrated sulfuric acid (0.1 mL, 1.87 mmol, 460 eq) were dissolved in methanol (20 mL). The solution was stirred at 50 °C under argon atmosphere for 15 h. Water (20 mL) and trimethylamine (1 mL) were added The color changed from green to purple, acetic acid (2 mL) and brine (10 mL) were added and the phase was extracted with dichloromethane (20 mL). The solvent was dried over Na$_2$SO$_4$ and the solvent was removed under reduced pressure. The ^{1}H NMR spectrum (in CD$_2$Cl$_2$) showed an unperturbed intensity ratio between the resonances of the porphyrin core, cobaltocenium and the methyl group (**A[PF$_6$]**).

ML-57-02: [Cc-NHCO-P(Zn)-COOMe][PF$_6$] **A[PF$_6$]** (4.5 mg, 4.05 µmol, 1.0 eq), water (1 mL) and concentrated sulfuric acid (0.15 mL, 2.82 mmol, 700 eq) were dissolved in dimethyl sulfoxide (10 mL). The solution was stirred at 95 °C under argon atmosphere for 18 h. Water (20 mL) and trimethylamine (1 mL) were added and the color changed from green to purple. Acetic acid (2 mL) and brine (10 mL) were added and the phase was extracted with dichloromethane (20 mL). The solvent was dried over Na$_2$SO$_4$ and the solvent was removed under reduced pressure. The ^{1}H NMR spectrum (in CD$_2$Cl$_2$) showed a decrease of the cobaltocenium to porphyrin intensity ratio due to the splitting of the dyad **A[PF$_6$]**.

5.3.2 Experimental Section to Chapter 3.3.3

ML61-01: H$_2$N-P(2H)-COOH **L** (10 mg, 15 µmol, 1.0 eq), sodium hydrogen carbonate (4.7 mg, 56 µmol, 3.8 eq) and di-*tert*-butyl carbonate (4.0 mg, 18 µmol, 1.3 eq) were dissolved/suspended in methanol

(5 mL). The mixture was sonicated for 4 h. The TLC control showed no turnover. ESI$^+$ mass spectrometry did not show Boc protected product resonances.

ML63-01: H$_2$N-P(2H)-COOH **L** (9.8 mg, 15 µmol, 1.0 eq), triethylamine (10 µL, 72 µmol, 4.9 eq) and di-*tert*-butyl carbonate (3.8 mg, 17 µmol, 1.2 eq) were dissolved in absolute tetrahydrofuran (20 mL) under argon atmosphere. The solution was stirred at 45°C for 20 h. ESI$^+$ mass spectrometry of the crude solution showed a signal for Boc protected product with an intensity of 12 % compared to the signal of the starting material **L**. The solvent was removed under reduced pressure and the crude product was purified by column chromatography (silica, hexanes/ethyl acetate 1:1; after the first spot, dichloromethane/methanol 9:1). ESI$^+$ mass spectrometry showed a signal for isocyanate protected product (O=C=N-P(2H)-COOH) with an intensity of 12 % compared to the resonances of the starting material.

ML63-02: H$_2$N-P(2H)-COOH **L** (10 mg, 15 µmol, 1.0 eq), triethylamine (10 µL, 72 µmol, 4.8 eq) and di-*tert*-butyl carbonate (76 mg, 350 µmol, 23 eq) were dissolved in absolute tetrahydrofuran (20 mL) under argon atmosphere. The solution was stirred under reflux for 3 h and additionally for 18h at r.t.. TLC control showed no turnover. A spatula tip of 4-(dimethylamino)pyridine was added and the solution was stirred for 5 h at r.t. The solvent was removed under vacuum, the crude product was purified by column chromatography (silica, hexanes/ethyl acetate 1:3 + 1 % trimethylamine; after second spot, dichloromethane/methanol 9:1). ^{1}H NMR spectroscopy showed no product resonances.

ML62-01: H$_2$N-P(2H)-COOMe **D** (10 mg, 15 µmol, 1.0 eq), trimethylamine (10 µL, 72 µmol, 4.9 eq) and di-*tert*-butyl carbonate (4.1 mg, 19 µmol, 1.3 eq) were dissolved in absolute tetrahydrofuran (20 mL) under argon atmosphere. The solution was stirred at 45°C for 20 h. The solvent was removed under reduced pressure. ^{1}H NMR spectroscopy showed no product resonances.

ML62-02: H$_2$N-P(2H)-COOMe **D** (10 mg, 15 µmol, 1.0 eq), triethylamine (10 µL, 72 µmol, 4.9 eq) and di-*tert*-butyl carbonate (76 mg, 350 µmol, 24 eq) were dissolved in absolute tetrahydrofuran (20 mL) under argon atmosphere. The solution was stirred under reflux for 3 h and additionally for 18 h at r.t.. TLC control showed a turnover of around 50 % (two equally intense colored spots). A spatula tip of 4-(dimethylamino)pyridine was added and the solution was stirred for 6 h at r.t. and additional 2 h at 40°C. The solvent was removed under reduced pressure, the crude product **E1/E2** was purified by column chromatography (silica, hexanes/ethyl acetate 3:1). A purple powder (12 mg, 12 µmol, 82 % yield) was isolated. ^{1}H NMR spectroscopy showed the doubly Boc protected product ((Boc)$_2$N-P(2H)-COOMe) **E2** resonances with some impurities in the aliphatic range.

(Boc)$_2$N-P(2H)-COOMe **E2**: R_f = 0.94 (hexanes/ethyl acetate 1:1). ^{1}H NMR (CD$_2$Cl$_2$): δ [ppm] = −2.86 (s, 2H, H^{NH}), 1.58 (s, 18H, H^{22}), 4.07 (s, 3H, H^{21}), 7.54 (d, 2H, $^3J_{HH}$ = 8.3 Hz, H$^{5.3}$), 7.82-7.74 (m, 6H,

$H^{10.3,10.4,20.3,20.4}$), 8.22-8.19 (m, 6H, $H^{10.2,5.2}$), 8.31 (d, 2H, $^3J_{HH}$ = 8.3 Hz, $H^{15.2}$), 8.42 (d, 2H, $^3J_{HH}$ = 8.3 Hz, $H^{15.3}$), 8.88-8.81 (m, 8H, $H^{2,3,7,8,12,13,17,18}$).
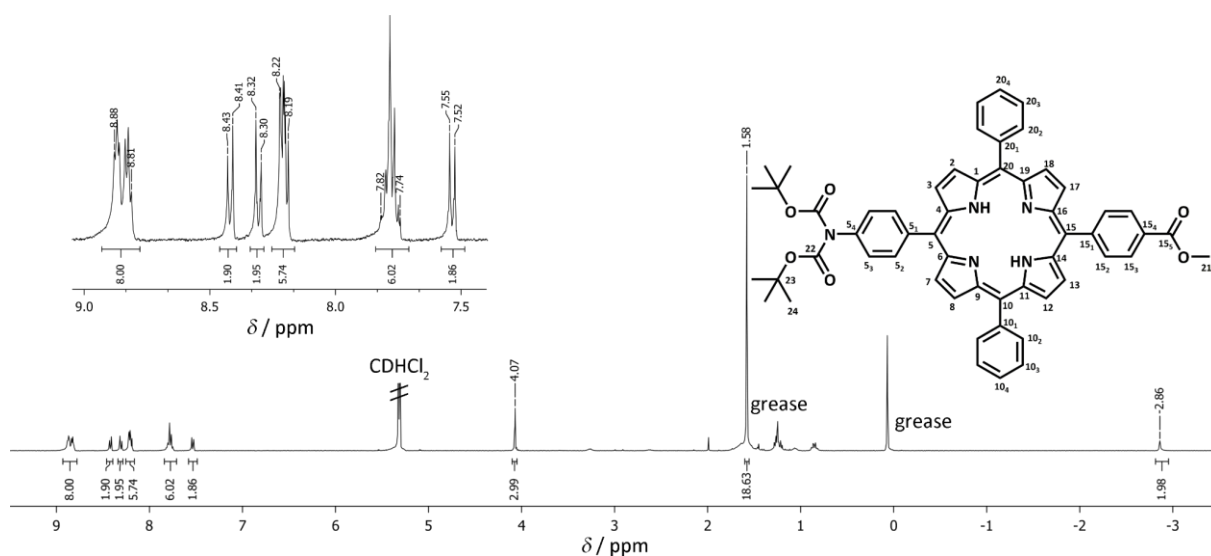

Figure S 1. ^{1}H NMR spectrum of (Boc)$_2$N-P(2H)-COOMe **E2** in d_2-dichloromethane. Atom numbering for NMR assignment.

5.3.3 Experimental Section to Chapter 3.3.4

ML67-02: Lithium hydroxide (95 %, 23 mg, 912 µmol, 6.2 eq) and 3 Å molecular sieve (40 mg) were suspended in absolute dimethylformamide (10 mL) and stirred for 90 minutes under argon atmosphere. H$_2$N-P(2H)-COOCH$_3$ **D** (101 mg, 146 µmol, 1.0 eq) was added and the solution was stirred for 45 minutes. Benzyl bromide (50 µL, 420 µmol, 2.9 eq) was added and the solution was stirred over night (14 h). TLC control showed no remaining starting material. Brine (50 mL) was added and the solution was extracted with dichloromethane (3x20 mL). The organic phase was washed with water (3x30 mL), dried over sodium sulfate and the solvent was removed under reduced pressure. The crude product **I1/I2** was purified by column chromatography (silica, hexanes/ethyl acetate 6:1, 2:1), yielding two purple powders. Yield 11.0 mg (14.1 µmol, 9.7 %) of mono benzylated **(I1)** and 56.0 mg (64.5 µmol, 44 %) of doubly benzylated **(I2)** product.

<u>Bn-NH-P(2H)-COOCH$_3$ **I1**</u>: R_f = 0.29 (hexanes/ethyl acetate 6:1). MS (FD, CH$_2$Cl$_2$): obs. m/z (%) = 777.42 (100) [M]$^+$; calcd for [M]$^+$ = 777.31. ^{1}H NMR (CD$_2$Cl$_2$): δ [ppm] = −2.81 (s, 2H, H^{NH}), 4.07 (s, 3H, H^{21}), 4.59 (s, 2H, H^{22}), 4.66 (s, 1H, H^{NH}), 7.03 (d, 2H, $^3J_{HH}$ = 8.3 Hz, H$^{5.3}$), 7.35 (t(overlaid), 2H, H^{26}), 7.45 (t, 1H, $^3J_{HH}$ = 7.5 Hz, H^{25}), 7.57 (d, 2H, $^3J_{HH}$ = 7.2 Hz, H^{24}), 7.75-7.80 (m, 6H, H$^{10.3,10.4,20.3,20.4}$), 8.00 (2H, d, $^3J_{HH}$ = 8.3 Hz, H$^{5.2}$), 8.22 (d, 4H, $^3J_{HH}$ = 6.0 Hz, H$^{10.2,20.2}$), 8.30 (d, 2H, $^3J_{HH}$ = 8.1 Hz, H$^{15.2}$), 8.42 (d, 2H, $^3J_{HH}$ = 8.0 Hz, H$^{15.3}$), 8.80-8.98 (m, 8H, H^{2,3,7,8,12,13,17,18}).

<u>Bn$_2$N-P(2H)-COOCH$_3$ **I2**</u>: R_f = 0.40 (hexanes/ethyl acetate 6:1). MS (FD, CH$_2$Cl$_2$): obs. m/z (%) = 867.54 (100) [M]$^+$; calcd for [M]$^+$ = 867.35. ^{1}H NMR (CD$_2$Cl$_2$): δ [ppm] = −2.76 (s, 2H, H^{NH}), 4.08 (s, 3H, H^{21}), 4.92 (s, 4H, H^{22}), 7.11 (d, 2H, $^3J_{HH}$ = 8.4 Hz, H$^{5.3}$), 7.33 (t, 2H, $^3J_{HH}$ = 6.8 Hz, H^{26}), 7.42-7.48 (m, 8H, H^{24,25}), 7.75-

7.80 (m, 6H, $H^{10.3,10.4,20.3,20.4}$), 8.00 (d, 2H, $^3J_{HH}$ = 8.4 Hz, $H^{5.2}$), 8.23 (d, 4H, $^3J_{HH}$ = 6.0 Hz, $H^{10.2,20.2}$), 8.30 (d, 2H, $^3J_{HH}$ = 8.0 Hz, $H^{15.2}$), 8.41 (d, 2H, $^3J_{HH}$ = 8.0 Hz, $H^{15.3}$), 8.80-9.01 (m, 8H, $H^{2,3,7,8,12,13,17,18}$).
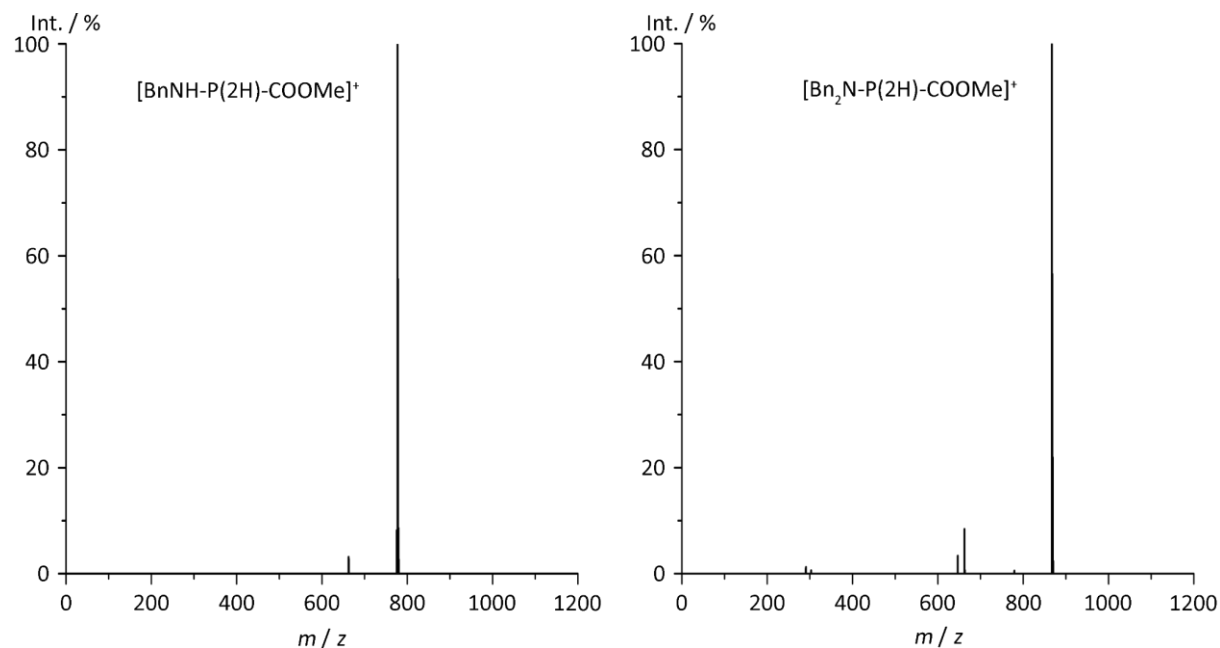

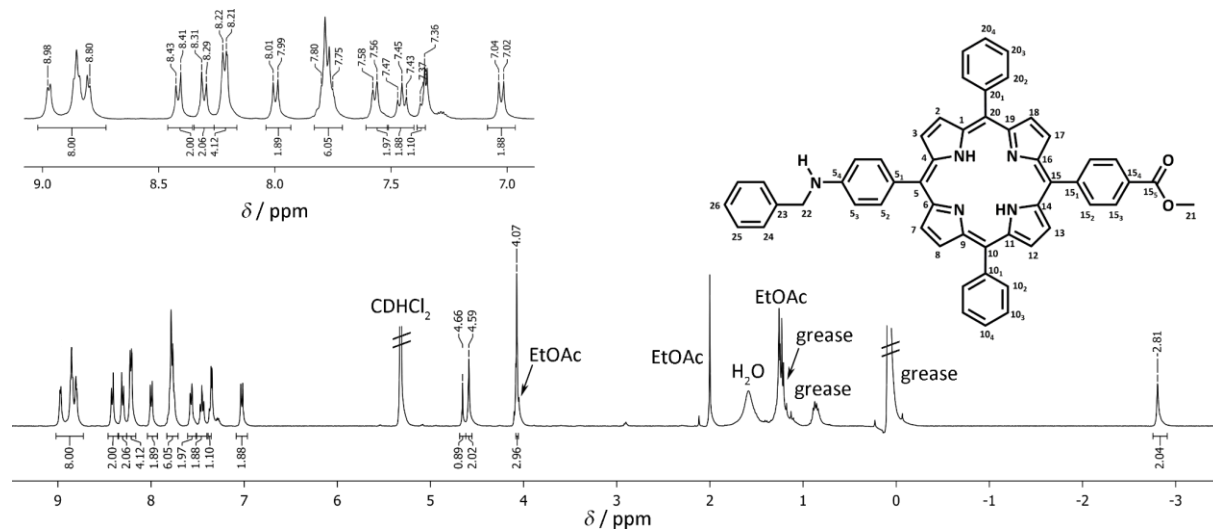**Figure S 2. FD mass spectra of Bn-NH-P(2H)-COOMe I1 (left) and Bn₂N-P(2H)-COOMe I2 (right) in dichloromethane.**

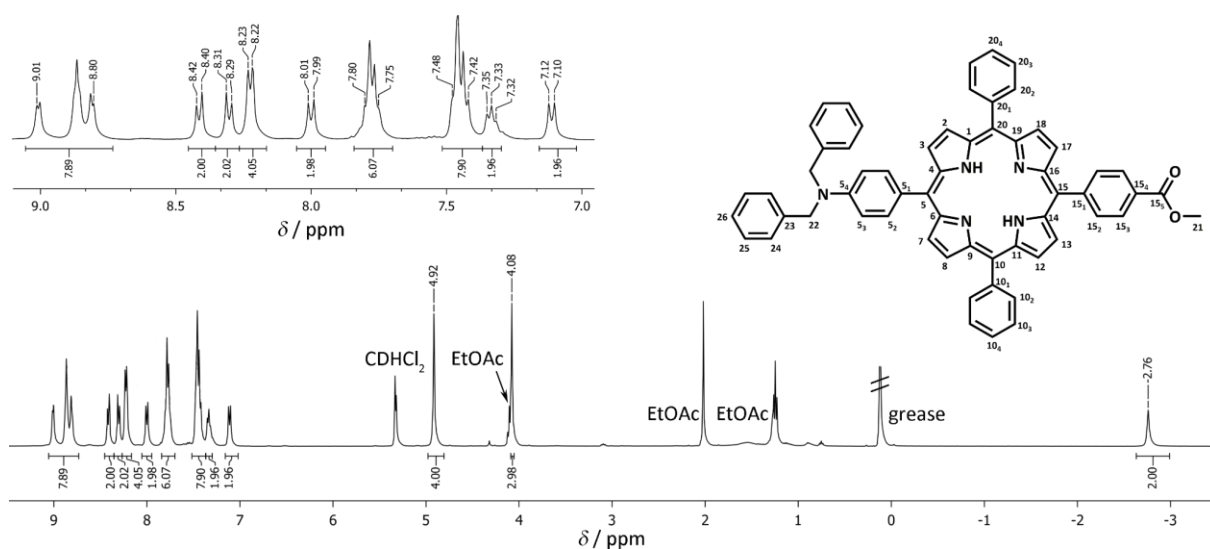**Figure S 3. ¹H NMR spectrum of Bn-NH-P(2H)-COOMe I1 in d_2-dichloromethane. Atom numbering for NMR assignment.**

Figure S 4. ^{1}H NMR spectrum of (Bn)$_2$N-P(2H)-COOMe I2 in d_2-dichloromethane. Atom numbering for NMR assignment.
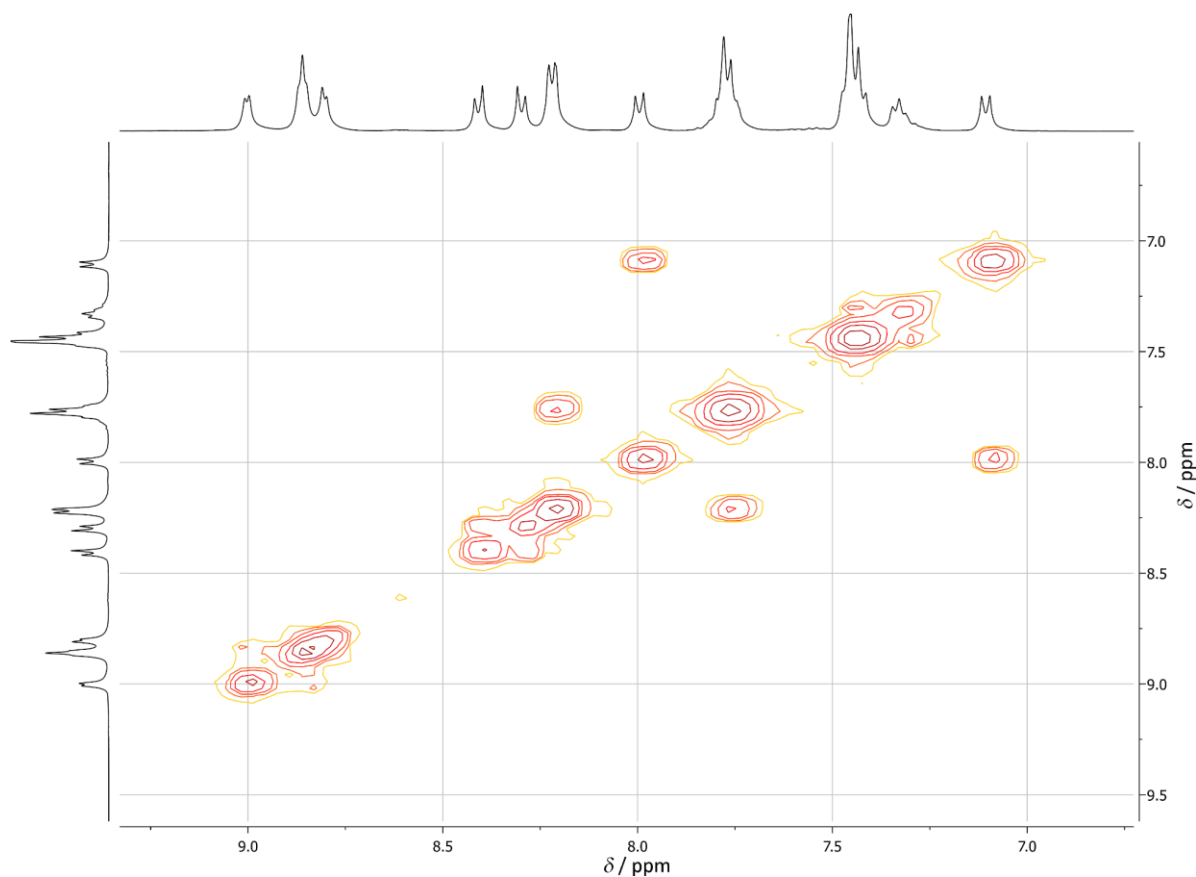
Figure S 5. [1]H[1]H COSY spectrum of (Bn)$_2$N-P(2H)-COOMe I2 in d_2-dichloromethane.

ML68-01: Bn-NH-P(2H)-COOCH$_3$ **I1** (11.0 mg, 14.1 µmol, 1.0 eq), potassium hydroxide (89 mg, 1.58 mmol, 113 eq) and water (2 mL) were dissolved in absolute tetrahydrofuran (30 mL) and refluxed for 20 h. TLC control showed no remaining starting material. The solvent was removed under reduced pressure, water (50 mL) was added and the solution was acidified with acetic acid until pH 4. The

solution was extracted with dichloromethane (3x20 mL), dried over sodium sulfate and the solvent was removed under reduced pressure, yielding **J1** as a purple powder.

<u>Bn-NH-P(2H)-COOH **J1**</u>: MS (ESI$^+$, MeOH/TFA): obs. *m/z* (%) = 764.32 (100) [M+H]$^+$; calcd for [M+H]$^+$ = 764.30. ^{1}H NMR (CD$_2$Cl$_2$): δ [ppm] = −2.81 (s, 2H, H^{NH}), 4.60 (s, 2H, H^{22}), 7.04 (d, 2H, $^3J_{HH}$ = 7.9 Hz, H$^{5.3}$), 7.36 (t, 1H, $^3J_{HH}$ = 7.2 Hz, H^{26}), 7.46 (t, 2H, $^3J_{HH}$ = 7.1 Hz, H^{25}), 7.58 (d, 2H, $^3J_{HH}$ = 7.0 Hz, H^{24}), 7.72-7.82 (m, 6H, H$^{10.3,10.4,20.3,20.4}$), 8.01 (2H, d, $^3J_{HH}$ = 8.0 Hz, H$^{5.2}$), 8.15-8.25 (m, 6H, H$^{10.2,20.2,15.2}$), 8.41 (d, 2H, $^3J_{HH}$ = 6.7 Hz, H$^{15.3}$), 8.80-9.00 (m, 8H, H^{2,3,7,8,12,13,17,18}), NH not observed.

ML72-01: Bn$_2$N-P(2H)-COOCH$_3$ **I2** (31.0 mg, 35.7 µmol, 1.0 eq), potassium hydroxide (98.5 mg, 1.75 mmol, 49 eq) and water (3 mL) were dissolved in absolute tetrahydrofuran (20 mL) and refluxed for 16 h. TLC control showed no remaining starting material. The solvent was removed under reduced pressure, water (50 mL) was added and the solution was acidified with acetic acid until pH 4. The solution was extracted with dichloromethane (3x20 mL), dried over sodium sulfate and the solvent was removed under reduced pressure, yielding **J2** as a purple powder. Yield 20.0 mg (23.4 µmol, 66 %).

<u>Bn$_2$-N-P(2H)-COOH **J2**</u>: ^{1}H NMR (CD$_2$Cl$_2$): δ [ppm] = −2.81 (s, 2H, H^{NH}), 4.95 (s, 4H, H^{22}), 7.14 (d, 2H, $^3J_{HH}$ = 8.6 Hz, H$^{5.3}$), 7.33 (t, 2H, $^3J_{HH}$ = 6.8 Hz, H^{26}), 7.42-7.52 (m, 8H, H^{24,25}), 7.74-7.82 (m, 6H, H$^{10.3,10.4,20.3,20.4}$), 8.01 (2H, d, $^3J_{HH}$ = 8.2 Hz, H$^{5.2}$), 8.21 (d, 4H, $^3J_{HH}$ = 6.1 Hz, H$^{10.2,20.2}$), 8.31 (d, 2H, $^3J_{HH}$ = 8.2 Hz, H$^{15.2}$) 8.46 (d, 2H, $^3J_{HH}$ = 8.5 Hz, H$^{15.3}$), 8.80-9.01 (m, 8H, H^{2,3,7,8,12,13,17,18}).
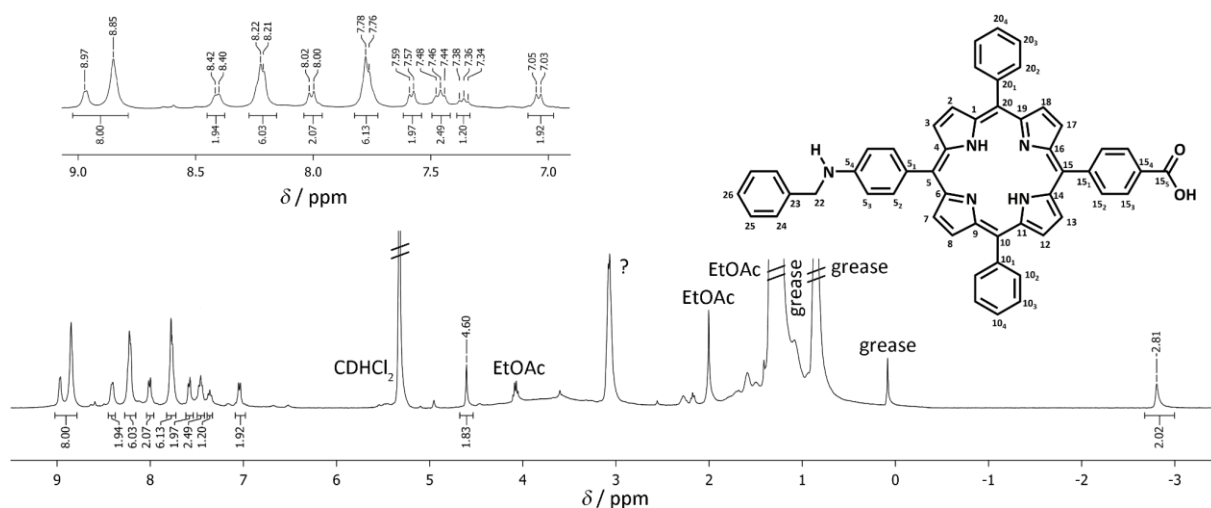

Figure S 6. ^{1}H NMR spectrum of Bn-NH-P(2H)-COOH J1 in *d*$_2$-dichloromethane. Atom numbering for NMR assignment.
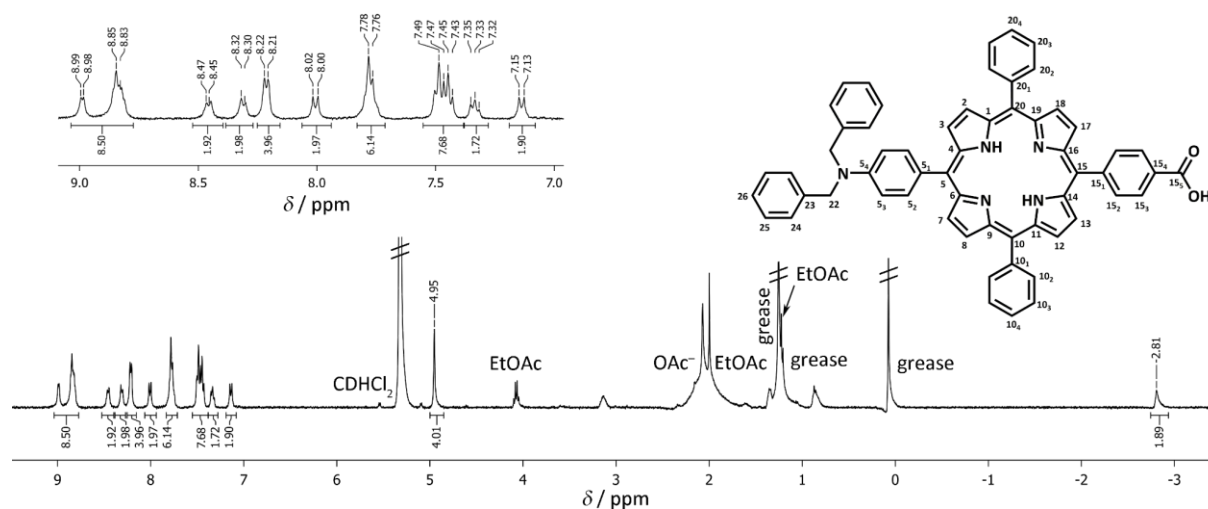
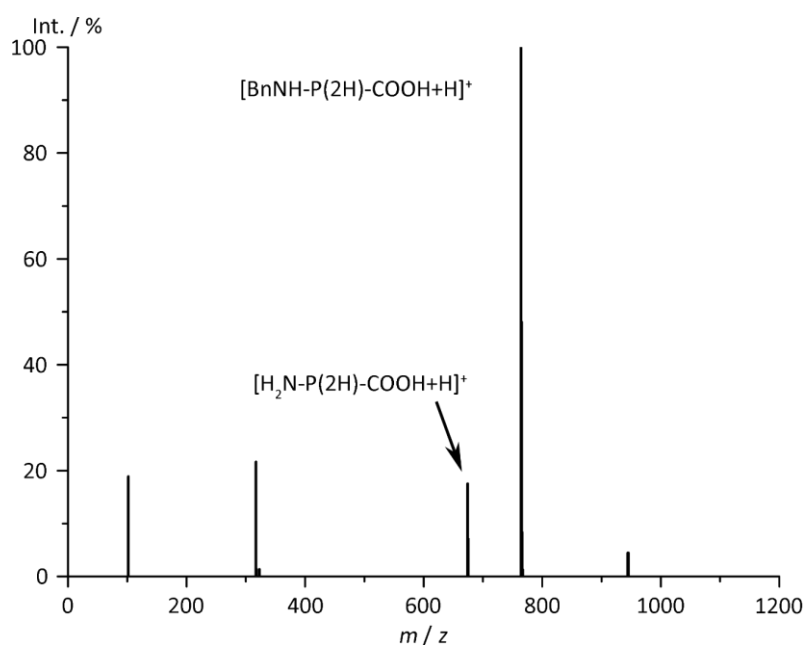**Figure S 7.** ^{1}H NMR spectrum of (Bn)$_2$N-P(2H)-COOH J2 in d_2-dichloromethane. Atom numbering for NMR assignment.

Figure S 8. ESI$^+$ mass spectrum of Bn-NH-P(2H)-COOH J1 in 90 % dichloromethane / 10 % acetonitrile.

ML73-04: Bn-NH-P(2H)-COOH **J1** (37.7 mg, 49.4 µmol, 1.0 eq), pyridine (0.7 mL) and thionyl chloride (0.1 mL, 1.37 mmol, 28 eq) were dissolved in absolute toluene (60 mL) under argon atmosphere and sonicated for 5 minutes. The solution was stirred for 220 min and the solvent was removed under reduced pressure. The solid was washed with absolute toluene (30 mL) and the solvent was removed under reduced pressure. Aminoferrocene (108 mg, 536 µmol, 11 eq), absolute triethylamine (1 mL) and absolute toluene (60 mL) were added and the solution was stirred for 18 h. The crude product **K1** was purified by column chromatography (silica, dichloromethane : triethylamine 100:2), yielding a purple powder of **K1**. Yield 10.2 mg (10.1 µmol, 20 %). Additional product **K1** (26 mg) could be separated, which was still contaminated with around 20 % aminoferrocene.

<u>Bn-NH-P(2H)-CONH-Fc **K1**</u>: MS (FD, CH$_2$Cl$_2$): obs. m/z (%) = 946.67 (100) [M]$^+$; calcd. for [M]$^+$ = 946.31.
^{1}H NMR (CD$_2$Cl$_2$): δ [ppm] = −2.79 (s, 2H, H^{NH}), 4.15 (s, 2H, H^{23}), 4.30 (s, 5H, H^{24}), 4.60 (s, 3H, H^{25,NH}),
4.87 (s, 2H, H^{22}), 7.05 (d, 2H, $^3J_{HH}$ = 8.1 Hz, H$^{5.3}$), 7.36 (t, 1H, $^3J_{HH}$ = 6.6 Hz, H^{29}), 7.46 (t, 2H, $^3J_{HH}$ = 7.1 Hz,
H^{28}), 7.58 (d, 2H, $^3J_{HH}$ = 7.0 Hz, H^{27}), 7.63 (s, 1H, H^{amide}), 7.74-7.83 (m, 6H, H$^{10.3,10.4,20.3,20.4}$), 8.01 (2H, d,
$^3J_{HH}$ = 8.1 Hz, H$^{5.2}$), 8.80-8.90 (m, 6H, H$^{10.2,20.2,15.2}$), 8.35 (d, 2H, $^3J_{HH}$ = 7.7 Hz, H$^{15.3}$), 8.80-9.01 (m, 8H,
H^{2,3,7,8,12,13,17,18}).
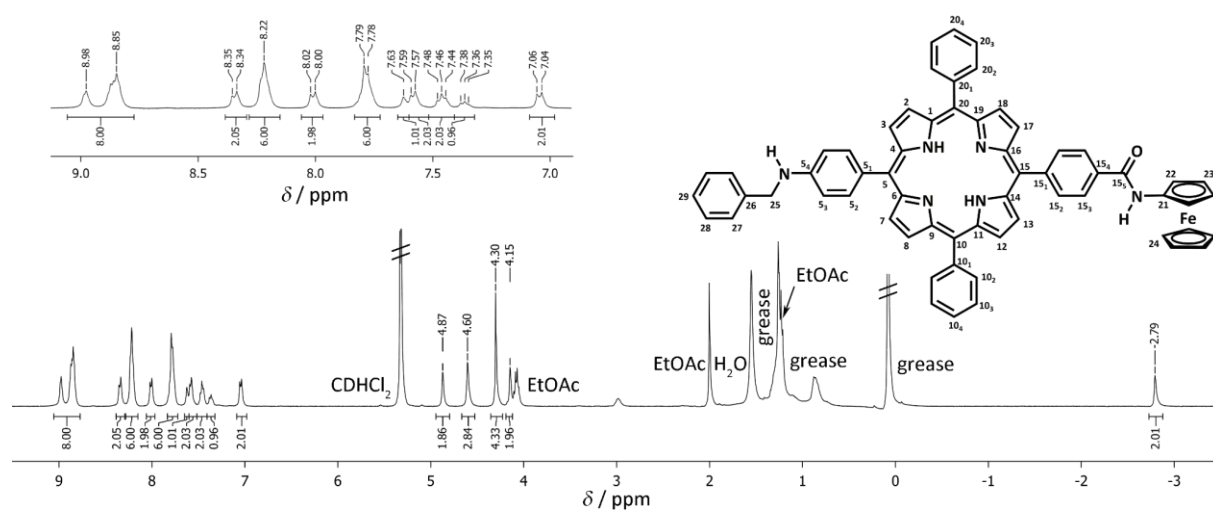
Figure S 9. ^{1}H NMR spectrum of Bn-NH-P(2H)-CONH-Fc K1 in d_2-dichloromethane. Atom numbering for NMR assignment.
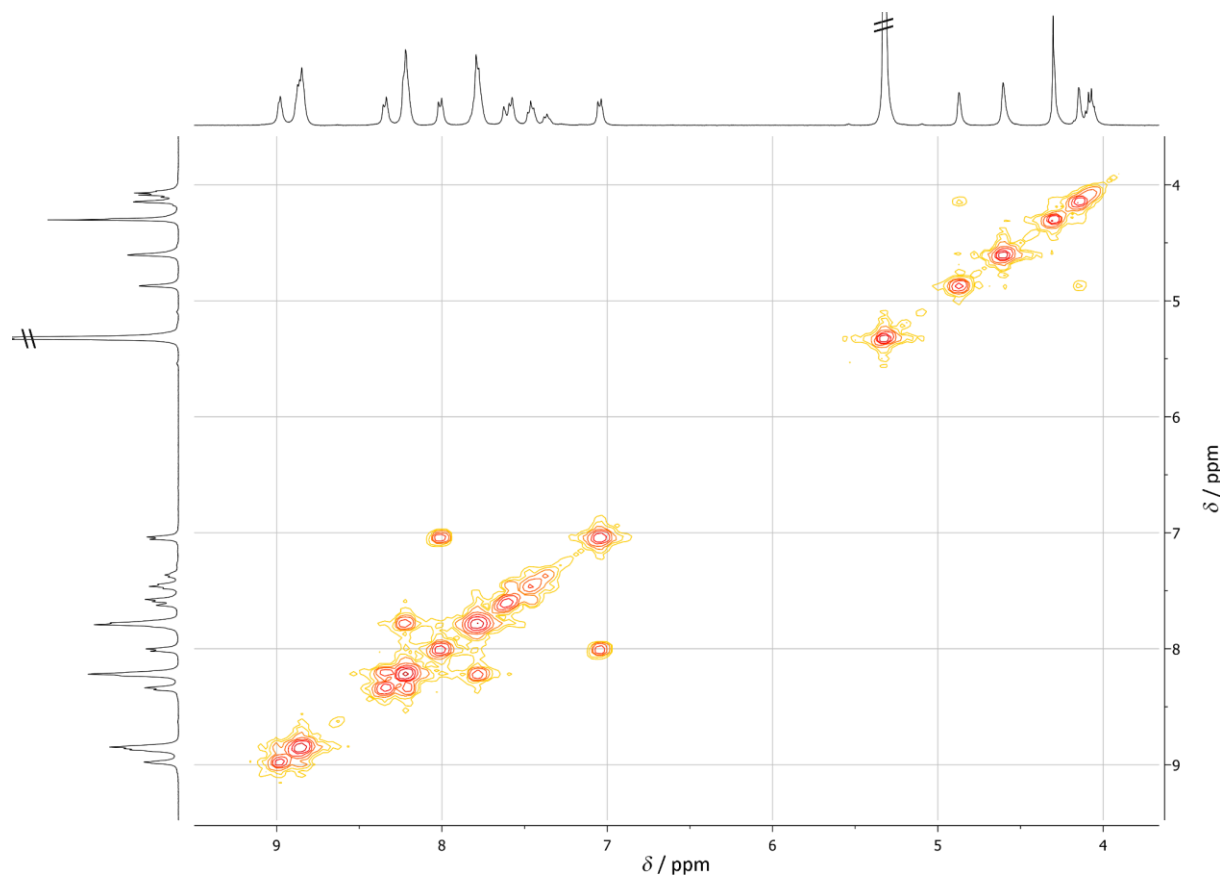

Figure S 10. ^{1}H^{1}H COSY spectrum of Bn-NH-P(2H)-CONH-Fc K1 in d_2-dichloromethane.
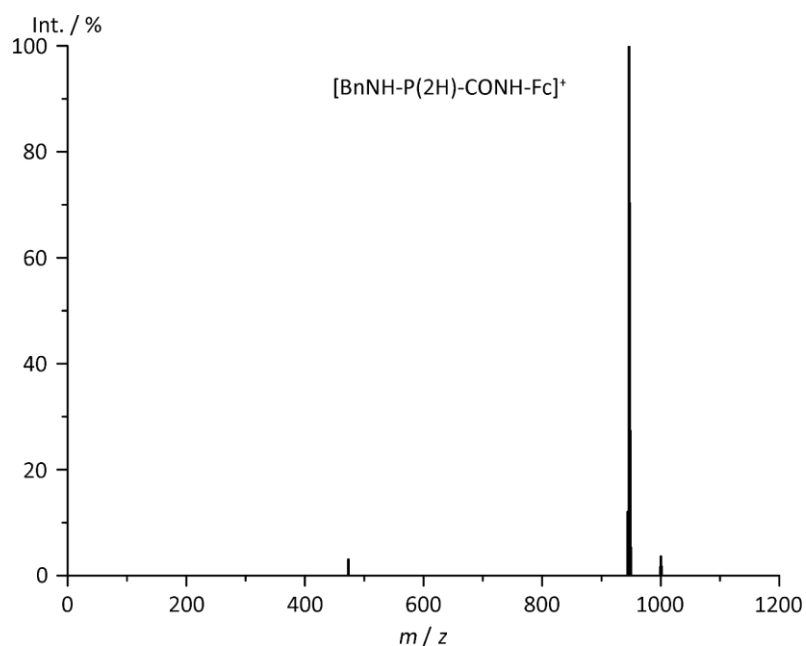
143

Figure S 11. FD mass spectrum of Bn-NH-P(2H)-CONH-Fc K1 in dichloromethane.

ML74-01: Bn-NH-P(2H)-CONH-Fc **K1** (1.86 mg, 1.96 µmol, 1.0 eq) and palladium on activated carbon (10 %, 0.23 mg, 0.2 µmol, 0.1 eq) were suspended in methanol (24 mL). The solution was "freeze pumped" twice to remove oxygen. The solution was frozen and the argon atmosphere was removed under reduced pressure. A ballon filled with hydrogen was connected and the reaction flask was charged with hydrogen. The frozen solution was melted and vigorously stirred. TLC control each hour showed one new spot. After 20 h the solvent was removed under reduced pressure and resolved in dichloromethane (10 mL). The solution was filtered through a 0.2 µm PTFE syringe filter and the solvent was removed under reduced pressure. Mass spectrometry showed peaks of the side product of the splitting of the amide bond (Bn-NH-P(2H)-CH(OH)-NH$_2$) instead of the benzyl group (**H**).

<u>Bn-NH-P(2H)-CH(OH)-NH$_2$:</u> MS (ESI$^+$, CH$_3$OH): obs. m/z (%) = 764.68 (100) [M]$^+$; calcd for [M]$^+$: = 764.33.
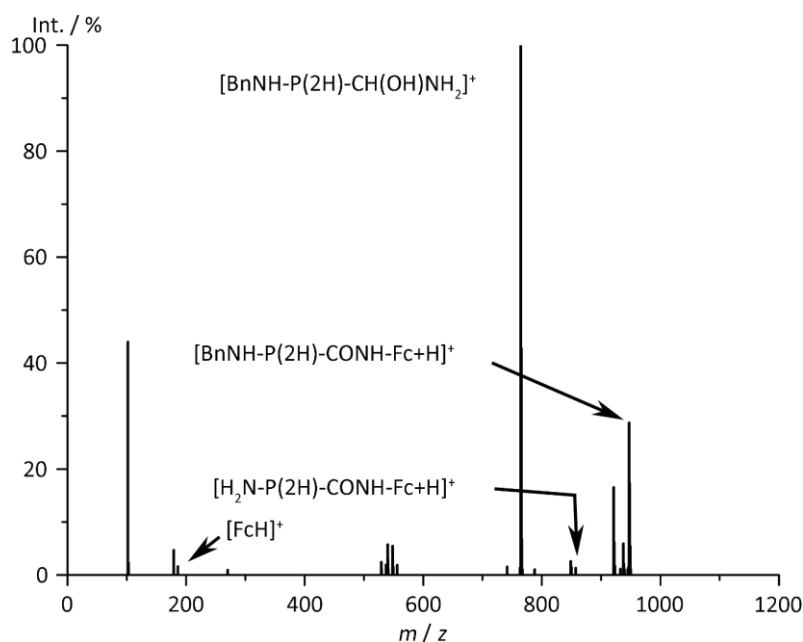
Figure S 12. ESI+ mass spectrum of Bn-NH-P(2H)-CH(OH)-NH$_2$ in methanol.

ML74-02: Bn-NH-P(2H)-CONH-Fc **K1** (0.8 mg, 0.8 µmol, 1.0 eq) and palladium on activated carbon (10 %, 0.23 mg, 0.2 µmol, 0.3 eq) were suspended in methanol (24 mL). The solution was sonicated for 5 minutes and under vigorous stirring, formic acid (0.5 mL) was added. The color changed to green immediately, and after 5 seconds to yellow/red. After 11 min the solvent was removed under reduced pressure and the residue resolved in dichloromethane (10 mL). The solution was filtered through a 0.2 µm PTFE syringe filter and the solvent was removed under reduced pressure. Mass spectrometry showed peaks of the side product of the splitting of the amide bond (Bn-NH-P(2H)-CH(OH)-NH$_2$) instead of the benzyl group (**H**).

5.3.4   Experimental Section to Chapter 3.3.5

*5.3.4.1   Fmoc-NH-P(2H)-COOH **L***

H$_2$N-P(2H)-COOH **L** (118 mg, 171 µmol, 1.0 eq) was dissolved in absolute dioxane (150 mL) under argon atmosphere. NaHCO$_3$ (938 mg, 11.1 mmol, 65 eq) and 9 flourenylmethoxycarbonyl chloride (196 mg, 758 µmol, 4.4 eq) were added and the solution was stirred for 1 h. Water (3 mL) was added and the solution was stirred until all starting material **L** was consumed (TLC control after overall 4 h). Acetic acid (6 mL) was added to decompose remaining NaHCO$_3$ and the solvent was removed under reduced pressure. Acetic acid (15 mL) and dichloromethane (50 mL) were added and the organic phase was washed with water (2x30 mL). The organic phase was dried over sodium sulfate and the solvent was removed under reduced pressure. The solid was washed on a silica column with acetone/triethylamine (100:5) and eluted with acetone/acetic acid (100:5). The solvent was removed under reduced pressure, the purple solid was washed on a second silica column with toluene/trimethylamine (100:5) and eluted

with toluene/dichloromethane/acetic acid (100:25:5). The solvent was removed under reduced pressure, yielding **M** as purple powder. Yield 96.2 mg (107 μmol, 63 %).

<u>Fmoc-NH-P(2H)-COOH</u> **M**: MS (FD, CH$_2$Cl$_2$): m/z (%) = 895.9 (100) [M]$^+$. HR-MS (ESI$^+$, MeOH): obs. m/z (%) = 896.3236; calcd for [M+H]$^+$: m/z (%) = 896.3237. ^{1}H NMR: (d_8-THF): δ [ppm] = −2.69 (s, 2H, H^{NH}), 4.37 (t, 1H, $^3J_{HH}$ = 5.8 Hz, H^{23}), 4.68 (d, 2H, $^3J_{HH}$ = 6.16 Hz, H^{22}), 7.35 (t, 2H, $^3J_{HH}$ = 7.3 Hz, H^{26}), 7.41 (t, 2H, $^3J_{HH}$ = 7.1 Hz, H^{27}), 7.73-7.82 (m, 8H, H$^{25,10.3,10.4,20.3,20.4}$), 7.84 (d, 2H, $^3J_{HH}$ = 7.2 Hz, H^{28}), 7.95 (s, 2H, H$^{5.3}$), 8.11 (d, 2H, $^3J_{HH}$ = 8.2 Hz, H$^{5.2}$), 8.19-8.24 (m, 4H, H$^{10.2, 20.2}$), 8.31 (d, 2H, $^3J_{HH}$ = 8.0 Hz, H$^{15.2}$), 8.44 (d, 2H, $^3J_{HH}$ = 8.0 Hz, H$^{15.3}$), 8.73-8.95 (m, 8H, (H^{2,3,7,8,12,13,17,18}), 9.32 (s, 1H, H^{amide}), OH not observed. ^{13}C{^{1}H} NMR (d_8-THF): δ [ppm] = 48.5 (C^{23}), 67 (C^{22}), 117.4 (C$^{5.3}$), 119.8 (C^{15}), 120.9 (C^{28}), 121.2 (C^{10,20}), 121.5 (C^5), 126.0 (C^{25}), 127.8 (C$^{10.3,20.3}$), 128.0 (C^{26}), 128.6 (C$^{10.4,20.4}$), 128.8 (C^{27}), 129.1 (C$^{15.3}$), 131.6 (C$^{15.4}$), 135.5 (C$^{10.2,20.2,15.2}$), 135.9 (C$^{5.2}$), 137.2 (C$^{5.1}$), 140.7 (C$^{5.4}$), 142.6 (C^{29}), 143.4 (C$^{10.1,20.1}$), 145.4 (C^{24}), 147.8 (C$^{15.1}$), 154.7 (C^{21}), 168.0 (C$^{15.5}$).
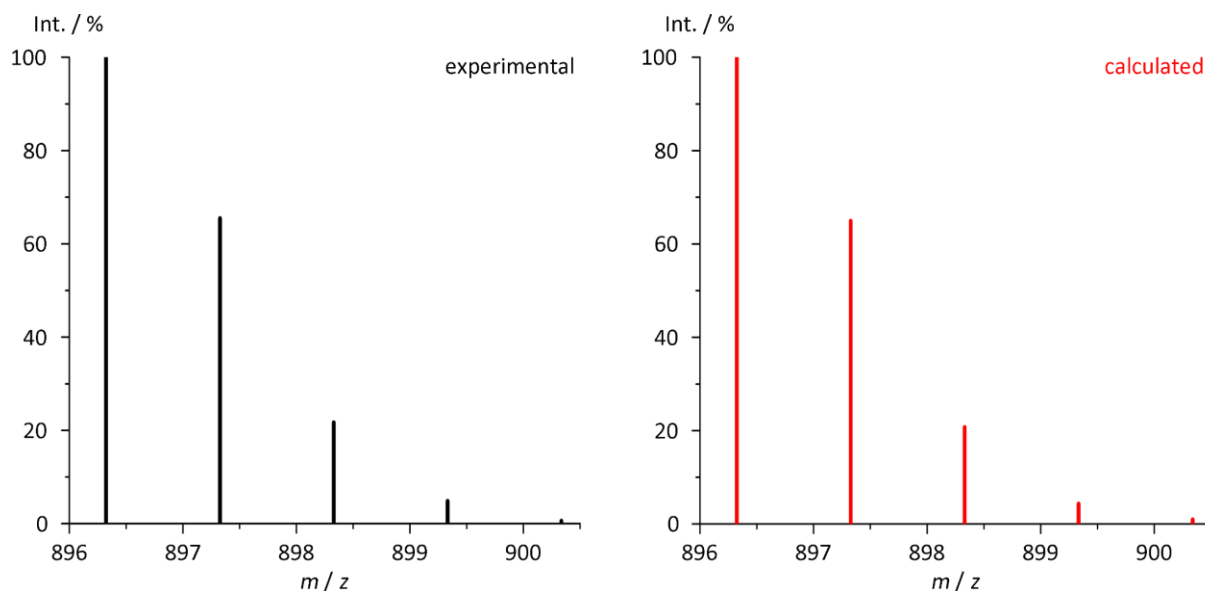

Figure S 13. HR-ESI$^+$ mass spectra of Fmoc-NH-P(2H)-COOH M in CH$_3$OH, experimental and calculated isotopic pattern of the molecular ion peak.
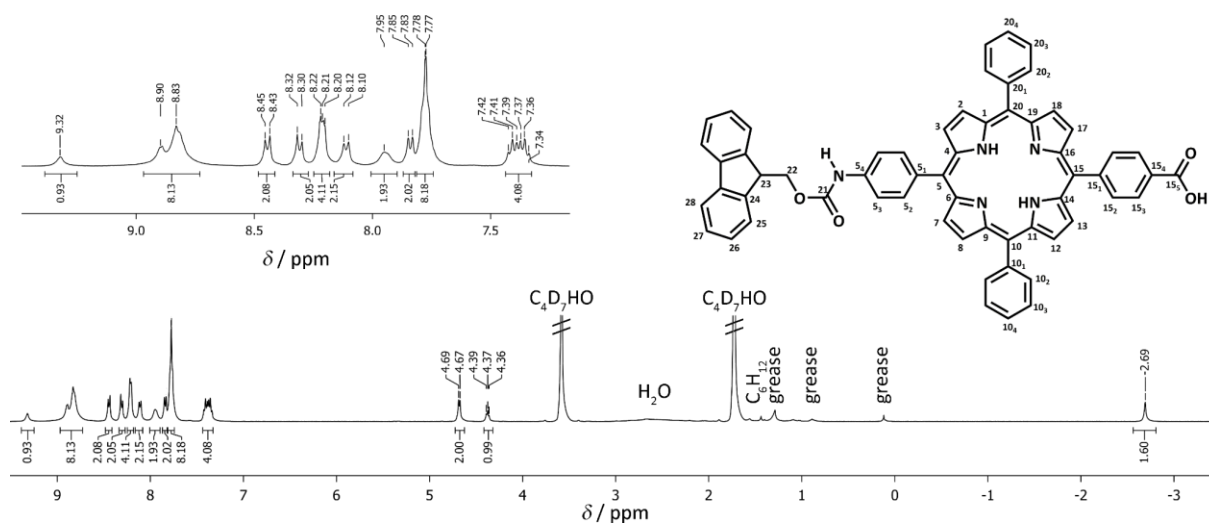
Figure S 14. ^{1}H NMR spectrum of Fmoc-NH-P(2H)-COOH M in d_8-tetrahydrofuran. Atom numbering for NMR assignment.
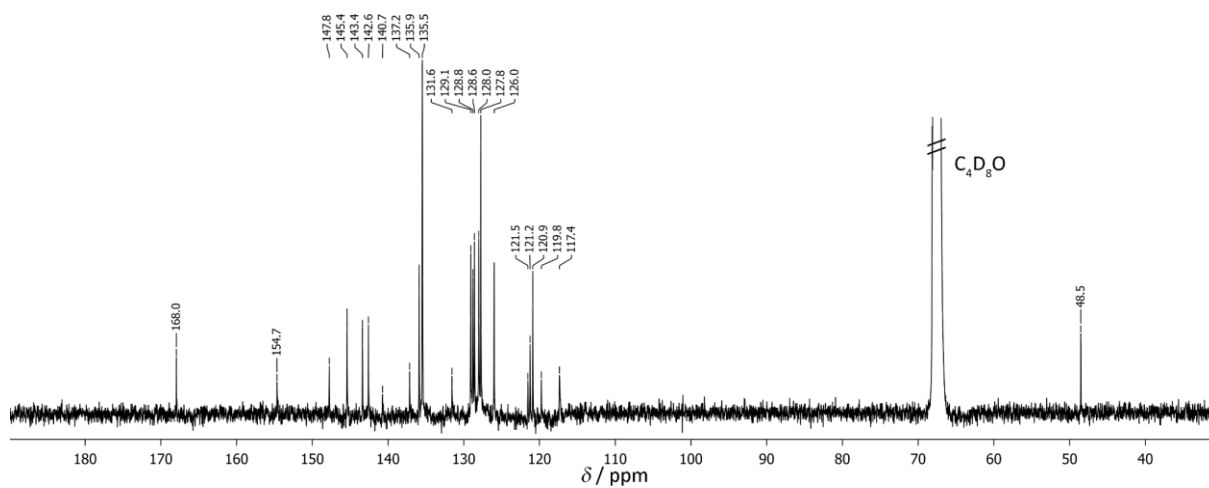

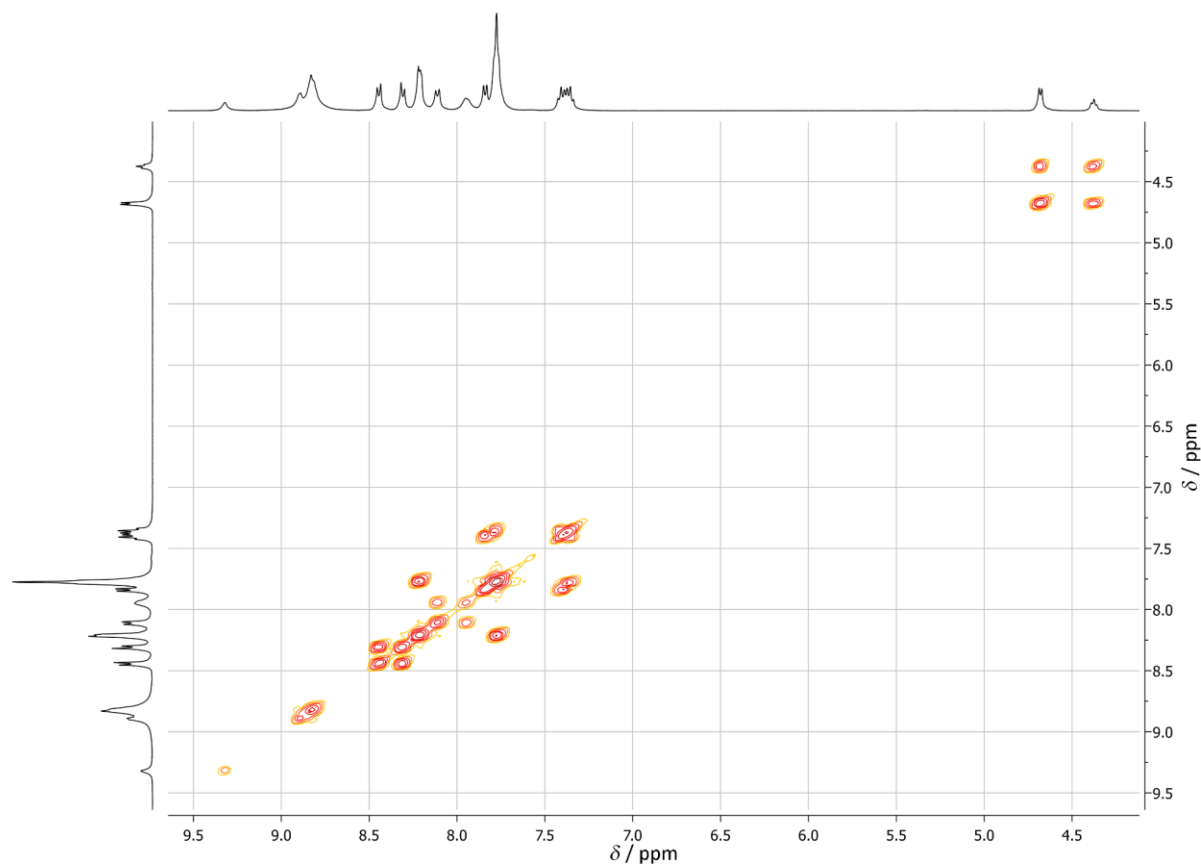**Figure S 15.** ^{13}C NMR spectrum of Fmoc-NH-P(2H)-COOH M in d_8-tetrahydrofuran.

Figure S 16. ^{1}H^{1}H COSY spectrum of Fmoc-NH-P(2H)-COOH M in d_8-tetrahydrofuran.
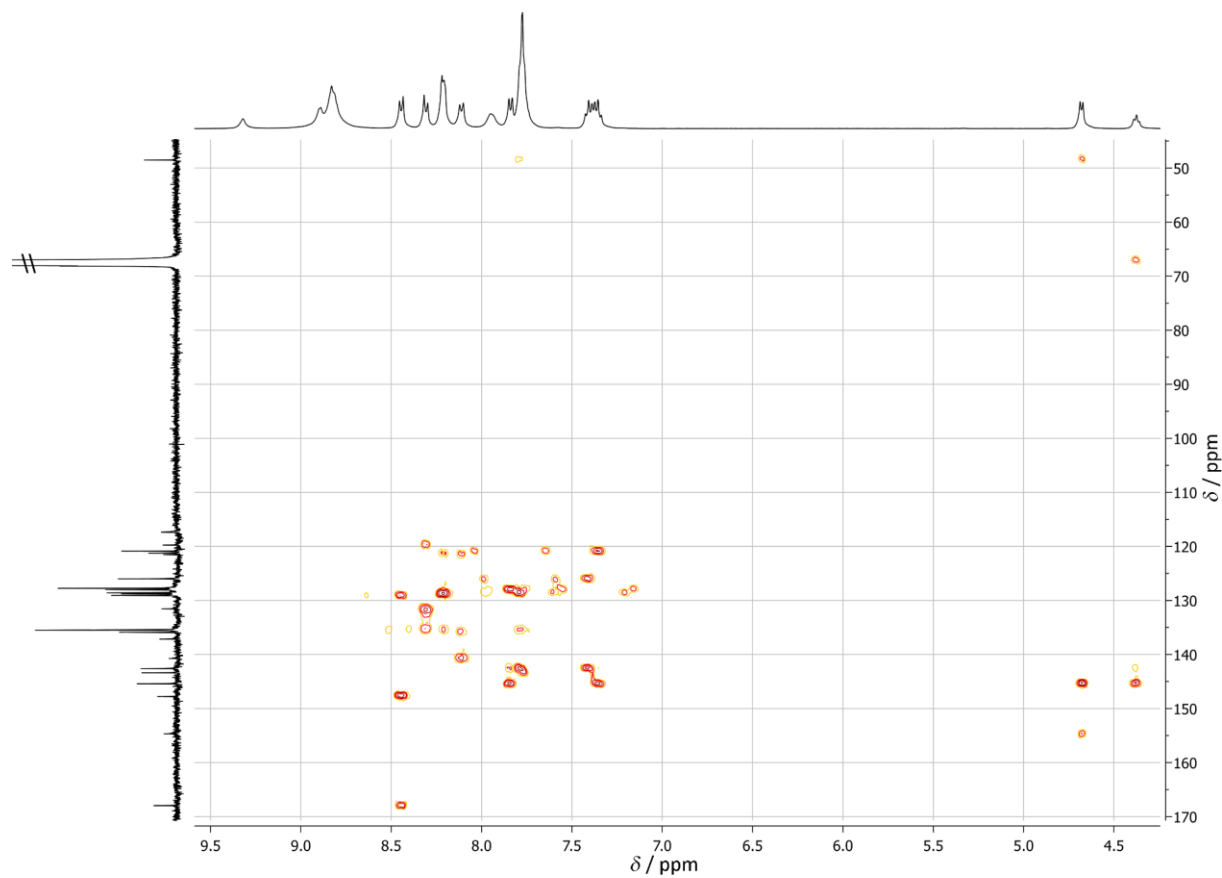

Figure S 17. ^{1}H^{13}C HMBC spectrum of Fmoc-NH-P(2H)-COOH M in d_8-tetrahydrofuran.

5.3.4.2 *H₂N-P(2H)-CONH-Fc* **H**

Fmoc-P(2H)-COOH **M** (70.4 mg, 78.6 µmol, 1.0 eq) was dissolved in absolute dichloromethane (50 mL) under argon atmosphere and Ghosez's reagent (1-chloro-*N,N,*2-trimethyl-1-propenylamine, 0.5 mL, 3.63 mmol, 46 eq) was added. The solution was refluxed for 7 h and the solvent was removed under reduced pressure. The residue was washed with absolute dichloromethane (30 mL) and the solvent was removed under reduced pressure. The solid was dissolved in absolute dichloromethane (60 mL), aminoferrocene (40.1 mg, 199 µmol, 2.5 eq) and absolute trimethylamine (0.35 mL) were added. The solution was stirred for 13 h (over night) and TLC control showed no starting material **M** anymore. Piperidine (2 mL, 20.2 mmol, 260 eq) was used to cleave the Fmoc group. TLC control showed an incomplete reaction. After 35 min, piperidine (3 mL) was added again. After additional 50 min, TLC control showed full conversion. After overall 100 min, the solution was washed with water (2x50 mL), dried over sodium sulfate and the solvent was removed under reduced pressure. The purple solid, mixed with a colorless solid, was purified by column chromatography (silica, toluene : ethyl acetate : triethylamine 100:50:2). The solid still contained small amounts of aminoferrocene, so the purification by column chromatography was repeated, yielding **H** as purple powder. Yield 66.1 mg (77.1 µmol, 98 %).

H₂N-P(2H)-CONH-Fc **H:** MS (ESI⁺, CH₃CN): *m/z* (%) = 428.634 (22.79) $[M+H]^{2+}$, 856.262 $[M]^+$, 857.267 $[M+H]^+$. HR-MS (ESI⁺, CH₃CN): obs. *m/z* (%) = 856.2620; calcd. for $[M]^+$ = 856.2613. ¹H NMR (CD₂Cl₂): δ [ppm] = –2.81 (s, 2H, H^{NH}), 4.10 (s, 2H, H^{NH2}), 4.31 (s, 2H, H^{23}), 4.39 (s, 5H, H^{24}), 5.02 (s, 2H, H^{22}), 7.07 (d, 2H, $^3J_{HH}$ = 8.1 Hz, $H^{5.3}$), 7.52 (s, 1H, H^{amide}), 7.73-7.83 (m, 6H, $H^{10.3,10.4,20.3,20.4}$), 7.98 (d, 2H, $^3J_{HH}$ = 8.1 Hz, $H^{5.2}$), 8.18 (d, 2H, $^3J_{HH}$ = 7.7 Hz, $H^{15.2}$), 8.22 (d, 4H, $^3J_{HH}$ = 6.0 Hz, $H^{10.2,\ 20.2}$), 8.33 (d, 2H, $^3J_{HH}$ = 7.8 Hz, $H^{15.3}$), 8.82-9.00 (m, 8H, ($H^{2,3,7,8,12,13,17,18}$). ¹³C{¹H} NMR (CD₂Cl₂): δ [ppm] = 62.5 (C^{22}), 65.4 (C^{23}), 69.9 (C^{24}), 95.6 (C^{21}), 113.8 ($C^{5.3}$), 118.8 (C^{15}), 120.8 ($C^{10,20}$), 122.1 (C^5), 125.9 ($C^{15.3}$), 127.3 ($C^{20.3,10.3}$), 128.3 ($C^{10.4,20.4}$), 131.1-132.5 ($C^{2,3,7,8,12,13,17,18}$), 132.2 ($C^{5.1}$), 134.7 ($C^{15.1}$), 135.1 ($C^{10.2,20.2}$), 135.3 ($C^{15.2}$), 136.3 ($C^{5.2}$), 142.6 ($C^{10.1,20.1}$), 146.1, 147.2 ($C^{5.4,15.4}$), 166.1 ($C^{15.5}$).
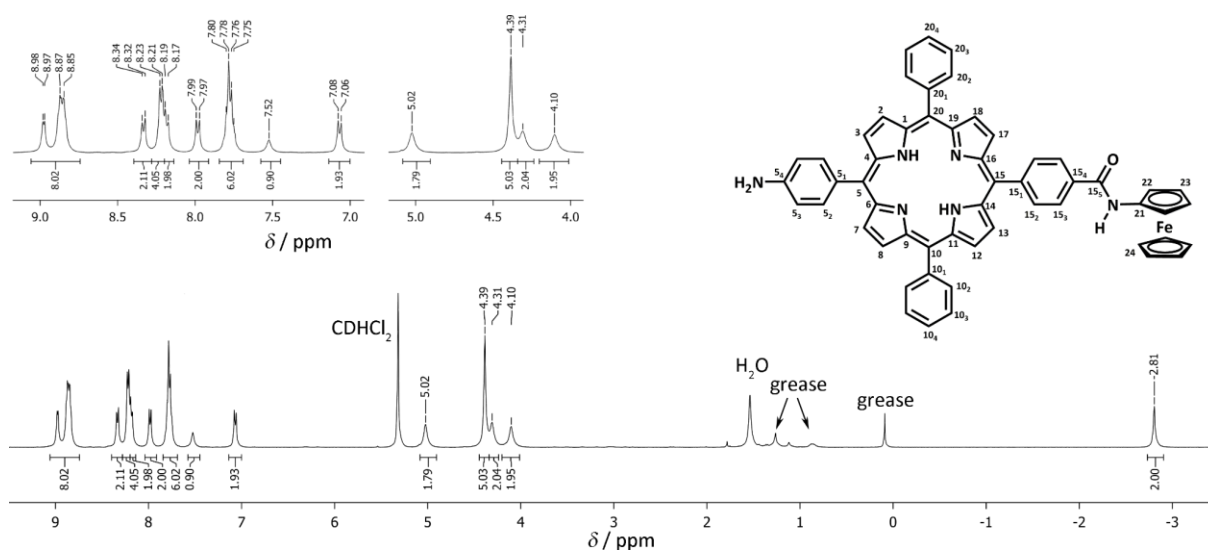
Figure S 18. ^{1}H NMR spectrum of H_2N-P(2H)-CONH-Fc H in d_2-dichloromethane. Atom numbering for NMR assignment.

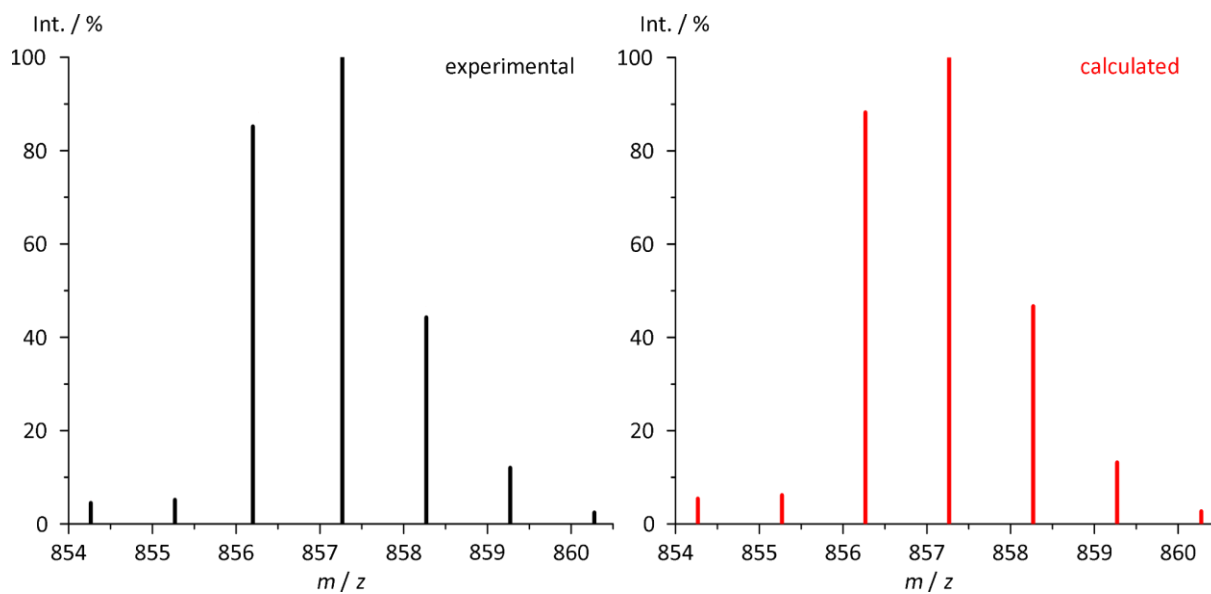**Figure S 19.** HR-ESI$^+$ mass spectra of H_2N-P(2H)-CONH-Fc H in acetonitrile, experimental and calculated isotopic pattern of the molecular ion peak.

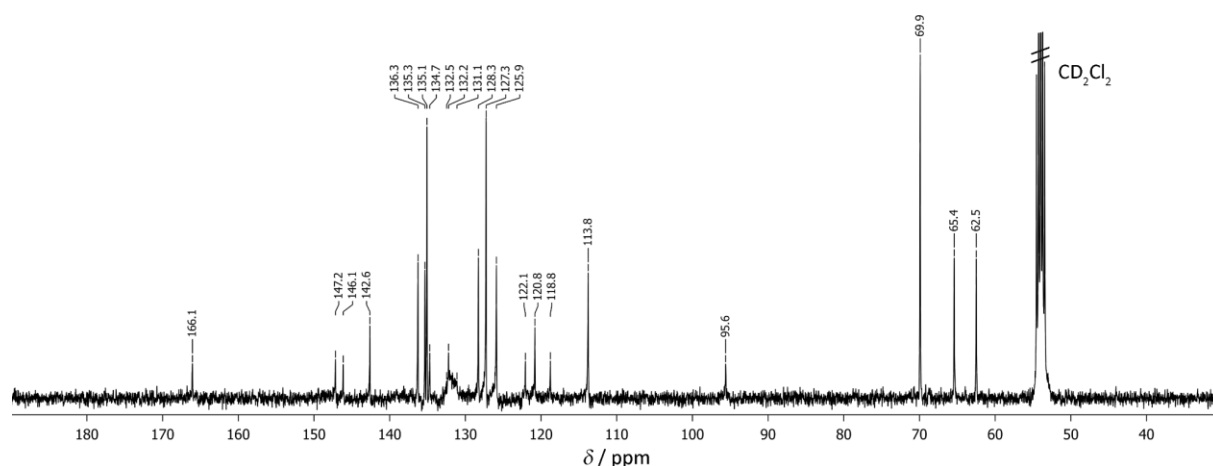**Figure S 20.** ^{13}C NMR spectrum of H$_2$N-P(2H)-CONH-Fc H in *d$_2$*-dichloromethane.

5.3.4.3   [Cc-CONH-P(Zn)-CONH-Fc][PF$_6$] 1[PF$_6$]

ML106: Carboxycobaltocenium hexafluoridophosphate (67.5 mg, 179 µmol, 2.3 eq) and Ghosez's reagent (0.4 mL, 2.90 mmol, 38 eq) were dissolved in dichloromethane (40 mL) under argon atmosphere and the solution was refluxed for 5 and 30 min. The solvent was removed under reduced pressure, the solid was washed with dichloromethane (30 mL) and the solvent was removed under reduced pressure. The solid was suspended in dichloromethane (60 mL), trimethylamine (1 mL) and H$_2$N-P(2H)-CONH-Fc **H** (66.1 mg, 77.1 µmol, 1.0 eq) were added. The solution was stirred for 14 h and a sample for mass spectrometry was taken, proving the formation of [Cc-CONH-P(2H)-CONH-Fc]$^+$. The solution was washed with water (2x75 mL) to remove excess of cobaltocenium salts. Potassium hexafluoridophosphate (1.01 g, 5.49 mmol, 71 eq), zinc acetate dihydrate (1.10 g, 5.01 mmol, 65 eq) and methanol (50 mL) were added and the solution was stirred under argon atmosphere for 210 min. A UV/vis measurement confirmed full metalation. Water (100 mL) was added and the solution was extracted with dichloromethane (2x 50mL). The organic phase was filtered over a celite pad. The solvent was removed under reduced pressure. ^{1}H NMR spectroscopy showed resonances of a porphyrin and aliphatic impurities. The solid product was overlaid with pentane, sonicated for 5 minutes and filtered over a glas frit. The procedure was repeated, ^{1}H NMR spectroscopy showed less aliphatic impurities but still porphyrin impurities. Purification by standard column chromatography was not possible. On silica, cobaltocenium salts stick on the material, on alumina oxide, porphyrin sticks on the material, extraction of the column material was not successful. Purification by column chromatography was successful on *Supelite DAX-8*, a "nonfunctionalised resin with strong hydrophobic organic matter endorsed to humic and fulvic acids" (Sigma Aldrich). Using less polar solvents, charged molecules stick on the surface, eluting methanol frees the charged molecules. The product was washed with toluene : tetrahydrofurane (2:1) (removing starting material) and eluted with methanol, resulting in a green solution. The solvent was removed under reduced pressure, the product was dissolved in a mixture of acetone : methanol (1:1, 200 mL) and filtered over a celite pad. Potassium

hexafluoridophosphate (250 mg, 1.87 mmol, 24 eq) was added and the solution was stirred for 5 h. The solvent was removed under reduced pressure, the solid was extracted with dichlorethane (50 mL) and the solvent was removed under reduced pressure, yielding 35 mg of **1[PF₆]** as purple powder (27.3 µmol, 35 %). ¹H NMR spectroscopy additionally showed some aliphatic impurities. Therefore, a purification by sonification in pentane was repeated like before, but ¹H NMR spectroscopy showed the cleavage of the ferrocene/amide bond.

[Cc-CONH-P(2H)-CONH-Fc][X] **1[X]** (crude solution): MS (ESI⁺, CH₃OH): obs. *m/z* (%) = 535.65 [M+H]²⁺, 1070.38 (74) [M-H]⁺, 1071.29 (100) [M]⁺; calcd. for [M]⁺ = 1071.25 [M]⁺.

[Cc-CONH-P(Zn)-CONH-Fc][PF₆] **1[PF₆]**: ¹H-NMR: (*d₈*-THF): δ [ppm] = 4.06 (s, 2H, H²³), 4.25 (s, 5H, H²⁴), 4.97 (s, 2H, H²²), 6.01 (s, 5H, H²⁹), 6.06 (s, 2H, H²⁸), 6.57 (s, 2H, H²⁷), 7.70-7.78 (m, 6H, H¹⁰·³,¹⁰·⁴,²⁰·³,²⁰·⁴), 8.17-8.24 (m, 6H, H⁵·²,¹⁰·²,²⁰·²·), 8.26-8.32 (m, 6H, H⁵·³,¹⁵·²,¹⁵·³), 8.82-8.93 (m, 8H, (H²,³,⁷,⁸,¹²,¹³,¹⁷,¹⁸), 9.22 (s, 1H, H^Fc amide), 10.11 (s, 1H, H^Cc+ amide). ³¹P NMR: (*d₈*-THF): δ [ppm] = −144.0 (p, 1P, 711 Hz, P^PF₆).
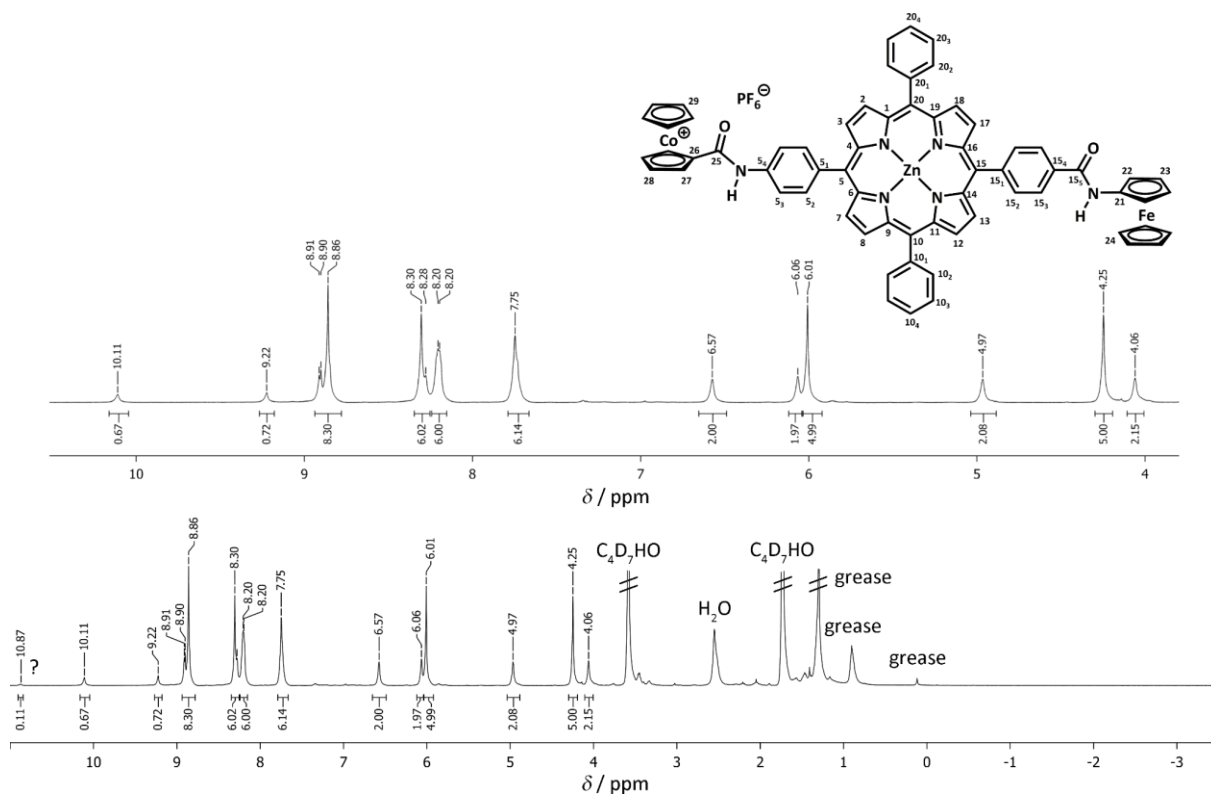

Figure S 21. ¹H NMR spectra of **[Cc-CONH-P(Zn)-CONH-Fc][PF₆] 1[PF₆]** in *d₈*-tetrahydrofuran. Atom numbering for NMR assignment.
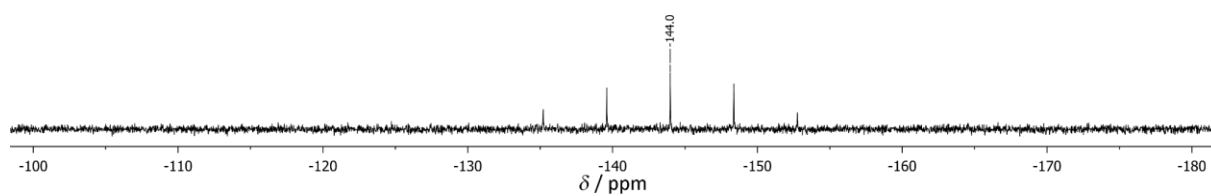
Figure S 22. ^{31}P NMR spectrum of [Cc-CONH-P(Zn)-CONH-Fc][PF$_6$] **1**[PF$_6$] in d_8-tetrahydrofuran.